T2R2 東京工業大学リサーチリポジトリ
Tokyo Tech Research Repository

論文 / 著書情報
Article / Book Information

題目(和文)	チタンドープヒドロキシアパタイト光触媒の開発と応用
Title(English)	Development and Application of Titanium-doped Hydroxyapatite Photocatalyst
著者(和文)	若村正人
Author(English)	Masato Wakamura
出典(和文)	学位:博士(工学), 学位授与機関:東京工業大学, 報告番号:乙第4099号, 授与年月日:2014年5月31日, 学位の種別:論文博士, 審査員:中島　章,鶴見　敬章,田中　順三,坂井　悦郎,松下　祥子,渡部　俊也
Citation(English)	Degree:Doctor (Engineering), Conferring organization: Tokyo Institute of Technology, Report number:乙第4099号, Conferred date:2014/5/31, Degree Type:Thesis doctor, Examiner:,,,,,
学位種別(和文)	博士論文
Type(English)	Doctoral Thesis

Powered by T2R2 (Tokyo Institute Research Repository)

Development and Application of Titanium-doped Hydroxyapatite Photocatalyst

チタンドープヒドロキシアパタイト光触媒の開発と応用

Masato Wakamura

若村　正人

Contents

CHAPTER 1

Introduction

1.1 Calcium hydroxyapatite (CaHAp)

1.1.1 Physical and Chemical Properties of CaHAp

Synthetic calcium hydroxyapatite $Ca_{10}(PO_4)_6(OH)_2$, designated as CaHAp, is a biologically important material used in bioceramics and in some other biomaterials as adsorbents due to its excellent affinity to biomaterials such as proteins. The term "apatite" originates from the Greek word "απαταω"(mislead). Apatite is a group of minerals and its general formulae is $M_{10}(RO_4)_6X_2$ (Table 1). All of these apatite minerals show almost identical XRD patterns featuring weak crystallinity [(1)]. Only a fluoroapatite called CaFAP, a native material, gives large single crystals, and its structure has been confirmed in 1930 [(2)]. CaHAps would easily undergo Ca^{2+} ion exchange with various transition metal ions giving various materials with different properties. They show excellent affinity to bio-organic materials such as proteins, viruses and bacteria.

The thermal properties such as heat capacity, thermal diffusivity and thermal conductivity of sintered bulk CaHAp (sintering temperature 1050 to 1450 °C) have been measured at temperature range between 130 to 1000 K by the laser flash method [(3)]. Typical reported room temperature values were 0.73 J g^{-1} K^{-1}, 0.0057 cm^2 s^{-1} and 0.013 J s^{-1} cm^{-1} K^{-1} respectively. Also some thermodynamic properties such as ΔH_0, ΔG^0 and S at 298.15 K have been compiled [(4)].

The linear (Δa/a) and volume (Δc/c) thermal expansions of CaHAp prepared at 900 °C, measured at temperature between 20 to 900 °C, were 13.5 ppm and 12.7 ppm per °C. A precipitated CaHAp also gave a similar linear thermal expansions of (Δa/a) 12.2 ppm and (Δc/c) 11.5 ppm per °C at the temperatures between 20 to 600 °C [5]. The electrical conductivity of compressed pellets of CaHAp has been measured between 200 and 800 °C. Here, OH^- ions have been considered as the charge carriers [6]. In some other studies, H^+ ions have been suggested as the charge carriers [7].

In these materials, lattice water is lost upon heating above 400 °C, accompanied by a slight contraction of the c-axis parameter. Acid phosphate, which is determined by the HPO_4 IR band at 875 cm^{-1}, may also lose in this temperature range, although the temperature for maximum formation of pyrophosphate from HPO_4^{2-} ions is generally between 400 to 700 °C.

1.1.2 Crystal Structure of CaHAp

The ideal CaHAp crystal is a monoclinic type, but due to lattice deficiencies crystal structure of true CaHAps exhibit an ionic hexagonal type with $P6_3/m$ space group, having 44 atoms per unit cell. The Ca^{2+} ions are separated into two different sites, one is a columnar site along the c axis, and the other is around OH ions. Since CaHAp has a complicated structure, variety of cations can be introduced into the apatite crystal structure (Figure 1). CaHAp is monoclinic with $P2_1/b$ space group [8] and the lattice parameters are: a = 9.4218, b = 2a, c = 6.8814 Å, γ = 120° [9]. Recent synchrotron radiation measurements have shown that b is slightly greater than 2a [10].

In the first investigation on hydrothermally grown CaHAp crystals, the structure was assigned to be in the space group $P6_3/m$ with the hydroxyl oxygen atoms at z = 1/4,

analogous to the fluoro-CaFAP. Later, neutron diffraction studies Holly Springs CaHAp and further XRD studied showed [11] that the hydroxyl oxygen and hydrogen atoms were located at 0, 0, 0.201 and 0, 0, 0.062 respectively, and no OH ions straddled the mirror plane at z = 1/4 within experimental error (Figure 2), except the OH^- ions are in the positions related by the mirror plane at z = 1/4. The positions of the OH^- ions indicated that there was at least short range ordering of these ions into columns, ···OH OH OH OH··· otherwise the hydrogen atoms would be too close. Two models were postulated to reconcile this ordering with the mirror plane of the space group $P6_3/m$ deduced from the diffraction results. They are: (1) a "disordered column" model in which the OH^- ion orientation was reversed at various places within a column; and (2) an "ordered column" model in which all OH^- ions in a given column were oriented the same way, but the choice of direction was random [11]. These models could not be distinguished from the diffraction data. It was proposed that the F^- ion impurities provided a point for column reversal in Holly Springs CaHAp via the sequence ···OH OH F OH OH···. Furthermore, synthetic CaHAp might follow either the "ordered column" model, or alternatively, a "disordered column" model with an occasional OH^- ions across a pseudo-mirror plane at z = 1/4, or an occasional pair of OH^- ions pointing generally towards each other from adjacent pseudo-mirror planes, but making a substantial angle with the c-axis so that the hydrogen atoms did not approach each other too closely [11]. Neutron diffraction results on the position of the hydrogen atom confirmed the orientation of the O-H bond previously determined by polarized IR studies [12]. They also showed that there was a large rocking motion of the hydrogen atom perpendicular to the c-axis about the oxygen atom, which was later confirmed by identification of a vibrational IR mode at 630 cm^{-1}. ESR measurements on monoclinic

CaHAp, after X-irradiation, have suggested that, at 92 K, instead of having a large rocking motion, the OH^- ions were tilted 6 to 7 degree to the c-axis with six orientations about the axis [13]. A precise XRD study of Holly Springs CaHAp has confirmed that the hydroxyl oxygen is on the c-axis with z parameter in the range 0.195 to 0.196. Direct refinement of the degree of substitution showed that 8 % of the OH^- ions were replaced by F^- ions at 0, 0, 1/4 [14].

An XRD study [9] of a single crystal synthetic CaHAp (made by heating ClAP in steam at 1300 °C for two weeks [15]) showed that the space group was $P2_1/b$. This lowering of the symmetry from hexagonal to monoclinic can also be seen in the XRD powder pattern of some CaHAp samples (Figure 3). The explanation given for the monoclinic space group of CaHAp was that the crystal was sufficiently pure so that there were few reversal points within the OH^- ion columns, therefore, the crystal could not adopt a "disordered column" structure, as described above for Holly Springs CaHAps. Instead there must be some arrangement of "ordered columns".

The structure determination confirmed that the OH^- ions were ordered within each column, so that they all had the same direction of displacement from z = 1/4. Furthermore, all the columns oriented in the same direction within a plane parallel to the a- and c- axes, but the direction of the displacements alternated between adjacent planes (Figure 4). The perpendicular separation between the planes was b hex cos30°. This ordered arrangement of OH^- ions changed the mirror planes in $P6_3/m$ into b glide planes in $P2_1/b$, and doubled the b-axis parameter. Therefore, cation substitution in CaHAps can be done easily. (this is used only for negative things), during the last few decades numerous cations have been evaluated to substitute Ca ions in CaHAp [16]–[18]. As for the photocatalytic properties of CaHAp, Nishikawa et al. have reported the generation

of • OH and O_2 • $^-$ radicals on CaHAp after heat treatment at 200°C and UV irradiation, and reported that methyl mercaptane and dimethyl disulfide under do photocatalytic decomposition upon UV irradiation [19]–[24].

1.2 Titanium dioxide

1.2.1 Physical and Chemical Properties of TiO_2

In 1942 Earle reported that rutile and anatase TiO_2 powders are n-type semiconductors, and that the conductivity decreases with increasing the O_2 partial pressure at temperatures above 600 °C [25]. The effect of O_2 was explained on the basis of the equilibrium involving thermal release of O_2 from the lattice. We recognize today that this leads to the creation of Ti^{3+} sites, which are responsible for the electronic conductivity. The activation energy for the electronic conductivity was found to be 1.75 eV for unsintered rutile powder, and 1.7 eV for sintered rutile powder. No evidence for ionic conduction was found. Cronemeyer and Gilleo reported in 1951 that rutile single crystals exhibit a band-gap energy of 3.05 eV [26]. Absorption spectra were reported for both normal and slightly reduced crystals. For the latter, blue color was based on a very broad absorption that peaked at 1.8 μm. In the following year, Cronemeyer published a very extensive study of the electronic properties of single crystal rutile in which the preliminary findings were verified [27]. Detailed photoconductivity measurements were made. Dark conductivity and photoconductivity measurements were also made on a slightly reduced sample (reduction in H_2 at 600 °C). Interestingly, it has been found clear hysteresis in the dark conductivity when the sample was raised from room temperature to 250 °C, and then cooled back to room temperature. After cooling under a high applied electric field, the blue color was found to be concentrated at the negative

electrode. It is believed that this behavior is due to interstitial hydrogen migration.

Strong reduction of various types of samples have been examined at various temperatures between 300 and 1150 °C. Due to strong reduction the samples turned blue–black. The activation energy for electronic conduction has been reported to be 0.07 eV at room temperature, exhibiting a conductivity of ca. 1 Ω^{-1} cm^{-1}. The conductivity was found to increase with increasing the reduction time. A ceramic sheet sample heated in hydrogen at 800 °C was found to undergo a weight loss of 0.1%, corresponding to a release of oxygen that would provide 3×10^{20} electrons per cm^{-3}. Hall effect measurements showed a close agreement between the number of carriers and that of calculated on the basis of the weight loss, indicating that all of the electrons were electrically active.

Tang et al studied the electronic properties of rutile and anatase thin films [28]. There was a large difference between the electronic conductivities of the two types of films after reduction by heating in vacuum at either 400 or 450 °C. The anatase films became mainly metallic, with no change in conductivity with temperature. The rutile films, in contrast, retained measurable activation energies, 0.076 eV at 400 °C and 0.06 eV at 450 °C. The difference in behavior was considered to be due to the following properties of rutile. Since the latter is similar to the distance between Ti^{4+} sites, there is a little overlap between the donor wave functions. Anatase has the following properties: static dielectric coefficient =~30, reduced effective mass =~ 1 m_0, donor state radius =~15 Å. Based on optical absorption spectra, the band-gap energies were estimated to be 3.0 eV for rutile and 3.2 eV for anatase. Forro et al. reported the electronic properties of high purity anatase single crystals, and found the activation energy for electronic conduction to be 0.004 eV [29].

Photocatalysis is generally thought as catalysis of a photochemical reaction at a solid surface, usually a semiconductor [30]-[45]. This simple definition is appropriate, however, it conceals the fact that there must be at least two reactions occurring simultaneously, the first involving oxidation from photogenerated holes, and the second involving reduction from photogenerated electrons. Both processes must be balanced precisely in order to remain the photocatalyst unchanged which is, after all, one of the basic requirements for a catalyst.

As explained in this review, principally on titanium dioxide, there is a series of possible photochemical, chemical and electrochemical reactions that occur on the photocatalyst surface. The types of reactions, their extent and reaction rates are still unknown. Furthermore, indeed, there can be changes that occur involving the surface and bulk structure, and even decomposition of the photocatalyst; a fact that appears to stretch the definition of the term.

The topic of photocatalysis started at its early stage of TiO_2 research, but it was considered a meaningless or has no real meaning to have work on titania-based paints [46], [47]. But later on, this topic gradually developed into a highly useful technology for water and air purification, and then into a method of maintaining surfaces clean and sterile. Along the way, it has also transformed into an approach to photolytically split water into hydrogen and oxygen [48]-[50], and also an approach to perform selective oxidation reactions in organic chemistry [51].

Clearly, with so many varied aspects, it is quite difficult to give a comprehensive review on photocatalysis. In the present review, we have tried to put together an overview of some of the fundamental aspects, which are scientifically interesting and are also needed to be better understood in order to make significant progress in

applications.

1.2.2 Structure of titanium dioxide

There are three main types of TiO_2 structures: rutile, anatase and brookite. The size dependence of the stability of various TiO_2 phases has recently been reported [52], [53]. The particle sizes of the most stable phases of rutile, anatase and brookite are greater than 31 nm, smaller than 11 nm and in between 11-35 nm, respectively, although the Grätzel group found that anatase is the only phase that gives nanocrystalline samples [54], [55].

Rutile has three main crystal faces, two of them have quite low energies and thus they are considered to be important for practical polycrystalline or powder materials [56]. The crystal faces of these are (110) and (100) (Figure 5a, b). The most thermally stable face would be (110), and therefore it has been the face most studied. It has rows of bridging oxygen connected to just two Ti atoms. The corresponding Ti atoms are 6-coordinate. In contrast, there are rows of 5-coordinate Ti atoms running parallel to the rows of bridging oxygen, and alternating with these. The exposed Ti atoms are low in electron density (Lewis acid sites). The (100) (Figure 5b) surface also has alternating rows of bridging oxygen and 5-coordinate Ti atoms, but there exist a different geometric relationship with each other. The (001) face (Figure 5c) is thermally less stable, and restructuring occurs above 475 °C [56]. There are double rows of bridging oxygen alternating with single rows of exposed Ti atoms, which are found to be equatorial type rather than axial.

Anatase has two low energy surfaces, (101) and (001) (Figure 6a, b), which are common in natural crystals [55], [57]. The (101) surface, which is the most prevalent face

for anatase nanocrystals [54] that exhibits a corrugated structure with alternating rows of 5-coordinate Ti atoms and bridging oxygen, which are at the edges of the corrugations. The (001) (Figure 6b) surface is rather flat, but can undergo (1 × 4) reconstruction [57, 58]. The (100) surface is less common in typical nanocrystals, but is observed in rod-like anatase grown hydrothermally under basic conditions (Figure 6c)[55]. This surface has double rows of 5-coordinate Ti atoms alternating with double rows of bridging oxygens. It also undergo a (1 × 2) reconstruction [59].

1.2.3 Self-cleaning surfaces by Photocatalysis property

TiO_2 surface can decompose organic contaminants with the aid of ultraviolet light. This behavior paves the way for the application of TiO_2 photocatalysis as a novel "self-cleaning" technique, i.e. TiO_2 surface coating can maintain the surface clean upon ultraviolet irradiation (Figure 7) [34, 38, 39, 60]. This technique obviously has a great value since it can utilize freely available solar light or waste ultraviolet emission from fluorescent lamps, thus saving maintenance costs, and reducing the use of detergents. Watanabe, Hashimoto and Fujishima first demonstrated this self-cleaning concept on a titania-coated ceramic tile in 1992 [60]. Heller [34] also independently presented a similar idea. One of the first commercialized products using this technique was the self-cleaning cover glass for highway tunnel lamps [38, 43, 61]. This type of lamps, which are often sodium lamps in Japan, emit UV light of about 3 mW cm^{-2} at the surface of the cover glass. This UV light is waste energy of lightings, but it is quite sufficient to decompose the organic contaminants from variety of exhausts. As a result, the cover glass can maintain transparency for long-term use. The efficacy of surface self-cleaning was found to be dependent on the relative rates of decontamination vs.

contamination. The TiO_2 photocatalyst can maintain the surface clean only when the photocatalytic decontamination rate is greater than that of the contamination. Wang et al., however, observed that the self-cleaning effect of TiO_2 surface could be enhanced in the presence of water flow, such as natural rainfall, on the surface [62]. They attributed that this enhancing phenomenon of water flow to the superhydrophilic property of TiO_2 surface, i.e., water penetrates the molecular-level space between the stain and the superhydrophilic TiO_2 surface [43], [44]. In other words, this phenomenon has effectively overcome the limitation of the self-cleaning function of TiO_2 photocatalysis, caused by the insufficient number of incident photons. Even though the number of photons is insufficient to decompose the adsorbed stain, the surface is kept clean when water is supplied to the surface. Thus, they suggested that the best use of self-cleaning TiO_2 surfaces would be in exterior construction materials, since these materials receive abundant sunlight and natural rainfall [38], [43], [44]. Such materials, including tiles, glass, aluminium sidings, plastic films, tent materials, cement and so on have already been commercialized in Japan since the late 1990s, and in other countries in recent years [44], [63]. Some examples are shown in Figure 8. As estimated by TOTO, Ltd., the pioneer of self-cleaning technology, a building in a Japanese city covered with ordinary tiles should be cleaned at least once in every five years to maintain a good appearance, while that covered with self-cleaning tiles remained clean over a span of twenty years without any cleaning. Therefore, self-cleaning technology can lead to large decrease in maintenance costs. We have been examining the efficiency of self-cleaning technology at the Photocatalyst Museum of our Institute. Figure 9 shows the results of one test on a self-cleaning tent material produced by Taiyo Kogyo Co. The tent material, made of PVC film, was coated with TiO_2 photocatalyst material on the left half. The test was

started on July 22nd, 2004; Initially, both the non-coated and TiO_2-coated halves had the same white appearance, as shown in Figure 9a. The photo shown in Figure 9b was taken on April 23rd, 2007. The TiO_2-coated part remains white in the photo, whereas the non-coated part, however, turned dark grey. Note that the tent was placed in a location surrounded by tall buildings, where a little direct sunlight could reach the surface. Nevertheless, even under such conditions, the self-cleaning effect is obvious. On clear days, contaminants accumulate on the whole surface, but during rain, these are washed off of the TiO_2-coated part of the surface. In Japan, several thousand tall buildings have been covered with TOTO's self-cleaning tiles. The Central Japan International Airport, which opened in February, 2005 in Nagoya, Japan, used over 20000 m^2 of self-cleaning glass manufactured by the Nippon Sheet Glass Co. Self-cleaning tent materials have been widely applied for storage structures, business facilities, bus and train stations, sports centers, and sunshades in parks and at seaside. The PanaHome Company, one of the major house manufacturers in Japan, has marketed “eco-life”-type houses since 2003; self-cleaning tiles and windows are provided, in addition to solar cell-covered roof-tops. New applications of self-cleaning technology are also under examination. Zhang et al. recently reported on antireflective TiO_2-SiO_2 self-cleaning coatings that may find application for the cover glass of solar cells [64], [65]. Conventional TiO_2-based coatings are highly reflective due to the large refractive index of the material, and thus the loss of transmittance by TiO_2 can be larger than that caused by contamination layers. Zhang et al. prepared nanoporous TiO_2-SiO_2 coatings that have a low refractive index; the coating enhanced the transmission of the glass exceeding 97% for visible light, greater than that of the usual glass of 90-92% (Figure 10) [64], [65]. TiO_2-coated textiles are another promising application of self-cleaning technology.

Recent studies by Kiwi and co-workers have shown that coffee and wine stains on TiO_2-treated cotton or synthetic textiles can be decolorized under sunlight [66], [67].

1.2.4 Water purification by Photocatalysis property

As noted in a previous chapter, the earliest reports of the cleaning properties of TiO_2 were those of Frank and Bard in 1977, in which they found that suspensions of TiO_2 powder in contaminated water were able to photocatalyze the conversion of cyanide to cyanate, thus detoxifying the water [68], [69]. One of the advantages of TiO_2 photocatalysis for water decontamination is that only the TiO_2 photocatalyst (immobilized or suspended) and UV light, either from solar light or artificial light sources, are needed, and thus the cost can be lower than other kinds of advanced oxidation techniques (UV=O_3; UV=H_2O_2, photo-Fenton). Moreover, no toxic intermediate products are generated in the photocatalytic decontamination process; this makes it very attractive for water cleaning, even for cleaning drinking water [70], [71], [72], [73].

However, it is generally accepted that TiO_2 photocatalysis is feasible only for the treatment of wastewater that contains contaminants at low to medium concentrations, because of its relatively low efficiency and the limited flux of ultraviolet light [72], [74]. Malato and co-workers studied the solar decontamination of industrial [75], agricultural [76], [77] (3,4), and municipal wastewater [78] in a pilot-plant scale, using compound parabolic collector (CPC) reactors and TiO_2 slurry photocatalysts. They observed the complete mineralization of organic matter at concentrations of approximately 50 mg L^{-1} within hours under sunlight. However, the decontamination rate was generally lower for TiO_2 photocatalysis than for the photo-Fenton process in their studies [79], [80]. Herrmann and co-workers reported a solar photo-reactor design based on the multi-step cascade

falling-film principle to ensure good exposure to sunlight and good oxygenation of the effluent to be treated [81]. These workers used an immobilized TiO_2 photocatalyst that was prepared by coating non-woven paper with anatase paste using aqueous SiO_2 colloid as a binder material in order to avoid the filtration procedure required in slurry photo-reactor. This film photo-reactor was found to be as efficient as the CPC slurry photo-reactor for 4-chlorophenol, metanate, and a mixture of pesticides in terms of total degradation under identical solar exposure. One important application of TiO_2 photocatalysis is to remove endocrine disruptor chemicals (EDC) in aqueous environment [82]-[85]. These chemicals which include natural hormones, dioxins, bisphenol-A and so on in aquatic resources have been considered as health hazards for humans, flora and fauna. They are assumed to disrupt normal endocrine functions through interaction with steroid hormone receptors, even at very low concentrations. Conventional biological methods to remove these EDCs require long periods of time, and chemical oxidation methods are in general not economical because of the low concentrations of the EDCs. Nakashima et al. designed a photocatalytic reactor using TiO_2-modified-PTFE mesh sheets as photocatalysts and utilized this to treat the water discharged from the Kitano sewage treatment plant, which is located next to the Tama River near Tokyo [85]. The concentration of estron in the discharged water was 140 ng L^{-1}. Under UV illumination (1.2 mW cm^{-2}), about 90% of the initial estron was decomposed in a very short time, with good reproducibility (Figure 11). Thus, TiO_2 photocatalysis can be applied in the treatment of sewage effluent as a safe method for removing natural and synthetic estrogens. This approach should also be suitable for the removal of other low-level EDCs in the aquatic environment. Hashimoto and co-workers recently reported the application of photocatalytic technology to the

hydroponic cultivation of tomatoes [43]. In conventional hydroponics, tomato plants are planted in an organic culture medium. The culture solution containing nitric acid, phosphoric acid, potash, and others flows through the culture medium in a circulated mode and provides nutrients to the plants. However, organic substances are released into the culture medium during circulation, and as a result, plant pathogens propagate in the system, thus spreading plant diseases. The researchers connected a photocatalytic-water treatment tank to the circulation system and used sunlight to decompose organic substances in solution. The method is effective, as evidenced by the apparent decrease in the total organic carbon in solution and the increased yields of tomatoes. Other important water-purification applications of TiO_2 photocatalysis include water disinfection [86], [87], [88]-[92] demetallization [93], [94] and oxidation of arsenite [95]. For developing countries, solar photocatalytic disinfection appears to be a promising process to produce drinking water, which could help in improving public health. Rincón et al. reported that real lake water contaminated with E. coli K12 at a level of 10^6 CFU mL^{-1} could be disinfected completely within 3 h on a clear day in summer, using a CPC reactor and a TiO_2 slurry catalyst [96]. In comparison, solar light alone is unable to effectively disinfect the contaminated water. Various active oxygen species, such as hydroxyl radicals, superoxide, hydrogen peroxide, singlet oxygen, etc., may participate in the disinfection process. In addition, the self-repairing action of microbes complicates the disinfection process [97].

There have been several types of water-purification systems on the market for various purposes. One of these is designed to remove volatile organic compounds (VOC), such as trichloroethylene, tetrachloroethylene, 1,3-dichlorobenzene, and dichloromethane and etc., from underground water or soil. These substances are widely used as

extracting solvents in industrial processes and in dry cleaning, and are released into the environment in large quantities. The facility basically involves drawing up underground water from a deep well dug in the polluted area, spraying the water to evaporate the VOCs into the gas phase, and decomposing the gaseous VOCs with a photocatalytic air-cleaning unit. VOCs at concentration levels ranging from several hundreds to several thousands of parts per million can be decomposed almost completely to carbon dioxide and hydrochloric acid in such a facility, with a maximum treatment capability of 5 kg VOCs per day in a 15-kW facility.

1.2.5 Air purification by photocatalysis

One of the most important applications of TiO_2 photocatalysis is to decontaminate, deodorize, and disinfect indoor air. Low-concentrations volatile organic compounds (VOCs), such as formaldehyde and toluene, emitted from interior furniture and construction materials, may lead to the "sick building syndrome" and other diseases. Besides, indoor air of public facilities, which are normally contaminated with bacteria, and fungi, threaten the health of users. Conventional air-purification systems often adapt filter-type components for cleaning polluted air. Pollutants are accumulated in the active carbon filters, and the filter becomes saturated with adsorbed substances, and loses its function after a certain period of use. Treatment of the used air filters may cause the risk of secondary pollution. Photocatalytic air-cleaning filters, however, can decompose the organic substances instead of accumulating them, and as a result, exhibit better performance than conventional systems [38], [44], [98], [99], [100]. Moreover, the photocatalytic filter can kill the bacteria floating in indoor air, which is also important for indoor air purification [101], [102]. Figure 12 shows images of two types of photocatalytic filters used

in air-purification devices. The filters feature either a honeycomb type construction or a three-dimensional porous structure for minimum pressure drop. TiO_2 nanoparticles are coated on the body of the filter with active carbon, zeolites, and etc., as co-adsorbents. The co-adsorbents facilitate the adsorption of VOCs on the filter, and ensure that no intermediate gaseous compounds diffuse into the atmosphere. The adsorbed substances diffuse on the surface of the adsorbent until they reach the TiO_2, and then undergo photo-decomposition. The oxidizing species on the photocatalyst can also diffuse to the surface of the adsorbent, and participate in oxidation reactions there. UV light, incidented on the filter surface from black-light lamps, is generally at the level of several mW cm^{-2}; this ensures the rapid mineralization of VOCs that typically exist in concentrations of about 1 ppm or even lower. After long-term use, the filter may be poisoned by HNO_3 or H_2SO_4 formed during removal of ammonia or hydrogen sulfide. In such a case, the poisoned filter can be regenerated by simply washing with water. The available air-cleaning devices based on photocatalytic filters include air cleaners, air conditioners, air-cleaning units for refrigerators, and the like. Among these applications, the air cleaner is the largest. There are more than thirty companies manufacturing photocatalyst-type air cleaners in Japan, with over one hundred product types available on the market. The consumers of photocatalyst-type air cleaners include hospitals, institutions for the elderly, pet stores, offices, smoking rooms, sports clubs, hotels, schools, restaurants, food manufacturers, or any location where indoor air purification is necessary. In addition to air cleaners, deodorizing sheets that are composed of TiO_2 photocatalyst and active carbon adsorbents are also available on the market. The sheet is able to remove malodorous substances in kitchens, refrigerators, vehicles, and shoes through the adsorption function of the activated carbon. Placing the

used sheet in sunlight readily decomposes the adsorbed pollutants by the action of the TiO_2 photocatalyst and regenerates the sheet.

Nitrogen oxides (NO_x) exhausted from automobiles have become a serious threat of air pollution in urban areas. Photocatalytic TiO_2 has the capability of removing nitrogen oxides [103), (104)]. It has been suggested that the nitrogen oxide (NO) in air is oxidized when the catalyst is exposed to light. Then, through the intermediate stage of nitrogen dioxide (NO_2), it is finally converted to nitric acid, which must then be stored. At the nitrogen dioxide stage, part of the gas may escape from the photocatalyst surface, but with an adsorbent like activated carbon mixed with the catalyst, this gas may be effectively trapped [(38)].

The range of concentrations of air pollutants that can be efficiently removed is from 0.01 ppm to 10 ppm. These concentrations correspond to the range from those in the ordinary environmental atmosphere to those in highway tunnels. Some companies in Japan are now considering covering roads with TiO_2 photocatalyst and removing the NOx exhausted from automobiles with sunlight. TiO_2-coated road bricks, which are used to cover pavements, have become available on the market. Interestingly, TiO_2 coatings for roadways are being prepared by mixing colloidal TiO_2 solutions with cement. Nitric acid, formed during the oxidation of nitrogen oxides, reacts with the cement to form calcium nitrate, which can be washed off by rainwater. This method, termed as “photo-road” technology, has been tested in more than fourteen places in Japan over the past nearly ten years (Figure 13). One of the places tested is on the 7th belt highway in Tokyo, with an area of about 300 m^2. Nitrogen oxide removed from this testing area was estimated to be 50-60 mg per day, corresponding to the amount of nitrogen oxide discharged by 1000 automobiles passing by.

More recently, this technology has been developed to a great extent in Europe. In particular, the Italian cement company Italcementi has initiated several demonstration projects, for example, in Rome and Paris, to check the actual photocatalytic effect of a TiO_2-coated highway in the conversion of NO_x and SO_x to more environmentally benign forms like NO_3^- and SO_4^{2-} [105].

1.3 Problems of TiO_2 photocatalysis technology for environmental purification

TiO_2 has been receiving much attention as a photocatalyst that photo-oxidizes organic substances in both water and air [106], [48]. As mentioned in chapter 1.1.2, hydroxyapatite (CaHAp) is used in biological applications. Hence, there is a great interest in preparing of composite materials of TiO_2 and CaHAp for photocatalytic decomposition of biomaterials such as proteins and lipids. Nonami et al. proposed a new structure for TiO_2-CaHAp composite films in which a porous CaHAp layer forms on a TiO_2 layer on a substrate in a pseudo body solution [107]. However, this composite structure was unable to activate photocatalysis, which requires UV irradiation of the TiO_2 layer. We attempted to develop a novel photocatalyst with a high affinity to biomaterials by atomic-level modification of a photocatalytic material and CaHAp, which was realized by modifying CaHAp particles with Ti(IV). The modification of CaHAp particles was performed by co-precipitation and ion exchange methods. Suzuki et al. have found that Ca(II) of CaHAp can be exchanged with various metal ions in aqueous media [108]-[116]. However, the surface structure and properties of the metal-substituted CaHAp have not been confirmed. Ribeiro et al. have studied the surface of CaHAp modified with Ti(IV) ions by immersion methods [117] and indicated the formation of a titanium phosphate,

$Ti(HPO_4)_2.nH_2O$ (n = 1-3), which probably has a double-layered structure [118].

Weiser et al. have coated a CaHAp solution on Ti metal substrate, which has been pre-doped and defused with Ca and P elements [119]. Zeng et al. have studied the adsorption of albumin on calcium phosphate (CaP) and Ti films deposited on a germanium ATR crystal by ion beam sputter deposition using CaHAp and metal Ti targets, and found that the CaP film adsorbs greater amounts of albumin than the surface of metal Ti; CaP shows a higher affinity for protein than metal Ti [120]. Since the CaHAp surface is known to show a high affinity for albumin [121), (122], CaHAp is used as an adsorbent in column chromatography for separating proteins. Feng et al. have reported the bactericidal effects of Ag-CaHAp thin films on alumina [123].

1.4 Objective and strategy of present work

TiO_2 is a conventional photocatalytic material. As photocatalytic degradation of organic materials occurs at the surface the photocatalyst, these organic materials are required to be adsorbed onto the catalyst surface. However, TiO_2 possess weak affinity to organic materials. Therefore, major objectives of this study is to realize a highly efficient catalyst for degradation of organic materials by inducing photocatalytic activity to CaHAp that exhibits a strong affinity to organic materials.

References

(1) Van Wazer, J. R.: Phosphorus and Its Compounds, *Interscience*, New York, (1958).

(2) Naray-Szabo, S.: Z. *Kristallogr*. **75**: 387-398 (1930).

(3) Kijima T, Tsutsumi M: Preparation and thermal properties of dense polycrystalline oxyhydroxyapatite. *J Am Ceram Soc* **62**:455-460 (1979).

(4) Tacker RC, Stormer JC: A thermodynamic model for apatite solid solutions, applicable to hight-temperature geologic problems. *Am Miner* **74**:877-888 (1989).

(5) Perdok WG, Christoffersen J, Arends J: The thermal lattice expansion of calcium hydroxyapatite. *J Cryst Growth* **80**:149-154 (1987).

(6) Takahashi T, Tanase S, Yamamoto O: Electrical conductivity of some hydroxyapatites. *Electrochim Acta* **23**:369-373 (1978).

(7) Maiti GC, Freund F: Influence of fluorine substitution on proton conductivity of hydroxyapatite. *J Chem Soc Dalton Trans*:949-955 (1981).

(8) Elliott JC: Monoclinic space group of hydroxyapatite. *Nature*, Physical Science **72**: 230 (1971).

(9) Elliot JC, Mackie PE, Young RA: Monoclinic hydroxyapatite. *Science* **180**: 1055-1057 (1973).

(10) Bauer M: Rontgenographishe und Dielektrische Untersuchungen an Apatiten. Dissertation, *Fakultat fur Physik*, Universitat Karlsruhe (1991).

(11) Kay MI, Young RA, Posner AS: Crystal structure of hydroxyapatite, *Nature*, **204**: 1050-1052 (1964).

(12) Elliott JC: Further studies of the structure of dental enamel and carbonate apatite using polarized infrared spectroscopy. *J Den Res* **41**: 1251 (1962).

(13) Mengeot M, Bartram RH, Gilliam OR: Paramagnetic hole like defect in irradiated calcium hydroxyapatite single crystals. *Phys Rev B* **11**: 4110-4120 (1975).

(14) Sudarsanan K, Young RA: Significant precision in crystal structural details: Holly Springs hydroxyapatite. *Acta Cryst* **B25**: 1534-1543 (1969).

(15) Elliott JC, Young RA: Conversion of single crystals of chlorapatite into single crystals of hydroxyapatite. *Nature* **214**: 904-6 (1967).

(16) Bjerrum N: Calcium orthophosphate. I. Die Festen Calcium orthophosphate. II. Komplexbildung in Losung von Calcium-und Phosphate-Ionen. *Math.-fys Medd Kong Danske Viden Selskab* 1958; **31**: 1-79. (Translated by M H Rand, Atomic Energy Res Est, Harwell, UK, Trans 841, 1959).

(17) Newesly H: Kristallche und mikromorphologische Untersuchungen schwerlo slicher Calciumphosphate. *Fortschr Chem Forsch* **5**:688-746 (1966).

(18) Gmelins Handbuch der Anorganischen Chemie, Calcium, Part 3, Lieferung 3, System No 28. *Weinheim, Verlag Chemie*, 1115-1223 (1961).

(19) Benard J: Combinations avec le phosphore; in Pascal P (ed): Nouveau Traite de Chimie Minerale, Tome IV, Le Calcium. Masson et C^{ie}, 455-488 (1958).

(20) Van Wazer JR: Phosphorus and its Compounds, Vol 1, New York, *Interscience Publishers*, 1958.

(21) Mooney RW, Aia M: Alkaline earth phosphates. *Chem Rev*, **61**:433-462(1961).

(22) Young RA, Brown WE: Structures of biological minerals; in Nancollas GH (ed): Biological Mineralization and Demineralization, Dahlem Konferenzen, 1981. Berlin, Springer-Verlag, 1982, pp 101-141.

(23) Brown EH, Lehr JR, Smith JP, Frazier AW: Preparation and characterization of some calcium pyrophosphates. *J Agr Food Chem* **11**: 214-222(1963).

(24) Lehr JR, Brown EH, Frazier AW, Smith JP, Thransher RD: Crystallographic Properties of Fertilizer Compounds, *Chemical Engineering Bulletin* **No 6.** Muscle Shoals, Tennessee Vally Authority, 1967.

(25) M.D. Earle: *Phys. Rev.* **61**: 56-62 (1942).

(26) D.C. Cronemeyer, M.A. Gilleo: *Phys. Rev*. **82**: 975 (1951).

(27) D.C. Cronemeyer: *Phys. Rev*. **87**: 876 (1952).

(28) H. Tang, K. Prasad, R. Sanjines, P.E. Schmid, F. Levy: *J. Appl. Phys*. **75**: 2042–2047(1994).

(29) L. Forro, O. Chauvet, D. Emin, L. Zuppiroli, H. Berger, F. Lévy: J. *Appl. Phys*. **75**: 633(1994).

(30) E. Pelizzetti, N. Serpone(Eds.), Homogeneous and Heterogeneous Photocatalysis, D. Reidel Publishing Company, Dordrecht, 1986.

(31) N. Serpone, E. Pelizzetti (Eds.), Photocatalysis Fundamentals and Applications, John Wiley & Sons, New York, 1989.

(32) P.V. Kamat, *Chem. Rev*. **93** (1993) 267.

(33) D. F. Ollis, H. Al-Ekabi (Eds.), Photocatalytic Purification and Treatment of Water and Air, Elsevier, Amsterdam, 1993.

(34) A. Heller, *Acc. Chem. Res.* **28** (1995) 503–508.

(35) M. R. Hoffmann, S. T. Martin, W. Choi, D. W. Bahnemann, *Chem. Rev.* **95** (1995) 69–96.

(36) A. Mills, S. LeHunte, *J. Photochem. Photobiol. A*: Chem. **108** (1997) 1–35.

(37) J. Peral, X. Domènech, D. F. Ollis, *J. Chem. Tech. Biotech*. **70** (1997) 117–140.

(38) A. Fujishima, K. Hashimoto, T. Watanabe, TiO_2 Photocatalysis: Fundamentals and Applications, BKC, Inc., Tokyo, 1999.

(39) A. Fujishima, T. N. Rao, D. A. Tryk, *J. Photochem. Photobiol. C* **1** (2000) 1–21.

(40) D. F. Ollis, C. R. Acad. *Sci. Paris, Serie II C, Chim*. **3** (2000) 405–411.

(41) D. A. Tryk, A. Fujishima, K. Honda, *Electrochim. Acta* **45** (2000) 2363–2376.

(42) A. Fujishima, D. A. Tryk, in: A. J. Bard, M. Stratmann, S. Licht (Eds.), Encyclopedia of Electrochemistry, Vol. 6: Semiconductor Electrodes and Photoelectrochemistry, Weinheim, 2002.

(43) K. Hashimoto, H. Irie, A. Fujishima, *Japan. J. Appl. Phys*. **44** (2005) 8269–8285.

(44) A. Fujishima, X. Zhang, *C. R. Chimie* **9** (2006).

(45) A. Fujishima, X. Zhang, D. A. Tryk, *Internat. J. Hydrogen Energy* **32** (2007) 2664–2672.

(46) C. Renz, *Helv. Chim. Acta* **4** (1921) 961–968.

(47) A.E. Jacobsen, *Ind. Eng. Chem.* **41** (1949) 523–526.

(48) A. Fujishima, K. Honda, *Nature* **238** (1972) 37–38.

(49) T. Watanabe, A. Fujishima, K. Honda, in: T. Ohta (Ed.), *Solar-Hydrogen Energy Systems,* Oxford, 1979, pp. 137–169.

(50) A. Fujishima, Innovative Hydrogen Production from Water (UNESCO), 2000.

(51) M.A. Fox, M.T. Dulay, *Chem. Rev.* **93** (1993) 341–357.

(52) H. Zhang, J. F. Banfield, *J. Phys. Chem. B* **104** (2000) 3481–3487.

(53) M. R. Ranade, A. Navrotsky, H. Z. Zhang, J. F. Banfield, S. H. Elder, A. Zaban, P. H. Borse, S. K. Kulkarni, G. S. Doran, H. J. Whitfield, *Proc. Nat. Acad. Sciences* **99** (2002) 6476–6481.

(54) V. Shklover, M. K. Nazeeruddin, S. M. Zakeeruddin, C. Barbe, A. Kay, T. Haibach, W. Steurer, R. Hermann, H. U. Nissen, M. Grätzel, *Chem. Mater.* **9** (1997) 430–439.

(55) S. D. Burnside, V. Shklover, C. Barbe, P. Comte, F. Arendse, K. Brooks, M. Grätzel, *Chem. Mater.* **10** (1998) 2419–2425.

(56) M. Ramamoorthy, D. Vanderbilt, R.D. King-Smith, *Phys. Rev. B* **49** (1994) 16721.

(57) R. Hengerer, B. Bolliger, M. Erbudak, M. Grätzel, *Surf. Sci.* **460** (2000) 162-169.

(58) Y. Liang, S. Gan, S.A. Chambers, E.I. Altman, *Phys. Rev. B* **63** (2001) 235-402.

(59) N. Ruzycki, G.S. Herman, L.A. Boatner, U. Diebold, *Surf. Sci.* **529** (2003) L239-L244.

(60) T. Watanabe, K. Hashimoto, A. Fujishima, 1st International Conference on TiO_2 Photocatalytic Purification and Treatment of Water and Air, 1992.

(61) H. Honda, A. Ishizaki, R. Sama, K. Hashimoto, A. Fujishima, *J. Illuminat. Eng. Soc. Winter* (1998) 1998.

(62) R. Wang, K. Hashimoto, A. Fujishima, M. Chikuni, E. Kojima, A. Kitamura, M. Shimohigoshi, T. Watanabe, *Adv. Mater.* **10** (1998) 135–138.

(63) L. Cassar, *MRS Bulletin* **29** (2004) 328-331.

(64) X.T. Zhang, O. Sato, M. Taguchi, Y. Einaga, T. Murakami, A. Fujishima, *Chem. Mater.* **17** (2005) 696-700.

(65) X. Zhang, A. Fujishima, M. Jin, A.V. Emeline, T. Murakami, *J. Phys. Chem. B* **110** (2006) 25142-25148.

(66) A. Bozzi, T. Yuranova, I. Guasaquillo, D. Laub, J. Kiwi, *J. Photochem. Photobiol. A: Chem.* **174** (2005) 156–164.

(67) A. Bozzi, T. Yuranova, J. Kiwi, *J. Photochem. Photobiol. A: Chem.* **172** (2005) 27–34.

(68) S. N. Frank, A. J. Bard, *J. Am. Chem. Soc.* **99** (1977) 303–304.

(69) S. N. Frank, A. J. Bard, *J. Phys. Chem.* **81** (1977) 1484–1488.

(70) D. F. Ollis, E. Pelizzetti, N. Serpone, *Environ. Sci. Technol.* **25** (1991) 1522–1529.

(71) D. Bahnemann, *Solar Energy* **77** (2004) 445–459.

(72) J. Blanco-Galvez, P. Fernandez-Ibanez, S. Malato-Rodriguez, *J. Solar Energy Eng.* **129** (2007) 4–15.

(73) J. M. Herrmann, *Top. Catalysis* **34** (2005) 49–65.

(74) T. N. Rao, A. Fujishima, D. A. Tryk, in: A. J. Bard, M. Stratmann, S. Licht (Eds.), Encyclopedia of Electrochemistry, in: *Semiconductor Electrodes and Photoelectrochemistry*, **vol. 6**, Weinheim, 2002.

(75) M. Kositzi, A. Antoniadis, I. Poulios, I. Kiridis, S. Malato, *Solar Energy* **77** (2004) 591–600.

(76) I. Oller, W. Gernjak, M. I. Maldonado, L. A. Pérez-Estrada, J. A. Sánchez-Pérez, S. Malato, *J. Hazard. Mater.* **138** (2006) 507–517.

(77) M. H. Pérez, G. Peñuela, M. I. Maldonado, O. Malato, P. Fernández-Ibáñez, I. Oller, W. Gernjak, S. Malato, *Appl. Catal. B: Environ.* **64** (2006) 272–281.

(78) M. Kositzi, I. Poulios, S. Malato, *J. Caceres, A. Campos, Water Res.* **38** (2004) 1147–1154.

(79) I. Oller, W. Gernjak, M. Maldonado, P. Fernández-Ibáñez, J. Blanco, J. Sánchez-Pérez, *S. Malato, Environ. Chem. Lett.* **3** (2005) 118–121.

(80) M. I. Maldonado, P. C. Passarinho, I. Oller, W. Gernjak, P. Fernández, J. Blanco, S. Malato, *J. Photochem. Photobiol. A: Chem.* **185** (2007) 354–363.

(81) C. Guillard, J. Disdier, C. Monnet, J. Dussaud, S. Malato, J. Blanco, M.I. Maldonado, J.-M. Herrmann, *Appl. Catal. B: Environ.* **46** (2003) 319–332.

(82) Y. Ohko, I. Ando, C. Niwa, T. Tatsuma, T. Yamamura, T. Nakashima, Y. Kubota, A. Fujishima, *Environ. Sci. Technol.* **35** (2001) 2365–2368.

(83) Y. Ohko, K. Iuchi, C. Niwa, T. Tatsuma, T. Nakashima, T. Iguchi, Y. Kubota, A. Fujishima, *Environ. Sci. Technol.* **36** (2002) 4175–4181.

(84) T. Nakashima, Y. Ohko, D. A. Tryk, A. Fujishima, *J. Photochem. Photobiol. A: Chem.* **151** (2002) 207–212.

(85) T. Nakashima, Y. Ohko, Y. Kubota, A. Fujishima, *J. Photochem. Photobiol. A: Chem.* **160** (2003) 115–120.

(86) C. McCullagh, J. M. C. Robertson, D. W. Bahnemann, P. K. J. Robertson, *Res. Chem. Intermed.* **33** (2007) 359–375.

(87) T. Matsunaga, R. Tomoda, T. Nakajima, H. Wake, *FEMS Microbiol. Lett.* **29** (1985) 211–214.

(88) T. Saito, T. Iwase, J. Horie, T. Morioka, *J. Photochem. Photobiol. B: Biol.* **14** (1992) 369–379.

(89) Z. Huang, P. C. Maness, D. M. Blake, E. J. Wolfrum, S. L. Smolinski, W. A. Jacoby, *J. Photochem. Photobiol. A: Chem.* **130** (2000) 163–172.

(90) A. G. Rincón, C. Pulgarin, *Appl. Catal. B: Environ.* **51** (2004) 283–302.

(91) P. Fernández, J. Blanco, C. Sichel, S. Malato, *Catal. Today* **101** (2005) 345–352.

(92) E. F. Duffy, et al., *Solar Energy* **77** (2004) 649–655.

(93) M. I. Litter, *Appl. Catal. B: Environ.* **23** (1999) 89–114.

(94) M. R. Prairie, L. R. Evens, B. M. Stange, S. L. Martinez, *Environ. Sci. Technol.* **27** (1993) 1776–1782.

(95) M. A. Ferguson, M. R. Hoffmann, J. G. Hering, *Environ. Sci. Technol.* **39** (2005) 1880–1886.

(96) A. G. Rincón, C. Pulgarin, *Solar Energy* **77** (2004) 635–648.

(97) T. Matsunaga, R. Tomoda, T. Nakajima, H. Wake, *FEMS Microbiol. Lett.* **29** (1985) 211–214.

(98) W. K. Jo, K. H. Park, *Chemosphere* **57** (2004) 555–565.

(99) P. Pichat, J. Disdier, C. Hoang Van, D. Mas, G. Goutailler, C. Gaysse, *Catal. Today* **63** (2000) 363–369.

(100) C. H. Ao, S. C. Lee, *J. Photochem. Photobiol. A: Chem.* **161** (2004) 131–140.

(101) J. H. Kim, G. Seo, D. L. Cho, B. C. Choi, J. B. Kim, H. J. Park, M. W. Kim, S. J. Song, G. J. Kim, S. Kato, *Catal. Today* **111** (2006) 271–274.

(102) S. A. Grinshpun, A. Adhikari, T. Honda, K. Y. Kim, M. Toivola, K. S. Ramchander Rao, T. Reponen, *Environ. Sci. Technol.* **41** (2007) 606–612.

(103) T. Ibusuki, K. Takeuchi, *J. Mol. Catal.* **88** (1994) 93–102.

(104) H. Ichiura, T. Kitaoka, H. Tanaka, *Chemosphere* **51** (2003) 855–860.

(105) Italcementi, http://www.italcementigroup.com/ENG/Research+and+ Innovation/Innovative+Products/Innovative+Products.htm, 2008.

(106) A. Fujishima and K. Honda: Photosensitive electrode reactions. III. Electrochemical evidence for the mechanism of the primary stage of photosynthesis. *Bull. Chem. Soc. Jpn.*, **44,** 4, p.1148-1150 (1971).

(107) T. Nonami and H. Taoda: Apatite Formation on TiO_2 Photocatalyst Film in a Pseudo Body Solution. *Materials Research Bulletin,* **33,** 1, p.125-132 (1998).

(108) T. Suzuki and Y. Hayakawa: *Proc. First Int Congr. on Phosphorus Compounds IMPHOS Paris*, p.381 (1977).

(109) T. Suzuki, T. Hatsushika, and Y. Hayakawa: Synthetic hydroxyapatites employed as inorganic cation exchangers. *J. Chem. Soc. Faraday Trans.,* **77,** 5, p.1059-1062 (1981).

(110) T. Suzuki, T. Hatsushika, and M. Miyake: Synthetic hydroxyapatites as inorganic cation exchangers. Part 2. *J. Chem. Soc. Faraday Trans. I,* **78,** 12, p.3605-3611 (1982).

(111) M. Miyake, T. Kobayashi, and T. Suzuki: Structural change of synthetic hydroxyapatite by ion- exchange reaction; cation exchange characteristics for tin (2+) ions. *Yogyo-Kyokai-Shi.* (in Japanese), **94,** 8, p.832-836 (1986).

(112) M. Miyake, K. Ishigaki, and T. Suzuki: Structure refinements of Pb^{2+} ion-exchanged apatites by x-ray powder pattern-fitting. *J. Solid State Chem.,* **61,** 2, p.230-235 (1986).

(113) Y. Tanizawa, T. Ujiie, K. Sawamura, and T. Suzuki: Reaction characteristics between dental apatite and tin (2+) ion. (in Japanese), *Denki Kagaku oyobi Kogyo Butsuri Kagaku,* **55,** 12, p.903-908 (1987).

(114) Y. Tanizawa, K. Sawamura, and T. Suzuki: Reaction characteristics of dental and synthetic apatites with iron (II) and iron (III) ions. *J. Chem. Soc. Faraday Trans.,* **86,** 7, p.1071-1075 (1990).

(115) Y. Tanizawa, K. Sawamura, and T. Suzuki: Reaction characteristics of dental and synthetic apatites with aluminum (III) and lanthanum (III) ions in acidic solutions. *J. Chem. Soc. Faraday Trans.,* **86,** 24, p.4025-4029 (1990).

(116) T. Suzuki and T. Hatsushika: Lattice-ion reaction characteristics of hydroxyapatite for iron(2+), iron(3+), and lead(2+) ions in acidic aqueous solutions. (in Japanese), *Gypsum and Lime,* **224,** p.15-20 (1990).

(117) C. C. Ribeiro, M. A. Barbosa, and A. A. S. C. Machado: Modifications in the molecular structure of hydroxyapatite induced by titanium ions. *J. Material Science Material in Medicine,* **6,** 12, p.829-834 (1995).

(118) S. R. Leadley, M. C. Davies, C. C. Ribeiro, M. A. Barbosa, A. J. Paul, and J. F. Watts: Investigation of the dissolution of the bioceramic hydroxyapatite in the presence of titanium ions using ToF-SIMS and XPS. *Biomaterials,* **18,** 4, p.311-316 (1997).

(119) E. Wieser, I. Tsyganov, W. Matz, H. Reuther, S. Oswald, T. Pham, and E. Richter: Modification of titanium by ion implantation of calcium and/or phosphorus. *Surface and Coatings Technology,* **111,** 1, p.103-109 (1999).

(120) H. Zeng, K. K. Chittur, and W. R. Lacefield: Analysis of bovine serum albumin adsorption on calcium phosphate and titanium surfaces. *Biomaterials,* **20,** 4, p.377-384 (1999).

(121) K. Kandori, T. Shimizu, A. Yasukawa, and T. Ishikawa: Adsorption of bovine serum albumin onto synthetic calcium hydroxyapatite: influence of particle texture. *Colloids and Surfaces B,* **5,** 1/2, p.81 (1995).

(122) K. Kandori, N. Horigami, H. Kobayashi, A. Yasukawa, and T. Ishikawa: J. Colloid Interface Sci., 191, p.498 (1997).

(123) Q. L. Feng, T. N. Kim, J. Wu, E. S. Park, J. O. Kim, D. Y. Lim, and F. Z. Cui: Antibacterial effects of Ag-HAp thin films on alumina substrates. *Thin Solid Films,* **335,** 1-2, p.214-219 (1998).

Table 1 Structural ion species of apatite.

site	ion species
M	H^{+}, Na^{+}, K^{+} Ca^{2+}, Sr^{2+}, Ba^{2+}, Pb^{2+}, Zn^{2+}, Cd^{2+}, Mg^{2+}, Fe^{2+}, Mn^{2+}, Ni^{2+}, Cu^{2+}, Hg^{2+} Al^{3+}, Y^{3+}, Ce^{3+}, Nd^{3+}, La^{3+}, Dy^{3+}, Eu^{3+}
RO_4	SiO_4^{2-}, CO_3^{2-}, HPO_4^{2-}, PO_3F^{2-} PO_4^{3-}, AsO_4^{3-}, VO_4^{3-}, CrO_4^{3-}, BO_3^{3-} SiO_4^{4-}, GeO_4^{4-} BO_4^{5-}, AlO_4^{5-}
X	OH^{-}, F^{-}, Cl^{-}, Br^{-}, I^{-} O^{2-}, CO_3^{2-} H_2O, vacancy

Greek : απαταω (delude, unknown)
Apatite
$M_{10}(RO_4)_6X_2$

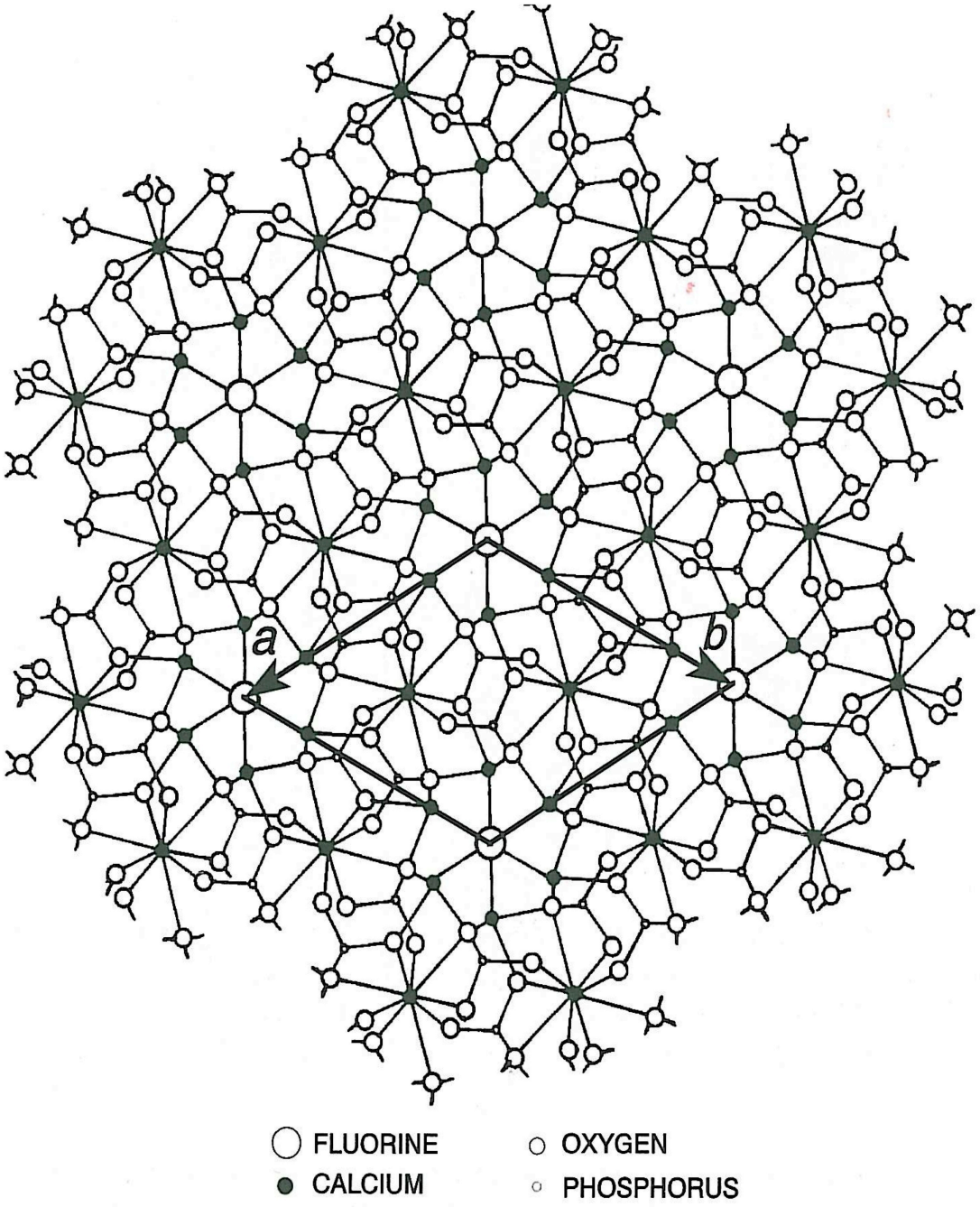

Figure 1 Projection of the apatite structure on to the basal plane (0001). The c-axis is out of the plane of the paper and the a- and b-axes are as marked on the outline of a unit cell.

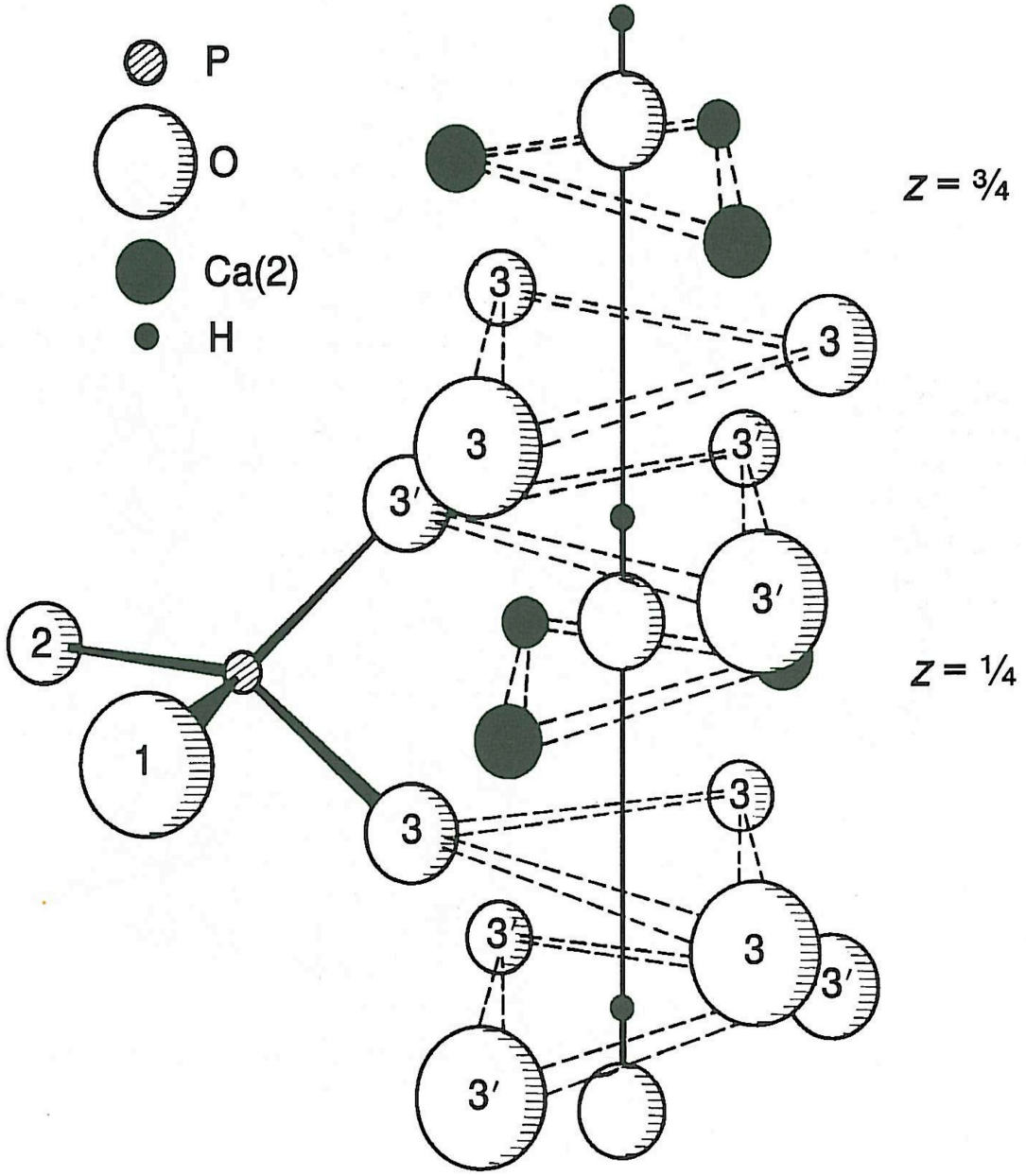

Figure 2 Arrangement of the ions around the vertical axis at the corners of the apatite unit cell in Figure 1. This axis is sometimes called the hexad or c-axis channel. The F^- ion is at the center of the triangle of Ca(2) ions, but the OH^- (illustrated) and Cl^- ions are above this position.

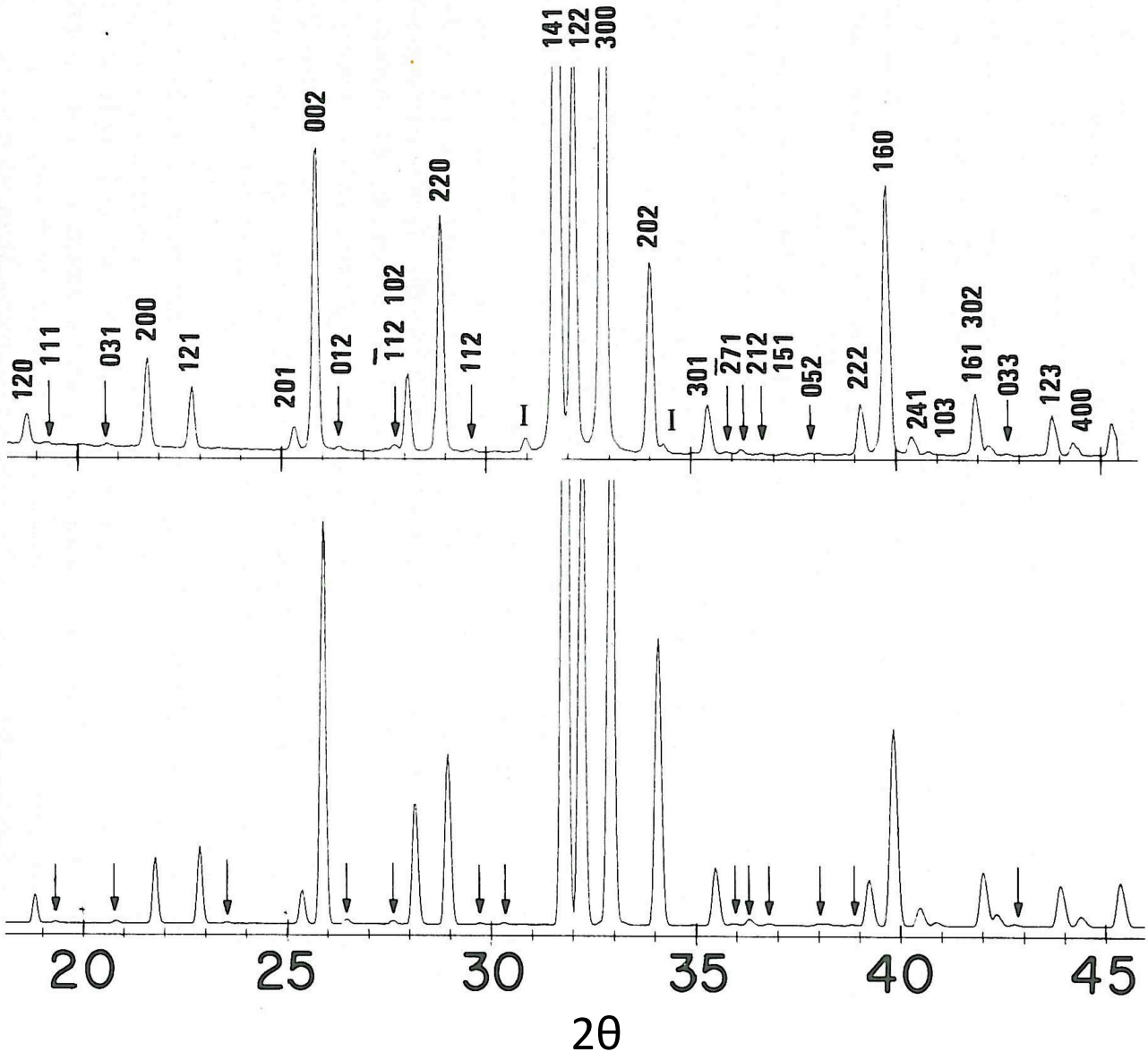

Figure 3 Observed (up) and calculated (down) XRD patterns (CuKα) of monoclinic CaHAp made by heating monoclinic ClAp powder in steam at 1300 °C . Monoclinic lines are arrowed and the I lines are β-TCP impurity.

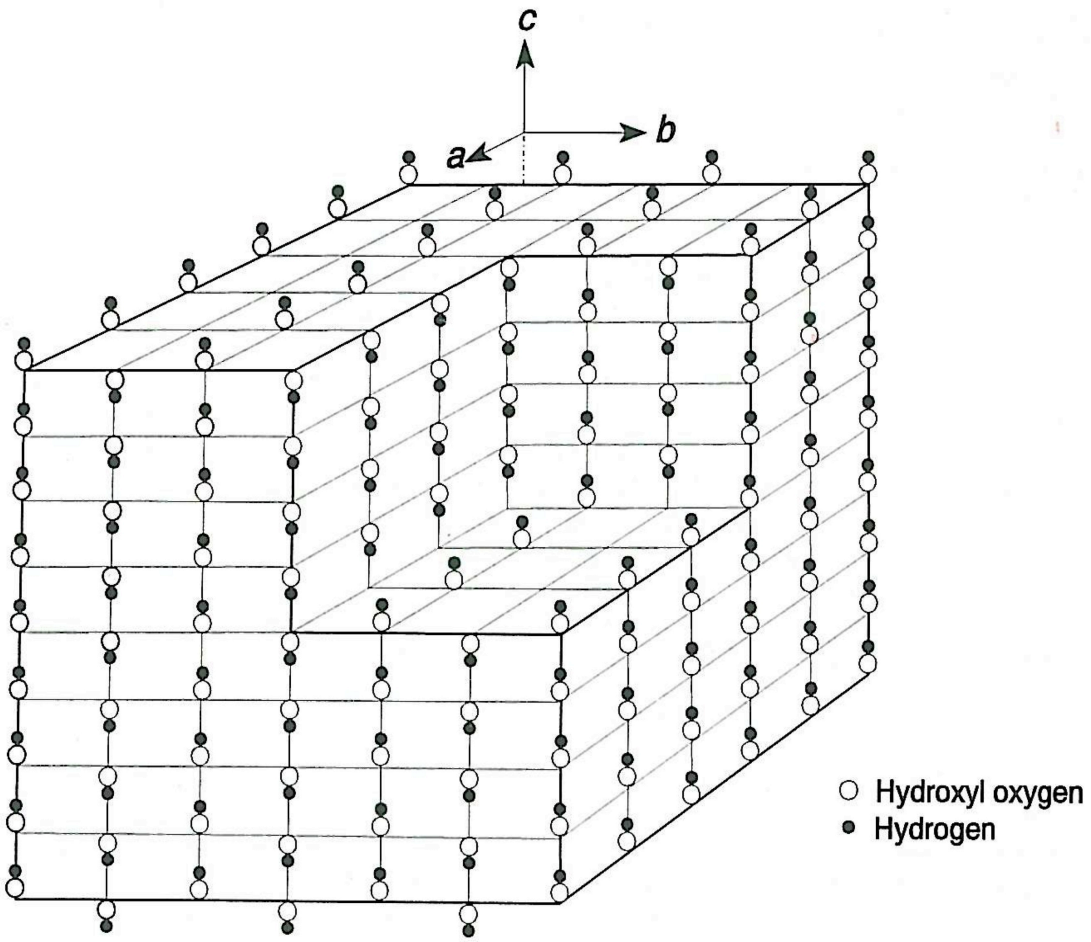

Figure 4 Ordered sheets of OH^- ions in monoclinic CaHAp. Note that the origin of the axes is displaced by 1/4b from the pseudohexagonal axis.

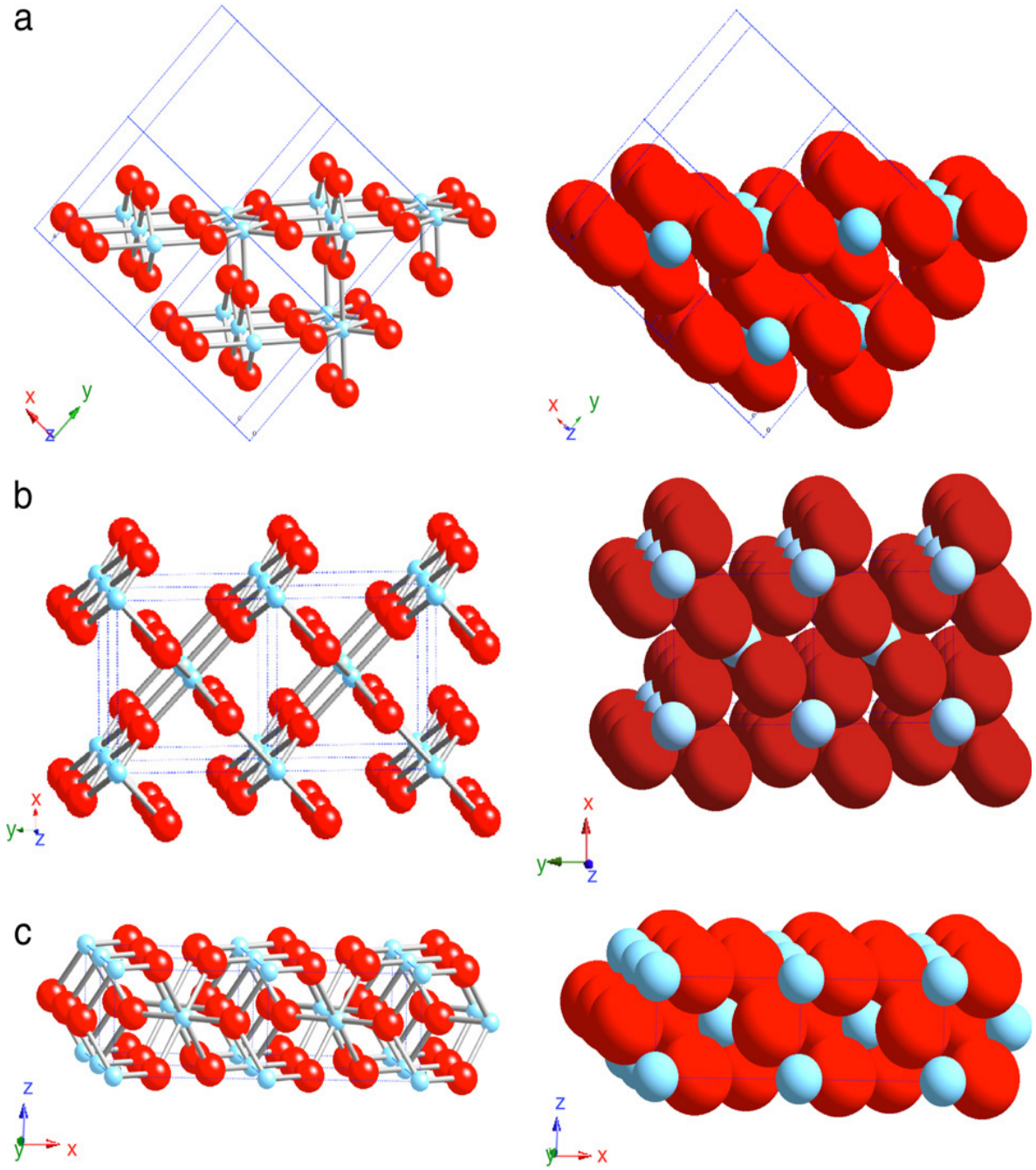

Figure 5 Schematic representations of selected low-index faces of rutile: (a) (110); (b) (100); and (c) (001).

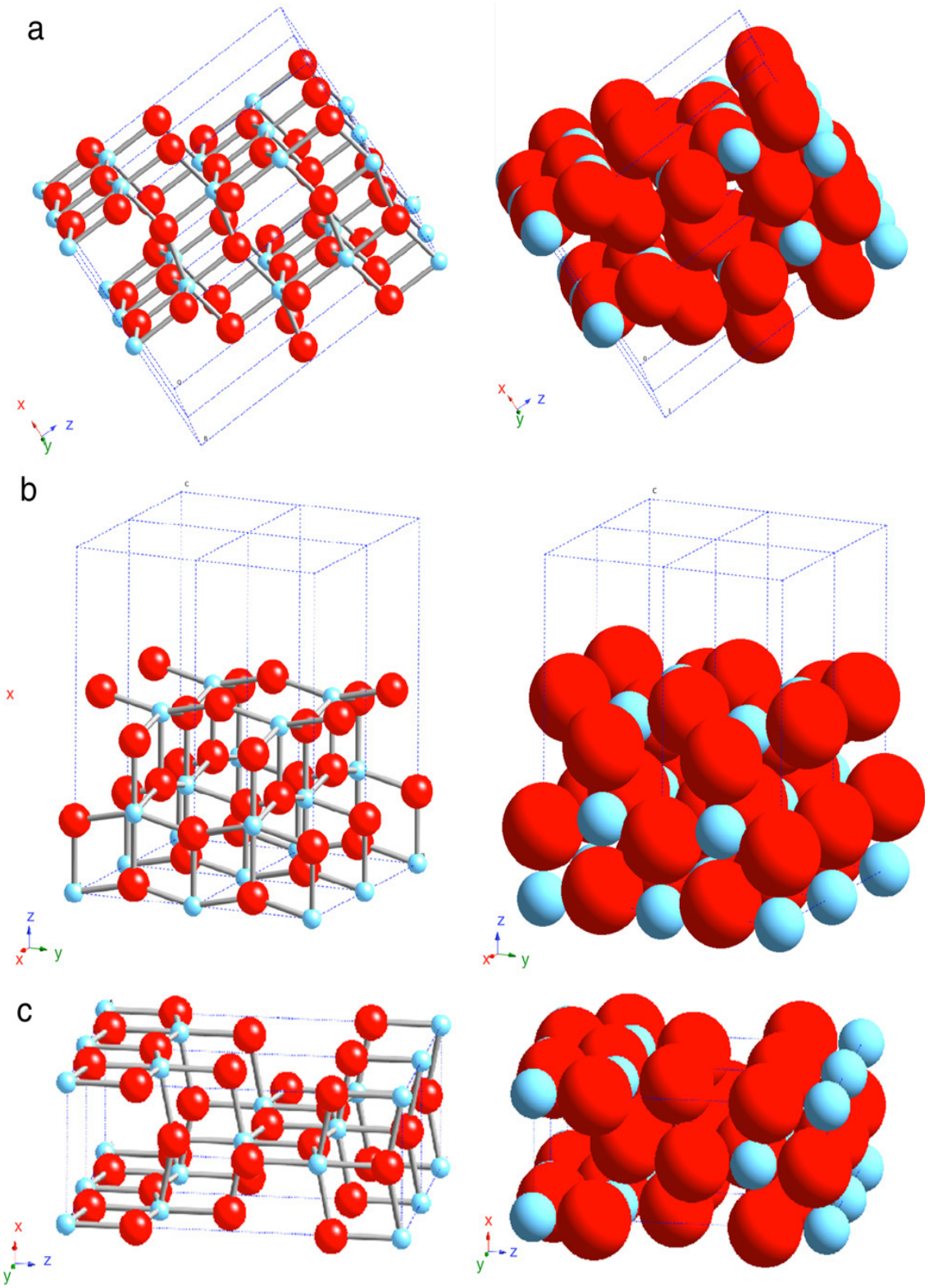

Figure 6 Schematic representations of selected low-index faces of anatase: (a) (101); (b) (100); and (c) (001).

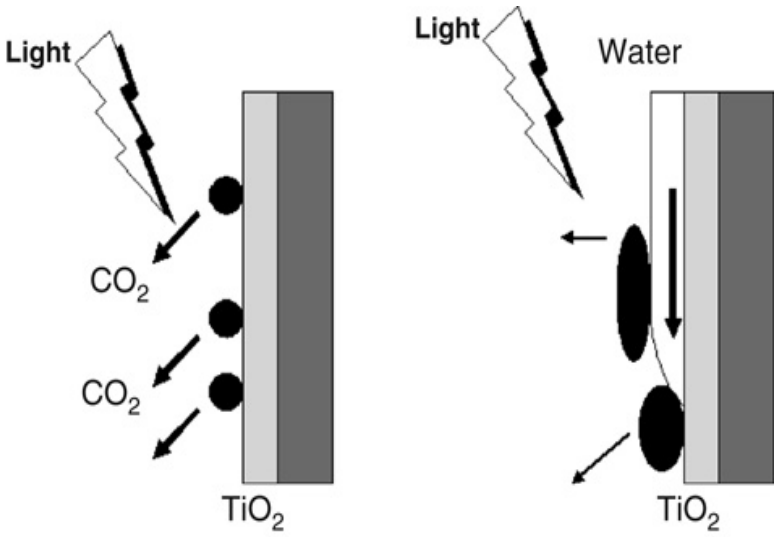

Figure 7 Schematic diagram of the decontamination process occurring on the superhydrophilic self-cleaning surface.

Figure 8 Application of self-cleaning exterior building materials. (a) Picture of the MM Towers, in Yokohama, coated with self-cleaning tiles (courtesy of TOTO). (b) Picture of the Matsushita Denso building covered with self-cleaning glass (courtesy of Nippon Sheet Glass). (c) Picture of the self-cleaning sound-proof wall (courtesy of Sekisui). (d) Eco-life-type houses using self-cleaning tiles and glass (courtesy of PanaHome). (e) Self-cleaning roof of a train station in Motosumiyoshi (courtesy of Taiyo Kogyo).

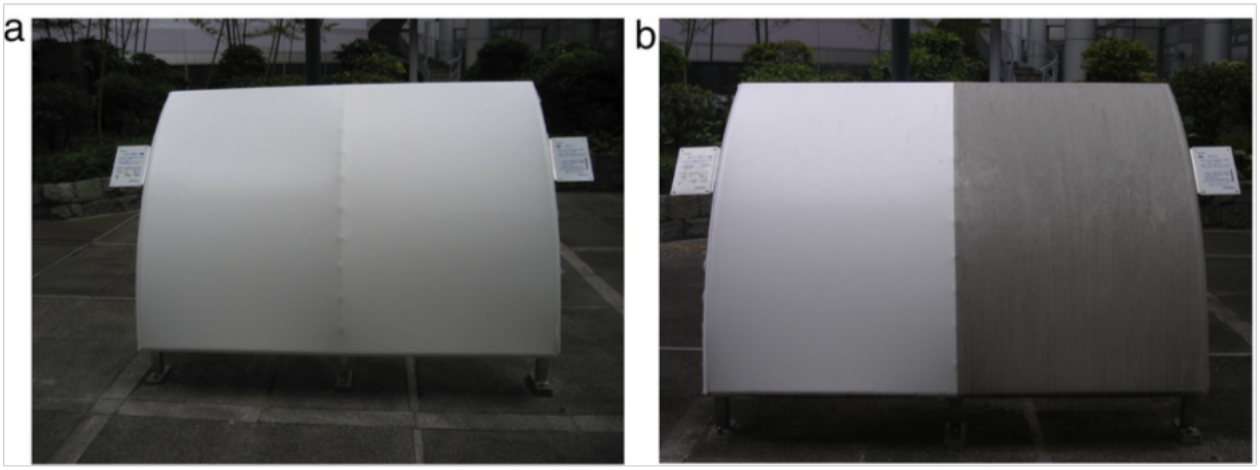

Figure 9 Outdoor exposure test for a PVC tent material manufactured by Taiyo Kogyo done in the Photocatalyst Museum, KAST. The left half part of the tent material was coated with TiO_2. (a) Picture taken in July 22, 2004. (b) Picture taken in April 23, 2007.

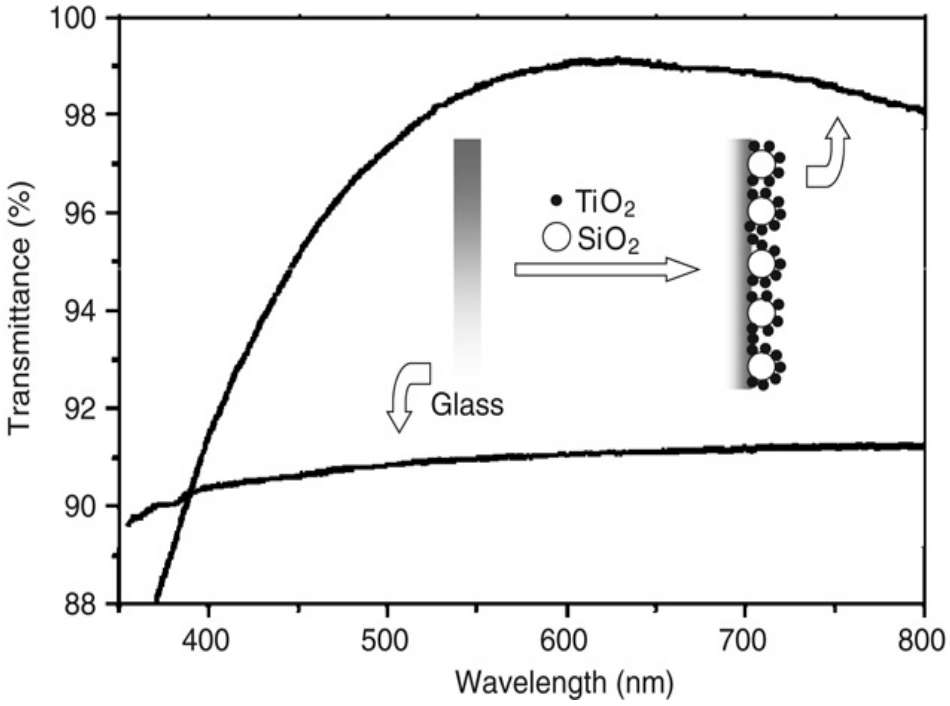

Figure 10 Transmission spectra of a bare glass and a glass coated with TiO_2-SiO_2 composite film. The maximum transmittance for the coated glass could be over 99%.

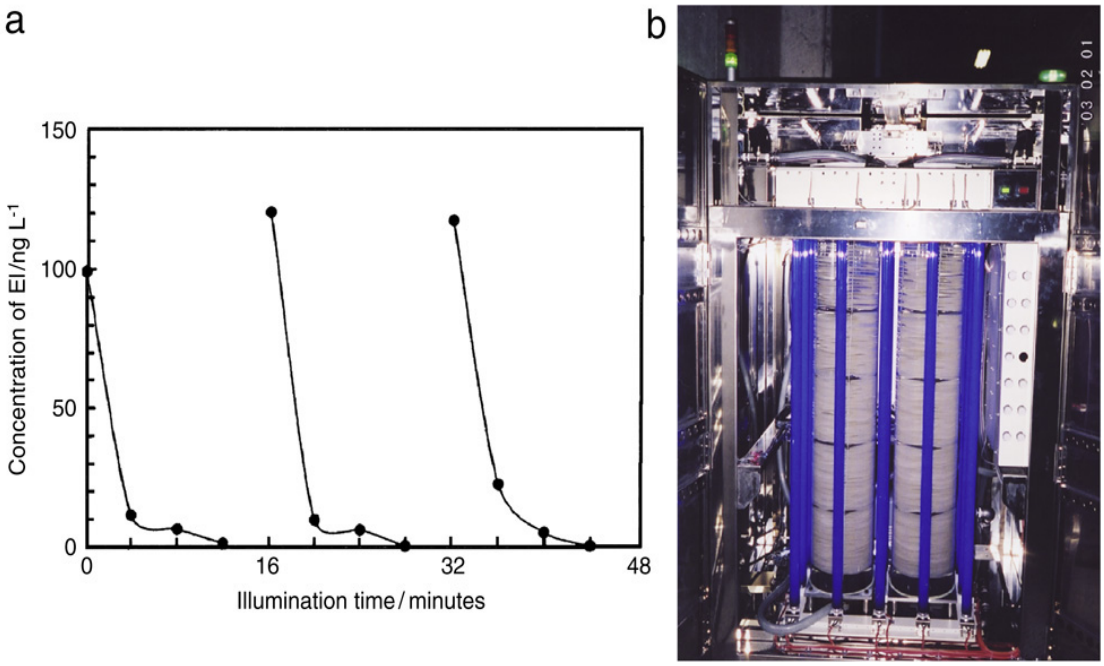

Figure 11 (a) Concentration change of estron (E1) in water discharged from a sewage-treatment plant during photocatalysis. The measurement was repeated three times (UV light intensity, 1.2 mW cm^{-2}; water temperature, 15 °C). (b) Picture of a photocatalytic reactor for treatment of sewage water. The reactor consists of two 34-L columns, 100 pieces of TiO_2-coated PTFE mesh sheet, and 12 black-light (40W) lamps which gave a light intensity of about 1.2 mW cm^{-2}.

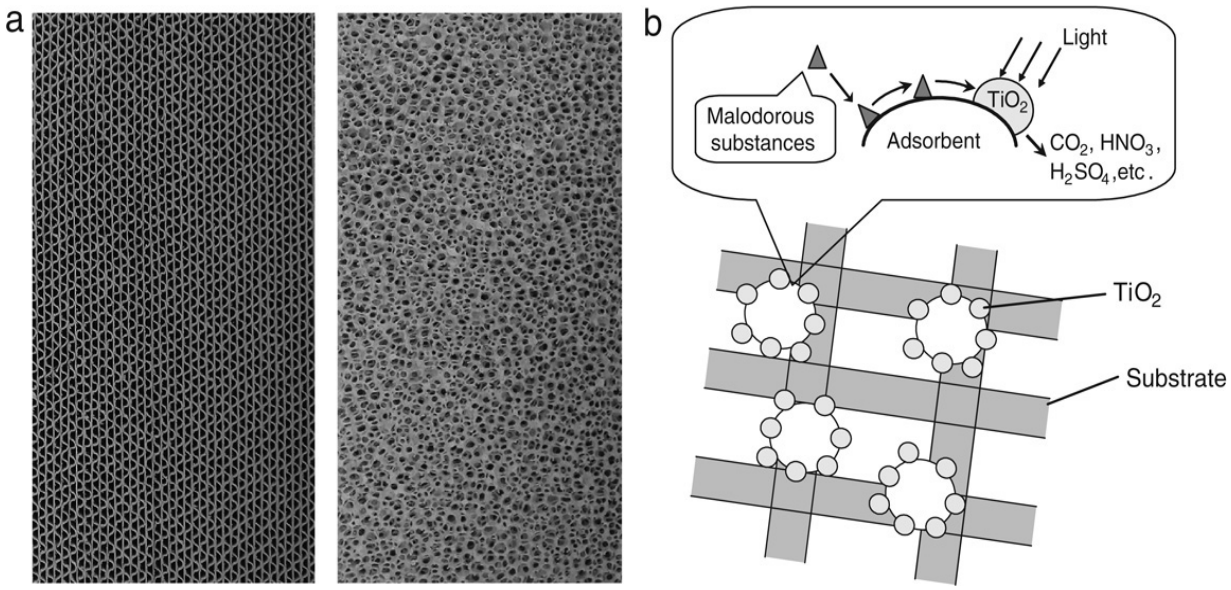

Figure 12 (a) Photographic images of a honeycomb-type air-cleaning filter (left) and a three-dimensional porous ceramic air-cleaning filter (right); (b) Schematic diagram of the microscopic structure of the air-cleaning filter; the substrate materials (ceramics, paper, fabrics) are coated with a composite of TiO_2 and adsorbent.

Figure 13 Usage of TiO_2-based photocatalytic material on roadway surfaces to convert nitrogen oxides (NOx) to nitrate: (left) application of the coating; and (right) finished roadway, with the coated surface showing a lighter color (courtesy of Fujita Road Construction Co., Ltd.).

CHAPTER 2

Processing and characterization of hydroxyapatite substituted with various metal ions

2.1 Calcium hydroxyapatite modified with Co^{2+}, Ni^{2+}, Cu^{2+}, Cr^{3+} ions

2.1.1 Introduction

Calcium hydroxyapatite, $Ca_{10}(PO_4)_6(OH)_2$, abbreviated as CaHAp, is not only a main component of hard tissues, such as bones and teeth, but also a material applied for bioceramics, adsorbents and catalysts. The surface structure and properties of CaHAp are fundamentally important in dental and medical fields and the usage of this material. Modification of the CaHAp surface is a technique available for developing catalysts and adsorbents with novel functions. Suzuki and coworkers have found that Ca^{2+} of CaHAp can be exchanged with various metal ions in aqueous media [(1)–(9)]. Hence, the surface structure and properties of CaHAp can be anticipated to be altered by ion exchange of Ca^{2+} with metal ions. It has been reported that Cu^{2+}, Ni^{2+} and Pb^{2+} doped into CaHAp influence the catalytic activity of this material [(10), (11)]. Nevertheless, the surface structure of the metal-substituted CaHAp is poorly understood. Information on the surface of modified CaHAp is requisite to give us new insights into not only the mechanism involved in adsorption and catalysis on this material but also the surface properties of bones and teeth contaminated with metal ions. There are coprecipitation and ion exchange methods for modification of the CaHAp surface with metal ions. These methods should modify CaHAp in different manners; the coprecipitation changes

both the surface and bulk structures whilst the ion-exchange modifies mainly the surface structure. Therefore, the employment of these two methods is significant for producing the materials modified to different degrees and for understanding of the modification mechanism. Previously we modified CaHAp with Fe^{3+} by coprecipitation and found that the surface Fe–OH groups formed are irreversible adsorption sites for CH_3OH as well as the surface P–OH groups [12].

The present study was intended to clarify the surface composition of the CaHAp particles modified with metal ions and the surface ion exchange reactions. Various transition metal ions, namely, Ni^{2+}, Co^{2+}, Cu^{2+} and Cr^{3+}, were doped into the particles by coprecipitation and ion exchange. The surface compositions of the modified CaHAp were examined. The modification mechanism is discussed on the basis of the obtained results.

2.1.2 Experimental

2.1.2.1 Coprecipitation method

The CaHAp particles doped with Ni^{2+}, Cu^{2+}, Co^{2+} and Cr^{3+} were prepared by coprecipitation. $Ca(NO_3)_2$ and nitrates of the metals were dissolved in 1 dm^3 deionized-distilled water free from CO_2 at various atomic ratios, metal/(Ca+metal), ranging from 0 to 0.1. The sum of the amounts of Ca^{2+} and metal ions contained in the solutions was held at 0.1 mol. H_3PO_4 (0.060 mol) was added to the solutions and the solution pH was adjusted to 9 by adding a 15 mol dm^{-3} NH_4OH solution. The resulting suspension was aged in a capped Teflon vessel at 100 °C for 6 h. After the aging the precipitates were filtered off, washed with 5 dm^3 deionized distilled water and finally

dried in an air oven at 70 °C. The obtained samples contained no NH_4^+ ion as confirmed by FTIR.

2.1.2.2 Ion-exchange method

The CaHAp particles were synthesized by the coprecipitation from the solution containing no other metal ions than Ca^{2+} as described above. The ion-exchange with Ni^{2+}, Cu^{2+}, Co^{2+} and Cr^{3+} was carried out by immersing 1.00 g of the CaHAp particles in 90 cm^3 of aqueous solutions comprising the metal nitrates at different concentrations of 0.001, 0.01 and 0.1 mol dm^{-3}. The suspensions were left at 30 °C for various periods up to 24 h and then the particles were separated by filtration, washed with 100 cm^3 of water and dried in an air oven at 70 °C.

2.1.2.3 Characterization

The CaHAp particles thus modified were examined by the following techniques. Morphology of the particles was observed using a Hitachi transmission electron microscope (TEM) at an accelerating voltage of 200 kV. The samples for TEM were prepared by a dispersing method. X-ray diffraction (XRD) patterns were taken by a powder method using a Rigaku high-intensity diffractometer with a rotating cathode using Cu K_α radiation (50 kV and 200 mA). Ca, Ni, Cu, Co, Cr and P contents were determined by a Perkin-Elmer induced coupled plasma spectrophotometer (ICP) employing wavelengths of 317.928 (Ca), 231.604 (Ni), 224.697 (Cu), 228.613 (Co), 205.558 (Cr) and 177.433 nm (P). The samples for ICP were dissolved in a dilute HNO_3 solution. X-ray photoelectron spectroscopy (XPS) was done using a Shimadzu spectrophotometer with Mg K_α radiation (20 kV and 30 mA). The samples were

mounted on the sample holder by a carbon tape. Transmission IR spectra were recorded in vacuo using a Perkin-Elmer Fourier transform infrared (FTIR) spectrophotometer by a self-supporting disk method in a vacuum cell. The sample powders (30 mg) were pressed into disks of 1 cm diameter under 572 kg cm^{-2}. Before taking the spectra the sample disks were outgassed at 300 °C for 2 h.

2.1.3 Results and discussion

2.1.3.1. Structure of coprecipitation products

Figure 1 displays TEM pictures of the particles produced by coprecipitation in the absence and the presence of Ni^{2+}, Co^{2+}, Cu^{2+} and Cr^{3+} whose atomic ratios, metal/(Ca+metal), in the starting solutions were 0.03. Hereafter the atomic ratio in the starting solutions is designated as X_{metal}. Figure 2 plots the average particle width and length, estimated from the images of the particles doped with the divalent metal ions in Figure 1, against X_{metal}. As seen from this figure, doping with the divalent ions reduces the particle sizes. It is of interest that trivalent Cr^{3+} markedly promotes particle growth, different from the divalent ions as seen from picture (e). The details of the effect of Cr^{3+} on the formation of CaHAp have been reported elsewhere [13].

Figure 3 compares the XRD patterns of the products coprecipitated with different amounts of Ni^{2+} and Cr^{3+}. All the patterns show only the peaks characteristic of CaHAp. The *a*- and *c*- dimensions of unit cell evaluated from these peaks are shown in Figure 4. The *a*-dimension is essentially not changed by doping with the divalent metal ions besides Cr^{3+}-substituted samples showing a maximum at $X_{Cr}=0.01$. The *c-dimension* is also almost constant except for Co^{2+} doping where the *c*-dimension decreases as X_{metal} increases. The noticeable decrease in the *c*-dimension by increasing X_{Co} is attributed to

a larger incorporation of Co^{2+} into the CaHAp crystals compared with the other divalent ions, as will be mentioned below. The maximum *a*-dimension observed on Cr^{3+} doped samples implies that the ion-exchange with Cr^{3+} is different from that with the divalent ions. As seen in Figure 3, the crystallinity of the products with Ni^{2+} dropped upon increasing X_{metal} while that of the products with Cr^{3+} dropped and then rose at $X_{Cr}=0.1$. This result for Cr^{3+} doping seems to correspond to the maximum *a*-dimension of unit cell at $X_{Cr}=0.01$ in Figure 4. The influence of Cr^{3+} substitution on the crystal structure of CaHAp, that is, the expansion of the *a-dimension* by Cr^{3+} doping, may be attributed detailed reason for the maximum *a-dimension* remains unclear at the moment. Interestingly, Fe^{3+} ions have been found to show similar results to Cr^{3+} [12]. Co^{2+} and Cu^{2+} lowered the crystallinity of CaHAp as well as Ni^{2+}, although the XRD patterns are not shown here. These XRD results signify that the decrease of particle sizes by doping with the divalent ions is caused by the suppression of the crystal growth of CaHAp. Consequently, the crystal growth of CaHAp is accelerated by Cr^{3+} ions while it is interfered with by Co^{2+}, Ni^{2+} and Cu^{2+}.

2.1.3.2 Composition of coprecipitation products

The contents of metal elements determined by ICP on the particles formed by the coprecipitation with Ni^{2+}, Cu^{2+}, Co^{2+} and Cr^{3+} are plotted against the atomic ratios of these ions in the starting solutions (X_{metal}) in Figure 5. The Cr and Co contents (mmol g^{-1}) increase linearly with an increase of X_{metal} and are larger than the Ni and Cu contents. Furthermore, for the products with Co^{2+} and Cr^{3+}, X_{metal} of the starting solution is close to that of the formed particles, meaning that all the Co^{2+} and Cr^{3+} ions added to the starting solutions are incorporated into the formed particles. On the other hand, only

a part of the Ni^{2+} and Cu^{2+} ions added into the starting solutions at $X_{metal} > 0.01$ is contained in the formed particles. Thus, Co^{2+} and Cr^{3+} are more easily incorporated into the CaHAp particles than Ni^{2+} and Cu^{2+}. The Ca content of the products was decreased by increasing the added metal ions, indicating that the Ca^{2+} ions in the particles are substituted with the metal ions.

To know the distribution of the added metal ions between the bulk and surface phases, the surface composition was determined by XPS and compared with the composition of the whole particle determined by ICP. The contents of Ni, Cu, Co and Cr in the surface phase were estimated from the area intensities of $2p_{3/2}$ peaks of these elements. Figure 6 plots the atomic ratios in the whole particle and the surface phase against X_{metal} (circles and triangles, respectively). Hereafter, the atomic ratios in the whole particle and the particle surface are designated X_w and X_s, respectively. As seen from Figure 6, the variations of X_w and X_s with X_{metal} are appreciably different for the kind of metal ions. In the substitution with Ni^{2+} and Cu^{2+}, X_s is much less than X_w, meaning that the surface phase contains only a small part of the metal ions incorporated in the particles. The replacement of Ca^{2+} with Ni^{2+} and Cu^{2+} should make the crystal structure of CaHAp unstable because of the considerably smaller radii of Ni^{2+} (0.069 nm) and Cu^{2+} (0.072 nm) than 0.099 nm of Ca^{2+}. It has been reported that Mg^{2+} ions with 0.066 nm radius interfere with the crystal growth of CaHAp [14), 15)]. On the contrary, divalent ions larger than Ca^{2+}, such as Sr^{2+}, Ba^{2+} and Pb^{2+}, are known to easily substitute for Ca^{2+} in CaHAp [16)–18)]. X_s of the products at $X_{Co} \leqq 0.03$ increases steeply with increasing X_{Co} and is larger than X_w (Figure. 6), which implies that the added Co^{2+} ions are concentrated in the surface phase in contrast to the substitution with Ni^{2+} and Cu^{2+}, though the ionic radius of Co^{2+} (0.072 nm) is close to those of Ni^{2+} (0.069 nm) and Cu^{2+} (0.072 nm).

Hence, the large X_s of the sample doped with Co^{2+} may be ascribed to a lower stability of the ammine complex of Co^{2+} than those of Ni^{2+} and Cu^{2+}. These complexes are presumed to be formed with NH_4OH used for adjusting the solution pH and it is well known that the stability constants (log K_1) of the ammine complexes of these ions are on the order of Co^{2+} (4.8)<Ni^{2+} (8.5)<Cu^{2+} (12.6). In the Cr substitution(Figure 6), X_s is less than X_w at $X_{Cr} \leqq 0.03$, while X_w and X_s are almost identical at $X_{Cr}=0.10$. Therefore, Cr^{3+} ions doped at $X_{Cr} \leqq 0.03$ exist in the bulk phase more than the surface phase and Cr^{3+} ions doped at $X_{Cr}=0.10$ are homogeneously distributed all over the particle. To get information on anions such as PO_4^{3-} and OH^- in the surface phase, the P and O contents were determined by XPS using the $P2p_{3/2}$ and $O1s_{1/2}$ peaks. The P and O contents are expressed as the atomic ratios in P/(Ca+metal+P+O) and O/(Ca+metal+P+O) and plotted against X_{metal} in Figure 7. Note that the atomic ratio of P in the Cr^{3+} doped materials is decreased by increasing X_{Cr} while the atomic ratio of O is increased. On the other hand, the atomic ratios of P and O of the products with Ni^{2+}, Cu^{2+} and Co^{2+} vary slightly with X_{metal}. The decrease of the P content with the increase of X_{metal} is indicative of the decrease of the surface PO_4^{3-} by Cr^{3+} doping. On the contrary, the increase of the O content with the increase of X_{metal} signifies the increase of the surface PO_4^{3-}. The reason for this contradiction will be interpreted below.

2.1.3.3 Composition of ion-exchanged materials

The ion exchange method was adopted to modify CaHAp and the composition of the modified materials was compared with those of the coprecipitation products discussed above. To estimate the period required for the ion exchange equilibrium, the samples

were treated in the solutions at different concentrations of metal ions at 30 °C for various periods up to 24 h. Figure 8 plots the Co content determined by ICP on the treated samples against the immersing time as a typical example. As seen from this figure, the Co content is constant after 5 min for the entire Co concentration of the treating solutions, proving that the equilibrium is achieved after 5 min. Such a rapid exchange has been reported on the exchange of CaHAp with Cd^{2+}, Zn^{2+} and Hg^{2+} [1]. Hence, the ion-exchange period of the samples discussed below was 5 min.

To compare the degree of ion exchange, the amounts of Ni^{2+}, Cu^{2+}, Co^{2+} and Cr^{3+} incorporated into the treated particles determined by ICP are plotted against the concentration of these ions in the treating solutions in Figure 9. The contents of all the metal ions in the particles are increased by raising the concentration of the treating solution up to 0.01 mol dm^{-3}. The exchangeability of these divalent ions is in the order $Cu^{2+}>Co^{2+}= Ni^{2+}$, corresponding to the reported order $Cu^{2+}>Zn^{2+}>Co^{2+}$ [19] and $Zn^{2+}>Ni^{2+}$ [2]. As seen in Figure 9, at a high concentration of 0.1 mol dm^{-3} the Cr content is larger than the contents of the other ions. Therefore, Cr^{3+} can be more easily incorporated into CaHAp than the other ions, despite the valence difference between Cr^{3+} and Ca^{2+}, in accord with the results of the coprecipitation method. This would occur because the mechanism of the exchange with Cr^{3+} differs from that of the exchange with the divalent ions. The details of this will be discussed below.

The surface composition of the particles modified with ion exchange was determined by XPS. Figure 10 compares the atomic ratio in the whole particle (X_w) with that in the surface phase (X_s) for the samples exchanged with various metal ions. As seen in Figure 10, when exchanged with Cu^{2+}, Co^{2+} and Cr^{3+}, X_s is 2–2.5 times X_w at a concentration of the treating solutions of 0.10 mol dm^{-3}. To know whether the doped metal ions are

located only in the surface phase of the particles, the volumes of the surface and bulk phases were estimated from the average particle size (20 nm×40 nm) assuming that the particles are cylindrical and the thickness of the surface phase is 1 nm, since the documented escaping depth of electrons in XPS for Ca, Ni, Co, Cu and Cr is 1.17, 0.61, 0.69, 0.53 and 0.95 nm, respectively [20]. The volumes of the surface phase and the whole particle thus calculated were 2.9×10^3 and 12.6×10^3 nm^3, respectively, that is, the volume of the whole particle was 4.3 times that of the surface phase. If the ion exchange takes place only in the surface phase, X_s should be more than 4.3 times X_w. As described above, X_s was less than 4.3 times X_w (Figure 10), which demonstrates that the doped metal ions exist not only in the surface phase but also in the bulk one. It is of interest that X_s and X_w in the Ni^{2+} exchange are almost identical (Figure 10). This implies that the doped Ni^{2+} ions are homogeneously distributed all over the particle and more easily diffuse into the particles compared with the other ions. This may be due to the radius of the Ni^{2+} ion of 0.069 nm, less than the 0.072 nm of Co^{2+} and Cu^{2+} ions. Since the exchange of Ca^{2+} with Cr^{3+} requires compensation of the charge imbalance, Cr^{3+} ions hardly ever enter into the crystal lattice in the bulk phase compared with the divalent ions. However, similarly to the coprecipitation products, X_s and X_w for the Cr^{3+} exchange are larger than those for the exchange with the divalent ions. Further, in the Cr^{3+} exchange X_s is larger than X_w (Figure 10). These facts indicate that the Cr^{3+} exchange more easily takes place in the surface phase than the bulk one.

The P and O contents in the surface phase of the particles exchanged with the metal ions were measured by XPS in the same manner as the coprecipitated samples mentioned above. Figure 11 shows the atomic ratios, P/(Ca+metal+P+O) and O/(Ca+metal+P+O), as a function of the concentration of metal ions in the treating

solutions. With increasing the Cr^{3+} concentration of the treating solutions the P/(Ca+metal+P+O) ratio decreases and the O/(Ca+metal+P+O) ratio increases. In the case of the divalent ions, both the ratios are essentially constant. Therefore, only the Cr^{3+} exchange reduces the surface PO_4^{3-} content as well as the coprecipitation with Cr^{3+} shown in Figure 7. However, the decrease of the surface PO_4^{3-} ions is in conflict with the increase 4 of the O content by the Cr^{3+} exchange. This point will be discussed below based on the FTIR results.

2.1.3.4 Surface characterization by FTIR

To elucidate the surface structures of the particles produced by the coprecipitation and ion exchange methods, the transmission IR spectra of the materials were taken in vacuo by a self-supporting disk method. Before measuring the spectra, the sample disks were outgassed at 300 °C for 2 h to remove adsorbed H_2O.

2.1.3.4.1 Coprecipitation products

Figure 12 displays the spectra of the products by the coprecipitation method with Ni^{2+}, Cu^{2+}, Co^{2+} and Cr^{3+}. The spectrum of the CaHAp formed in the absence of the metal ions gives rise to three bands at 3680, 3673 and 3657 cm^{-1} as shown by the dashed curves. In our previous study, these three bands were assigned to the O–H stretching vibration modes of the surface P–OH groups formed by protonation of the surface [21, 22]. From observing Figure 12 the influence of the doped metal ions on the surface P–OH bands depends on the kind of metal ions. Ni^{2+} and Cu^{2+} ions show no pronounced influence on the surface P–OH bands (Figure 12), though the 3680 cm^{-1} band becomes slightly sharp on increasing X_{metal}. Such a less influence of Ni^{2+} and Cu^{2+} ions can be

understood from the XPS results that few of these ions exist in the surface phase as seen from Figure 6. The 3657 cm^{-1} band of the product with Co^{2+} is weakened by increasing X_{Co} (Figure 12). All the surface P–OH bands of the products with Cr^{3+} disappear with increasing X_{Cr} (Figure 10). These results are consistent with the fact that the X_s values of the products with Co^{2+} and Cr^{3+} are larger than those of the products with Ni^{2+} and Cu^{2+} (Figure 6). These FTIR results indicate the decrease of the surface P–OH groups with the substitution by Co^{2+} or Cr^{3+}. However, the decrease of the surface P–OH groups cannot be explained only by cation exchange of the protons of P–OH with these metal ions, because the surface P content was decreased by Cr^{3+} doping and the surface O content was increased (Figure 7). This conflict may be solved by an anion-exchange mechanism that the surface $H_2PO_4^-$ ions are replaced by hydrated $Cr(OH)_4^-$ ions which contain a larger amount of O than the phosphate ions. There is no probability for the exchange of the phosphate ions with $Cr_2O_7^{2-}$ or CrO_4^{2-}, because the added Cr^{3+} ions exist as a trivalent state, as can be inferred from the fact that the binding energy of the $Cr2p_{3/2}$ peak (577.7 eV) of the products with Cr^{3+} was identical to 577.7 eV of the same peak of Cr_2O_3, while the binding energies of the $Cr2p_{3/2}$ peak for CrO_3 and $K_2Cr_2O_7$ were 581.2 and 581.9 eV, respectively. Furthermore, a strong broad IR band centered at 3200 cm^{-1} was detected only on the samples doped with Cr^{3+}, which is assignable to the O–H stretching vibration of the OH^- and H_2O of the hydrated $Cr(OH)_4^-$, though the spectra are not shown. These results also support the exchange of the surface $H_2PO_4^-$ with the hydrated $Cr(OH)_4^-$. In general, Cr^{3+} ions are more easily hydrolyzed compared to Ni^{2+}, Co^{2+} and Cu^{2+} ions and the main hydrolysis product of Cr^{3+} is $Cr(OH)_4^-$ at pH>8.8 [23]. Consequently, in the coprecipitation the anion exchange takes place for Cr^{3+} and the cation exchange for Ni^{2+}, Co^{2+} and Cu^{2+}.

2.1.3.4.2 Ion-exchanged CaHAp

Figure 13 displays the IR spectra in vacuo of the CaHAps exchanged with Ni^{2+}, Co^{2+}, Cu^{2+} and Cr^{3+} by treating in the solutions with different concentrations of these metal ions. In the exchange with the divalent ions the surface P–OH bands are weakened by the treatment at a low concentration but do not completely disappear even at 0.1 mol dm^{-3} (Figure 13). The surface P–OH bands would be diminished by cation exchange of the protons of the surface P–OH groups with the divalent metal ions by the following reactions:

$O_2P(OH)_2+M^{2+}\rightarrow O_2PO_2M+2H^+$

$2O_3P(OH)+M^{2+}\rightarrow O_3POMOPO_3+2H^+$

where M^{2+} represents the divalent metal ions. On the other hand, the Cr^{3+} exchange does not influence the surface P–OH band at 3680 cm^{-1} and diminishes the 3657cm^{-1} band as seen from Figure 13, distinct from the exchange with the divalent ions. This can also be interpreted by the anion exchange mechanism proposed for the modification by coprecipitation. However, no new band due to the surface Cr–OH was detected.

2.1.4. Conclusions

The surface of CaHAp particles could be modified by the coprecipitation and ion exchange methods with divalent and trivalent metal ions. The surface modification by the coprecipitation with Ni^{2+}, Cu^{2+} and Co^{2+} was less effective compared with that by the ion exchange with these ions. The modification with Cr^{3+} took place by a different mechanism from the divalent ions. In the modification with Cr^{3+} the surface $H_2PO_4^-$ of CaHAp were replaced by hydrated Cr $(OH)_4^-$, whereas in the modification with Ni^{2+},

Cu^{2+} and Co^{2+} the protons of the surface P–OH groups were exchanged with these cations.

2.2 Calcium hydroxyapatites substituted with Al(III), La(III) and Fe(III) ions

2.2.1 Introduction

Ca(II) ions of calcium hydroxyapatite $Ca_{10}(PO_4)_6(OH)_2$, designated as CaHAp, are exchanged by other metal ions, that is anticipated to affect many characteristics of CaHAp, such as nonstoichiometry, crystallinity, thermal stability, catalytic activity, solubility, and so forth. Since CaHAp is a principal component of vertebrate animals' bones and teeth, the incorporation of metal ions into the hard tissues is of interest in medical and dental sciences concerned with denaturation of bones by metal ions and accumulation of harmful or radioactive metal ions [(24)-(28)]. A synthetic CaHAp attracts attention as bioceramics, acid–base catalysts in various reactions and adsorbents for separation of biomaterials. So far, CaHAp particles substituted with metal ions, such as Cu(II) [(29)-(31)], Ni(II) [(31)] and Pb(II) [(32)], have been investigated as catalysts for different reactions. However, their surface structures and properties have not been thoroughly characterized. Although there are some investigations on influences of metal ions on dissolution of CaHAp [(33)-(35)] and ion-exchange with metal ions [(36)-(38)], little attention has been given to the morphology and surface structure of CaHAp substituted with trivalent metal ions. Moreover, to our knowledge, the influences of trivalent metal ions on the formation of CaHAp particles have not been thoroughly studied, though there were the studies on the reaction of CaHAp particles with Al(III) [(39)], La(III) [(39)] and Fe(III) [(40)] at rather low pH≦ca. 4. However, they did not study the coprecipitation of

CaHAp with these ions. We previously examined the surface structure and composition of the CaHAp particles coprecipitated with various metal ions and found that Ni(II), Cu(II) and Co(II) interfere with the particle growth of CaHAp while Cr(III) promotes the particle growth [41]. Furthermore, the divalent ions replace Ca(II) of CaHAp crystals, whereas Cr(III) replaces surface phosphate ion by exchange with Cr(III) hydroxo anions. The fact that the influence of metal ions on the formation and structure of CaHAp depends on their valences attracts our attention concerning with the modification of CaHAp and the calcification in the presence of metal ions in vivo.

In the present study, to get further insight into the influence of metal ions on the formation and structure of CaHAp, we investigated the composition and structure of CaHAp substituted with trivalent metal ions of Al(III), La(III) and Fe(III), which are of interest in clinical field. It has been reported that Fe(III) is responsible for black or brown tooth stains [42), 43], and La(III) and Al(III) inhibit dental caries [44), 45]. The CaHAp particles modified by the coprecipitation and immersion methods were characterized by various means. The discrimination between these two substitution methods was discussed.

The obtained results must serve not only to elucidate the interaction of hard tissue with metal ions but also to modify the CaHAp with metal ions for the preparation of novel ceramics and catalysts.

2.2.2 Experimental

2.2.2.1 Substitution with coprecipitation

Colloidal CaHAp particles were prepared by coprecipitation reactions of $Ca(NO_3)^2$ and H_3PO_4 in aqueous solutions containing varied amounts of Al(III), La(III) and

Fe(III). Prior to the aging of the resulting precipitates the solution pH was adjusted to 9 by an NH_4OH solution. The detailed preparation conditions were described in the previous paper [41]. The substitution with metal ions was done at different atomic ratios ranging from 0 to 0.1 in metal/(Ca+metal).

2.2.2.2 Substitution with ion-exchange

The CaHAp particles were prepared by the above-mentioned coprecipitation method without adding the metal ions. 1.00 g of the particles was immersed at 30°C in 90 cm^3 of aqueous solutions dissolving nitrates of Al(III), La(III) and Fe(III) whose the concentrations were varied from 0 to 0.01 mol dm^{-3}. The solution pH before the immersion was adjusted to 5, because more than 0.01 mol dm^{-3} Al(III) and Fe(III) solutions generated hydroxide precipitates at pH>5.0. To attain the ion exchange equilibrium required more than 5 min. After the equilibrium the CaHAp particles were separated by a Millipore filter from the solutions, washed with 100 cm^3 of deionized distilled water and then dried in air at 70°C. To know the reproducibility of the immersion, the immersion experiment was repeated three times in the same conditions. The metal ions contained in the particles were assayed as described below, so that the experimental error was confirmed to be less than 5%.

2.2.2.3 Characterization

The materials were characterized by various techniques involving powder X-ray diffraction (XRD), transmission electron microscopy (TEM), induced coupled plasma (ICP) spectrometry, X-ray photoelectron spectroscopy (XPS), Fourier transformed

infrared (FTIR) spectrometry and thermogravimetry (TG). The detailed conditions of these measurements were noted in the previous paper [41].

2.2.3 Results and discussion

2.2.3.1 Structures of coprecipitation products

Figure 14 shows the TEM pictures of the particles formed at different concentrations of Al(III), La(III) and Fe(III) in comparison with the particles produced with Cr(III) reported in the previous paper [41]. Hereafter, the atomic ratios of the metal ions in the starting solutions, metal/(Ca+metal), are noted as X_{metal}. As seen in Figure 14 the short rod-shaped particles formed at $X_{metal} = 0$ are elongated on adding metal ions at $X_{metal} = 0.10$ and the extent of the particle growth is in the order of Al(III) < La(III) < Fe(III) < Cr(III). In Figure 15 is plotted the mean particle length estimated from the TEM images against X_{metal} by filled marks. It is seen that the particle length is essentially unchanged with adding the metal ions while increases at $X_{Fe}=0.1$ as shown by the filled squares. Note that the effect of Fe(III) on the growth of CaHAp particles is more remarkable than those of Al(III) and La(III), though the reason for this difference remains unclear at the present.

Figure 16 displays XRD patterns of the products at different X_{Al}. The crystallinity of the materials is slightly lowered by increasing X_{Al}. All the patterns are characteristic of CaHAp (JPCDS 9-432) besides two very weak peaks detected on the sample with $X_{Al}=0.10$ at 2θ=14.3 and 20.3° which are assigned to $Ca_5Al(PO_4)_3OH$ (JPCDS 45-1483). A similar result was obtained on the products with La(III) and Fe(III), though the XRD patterns are not shown here. The slight depression of crystallinity by the substitution with metal ions does not coincide with the aforementioned TEM observation that the

particles grew with increasing X_{metal}, suggesting that the substituted particles are polycrystalline. To corroborate this the crystallite sizes of the particles were evaluated using the Scherrer equation from the half height width of the XRD peak at 2θ = 25.8° due to the (002) plane. They are shown by open marks in Figure 15.

The crystallite sizes for all the metal ions slightly decrease at $X_{metal} \leqq 0.01$ and then are essentially constant. The crystallite size of the sample without substitution nearly equals the length of the particles along c-axis of the CaHAp crystal (filled marks), whereas the crystallite sizes of the samples with substitution are less than the particle length, showing that the particles are not a single-crystal. The polycrystallinity of the particles is most pronounced for the product at X_{Fe} =0.10.

2.2.3.2 Composition of coprecipitation products

To determine the composition of the products by the coprecipitation, Ca, Al, La, Fe and P in the formed particles were assayed by ICP. Figure 17 plots the contents of Ca(II) and the metal ions against X_{metal} by filled triangle and circle marks, respectively. Ca(II) contents of the products with all the metal ions are reduced by increasing X_{metal}, which indicates that Ca(II) ions of CaHAp are replaced by the metal ions. Besides the exchange with Ca(II) the physical adsorption and ion exchange with protons of the surface P–OH groups of the CaHAp particles are anticipated. However, the physical adsorption and ion exchange with the surface protons can be thought to be less than the exchange with Ca(II), because the samples were thoroughly washed and the surface P–OH group were only slightly decreased by the substitution with metal ions as will be described in the section of IR spectra (Figure 20). Therefore, the uptake of metal ions by the present samples is mainly due to the exchange with Ca(II). The substituting ratio, i.e.

the number of Ca(II) ions replaced by a metal ion, can be estimated from the ratios of the slopes of straight lines in Figure 17 (filled marks). The obtained ratios, Ca/metal in atomic ratio, for the substitution with Al(III), La(III) and Fe(III) are respectively 1.5, 2.6 and 1.0. Taking account of the charge balance of CaHAp crystal, the substitution ratio for the exchange of Ca(II) with trivalent ions should be 3/2 = 1.5. The ratio for Al(III) substitution is identical with the theoretical ratio, whilst the ratio for La(III) substitution is larger than the theoretical ratio and that for Fe(III) substitution is less, signifying that the charge is not balanced in the substitution by La(III) and Fe(III). Thus, to keep the charge balance, Fe(III) would be incorporated into the particles as lower valence ions such as hydroxo ions; $Fe(OH)_2^+$ or $Fe(OH)_2^+$. The existence of these hydroxo ions in the products can be confirmed by the FTIR result that the IR spectra in vacuo of the Fe(III) substituted samples outgassed at 300 °C showed a broad band centered at 3400 cm^{-1} assigned to the stretching mode of OH^- ions of the hydroxo ions.

On the contrary, the materials substituted with La(III) exhibit a larger exchange ratio of 2.6 than the theoretical one (1.5), leading to the excess negative charge. Therefore, for the charge balance, the substitution should accompany the deficiency of anions such as PO_4^{3-} and OH^-, or protonation of PO_4^{3-} to HPO_4^{2-} and $H_2PO_4^-$ or 4424 that of OH^- to H_2O. To discuss this point the P content of the samples was determined by ICP. The P contents of the samples substituted with all metal ions at $X_{metal}=0–0.1$ were 5.3–5.4 mmol/g being within the experimental error, that excludes a possibility of the PO_4^{3-} deficiency. IR spectra in vacuo of the La(III) substituted samples outgassed at 300 °C, not shown here, had a strong band at 3320 cm^{-1} assigned to H_2O molecules strongly bound to the particle surface which were not removed by the outgassing. Such a strong H_2O band was not observed on substituting with Fe(III) and Al(III). Consequently, the

substitution with La(III) accompanies the protonation of OH^- to H_2O in the layer of the particles.

To know the extent of incorporation of metal ions into CaHAp particles, the atomic ratios, metal/(Ca + metal), determined by ICP and designated as X_w are plotted against the atomic ratios of metal ions in the starting solutions (X_{metal}) by open circle marks in Figure 17. For all the metal ions, X_w is larger than the dashed line representing X_{metal}. This result suggests that all the metal ions are more easily incorporated into the particles than Ca(II) in the coprecipitation method. For determining the surface composition of the particles, XPS spectra were taken on the products with metal ions. The atomic ratios, metal/(Ca+metal), in the surface layer of the particles, noted as X_s, were estimated from the area intensity of XPS peaks of Ca(2p), Al(2p), La($3d_{5/2}$) and Fe($2p_{3/2}$). The X_s values obtained for the products with Al(III), La(III) and Fe(III) are plotted against X_{metal} by the open triangles with error bars in Figure 17. In the substitution with Al(III) X_s is larger than X_w at $X_{Al} \leqq 0.03$ and less than X_w at $X_{Al} = 0.1$, that is the surface layer contains more Al(III) than the bulk ones. The substitution with La(III) gives the similar result as with Al(III). In the Fe(III) substitution X_s is equivalent to X_w at $X_{Fe} \leqq 0.01$ but less than X_w at $X_{Fe} \geqq 0.03$ as well as the substitution with Al(III) and La(III). These results imply that metal ions are incorporated into the particles in different manners, especially Fe(III) at $X_{Fe} \leqq 0.01$ takes place homogeneously over the whole particle, different from the cases of Al(III) and La(III).

2.2.3.3 Composition of ion-exchanged CaHAp

Figure 18 shows the contents of Ca(II), Al(III), La(III) and Fe(III) in the CaHAp particles determined by ICP after treating with solutions containing different concentrations of these metal ions. The Ca content shown by triangles decreases with increasing the concentration of metal ions in the immersing solutions while the contents of metal ions in the particles shown by circles increases. This implies that Ca(II) in the particles is substituted by the metal ions. The contents of the metal ions (circles) are in the order of Al(III)= Fe(III)>La(III). This result is not interpreted by the difference of ionic radii of Ca(II) (0.099 nm), Al(III) (0.051), Fe(III) (0.064) and La(III) (0.114), because La(III) with an ionic size close to that of Ca(II) is expected to displace for Ca(II) more easily than Al(III) and Fe(III). On the other hand, the charge density, i.e. atomic valency per volume of these ions is in the order of Al(III)>Fe(III)> La(III). Therefore, the ion exchange with these ions seems to depend on their charge density. The exchange ratios of Ca(II) by Al(III), La(III) and Fe(III) were estimated from the straight lines in Figure 18, where the contents of the metal ions in the CaHAp particles are plotted against the concentrations of these metal ions in the immersing solutions. The exchange ratios (Ca/metal) in the exchange with Al(III), La(III) and Fe(III) are 0.5, 0.7 and 1.3, respectively, being less than the theoretical one of 3/2=1.5. From the low exchange ratios Ca(II) ions in the surface phase seem to be exchanged by mono- or divalent metal hydroxo ions. Since the solution pH was increased by the immersion from pH 5 to pH 5.5–6.5 depending on the kind and concentration of metal ions, the exchange with the hydroxo ions appears to generate OH^- by the following surface reactions,

(a) $2CaOH(s) + Me(OH)^{2+}(a) \rightarrow -Me(OH)(s)$

$+2CaOH^+(a) \rightarrow -Me(OH)(s)$

$$+2Ca^{2+}(a)+2OH^{-}(a)$$

(b) $CaOH(s) + Me(OH)_2^{+}(a) \rightarrow -Me(OH)_2(s)$

$$+CaOH^{+}(a) \rightarrow -Me(OH)_2(s)$$

$$+Ca^{2+}(a)+OH^{-}(a)$$

where (s) and (a) represent the species in particle surface and aqueous solution, respectively.

Fe(III) and La(III). *Xs* is much larger than *Xw* in the exchange with Al(III) and La(III), that is reasonable for the substitution in the surface phase of the particles. In the Fe(III) substitution X_s is close to X_w, meaning that Fe(III) is distributed in the whole of the particles. This seems to pertain to the fact that the crystal structure of CaHAp was collapsed to be amorphous by immersing in the Fe(III) solution [40]. Note that such extreme destruction of CaHAp crystal was observed only for the substitution with Fe(III) by the immersion method. This is of interest concerning the denaturation of hard tissue by Fe(III). Tanizawa et al. reported that CaHAp reacts with Al(III) and La(III) in an acidic solution of pH< ca. 4 to reduce the crystallinity of CaHAp [39]. However, in the present study, Al(III) and La(III) were only ex changed for Ca(II) of CaHAp without drastic reaction. This conflict would be ascribed to the pH difference of the immersing solutions; pH 5 in the present study and pH< ca. 4 in the literature [39], [40], because CaHAp is unstable at low pH. From the solubility isotherm of CaHAp documented by Elliott [46], the solubility at pH 5 is estimated to be 3 mmol dm^{-3} in Ca^{2+} concentration. In the present immersion solutions 1.00 g of the CaHAp samples were dispersed in 90 cm^3 of the solutions as mentioned in the experimental section. If the sample is completely dissolved, the solubility amounts 50 mmol dm^{-3} larger than the equilibrium

one mentioned above. Consequently, the quantity of the samples is enough to saturate the solutions with CaHAp, so that no drastic structural change would take place.

2.2.3.4 IR Spectra

The surface of the CaHAp particles substituted with Al(III), Fe(III) and La(III), was characterized by taking the transmission IR spectra in vacuo of the samples outgassed at 300 °C for 2 h by a self supporting disk method. Figure 20 shows the spectra of the CaHAps modified with the coprecipitation method. The spectrum of the sample without substitution shown by dashed line has three bands at 3680, 3673 and 3657 cm^{-1} overlapping each other, which have been assigned to surface P–OH groups [47]. In the case of the Al(III) substituted samples, several weak bands appear at 3784, 3744, 3735 and 3712 cm^{-1} in addition to the surface P–OH bands whose the intensities are reduced by the substitution. These new peaks can be assigned to the OH stretching modes of surface Al–OH groups by H–D exchange repeating adsorption description of D_2O. Peri found five bands at 3800, 3780, 3744, 3733 and 3700 cm^{-1} due to surface Al–OH groups of alumina [48]. The 3780, 3744 and 3733 cm^{-1} bands out of the five bands are close to the bands observed on the Al(III) substituted sample. This verifies the substitution of Ca(II) with Al(III) hydroxo ions. The Fe(III) substituted samples shows a band at 3704 cm^{-1} in addition to the surface P–OH bands, that is assigned to the surface Fe–OH groups. This result also justifies the exchange with Fe(III) hydroxo ions. On the other hand, the samples substituted with La(III) show no bands besides the surface P–OH bands. It remains unclear whether there is no surface La–OH group or the La–OH band overlaps the surface P–OH band.

IR spectra in vacuo of the CaHAps substituted with Al(III) and La(III) by the immersion method were substantially similar to those of the coprecipitation products in Figure 20 though the former spectra are not shown here. The samples substituted with Fe(III) gave rise to no surface Fe−OH band distinct from the coprecipitation products and their surface P–OH bands are weakened as the Fe(III) concentration of the immersing solutions increases, reflecting the destruction of CaHAp crystals by reaction with Fe(III) as described in the above section.

2.2.4 Conclusions

Ca(II) of CaHAp was exchanged by Al(III), La(III) and Fe(III) by the coprecipitation and immersion methods. In the coprecipitation these metal ions accelerated the growth of CaHAp particles, markedly for Fe(III). The CaHAp particles substituted with Al(III) by both the methods possessed several kinds of surface Al–OH in addition to the surface P–OH while no surface La–OH was detected on the La(III) substituted CaHAp. The CaHAp substituted with Fe(III) by the coprecipitation method had one kind of surface Fe–OH, but those by the immersion method had no surface Fe–OH. The exchange mechanism with metal ions depends on the substituting methods and kind of metal ions. It is therefore concluded that the surface structure and composition of CaHAp can be controlled by the substitution with metal ions.

2.3 Influence of chromium(Ill) on the formation of calcium hydroxyapatite

2.3.1 Introduction

Calcium hydroxyapatite $Ca_{10}(PO_4)_6(OH)_2$ (noted CaHAp) has been extensively investigated with the intention to use this material as adsorbents, catalysts and bioceramics. Since the structure and nature of CaHAp depend on its nonstoichiometry, controlling of the stoichiometry is anticipated to generate materials having interesting functions. However, the chemical composition of CaHAp is very sensitive to various preparation conditions, so that it is rather hard to regulate its nonstoichiometry reproducibly. The replacement of Ca^{2+} ions in CaHAp with trivalent ions is a method to control its nonstoichiometry. The ion-exchange reaction of CaHAp with trivalent ions such as Fe^{3+}, Al^{3+} and La^{3+} ions has been investigated in relation to their dental application [49]-[51]. On the other hand, there are few studies of the substitution by a coprecipitation method that can offer more pronounced modification of the CaHAp structure compared with the ion-exchange method. In the previous study [52], we found that Fe^{3+} ions can be doped into CaHAp up to ca 0.11 in mole ratio Fe/(Ca + Fe) with a coprecipitation method and resulted in reduction of the crystallinity and increase in the specific surface area. However, to establish the influence of trivalent ions on the formation and structure of CaHAp, other trivalent ions having different sizes should be doped.

This study was conducted to elucidate the effect of Cr^{3+} ions on the formation and structure of CaHAp. The radius of this ion (0.069 nm) is closer to that of Ca^{2+} ions (0.099 nm) than that of Fe^{3+} ion (0.064 nm) used in the previous study and the solubility of chromium phosphate formed by coprecipitation is much lower than that of ferric phosphate. Thus, the effect of Cr^{3+} ions could be presumed to differ from that of Fe^{3+} ions. It is known that Cr^{3+} and Fe^{3+} ions are normally present in the organism [53]. The CaHAp particles formed in the presence of different amounts of Cr^{3+} ions were

characterized. The noticeable influence of this ion on the crystal growth of CaHAp was found and the detailed results are reported in this paper.

2.3.2 Experimental

2.3.2.1 Materials

The preparation of the samples was done by a wet method. 0.1 mol of $Ca(NO_3)_2 \cdot 4H_2O$ was dissolved in 1 dm^3 deionized and distilled water free from CO_2. 0.060 mol H_3PO_4 were added to the $Ca(NO_3)_2$ solution and pH of the solution was adjusted to 9 by a 15 mol dm^3 NH_4OH solution. The resulting suspension was aged in a capped Teflon vessel at 100 °C for 6 h. After the aging the precipitates were filtered off, washed with 5 dm^3 deionized and distilled water and finally dried in an air oven at 70 °C. Cr^{3+} ions were doped by adding $Cr(NO_3)_3$ to the $Ca(NO_3)_2$ solutions at mole ratios Cr/(Ca + Cr) varying from 0 to 1 before adding the NH_4OH solution.

2.3.2.2 Characterization

X-ray powder diffraction (XRD) of the obtained materials was done on a Rigaku high intensity diffractometer using a CuK_α radiation (0.15418 nm) at 50 kV and 200 mA. P, Ca and Cr contents were determined by a Perkin-Elmer induced coupled plasma spectrometer (ICP). The samples for ICP were dissolved in a dilute HNO_3 solution. Morphology of the particles was observed on a Hitachi transmission electron microscope (TEM). To assay a single particle, electron probe microanalysis (EPMA) was carried out with a spot diameter of 1 nm. Thermogravimetry (TG) curves were recorded on a Rigaku thermoanalyser in an air stream at a heating rate of 5 °C/min. X-ray photoelectron spectroscopy (XPS) were cariied out by a Shimadzu XPS

spectrometer. The binding energy was calibrated against $OlS_{1/2}$ peak. Infrared spectra (IR) were taken using a Digilab FTIR spectrometer by KBr method. The specific surface areas were evaluated by the BET method from N_2 adsorption isotherms measured by an automatic volumetric apparatus. Before the adsorption the samples were outgassed at 300 °C for 2 h.

2.3.3 Results and discussion

2.3.3.1 Composition of Cr doped CaHAp

Tile Cr/(Ca + Cr) ratios of the formed particles were noted as X_{cr} below. In Figure 21 the X_{cr} values are plotted against the Cr/(Ca + Cr) ratios of the starting solutions. The X_{Cr} values are almost equal to the Cr/(Ca + Cr) ratios of the starting solutions. This indicates that all of the Cr^{3+} ions added to the starting solutions are included in the formed particles. Figure 22 shows Ca and P contents of the formed particles as a function of X_{Cr} With increasing X_{Cr}, the Cr content increases as shown by the open squares and the Ca content decreases as shown by the solid squares. At $X_{Cr} \leqq 0.23$ both the contents linearly vary with X_{Cr}. The substitution ratio of Ca^{2+} ions with Cr^{3+} ions, that is, the number of Cr^{3+} ions replacing one Ca^{2+} ion was estimated from the slopes of the lines for Ca and Cr contents at $X_{Cr} \leqq 0.23$. The substitution ratio amounted 1.0, meaning that Ca^{2+} ions are replaced by Cr^{3+} ions in one to one in spite of the charge difference between these ions. Hence no cation vacancy forms, leading to the production of excess positive charges. These positive charges could be compensated by formation of another compound on the CaHAp surface and/or separately as confirmed by TEM later. The (Ca + Cr)/P ratios of the materials with varied X_{Cr} are shown by the

circle symbols in Figure 22. The ratios increase from 1.66 to 3.25 with increasing X_{Cr} from 0 to 1, being more than 1.67 of the stoichiometric ratio except the material without doping. Since CO_3^{2-} ions were not detected by FTIR but OH ions were detected, such large mole ratios would be ascribed to formation of another compound like chromium phosphate hydroxide. As will be described in the TEM result, irregular shaped particles were observed besides CaHAp particles at $X_{Cr} \geqq 0.13$ and increased with increasing X_{Cr} though no additional XRD peak appeared. It seems most likely therefore that another compound besides CaHAp is generated.

2.3.3.2 Change of the crystal structure of CaHAp

Figure 23 compares the XRD patterns of the materials formed in the presence of different amounts of Cr^{3+} ions. At X_{Cr} of 0.50 and less the patterns of all the materials possess only diffraction peaks due to CaHAp. The materials with $X_{Cr} = 0.015$ and 0.041 are less crystallized compared with other materials except for the materials with $X_{Cr} = 0.80$ and 1.00 showing only a weak peak at $2\theta = 17.3°$ that cannot be assigned for the moment. We estimated the influence of Cr^{3+} ions on the crystallinity of CaHAp from half height width (noted HHW) of the XRD peak due to (002) plane. The HHW values are plotted against X_{Cr} by the open circles in Figure 24. The materials with $X_{Cr} = 0.015$ and 0.041 show large HHW, which signifies that these materials have smaller crystallites and/or more distorted crystals. The change of crystallite sizes with doping can be estimated from the specific surface areas. The specific surface areas are shown along with the HHW values by the solid circles in Figure 24. As seen in this figure the variation of surface area with X_{Cr} is well in accord with that of HHW. This reveals that the crystallite size is decreased by doping small amount of Cr^{3+} ions and increased with

increasing X_{Cr} at Xcr ≧ 0.13. It is of interest that doping of Cr^{3+} ions results in the growth of CaHAp crystallites.

2.3.3.3 Morphology of Cr-doped CaHAp particles

Figure 25 displays TEM pictures of the materials doped with different amounts of Cr^{3+} ions. The CaHAp particles without doping are small short needles and they grow into large long particles upon increasing X_{Cr}. However, the larger particles with X_{Cr} ≦ 0.13 have higher surface area and larger HHW compared to the particles without doping and with X_{Cr} ≧ 0.13 (Figure 24). Thus, the particles with X_{Cr} = 0.015 and 0.041 seem to be agglomerates of minute primary particles as observed in the TEM pictures. The materials with X_{Cr} = 0.13, 0.23 and 0.50 are made up of long thin rectangular particles and a small amount of irregular particles. The irregular particles increase as X_{Cr} increases. At X_{Cr} ≧ 0.80 no long rectangular particles are observed and only small cube like particles are observed. The irregular and cube like particles are supposed to be not CaHAp. To verify this, we carried out EPMA on the materials with X_{Cr} = 0.041 and 0.13. Ca, Cr and P contents of thin long particles in the material with X_{Cr} = 0.041 and both thin long and irregular particles in the material with X_{Cr} = 0.13 were determined. Table 1 shows the contents averaged for 10 particles of each kind of particles. The mole ratios of X_{Cr} and (Ca + Cr)/P measured by EPMA on the particles with X_{Cr} = 0.041 are close to X_{Cr} and (Ca + Cr)/P obtained by ICP, respectively, taking account of the deviations. On the other hand, in the case of the material formed with X_{Cr} = 0.13, the irregular and long rectangular particles show quite different X_{Cr} and (Ca + Cr)/P determined by EPMA; the irregular particles show larger mole ratios than the long

rectangular ones. It is clear from these EPMA results that the irregular particles are not CaHAp and the long rectangular particles are CaHAp. From the EPMA and IR results shown later, the composition formula of the irregular particles in the material with X_{Cr} = 0.13 is expressed as $Ca_{0.3}Cr_{0.7}(PO_4)_{0.3}(OH)_{1.8}$ using X_{Cr} = 0.71 and (Ca + Cr)/P = 3.2 shown in Table 1. This substance is hydrated as shown by TG and it is less crystalline since no XRD additional peak appeared (Figure 23). As shown in Figure 22, (Ca + Cr)/P ratio increased from 1.66 to 3.3 with increasing X_{Cr} from 0 to 1.0. This can be explained by the formation of another compound with a large (Ca + Cr)/P ratio. At X_{Cr} ≧ 0.13, this compound forms as irregular particles, as shown by TEM. The composition formula of the cube like particles formed without Ca^{2+} ions (X_{Cr} = 1.0), estimated from the Cr and P contents determined by ICP, is $Cr_{3.3}(PO_4)(OH)_{6.9}$. This material is also hydrated as will be shown.

2.3.3.4 Thermal analysis of Cr doped CaHAp

To examine the thermal stability of Cr doped CaHAp, TG curves of the materials with varied X_{Cr} were measured. The TG curves are shown in Figure 26. The material without doping gives rise to continuous weight loss continued to 1000 °C, which is mainly due to adsorbed and/or strongly bound H_2O as has been confirmed by FTIR [54]. The materials with X_{Cr}, ≧ 0.13 show a small weight loss from ca 550 °C in addition to the weight loss observed on the material without doping. This weight loss may be due to the release of OH^- ions as H_2O in the irregular particles. The total weight loss markedly increases with increasing X_{Cr}, showing that the materials with larger X_{Cr} contain more OH^- ions as speculated from the composition proposed above. However, the weight loss

due to dehydroxylation of the material with X_{Cr} = 1.0, estimated from the composition $Cr_{3.3}(PO_4)(OH)_{6.9}$, amounts to 16.2 wt.%, much smaller than the weight loss of 38.8 wt.% at 25 to 1000 °C in the TG curve. This large weight loss seems to be attributable to release of the bound H_2O. Consequently, the composition of the material with X_{Cr} = 1.0 can be regarded as $Cr_{3.3}(PO_4)\ (OH)_{6.9}\cdot 7.9H_2O$.

2.3.3.5 XPS and IR spectra of Cr doped CaHAp

XPS spectra of the samples with different X_{Cr} were taken to clarify the state of Cr^{3+} ions doped in CaHAp. Figure 27 shows the peaks due to $P2p_{2/3}$, $Ca2p_{1/2}$, $Ca2p_{3/2}$ and $Cr2p_{3/2}$ of the materials with different X_{Cr}. These peaks are not markedly shifted by doping. The binding energy of $Cr2p_{3/2}$ peak is 577.5 to 577.9 eV. The binding energies of $Cr2p_{3/2}$ peaks determined on various chromium compounds are 573.8(metal Cr), 576.7(Cr_2O_3), 578.8(CrF_3), 579.2(CrO_3) and 579.9($K_2Cr_2O_7$) eV. Since the binding energy of $Cr2p_{3.2}$ peak for Cr doped CaHAp lies between those for Cr_2O_3 and CrF_3, the doped Cr^{3+} ions seem to exist as trivalent ions. Furthermore, the binding energy of 577.9 eV of the material with X_{Cr} = 0.041 is close to 577.8 eV of the material with X_{Cr} = 1.0 of which the formula is $Cr_{3.3}(PO_4)(OH)_{6.9}\bullet 7.9H_2O$. It seems therefore that the doped Cr^{3+} ions are coordinated by OH^- and PO_4^{3-} ions and H_2O molecules.

As mentioned already, less crystallized irregular particles formed with larger X_{Cr} are supposed to be hydrated chromium phosphate hydroxide, for instance, such as $Cr_{3.3}(PO_4)(OH)_{6.9}\bullet 7.9H_2O$ for the material with X_{Cr} = 1.0. For further verification of this, IR spectra of the materials with varied X_{Cr}, were measured and are depicted in Figure 28. The spectrum of the material without doping shows the bands at 1090 and 1040 cm^{-1} due to the stretching mode (v3) of O−P, the weak bands at 960 cm^{-1} due to the

stretching mode (ν1) of O--P and the bands at 630, 605 and 560 cm^{-1} due to the deformation mode (ν4) of O−P−O[55]. The intensities of these PO_4^- bands increase with increasing X_{Cr} and the PO_4^- bands of the material with $X_{Cr} = 0.13$ are very strong. At $X_{Cr} \geqq 0.23$ the PO_4^- bands are weakened with increasing X_{Cr} and are very broad at $X_{Cr} \geqq 0.80$. These FTIR results are in good agreement with the XRD results; highly crystallized materials give rise to strong sharp PO_4^- bands. The materials with $X_{Cr} \geqq 0.80$ show a strong broad band centered at 3400 cm^{-1} with a shoulder at 3200 cm^{-1} due to the stretching modes of OH ions and stretching modes (ν1 and ν3) of H_2O molecules, and a strong band at 1630 cm^{-1} due to the deformation mode (ν2) of H_2O molecules, although the spectra are not shown here. This proves that the material with $X_{Cr} \geqq 0.80$ contains larger amount of OH ions and H_2O molecules compared to the other materials, supporting the proposed chemical composition.

2.3.3.6 Effect of Cr^{3+} ions on the crystal growth of CaHAp

As seen from Figure 25, doping of Cr^{3+} ions causes a marked growth of CaHAp particles. Such uniform large particles observed in the materials with $X_{Cr} = 0.23$ and 0.50 shown in Figure 25 did not form when substituted with Mg^{2+} ions by a precipitation method, while large agglomerates of small primary CaHAp particles were produced [56]. It has been reported that the ion exchange of CaHAp with Fe^{3+}, Al^{3+} and La^{3+} ions in acidic solutions destroys the CaHAp crystals to form phosphates of these ions [49]-[51]. However, the crystal growth of CaHAp found in the present study did not take place in the ion exchange. Various trivalent ions such as Al^{3+}, Cr^{3+} and La^{3+} ions reduce the dissolution of CaHAp in solutions less than pH 7 but Fe^{3+} ions do not

influence this [57)-(59)]. This effect can be explained by the formation of phosphates of the former three ions with lower solubility than CaHAp. However, the materials of this study were synthesized in basic solutions of pH 9 where the solubility of CaHAp is much lower than that of metal phosphates [(60)]. Hence, the hydrated chromium phosphate hydroxide resulted by doping of Cr^{3+} ions would not influence dissolution of CaHAp particles. According to the EPMA result, long rectangular CaHAp particles formed with $X_{Cr} \leqq 0.13$ contain Cr^{3+} ions less than ca. 0.03 in X_{Cr}. Such a small amount of Cr^{3+} ions cannot interfere with the crystal growth of CaHAp. The Cr^{3+} ions doped at $X_{Cr} >$ ca 0.03 are consumed to produce hydrated calcium chromium phosphate hydroxide that is less crystallized irregular particles. This substance is considered to control the crystal growth of CaHAp by decreasing the number of precursor nuclei and acting as the reservoir of the solutes for the crystal growth.

In conclusion, the crystal growth of CaHAp is strongly promoted on doping Cr^{3+} ions by the coprecipitation method with basic solutions. Long rectangular CaHAp particles resulted on doping at $X_{Cr} \geqq 0.23$, containing a small amount of Cr^{3+} ions. The residual doped Cr^{3+} ions are consumed to produce hydrated calcium chromium phosphate hydroxides which concern the crystal growth of CaHAp.

References

(1) T. Suzuki, Y. Hayakawa, Proc. First Int. Congr. on Phosphorus Compounds, IMPHOS, Paris, 1977, p. 381.

(2) T. Suzuki, T. Hatsushika, Y. Hayakawa, *J. Chem. Soc., Faraday Trans*. I **77** (1981) 1059.

(3) T. Suzuki, T. Hatsushika, M. Miyake, *J. Chem. Soc., Faraday Trans. I* **78** (1982) 3605.

(4) M. Miyake, T. Kobayashi, T. Suzuki, *Yogyo-Kyokai-Shi* **94** (1986) 136.

(5) M. Miyake, K. Ishigaki, T. Suzuki, *J. Solid State Chem.* **61** (1986) 230.

(6) Y. Tanizawa, T. Ujiie, K. Sawamura, T. Suzuki, *Denki Kagaku* **55** (1987) 903.

(7) Y. Tanizawa, K. Sawamura, T. Suzuki, *J. Chem. Soc., Faraday Trans.* **86** (1990) 1071.

(8) Y. Tanizawa, K. Sawamura, T. Suzuki, *J. Chem. Soc., Faraday Trans.* **86** (1990) 4025.

(9) T. Suzuki, T. Hatsushika, *Gypsum and Lime* **224** (1990) 15.

(10) M. Misono, W.K. Hall, *J. Phys. Chem.* **77** (1973) 791.

(11) Y. Matsumura, J.B. Moffat, S. Sugiyama, H. Hayashi, N. Shigemoto, K. Saitoh, *J. Chem. Soc., Faraday Trans.* **90**(1994) 2113.

(12) T. Ishikawa, H. Saito, A. Yasukawa, K. Kandori, *Bull. Chem. Soc. Jpn.* **69** (1996) 899.

(13) M. Wakamura, K. Kandori, T. Ishikawa, *Polyhedron* **16**(1997) 2047.

(14) A. Yasukawa, S. Ouchi, K. Kandori, T. Ishikawa, *J. Mater. Chem.* **6** (1996) 1401.

(15) A.L. Boskey, A.S. Posner, *Mater. Res. Bull.* **9** (1974) 907.

(16) R.L. Collin, *J. Am. Chem. Soc.* **81** (1959) 5275.

(17) A. Bigi, E. Foresti, F. Marchetti, A. Ripamonti, N. Roveri, *J. Chem. Soc., Dalton Trans.* (1984) 1091.

(18) M. Muller, *Helv. Chim. Acta* **30** (1947) 2069.

(19) S. Sugiyama, T. Moriga, M. Goda, H. Hayashi, J.B. Moffat, *J. Chem. Soc., Faraday Trans.* **92** (1996) 4305.

(20) D.R. Penn, *J. Electron Spectrosc.* **9** (1976) 29.

(21) T. Ishikawa, M. Wakamura, S. Kondo, *Langmuir* **5**(1989) 140.

(22) T. Ishikawa, in: A. Dabrowski, V.A. Tertykh (Eds.), Adsorption on New and Modified Inorganic Sorbents, Elsevier, Amsterdam, 1996, p. 301.

(23) C.F. Baes, J.R. Mesmer, The Hydrolysis of Cations, Wiley, New York, 1976, p. 211.

(24) R.A. Young, *J. Dent. Res. Supp.* **253** (1974) 193.

(25) J.A. Weatherell, C. Robinson, *Proc. Finn. Dent. Soc.* **78** (1982) 81.

(26) R.M.H. Verbeeck, C.J. Lassuyt, H.J.M. Heijligers, F.C.M. Driessens, J.W.G.A. Vrolijk, *Calcif. Tissue Int.* **33** (1981) 247.

(27) R.L. Collin, *J. Am. Chem. Soc.* **81** (1959) 5275.

(28) A.E. Sobel, J. Cohen, B. Kramer, *Biochem. J.* **29** (1935) 2646.

(29) W.T. Reichle, *J. Catal.* **17** (1970) 297.

(30) N.S. Figoli, H.R. Keselman, P.C. L'Argentiere, C.L. Lazzaroni, *J. Catal.* **77** (1982) 64.

(31) M. Misono, W.K. Hall, *J. Phys. Chem.* **77** (1973) 791.

(32) Y. Matumura, J.B. Moffat, S. Sugiyama, H. Hayashi, N. Shigemoto, K. Saitoh, *J. Chem. Soc. Faraday Trans.* **90** (1994) 2133.

(33) M.R. Christoffersen, J. Christoffersen, Calcif. *Tissue Int.* **37** (1985) 637.

(34) M.R. Christoffersen, H.C. Thyregod, J. Christoffersen, Calcif. *Tissue Int.* **41** (1987) 27.

(35) P. Schaad, P. Gramain, F. Gorce, J.C. Voegel, *J. Chem. Soc. Faraday Trans.* **90** (1994) 3405.

(36) T. Suzuki, T. Hatsushika, Y. Hayakawa, *J. Chem. Soc. Faraday Trans.* **177** (1981) 1059.

(37) T. Suzuki, T. Hatsushika, M. Miyake, *J. Chem. Soc. Faraday Trans.* **178** (1982) 3605.

(38) X. Yuping, F.W. Schwartz, *Environ. Sci. Technol.* **28** (1994) 1472.

(39) Y. Tanizawa, K. Sawamura, T. Suzuki, *J. Chem. Soc. Faraday Trans.* **86** (1990) 4025.

(40) Y. Tanizawa, K. Sawamura, T. Suzuki, *J. Chem. Soc. Faraday Trans.* **86** (1990) 1071.

(41) M. Wakamura, K. Kandori, T. Ishikawa, *Coll. Surf. A* **142** (1998) 107.

(42) J.S. Reid, J.A. Beeley, D.G. MacDonald, *J. Dent. Res.* **56** (1977) 895.

(43) P. Torell, *Swed. Dent. J.* **12** (1988) 113.

(44) C.K. Kleber, M.S. Putt, *J. Dent. Res.* **64** (1985) 437.

(45) H. Negishi, T. Fujihara, N. Yamazaki, A. Miyagi, M. Higaki, S. Saito, *Jpn. J. Oral Biol.* **29** (1987) 541.

(46) J.C. Elliott, Structure and Chemistry of the Apatites and Other Calcium Orthophosphates, Elsevier, Amsterdam, 1994, p. 4.

(47) T. Ishikawa, M. Wakamura, S. Kondo, *Langmuir* **5** (1989) 140.

(48) J.B. Peri, *J. Phys. Chem.* **69** (1965) 220.

(49) Y. Tanizawa, K. Sawamura and T. Suzuki, *J. Chem. Soc., Faraday Trans.* 1990, **86**, 1071.

(50) Y. Tanizawa, K. Sawamura and T. Suzuki, *J. Chem. Soc., Faraday Trans.* 1990, **86**, 4025.

(51) T. Suzuki and T. Hatsushika, *Gypsum Lime* 1990, **244**, 15.

(52) T. Ishikawa, H. Saito, A. Yasukawa and K. Kandori, *Bull. Chem. Soc. Jpn.* 1996, **69**, 899.

(53) J. A. Weatherell and C. Robinson, *Proc. Finn. Dent. Soc.* 1982, **78**, 81.

(54) T. Ishikawa, M. Wakamura and S. Kondo, *Langmuir* 1989, **5**, 140.

(55) J. C. Elliott, Structure and Chemistry of the Apatites and Other Calcium Orthophosphates, p. 171. Elsevier, Amsterdam (1994).

(56) A. Yasukawa, S. Ouchi, K. Kandori and T. Ishikawa, *J. Mater. Chem.* 1996, **6**, 1401.

(57) M. R. Christoffersen and J. Christoffersen, *Calcif. Tissue Int.* 1985, **37**, 673.

(58) M. R. Christoffersen, H. C. Thyregod and J. Christoffersen, *Calcif. Tissue Int.* 1987, **41**, 27.

(59) P. Schaad, P. Gramain, F. Gorce and J. C. Voegel, *J. Chem. Soc., Faraday Trans.* 1994, **90**, 3405.

(60) W. Stumm and J. J. Morgan, Aquatic Chemistry p. 283. Wiley Interscience, New York (1981).

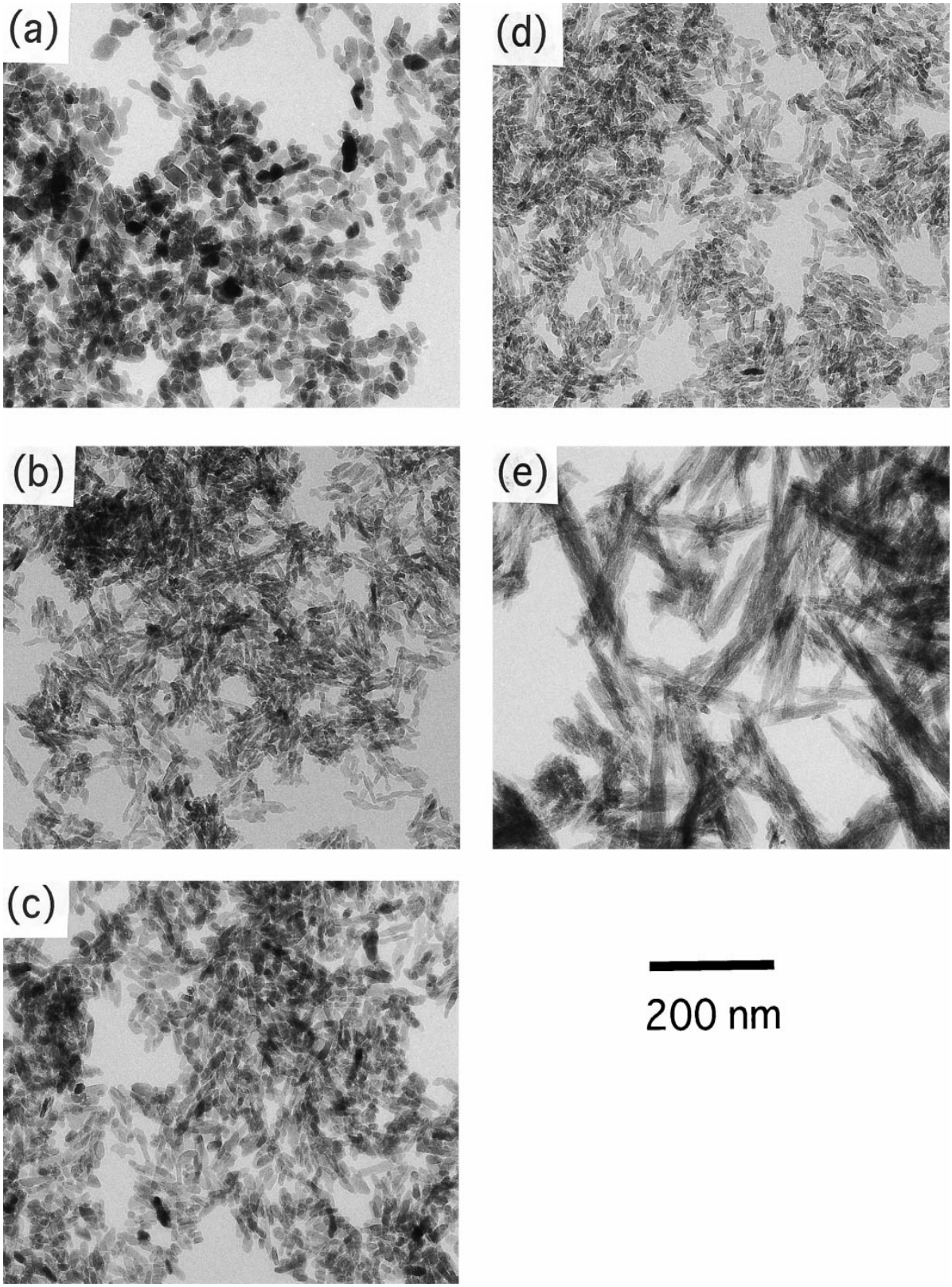

Figure 1 TEM picture of the particles formed by the coprecipitation with various metal ions at Xmetal=0.03: (a) original sample; (b) Ni^{2+} ; (c) Cu^{2+} ;(d) Co^{2+}; (e) Cr^{3+}

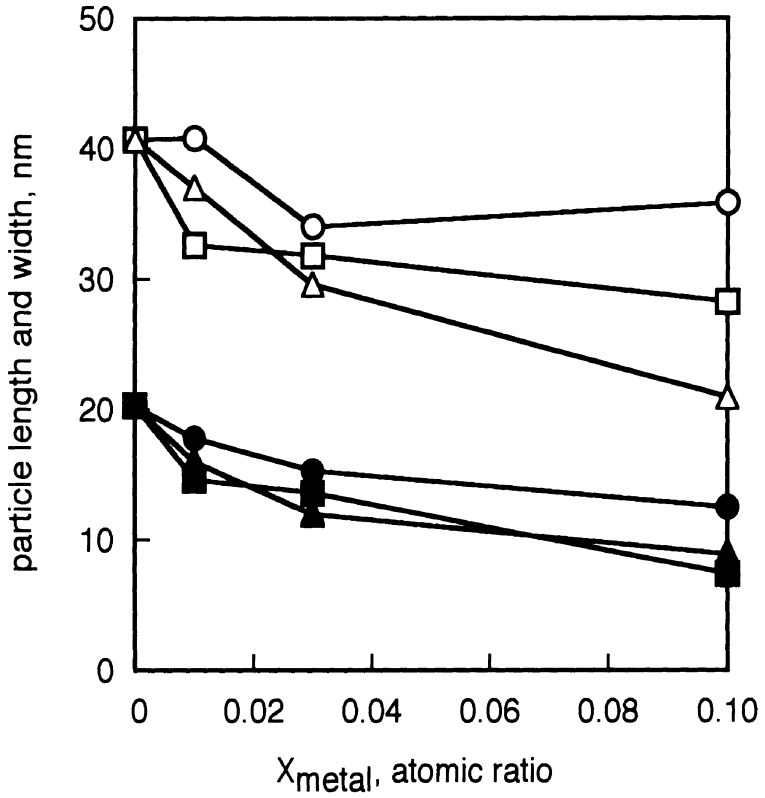

Figure 2 Average lengths (open symbols) and widths (solid symbols) of the particles formed by the coprecipitation with various metal ions vs. Xmetal: □, ■ Ni^{2+}; ○, ● Cu^{2+} ;△, ▲ Co^{2+}.

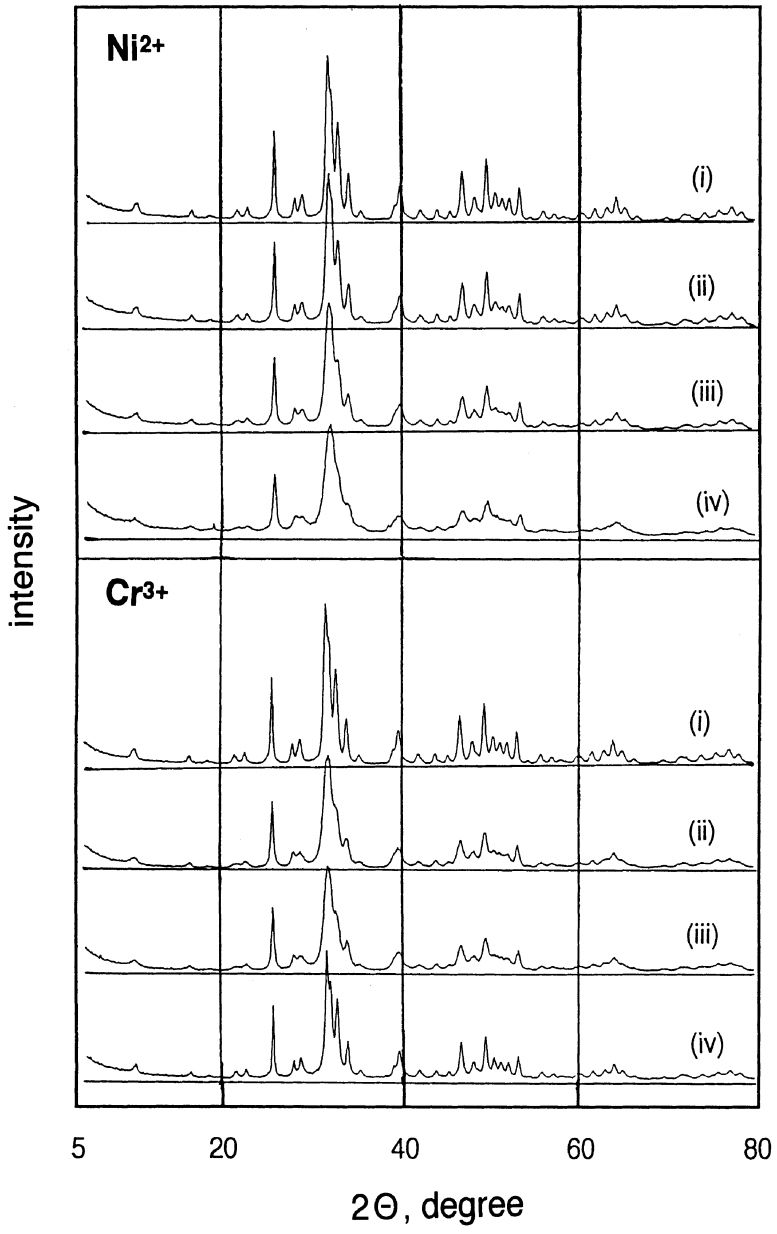

Figure 3 XRD patterns of the coprecipitation products with Ni^{2+} and Cr^{3+} at different Xmetal: (i) 0; (ii) 0.001; (iii) 0.01; (iv) 0.1.

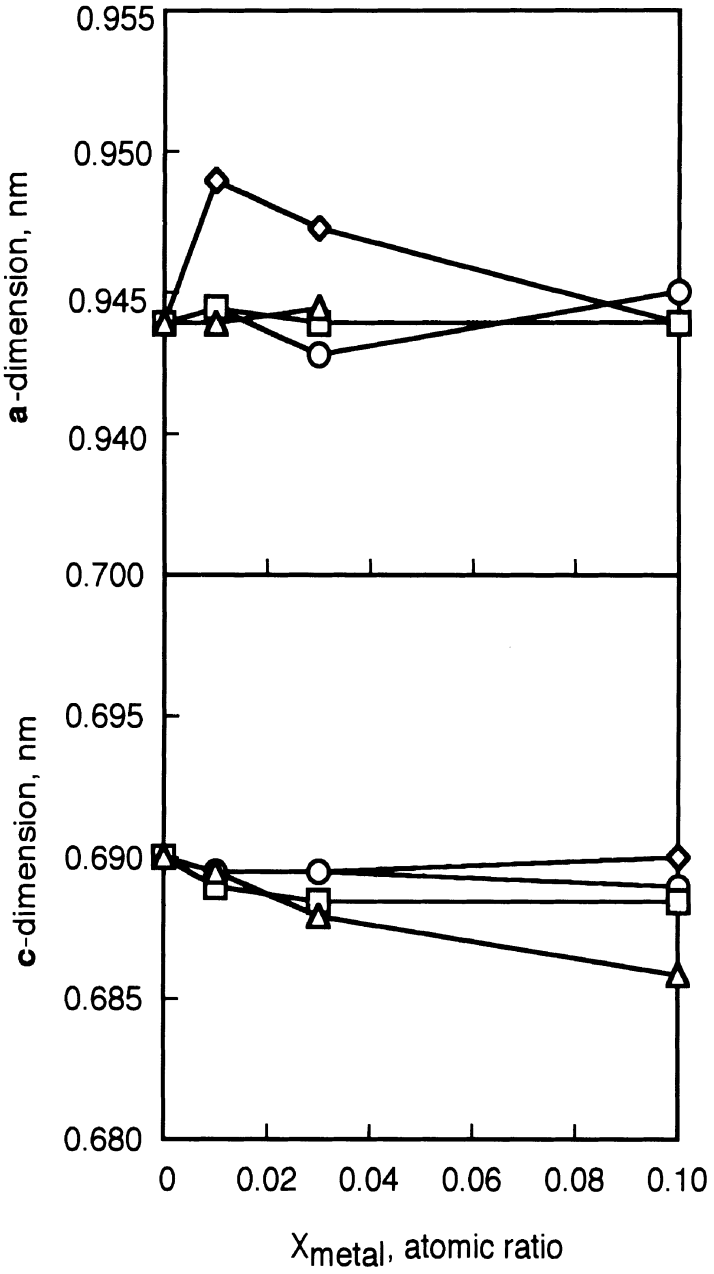

Figure 4 Unit cell dimensions of the coprecipitation products with various metal ions vs. Xmetal: □ Ni^{2+} ; ○ Cu^{2+} ; △ Co^{2+}; ◇ Cr^{3+}

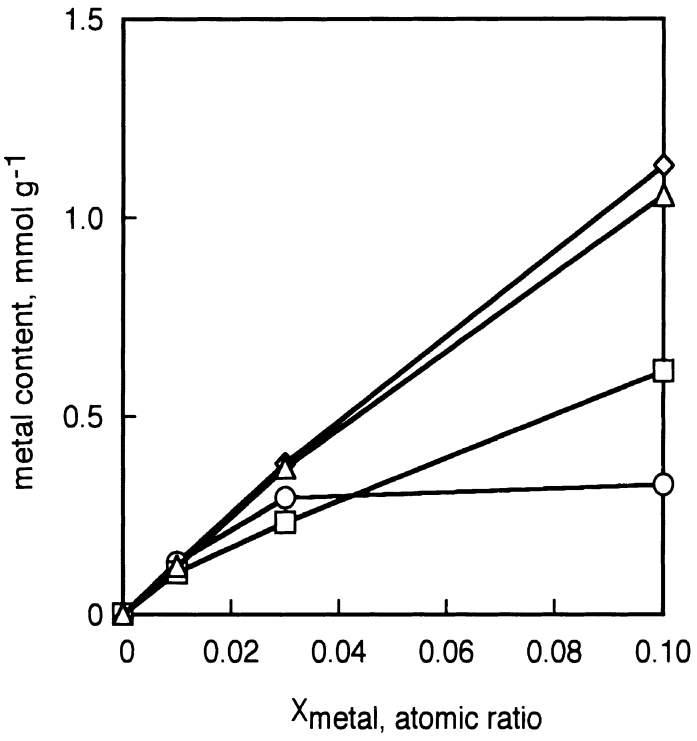

Figure 5 Metal contents of the coprecipitation products with various metal ions vs. Xmetal: □ Ni^{2+} ; ○ Cu^{2+} ; △ Co^{2+}; ◇ Cr^{3+}

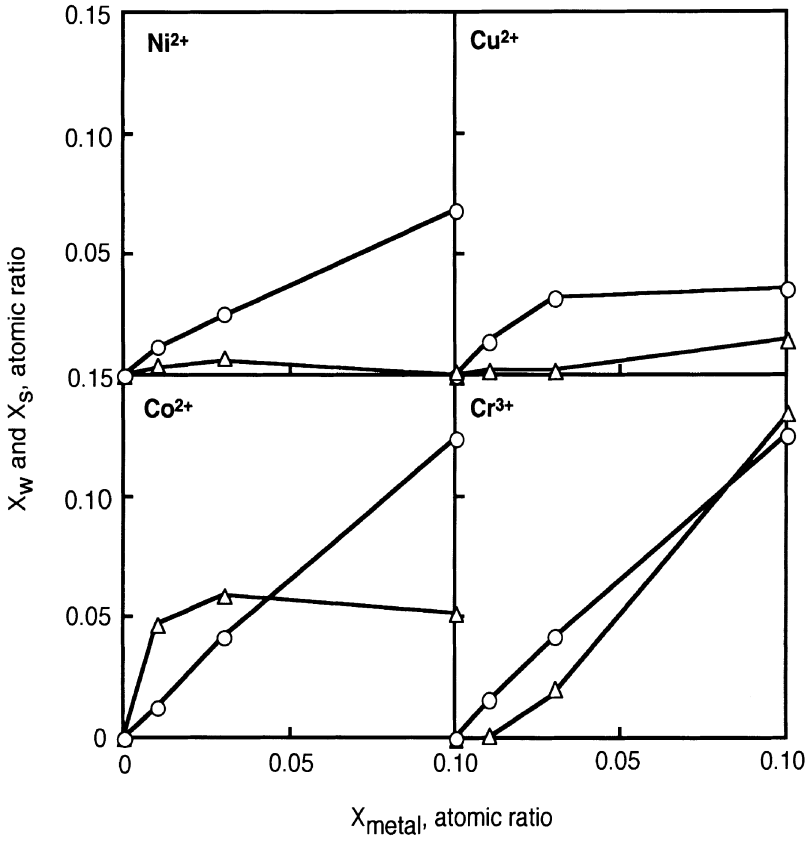

Figure 6 Atomic ratio in the whole particle (Xw, ○) and in the surface phase (Xs, △) of the particles formed with the coprecipitation Ni^{2+} , Cu^{2+}, Co^{2+} and Cr^{3+}.

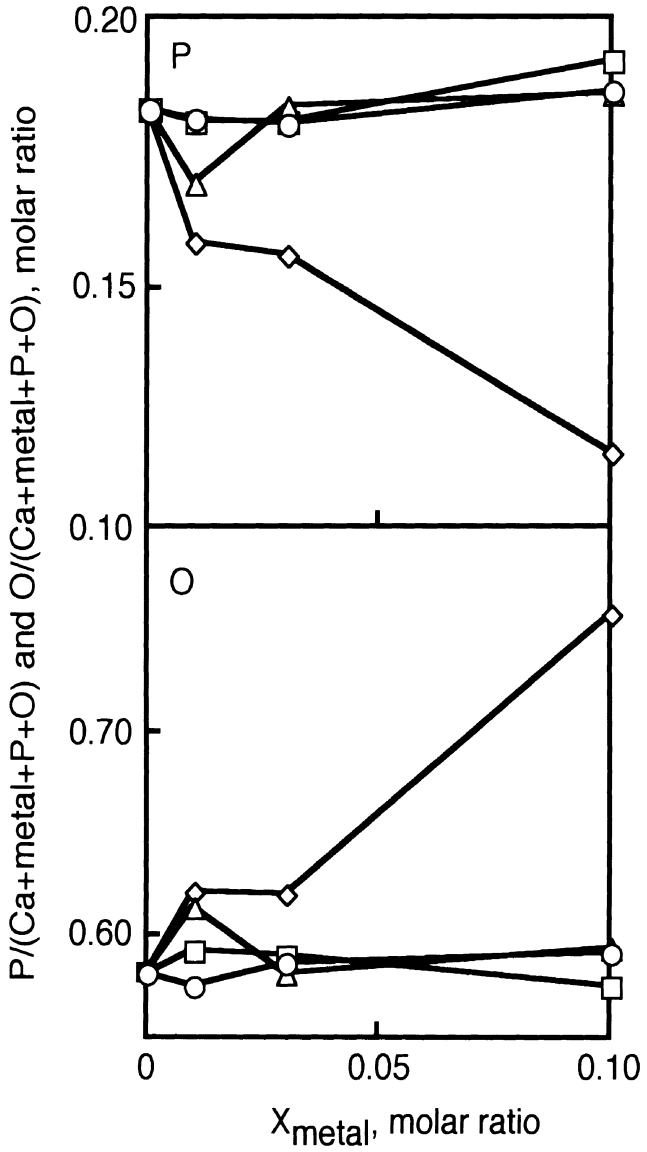

Figure 7 Surface atomic ratios of P and O of the particles formed with the coprecipitation with various metal ions: □ Ni^{2+} ; ○ Cu^{2+} ; △ Co^{2+}; ◇ Cr^{3+}.

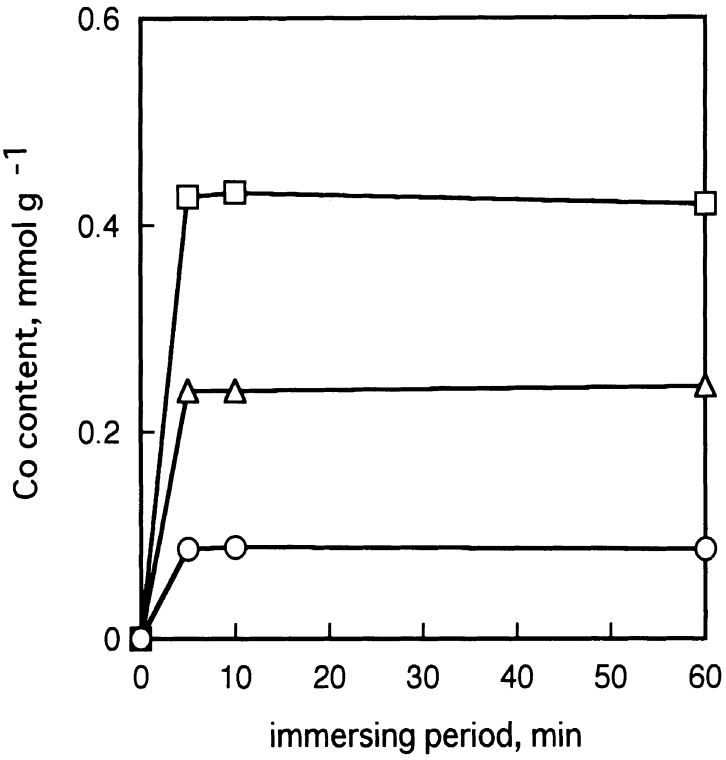

Figure 8 Co contents of the CaHAps immersed for varied periods in the solutions containing different concentrations of Co^{2+}:○ 0.001; △ 0.01; □ 0.1 mol dm^{-3}.

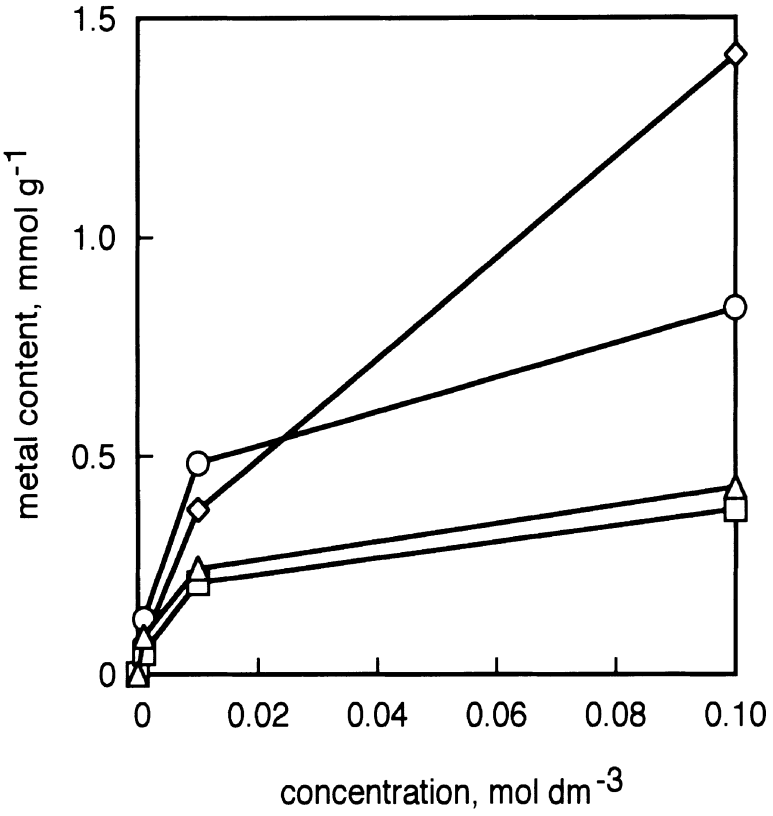

Figure 9 Metal contents of the CaHAp immersed in the solutions of various metal ions: □ Ni^{2+} ; ○ Cu^{2+} ; △ Co^{2+}; ◇ Cr^{3+}.

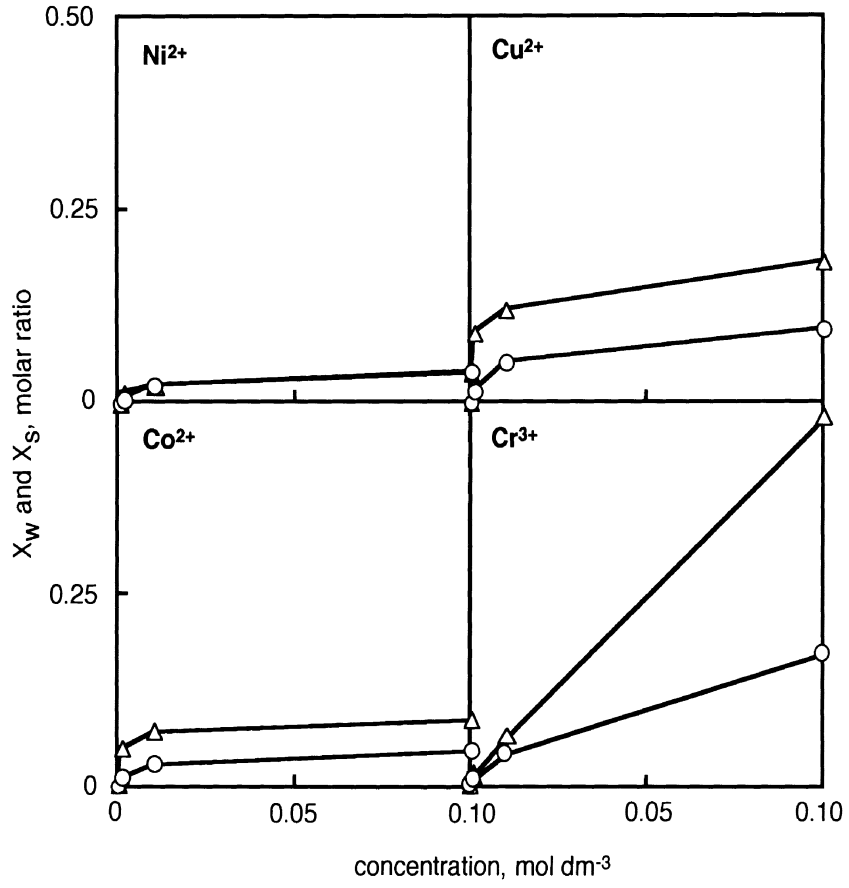

Figure 10 Atomic ratios in the whole particle (Xw, ○) and in the surface phase(Xs, △) of the CaHAp particles modified by the exchange with Ni^{2+} , Cu^{2+}, Co^{2+} and Cr^{3+}.

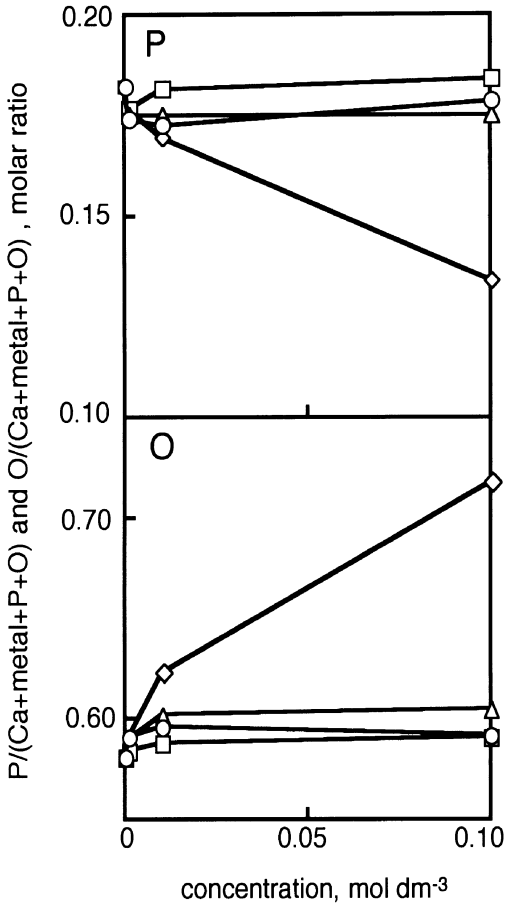

Figure 11 Surface atomic ratios of P and O of the CaHAp particles modified by the exchange with various metal ions: □ Ni^{2+} ; ○ Cu^{2+} ; △ Co^{2+}; ◇ Cr^{3+}.

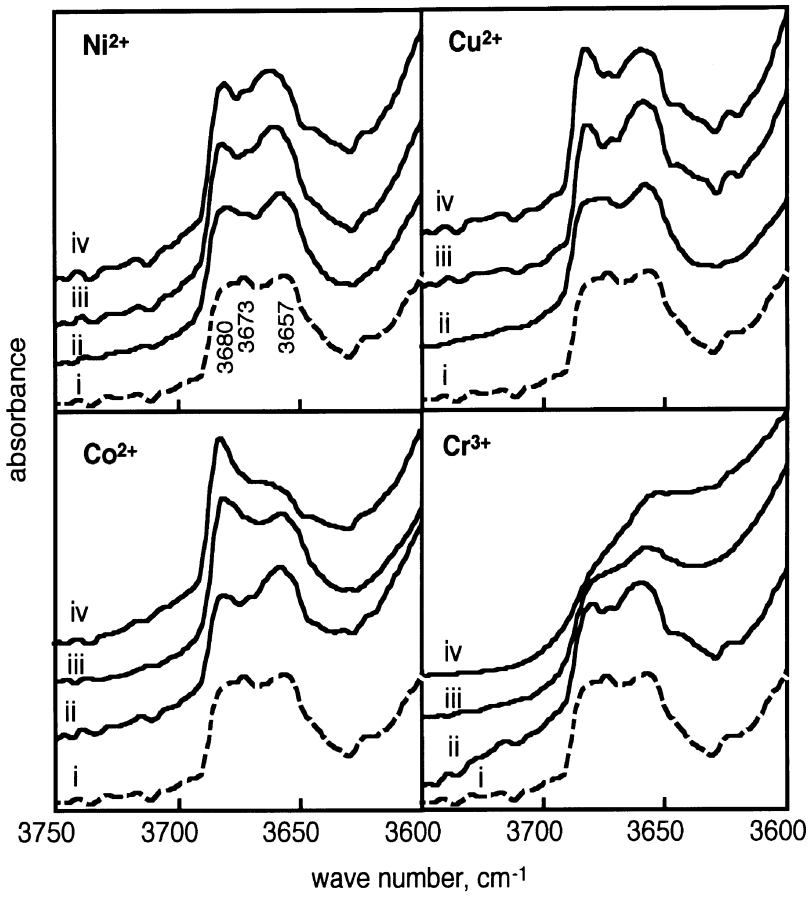

Figure 12 IR spectra of the coprecipitation products Ni^{2+}, Cu^{2+}, Co^{2+} and Cr^{3+}. The atomic ratios (Xmetal) of the metal ions added to the starting solutions were: (i) 0; (ii) 0.001; (iii) 0.01; (iv) 0.1.

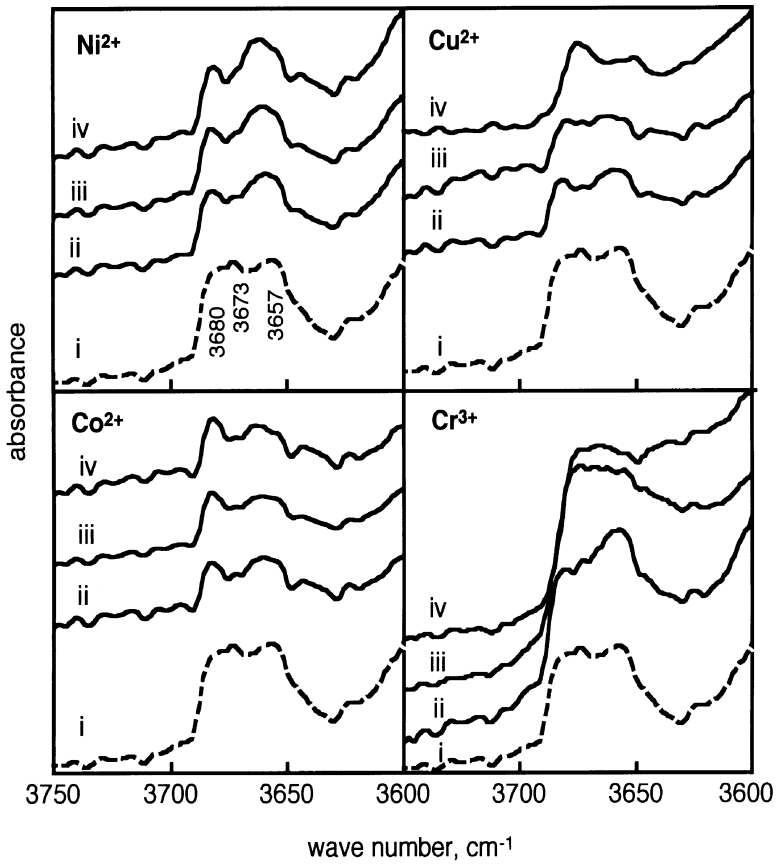

Figure 13 IR spectra of the CaHAp particles modified by the exchange with Ni^{2+}, Cu^{2+}, Co^{2+} and Cr^{3+}. The concentrations of the metal ions in the treating solutions were: (i) original sample; (ii) 0.001; (iii) 0.01; (iv) 0.1 mol dm^{-3}.

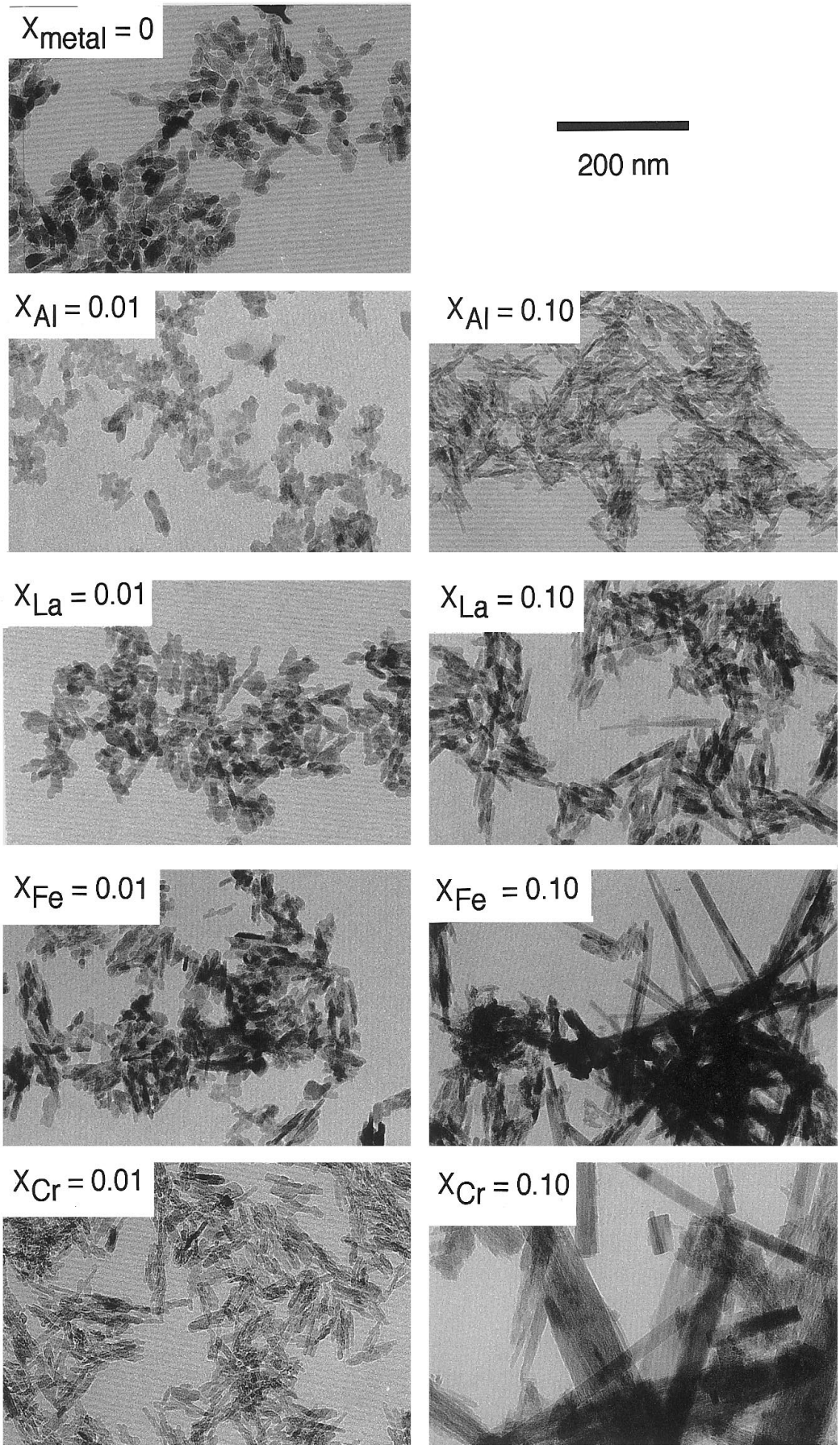

Figure 14 TEM pictures of the particles formed at varied Xmetal by the coprecipitation method.

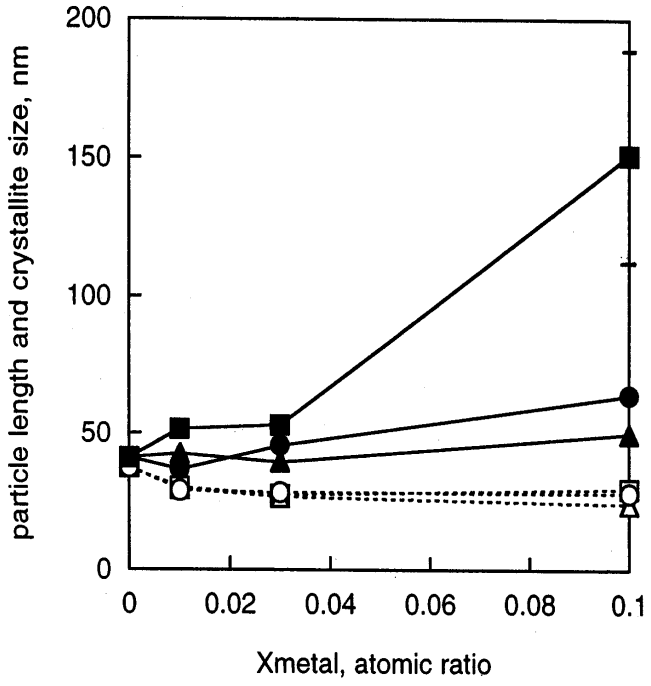

Figure 15 Mean particle length and crystallite size of the particles formed with Al(III)(○●), La(III)(△▲) and Fe(III)(□■) by the coprecipitation method. The filled and open marks represent respectively mean particle length and crystallite size.

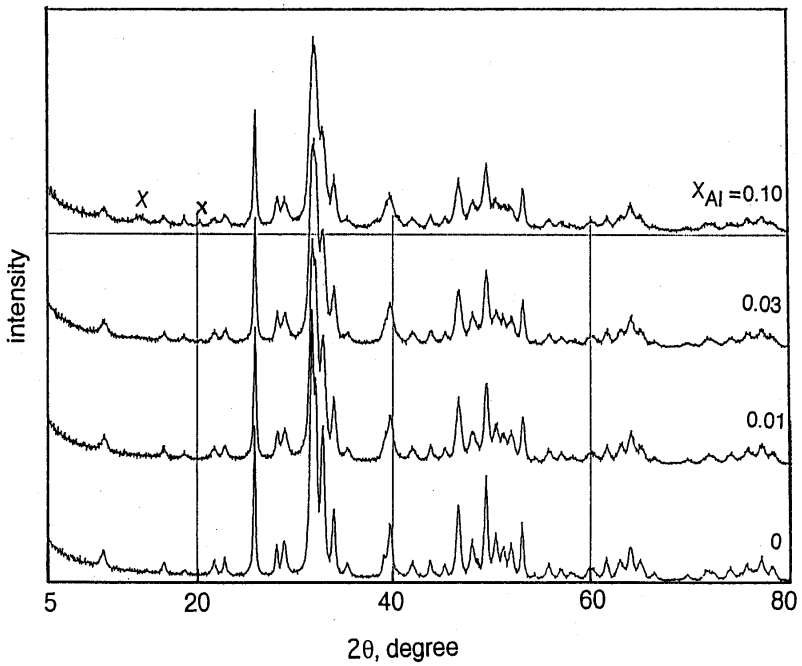

Figure 16 XRD patterns of the products at varied X_{Al} by the coprecipitation method.

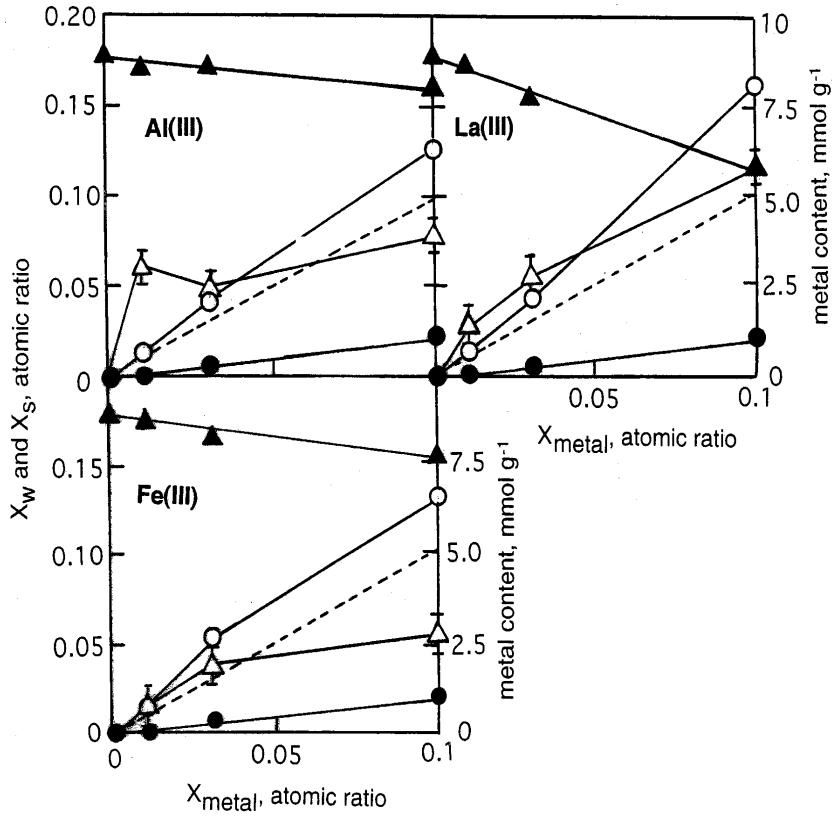

Figure 17 The contents of Ca(II) (▲) and metal ions (●), Xw (○) and Xs (△) in the particles formed with Al(III), La(III), Fe(III) by the coprecipitation method. The dashed lines represent Xmetal.

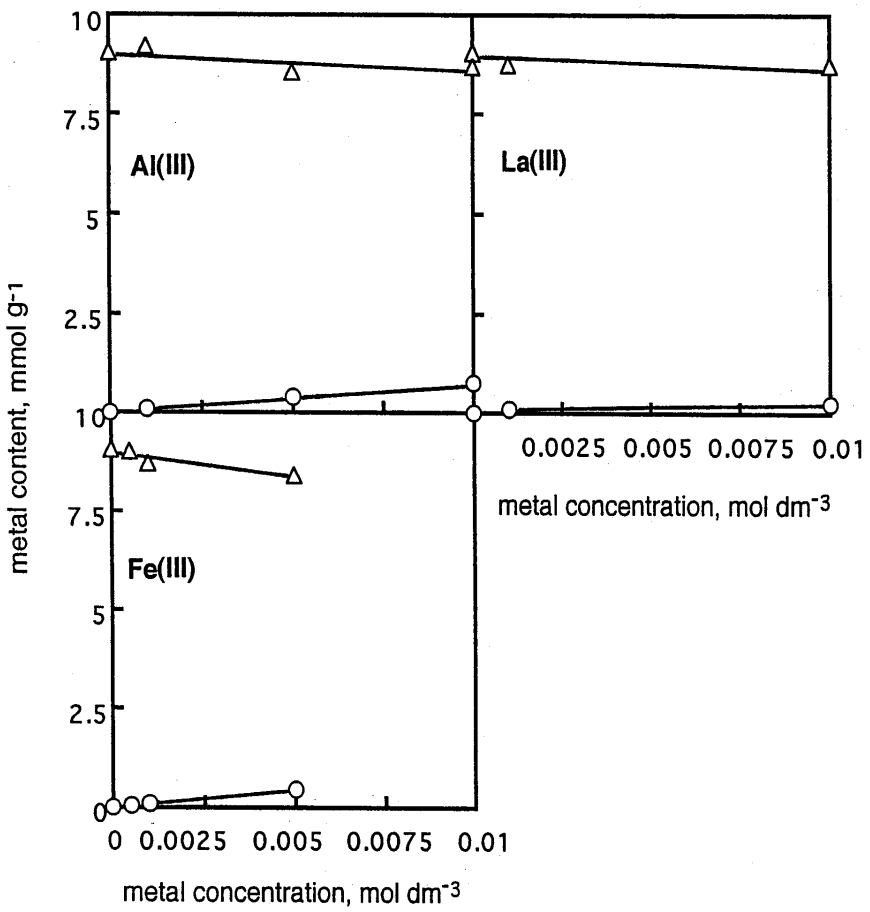

Figure 18 The contents of Ca(II) (△) and metal ions (○) in the particles ion exchanged by immersing in the solutions containing different concentrations Al(III), La(III) and Fe(III) .

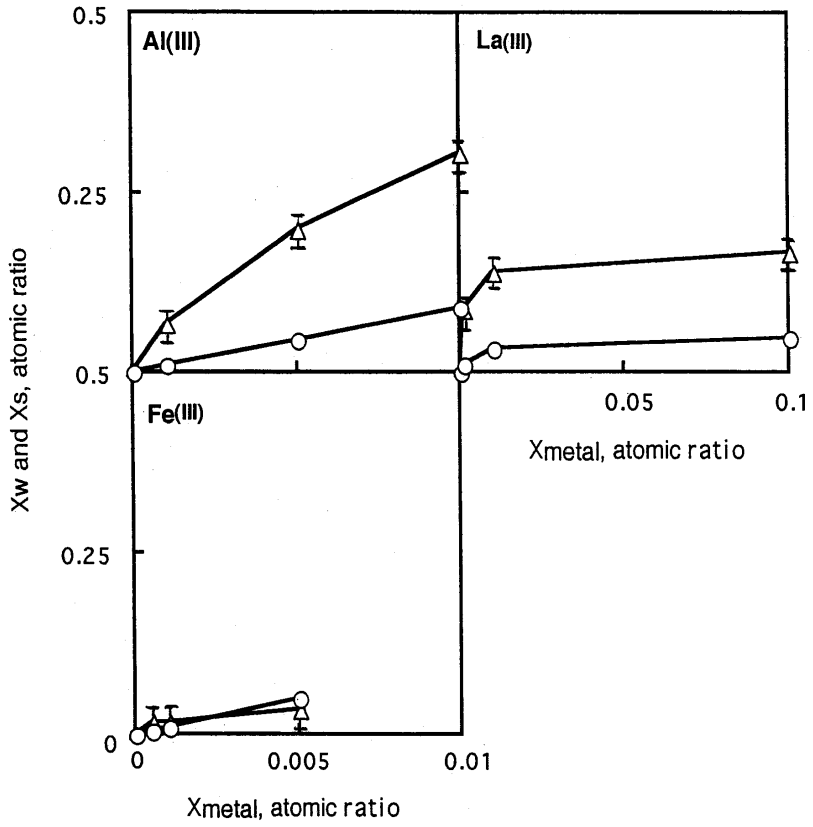

Figure 19 Xw (○) and Xs (△) of the particles ion exchanged by immersing in the solutions containing different concentrations of Al(III), La(III) and Fe(III).

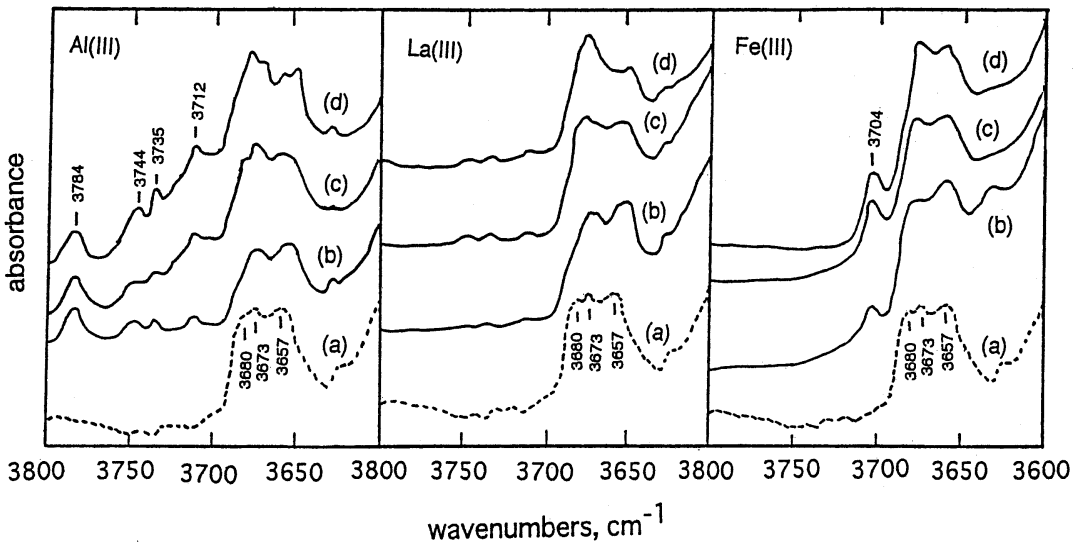

Figure 20 IR spectra of the products with Al(III), La(III) and Fe(III) by the coprecipitation method. Xmetal, (a) 0; (b) 0.01; (c) 0.03; (d) 0.10.

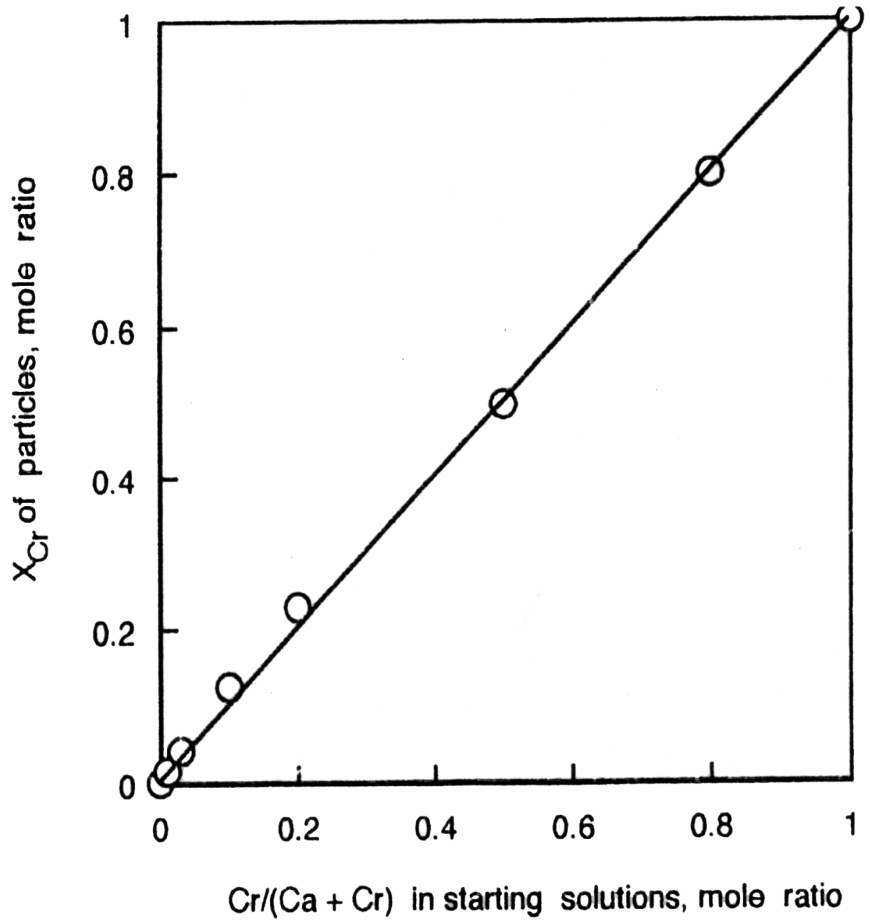

Figure 21 Relationship between X_{Cr} of the formed particles and Cr/(Ca+Cr) in the starting solutions.

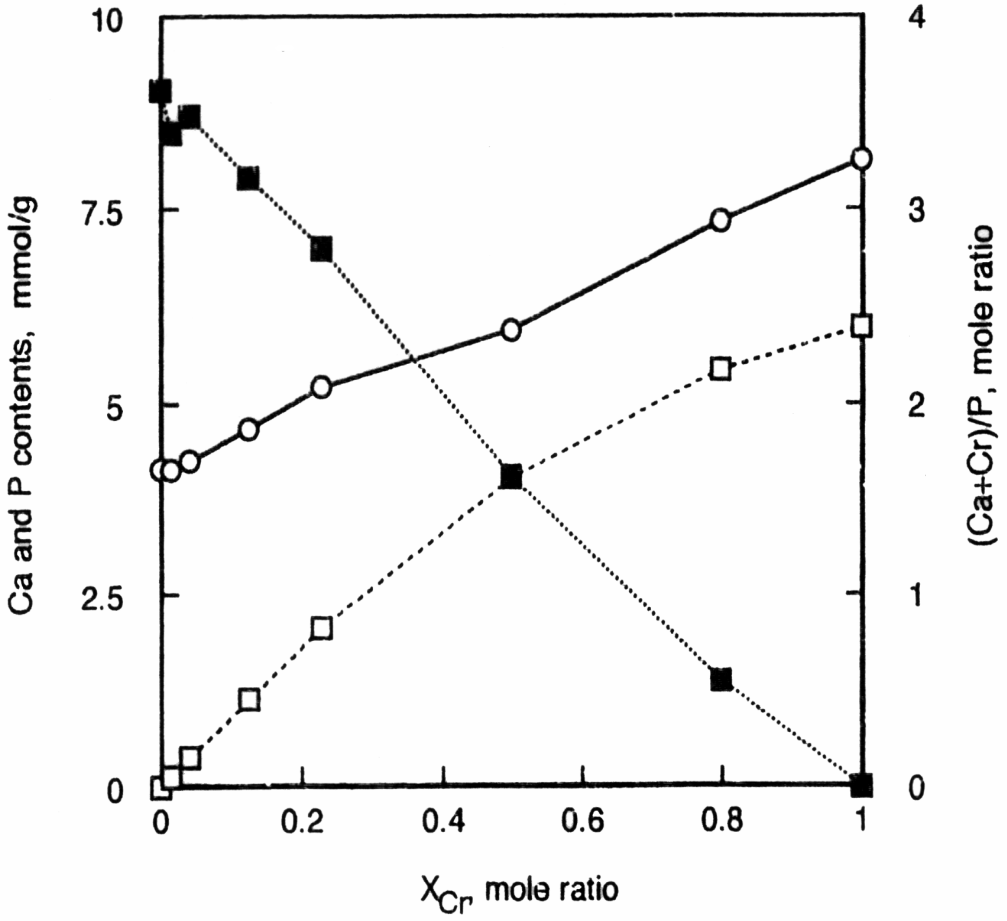

Figure 22 Plots of Ca and Cr contents and (Ca+Cr)/P ratios against X_{Cr}; ■, Ca content; □, Cr content; ○, (Ca+Cr)/P.

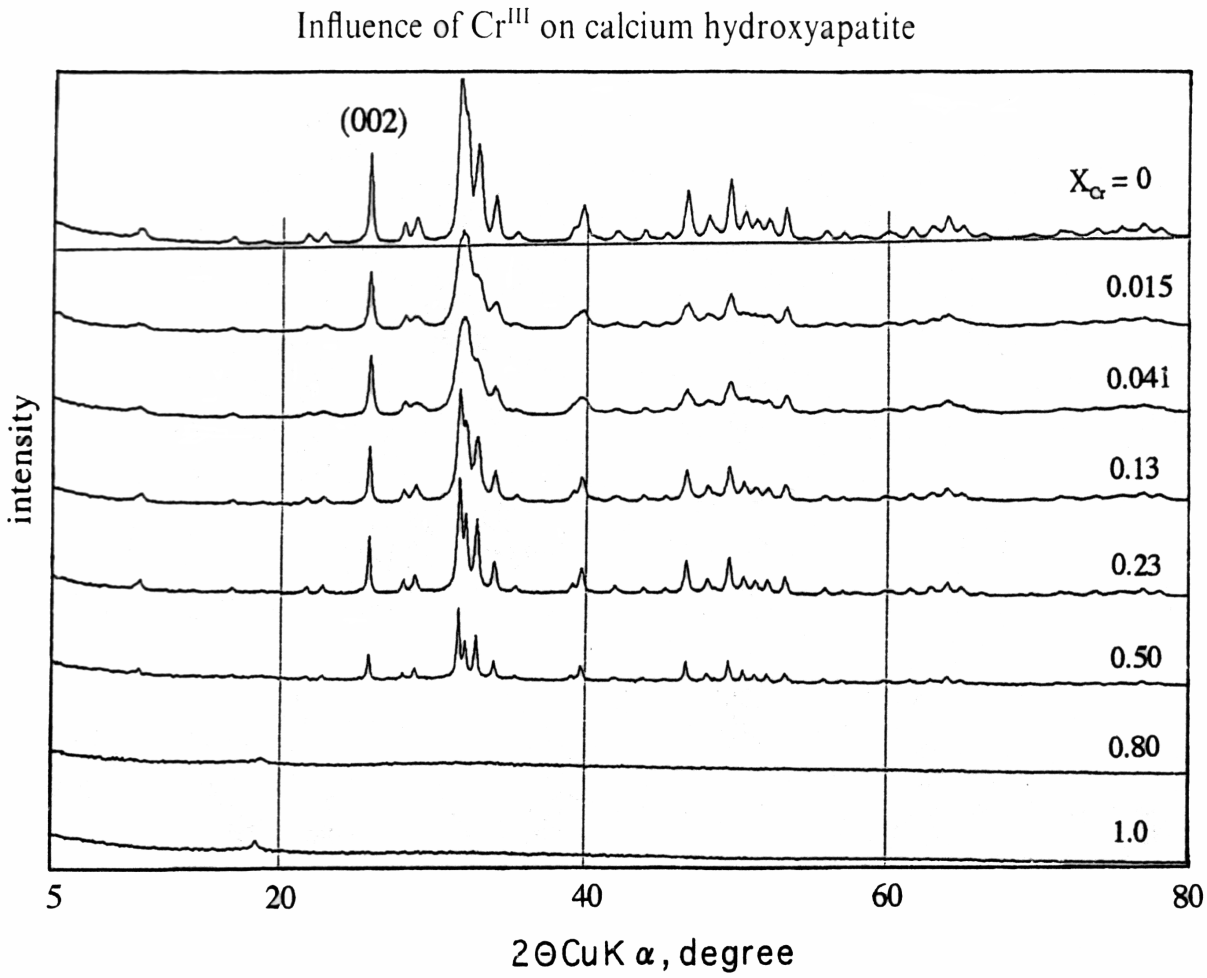

Figure 23 XRD patterns of the materials with different X_{Cr}.

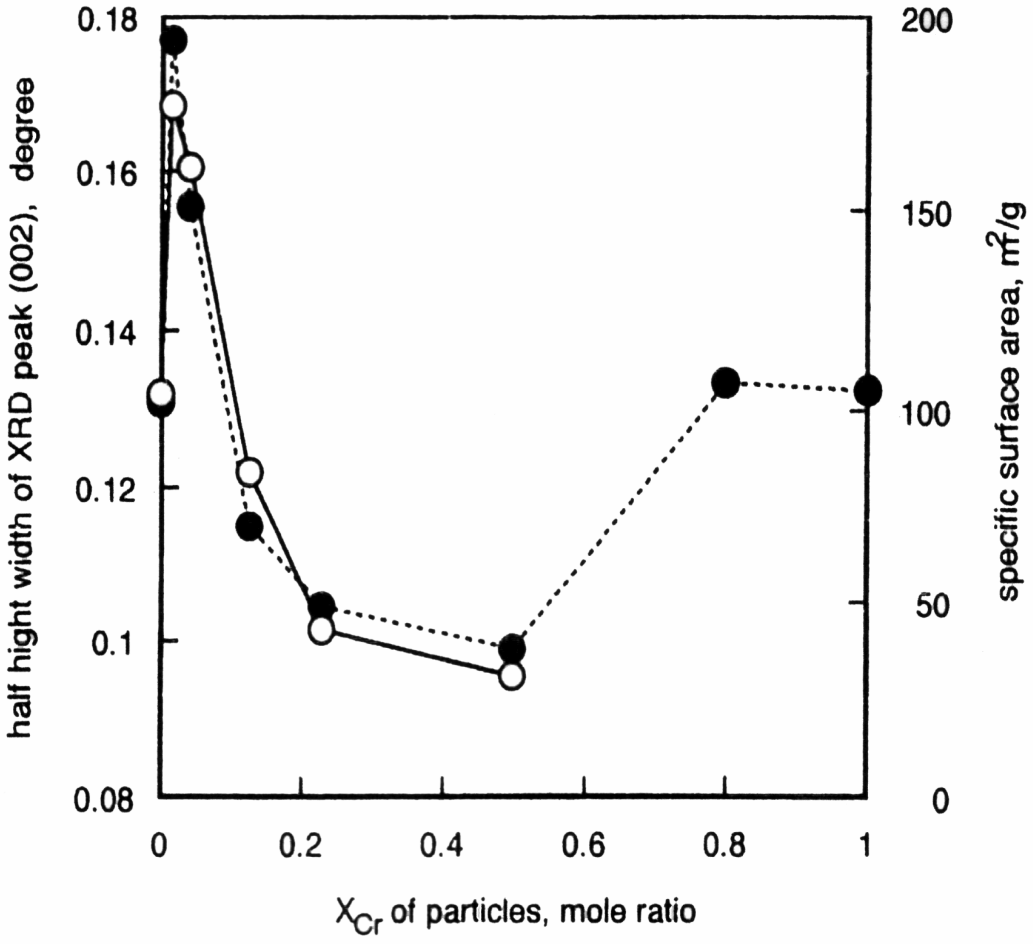

Figure 24 Half height width (HHW) of XRD peak due to (002) plane (open symbols) and specific surface area (full symbols) of the materials with varied X_{Cr}.

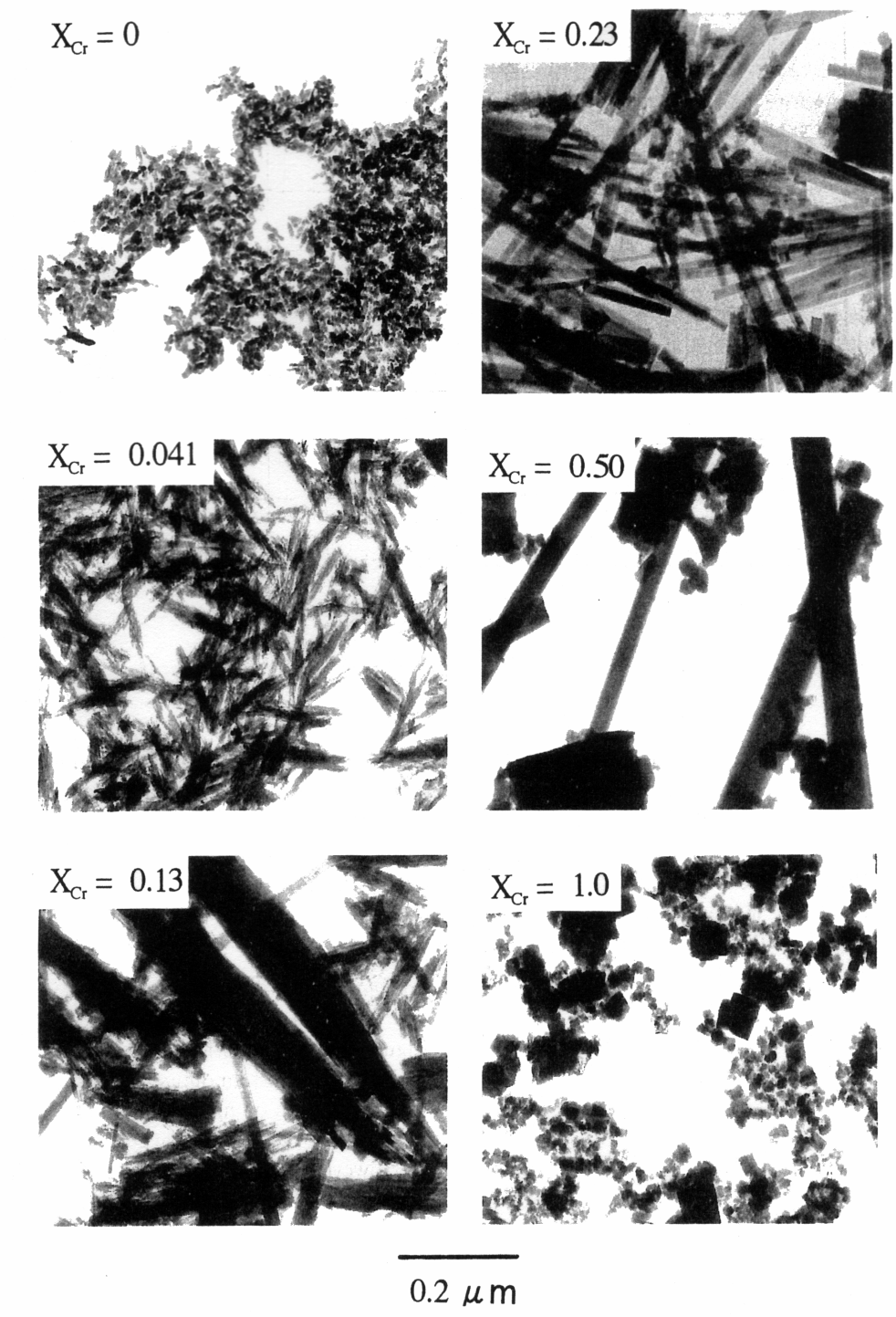

Figure 25 TEM pictures of the materials with different X_{Cr}.

Table 1 X_{Cr} and (Ca+Cr)/P of the materials with X_{Cr} = 0.041 and 0.13 determined by ICP and EPMA

X_{Cr}		(Ca + Cr)/P	
ICP	EPMA	ICP	EPMA
0.041	0.046 ± 0.021	1.71	1.56 ± 0.31
	0.026 ± 0.008[a]		1.50 ± 0.30[a]
0.13		1.87	
	0.71 ± 0.08[b]		3.2 ± 0.1[b]

Symbols [a] and [b] represent long rectangular particles and irregular ones, respectively.

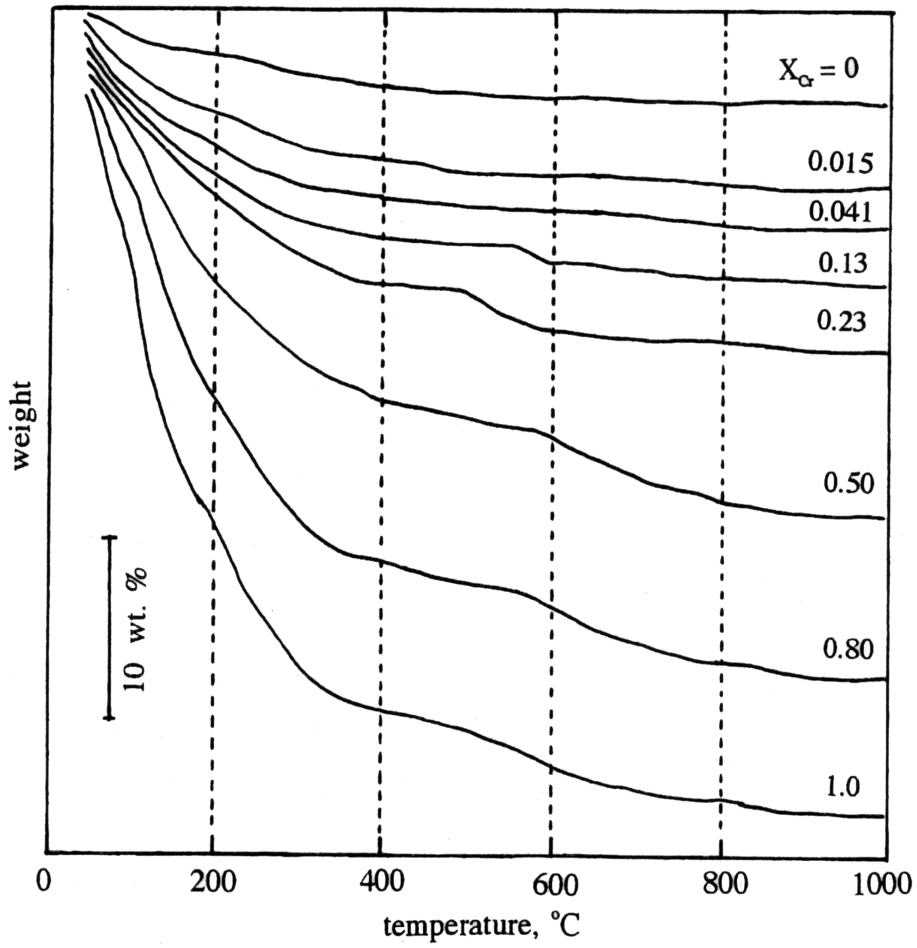

Figure 26 TG curves of the materials with different X_{Cr}.

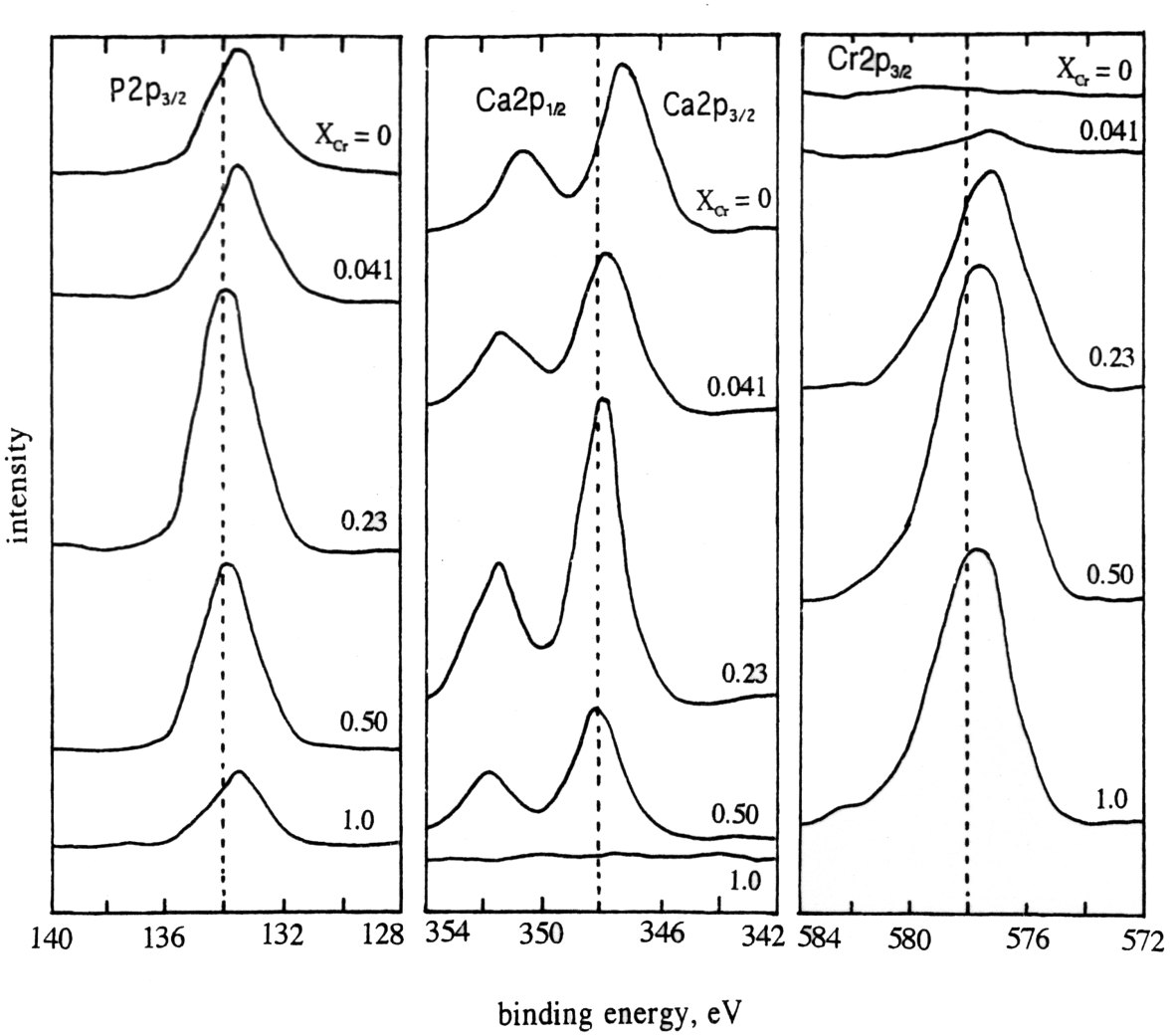

Figure 27 XPS spectra of the materials with different X_{Cr}.

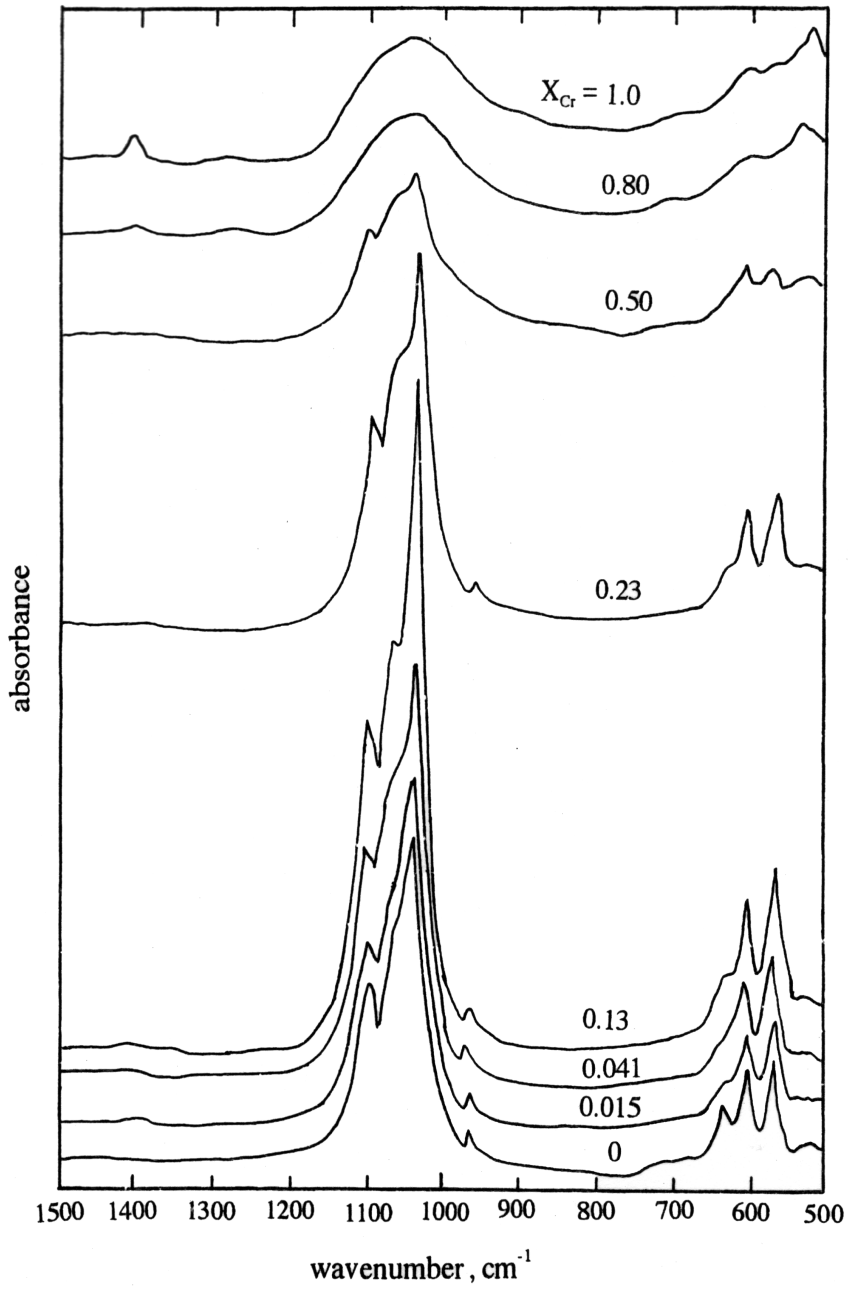

Figure 28 IR spectra of the materials with different X_{Cr}.

CHAPTER 3

Processing and photocatalytic activity of Ti-doped hydroxyapatite powders

3.1 Introduction

Recently, titanium dioxide TiO_2 has received much attention as a photocatalyst which photooxidizes organic substances in both water and air [(1), (2)]. Synthetic calcium hydroxyapatite $Ca_{10}(PO_4)_6(OH)_2$, denoted as CaHAp, is biologically important and is used in bioceramics and adsorbents for biomaterials, because it was established that CaHAp shows an excellent affinity to biomaterials such as proteins. Hence, it is of interest to prepare composite materials of TiO_2 and CaHAp for photocatalytic decomposition of biomaterials, such as proteins and lipids. Nonami et al. proposed a new structure for TiO_2-CaHAp composite films in which porous CaHAp layer forms on TiO_2 layer on a substrate in a pseudo body solution [(3)]. However, this composite structure is inefficient for photocatalysis which requires UV light irradiation on the TiO_2 layer. We attempted to develop a novel photocatalyst with a high affinity to biomaterials by an atomic level composite of photocatalytic material and CaHAp, which could be realized by modifying CaHAp particles with Ti(IV). The modification of CaHAp particles was performed by coprecipitation and ion exchange methods. Suzuki et al. have found that Ca(II) of CaHAp can be exchanged with various metal ions in aqueous media [(4)-(12)]. However, the surface structure and property of the metal substituted CaHAp have not been clarified. Ribeiro et al. have studied the surface of

CaHAp modified with Ti(IV) ions by immersion methods [13] and indicated the formation of a titanium phosphate, $Ti(HPO_4)_2,nH_2O$ (n=1-3), which probably has a double layered structure [14]. Weiser et al. have coated metal Ti with CaHAp by doping and diffusing of Ca and P elements into the metal before the coating to obtain a high quality CaHAp film on the metal Ti surface [15]. On the other hand, Zeng et al. have studied the adsorption of albumin on calcium phosphate (CaP) and Ti films deposited on a germanium ATR crystal by ion beam sputter deposition from CaHAp and metal Ti targets and found that the CaP film adsorbs a greater amount of albumin than the surface of metal Ti; CaP shows a higher affinity to protein than metal Ti [16]. Since CaHAp surface is known to show a high affinity to albumin [21), (22)], CaHAp is used as an adsorbent of column chromatography for separating proteins. The bactericidal effects of Ag-CaHAp thin films on alumina have been reported by Feng et al [23]. Although Ti(IV)-modified CaHAp is anticipated to show a bactericidal effect, there has been no study on the bactericidal character of this material. Wakamura et al. previously investigated the surface structure and composition of the CaHAp particles modified with various metal ions by coprecipitation and ion exchange methods [17)-(19)]. In the present study, CaHAp particles modified with Ti(IV) by a coprecipitation method were characterized by various techniques. Photocatalytic activities of the well characterized, modified CaHAp particles were examined by decomposition reactions of acetaldehyde and albumin. On the basis of the obtained results, we discussed the surface structure and photocatalysis of the modified CaHAp particles. Further, the bactericidal function of the materials was examined using a colon bacillus [24] and a noble photocatalyst was able to be developed.

3.2 Experimental Section

3.2.1 Materials

Colloidal CaHAp particles doped with Ti(IV) were prepared by coprecipitation. $Ca(NO_3)_2$ and $Ti(SO_4)_2$ were dissolved in 1 dm^3 deionized distilled water free from CO_2 at different atomic ratios Ti/(Ca + Ti) =X_{Ti} from 0 to 0.8. The total amount of Ca and Ti in the solutions was held at 0.1 mol; 0.060 mol of H_3PO_4 was added to the solutions and the solution pH was adjusted to 9 by adding a 15 mol dm^{-3} NH_4OH solution. The resulting suspension was aged in a capped Teflon vessel at 100 °C for 6 h. The resulted precipitates were filtered off, washed with 5 dm^3 deionized distilled water, and finally dried in an air oven at 70 °C. Ninhydrin and albumin supplied by Wako Pure Chemicals were used as received.

3.2.2 Characterization

The CaHAp particles thus modified with Ti(IV) were examined by various conventional methods as follows. The morphology of the particles was observed using a JEOL transmission electron microscope (TEM) at an accelerating voltage of 200 kV. The samples for TEM were prepared by a dispersing method. X-ray diffraction (XRD) patterns were taken by a powder method using a Shimadzu high intensity diffractometer with a rotating cathode using Cu Kα radiation (50 kV and 200 mA). Transmission IR spectra were recorded in vacuo using a Perkin-Elmer Fourier transform infrared (FTIR) spectrophotometer by a self-supporting disk method in a vacuum cell. The sample powders (30 mg) were pressed into disks of 1 cm diameter under 572 kg cm^{-2}. Before the spectra were taken, the sample disks were outgassed at 300 °C for 2 h. Reflection UV-VIS spectra were taken using a UV spectrometer (JASCO V-560) at 200-400 nm.

The specific surface area was calculated by applying the BET equation to the N_2 adsorption isotherm measured at -196 °C using an automatic volumetric apparatus.

3.2.3 Chemical Analysis

Ti and P contents were determined by a Perkin-Elmer induced coupled plasma spectrometer (ICP-AES) employing wavelengths of 317.933 (Ca), 334.941 (Ti) and 213.618 nm (P). The samples for ICP-AES were dissolved in a dilute HNO_3 solution. X-ray photoelectron spectroscopy (XPS) was done using a Perkin-Elmer spectrophotometer with Mg K α radiation (20 kV and 30 mA), where the samples were mounted on the sample holder by a carbon tape.

3.2.4 Acetaldehyde Decomposition Test

The photocatalytic activities were estimated from the decomposition of acetaldehyde vapor under 1 mW cm^{-2} UV irradiation. The samples used for photocatalysis were CaHAp modified at X_{Ti} = 0 and 0.1. The sample weight was decided by adjusting the surface area of the samples as a constant value of 85 m^2 using the BET specific surface area. The samples were settled in the bottom of a 500 cm^3 cylindrical glass vessel sealed with a quartz plate with 5 mm thickness using an O-ring. A mixed gas (N_2, 80%; O_2, 20%) was introduced into the vessel through the gas inlet to replace air by the mixed gas, and then acetaldehyde vapor was injected into the vessel, followed by keeping it in the dark to achieve equilibrium. Then ultraviolet irradiation (1 mW cm^{-2}) and holding in the dark were repeated at 24 h intervals. After the reaction, the concentrations of acetaldehyde and CO_2 in the reaction vessel were determined by a gas chromatograph (FID).

3.2.5 Ninhydrin Test of Albumin Decomposition

The affinity to biomaterials and photocatalytic activities were estimated from adsorption and decomposition of albumin. The ninhydrin test was employed to identify albumin before and after the decomposition reaction. Samples of 1 g of CaHAp modified at X_{Ti} = 0 and 0.1 and 1 g of TiO_2 were immersed in 1 g dm^{-3} albumin solutions at 30 °C for 12 h. The particles were filtered, washed with 10 dm^3 deionized distilled water, and dried in an air oven at 50 °C. Each sample was divided into two parts (each 0.5 g); one was kept in a dark box and the other was irradiated by 1 mW cm^{-2} UV light for 24 h at room temperature. Finally, the samples were sprayed with a ninhydrin indicator and dried in an air oven at 150 °C.

3.2.6 Bactericidal Test by *Escherichia coli (E. coli)*

The suspensions of CaHAp modified at X_{Ti} = 0 and 0.1 and TiO_2 homogeneously dispersed in silica sols were deposited on a glass plate (5 × 5 cm) by a spin coating method. The films on glass were sterilized by drying at 180 °C for 30 min. *E. coli* cells (IFO 3310 strain) were grown aerobically in 2.5 cm^3 of nutrient broth (“Daigo”, Nippon Seiyaku) at 30 °C for 16-18 h. The cells were centrifuged at 4000 rpm and suspended in sterilized water with appropriate dilution. An *E. coli* cell suspension (150×10^{-6} dm^3, 2×10^5 cells cm^{-3}, total 3×10^4 cells) was pipetted onto glass plates coated with CaHAps (modified at X_{Ti} = 0 and 0.1) and TiO_2, spread out to give a liquid film of approximately 1 cm in diameter and placed in an airtight illumination chamber to prevent drying. This chamber was illuminated with a 15 W black light, and the light intensity with peaks around 360 nm was 1.0 mW cm^{-2}, which was measured using a UV radiometer

(UVR-36, Tepcon) at the sample position. After the illumination, the cells were removed using a gauze patch and collected in a 0.15 mol dm^{-3} NaCl solution. This solution was spread onto nutrient agar medium (Standard Method Agar "Nissui", Nissui Seiyaku) and incubated for 24 h in order to determine the number of viable cells in terms of colony forming units.

3.3 Results and Discussion

Figure 1 displays TEM micrographs of Ti(IV) doped CaHAp particles. The CaHAp particles formed at $X_{Ti} \leqq 0.1$ are short rods. The particles formed at $X_{Ti} \geqq 0.5$ are a mixture of long rectangular and irregular particles, although (d) and (e) show only long rectangular and irregular particles, respectively. The irregular particles increased with increase of X_{Ti}. Although the detailed reason for the formation of the long particles remains unclear, the charge difference between Ca(II) and Ti(IV) seems to influence the particle formation of CaHAp as found in the previous study on the modification with Cr(III) [19].

Figure 2 displays XRD patterns of the products at different X_{Ti} values. Their peak intensity is lowered by increasing X_{Ti} at $X_{Ti} \leqq 0.5$, and the product at $X_{Ti} = 0.8$ is poorly crystallized. Except for the product at $X_{Ti} = 0.8$, the patterns are characteristic of CaHAp (JPCDS 9-432), verifying that the long rectangular particles formed at $X_{Ti} \geqq 0.5$ are well crystallized CaHAp. This finding suggests that CaHAp crystals can be doped with Ti(IV) up to $X_{Ti} = 0.1$.

To determine the composition of the products, Ca, Ti, and P in the formed particles were assayed by ICP-AES. Figure 3 plots the contents of Ca(II) and Ti(IV) ions against X_{Ti} by open circles and triangles, respectively. The increase of Ti(IV) in the formed

particles accompanies an equivalent decrease of Ca(II), which means that Ti(IV) in the crystal of CaHAp is present as a divalent ion, such as $[Ti(OH)_2]^{2+}$ and $[Ti(HPO_4)]^{2+}$. Figure 4 plots X_{Ti} of the whole particle and the surface phase of particles determined by ICP- AES and XPS, respectively. For all the materials X_{Ti} of the surface phase (noted as *Xs)* was less than that of the whole particle (noted as *Xw),* which can be interpreted by considering that Ti(IV) is more easily precipitated than Ca(II) to be more contained in the inner part of particle. *Xw* is larger than X_{Ti} in the starting solutions, implying that Ti(IV) is incorporated into the particles more than Ca(II). These results are ascribed to the higher hydrolysis constant of Ti(IV) than Ca(II).

Figure 5 shows FTIR spectra of the CaHAp particles modified with Ti(IV). The spectrum of the sample formed at $X_{Ti} = 0$ gives rise to three bands at 3680, 3673, and 3657 cm^{-1}. We previously assigned these three bands to the O-H stretching vibration modes of surface P-OH groups which are considered to form due to protonation of surface PO_4^{3-} ions to balance the surface charge [20]. The spectrum of the samples formed at $X_{Ti} = 0.1$ shows three additional IR bands at 3738, 3729, and 3717 cm^{-1} that would be ascribed to surface Ti-OH groups.

Figure 6a-c illustrates the reflection UV-vis spectra of the products at varied X_{Ti} along with that of TiO_2 (Figure 6d). The UV absorption above ca. 370 nm is observed in spectra b and c of the samples modified at $X_{Ti} = 0.01$ and 0.1 but not in spectrum a of the unmodified CaHAp. With increasing X_{Ti} the absorbance rises to that of TiO_2. These results clearly imply that the surface of CaHAp particles is modified by substituting with Ti(IV).

Figure 7 plots the concentrations of acetaldehyde and CO_2 against the UV irradiation time. It is clearly seen in Figure 7b that CO_2 is increased (open circles) and

acetaldehyde is decreased (closed circles) on irradiating the UV beam to the material modified at X_{Ti} = 0.1 and on stopping the irradiation the concentrations of acetaldehyde and CO_2 are essentially not changed. However, as shown in Figure 7a, the unmodified sample shows less concentration change of CO_2 and acetaldehyde than the modified sample. Therefore, it can be confirmed that Ti(IV) modified CaHAp exhibits higher activity in photocatalysis than the unmodified CaHAp.

Figure 8 shows the results of the ninhydrin colored test: the photographs of TiO_2 (a), the unmodified CaHAp (b), and Ti(IV) modified CaHAp (c) unirradiated and irradiated by UV after albumin adsorption. TiO_2 (a) shows no ninhydrin color under UV irradiation and unirradiation, although a slight blue color is detected due to albumin weakly adsorbed. The unmodified CaHAp (b) is colored by ninhydrin under UV irradiation and unirradiation. Ti(IV) modified CaHAp (c) is colored only under UV unirradiation. These results indicate that TiO_2 does not strongly adsorb albumin, whereas the unmodified CaHAp adsorbs albumin but shows no activity of photocatalytic decomposition and Ti(IV) modified CaHAp adsorbs albumin and decomposes it by photocatalysis.

Figure 9 compares the results of the bactericidal test by colon bacilli. TiO_2 gives rise to essentially no photo catalysis in the dark and kills less than 10% of the colon bacilli, while TiO_2 kills 80% of the bacilli under UV irradiation. On the other hand, Ti(IV) modified and unmodified CaHAps show bactericidal effects even in the dark, killing ca. 50% of the bacilli. It should be noted that the bactericidal effect of Ti(IV) modified CaHAp was enhanced by UV irradiation and only ca. 30% of the bacilli survive after UV irradiation. These findings indicate that Ti(IV) modified CaHAp exhibits a higher bactericidal effect than TiO_2 both in the dark and under UV irradiation. The Ti(IV)

modified CaHAp generate positive holes (h^+) as well as TiO_2 catalysts. The formed positive holes interact with adsorbed H_2O to yield hydroxyl radicals (OH^+) with a strong oxidation ability which would decompose various organic materials to show the bactericidal effect. To verify the details of this mechanism, further analysis of the band structure of Ti(IV)-modified CaHAp is required.

3.4 Conclusion

From the obtained results, we can draw the following conclusions. CaHAp has a feature that Ca(II) ions in the crystal are exchanged with Ti(IV) up to X_{Ti} = 0.1 in atomic ratio. The added Ti(IV) exists in the CaHAp crystals as divalent cations such as $[Ti(OH)_2]^{2+}$ and $[TiHPO_4]^{2+}$. Ti(IV) substituted CaHAp has surface OH groups originating from HPO_4^{2-} and OH^- coordinating to Ti(IV). The CaHAp particles penetrated by Ti(IV) into the crystals absorb UV beam at a wavelength less than 380 nm, so that it exhibits a photocatalytic activity in oxidation and decomposition of acetaldehyde. This character of Ti(IV) modified CaHAp resembles the case of oxidative decomposition of organisms by TiO_2. However, CaHAp has a high affinity to organisms such as proteins although TiO_2 shows no affinity to organisms. Therefore, distinct from TiO_2 photocatalyts, Ti(IV) modified CaHAp has both adsorption affinity and photocatalytic activity for organisms. To make matters better, Ti(IV) modified CaHAp shows the bactericidal effect even in the dark although TiO_2 shows it only under UV irradiation.

References

(1) Fujishima, A.; Honda, K. *Bull. Chem. Soc. Jpn.* **1971,** *44,* 1148.

(2) Fujishima, A.; Honda, K. *Nature* **1972,** *238,* 5358.

(3) Nonami, T.; Taoda, H. *Mater. Res. Bull.* **1998,** *33,* 1, 125.

(4) Suzuki, T.; Hayakawa, Y. *Proceedings of the First International Congress on Phosphorus Compounds IMPHOS, Paris;* 1977; p 381.

(5) Suzuki, T.; Hatsushika, T.; Hayakawa, Y. *J. Chem. Soc., Faraday Trans. 1* **1981,** *77,* 1059.

(6) Suzuki, T.; Hatsushika, T.; Miyake, M. *J. Chem. Soc., Faraday Trans. 1* **1982,** *78,* 3605.

(7) Miyake, M.; Kobayashi, T.; Suzuki, T. *Yogyo-Kyokai-Shi* **1986,** *94,* 136.

(8) Miyake, M.; Ishigaki, K.; Suzuki, T. *J. Solid State Chem.* **1986,** *61,* 230.

(9) Tanizawa, Y.; Ujiie, T.; Sawamura, K.; Suzuki, T. *Denki Kagaku* **1987,** *55,* 903.

(10) Tanizawa, Y.; Sawamura, K.; Suzuki, T. *J. Chem. Soc., Faraday Trans.* **1990,** *86,* 1071.

(11) Tanizawa, Y.; Sawamura, K.; Suzuki, T. *J. Chem. Soc., Faraday Trans.* **1990,** *86,* 4025.

(12) Suzuki, T.; Hatsushika, T. *Gypsum Lime* **1990,** *224,* 15.

(13) Ribeiro, C. C.; Barbosa, M. A.; Machado, A. A. S. C. *J. Mater. Sci. Mater. Med.* **1995,** *6,* 829.

(14) Leadley, S. R.; Davies, M. C.; Ribeiro, C. C.; Barbosa, M. A.; Paul, A. J.; Watts, J. F. *Biomaterials* **1997,** *18,* 311.

(15) Wieser, E.; Tsyganov, I.; Matz, W.; Reuther, H.; Oswald, S.; Pham, T.; Richter, E. *Surf. Coat. Technol.* **1999,** *111,* 103.

(16) Zeng, H.; Chittur, K. K.; Lacefield, W. R. *Biomaterials* **1999,** *20,* 377.

(17) Wakamura, M.; Kandori, K.; Ishikawa, T. *Colloids Surf., A* **1998,** *142,* 107.

(18) Wakamura, M.; Kandori, K.; Ishikawa, T. *Colloids Surf., A* **2000,** *164,* 297.

(19) Wakamura, M.; Kandori, K.; Ishikawa, T. *Polyhedron* **1997,** *16,* 12, 2047.

(20) Ishikawa, T.; Wakamura, M.; Kondo, S. *Langmuir* **1989,** *5,* 140.

(21) Kandori, K.; Shimidu, T.; Yasukawa, A.; Ishikawa, T. *Colloids Surf., B* **1995,** *5,* 81.

(22) Kandori, K.; Horigami, N.; Kobayashi, H.; Yasukawa, A.; Ishikawa, T. *J. Colloid Interface Sci.* **1997,** *191,* 498.

(23) Feng, Q. L.; Kim, T. N.; Wu, J.; Park, E. S.; Kim, J. O.; Lim, D. Y.; Cui, F. Z. *Thin Solid Films* **1998,** *335,* 214.

(24) Kikuchi, Y.; Sunada, K.; Iyoda, T.; Hashimoto, K.; Fujishima, A. *J. Photochem. Photobiol., A* **1997,** *106,* 51.

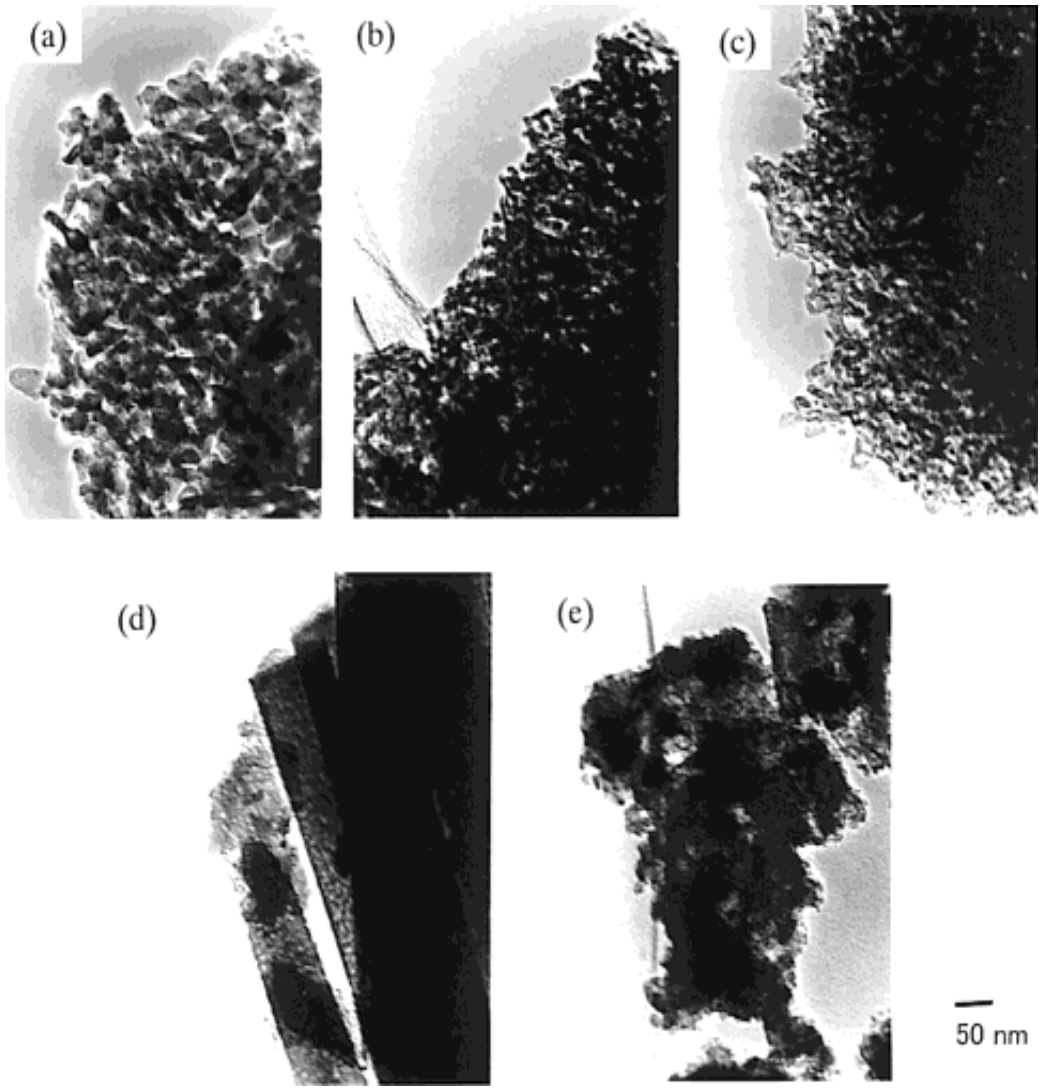

Figure 1 TEM picture of the particles formed at varied X_{Ti} values by coprecipitation method: X_{Ti} = (a) 0, (b) 0.03, (c) 0.1, (d) 0.5, and (e) 0.8.

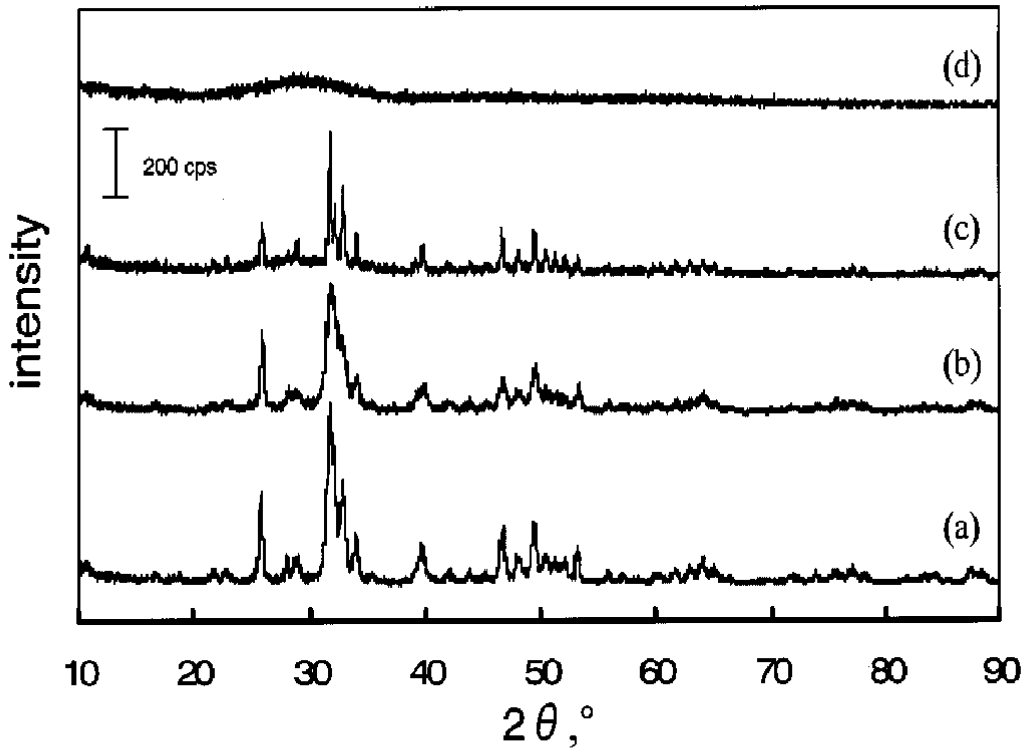

Figure 2 XRD patterns of the products at varied X_{Ti} values by coprecipitation method: X_{Ti} = (a) 0, (b) 0.1, (c) 0.5, (d) 0.8.

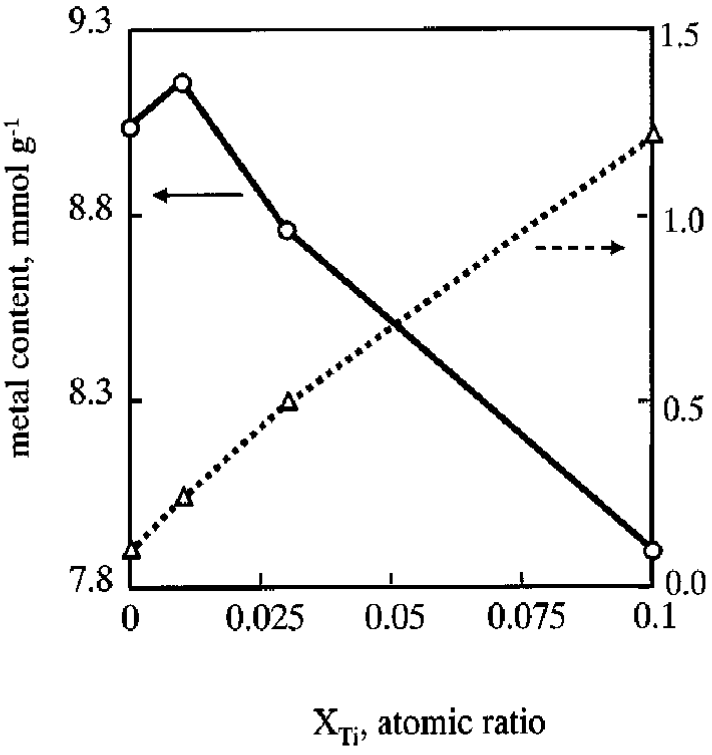

Figure 3 Plots of Ca and Ti contents against X_{Ti} : ○, Ca content; △, Ti content.

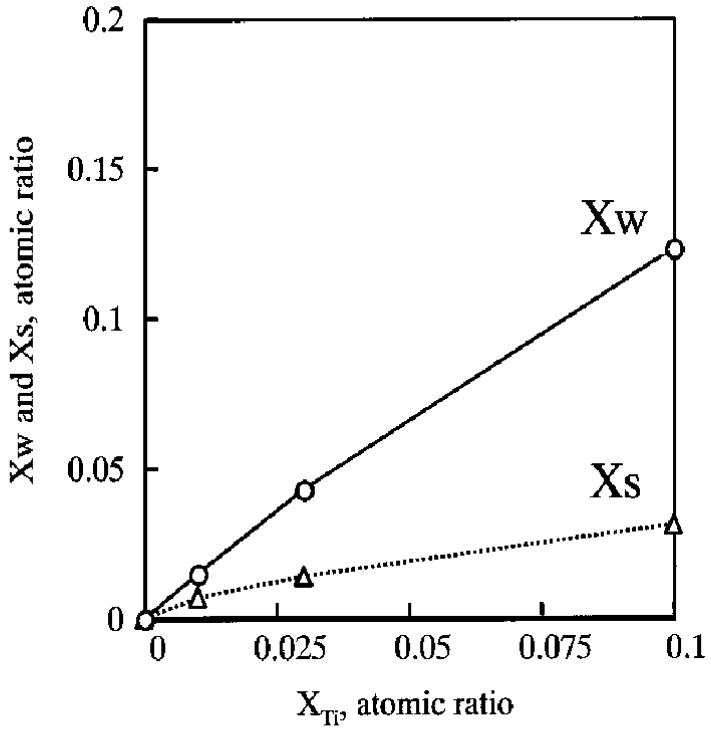

Figure 4 Atomic ratio in the whole particle (Xw; ○) and in the surface phase (Xs; △) of Ti(IV)-modified CaHAp particles.

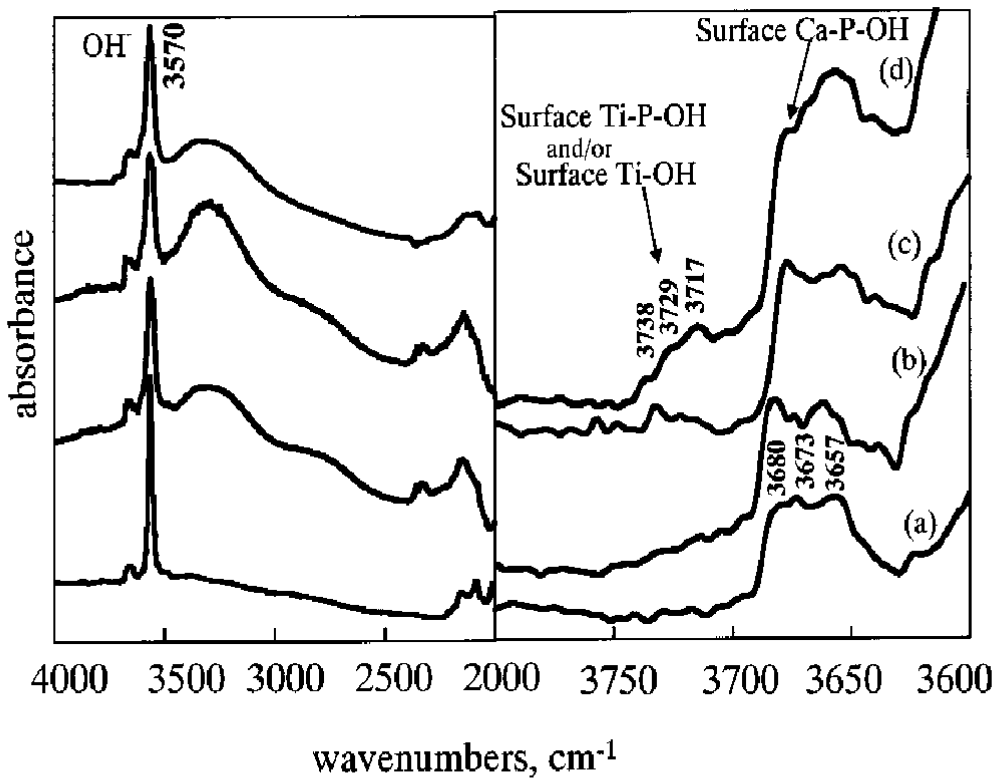

Figure 5 IR spectra of CaHAp particles modified with Ti(IV) by coprecipitation at various X_{Ti} = (a) 0, (b) 0.01, (c) 0.03, (d) 0.1.

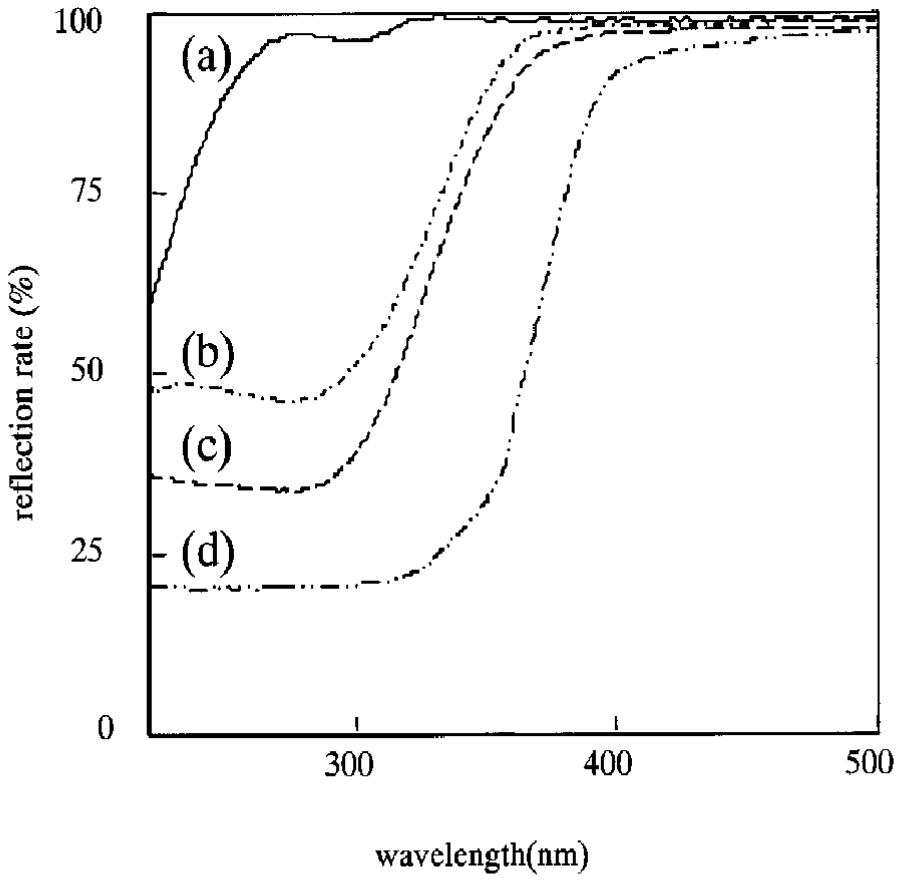

Figure 6 Reflection UV-VIS spectra of CaHAp particles modified with Ti(IV) by coprecipitation at various X_{Ti} values and TiO_2: X_{Ti} = (a) 0, (b) 0.01, and (c) 0.1, (d) TiO_2.

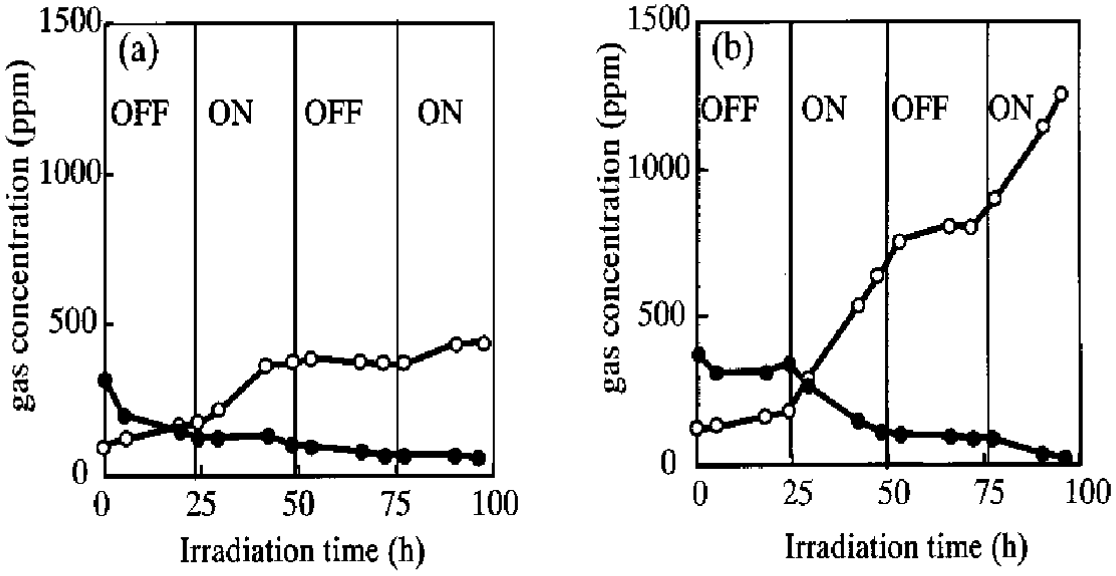

Figure 7 Concentration of acetaldehyde (closed symbols) and CO_2 (open symbols) vs UV irradiation time: (a) unmodified CaHAp; (b) Ti(IV)-modified CaHAp at $X_{Ti} = 0.1$.

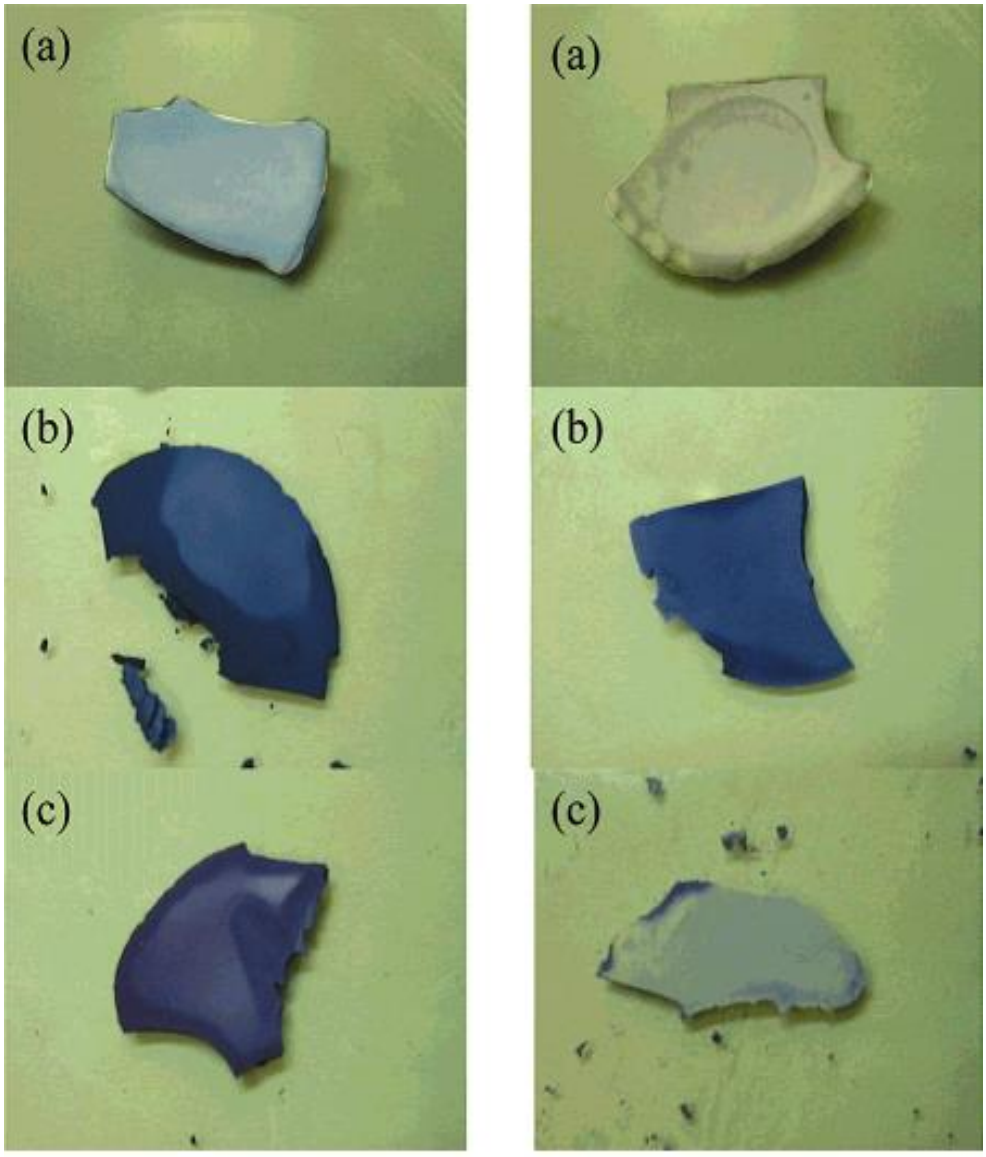

Figure 8 Results of adsorption and photocatalysis decomposition of albumin obtained by ninhydrin colored tests: (a) TiO_2; (b) CaHAp; (c) Ti(IV)-modified CaHAp.

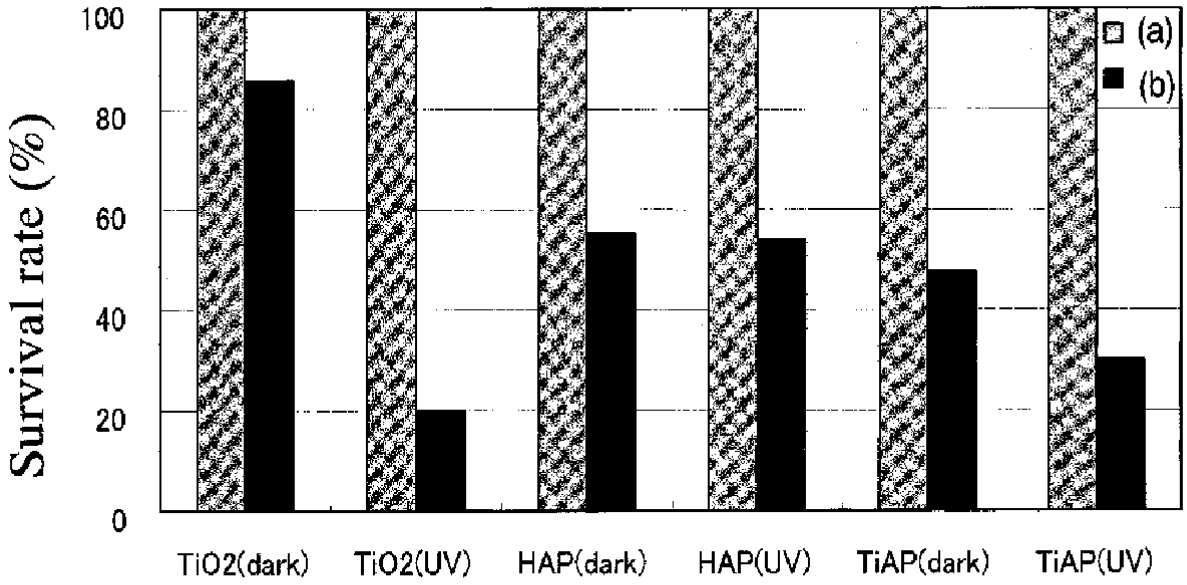

Figure 9 Results of bactericidal test using colon bacillus: (a) 0 h; (b) after 4 h.

CHAPTER 4

Preparation of transparent thin film of Ti-doped hydroxyapatite by so-gel method

4.1 Introduction

Previously, we have reported a novel apatite-based photocatalyst (Ti-CaHAp) [(1)], which has calcium hydroxyapatite structure partially substituted with Ti ions at calcium sites. This photocatalyst is different from composite systems of TiO_2 and an adsorbent (activated carbon, zeolite, apatite, and so on) [(2), (3)], which are widely studied in terms of an application to water or air purification. Yoneyama et al. have revealed that the stronger adsorbent lowers the photocatalytic activity of TiO_2 composite because it prevents diffusion of adsorbed pollutions on the composite surface [(2)]. Therefore, it is essential for fabricating a photocatalyst adsorbent composite system for practical use to choose an adsorbent of appropriate adsorptive ability. The problem of these systems is attributable to a distance between a photocatalytic site and an adsorptive site. However, it seems that our apatite based photocatalyst does not have such problem, and the strong adsorptive ability of apatite may be effectively available for photocatalytic decomposition.

For a wide application of a photocatalyst, it is essential to develop a coating method. Especially, transparency is often required, e.g., in order to apply to the photocatalytic coating on glass. However, to the best of our knowledge, there have been few reports on transparent thin film coating of apatite, although the preparation of hydroxyl- and

fluoroapatite film [4]-[6] has been reported. In this paper, we report the preparation of transparent thin films of Ti-doped calcium hydroxyapatite (Ti-CaHAp) for a photocatalytic coating.

4.2 Experiment

A cleaned glass (Corning 1737 glass 5 × 7 cm, or quartz cover glass 2 × 2cm) was used as a substrate. To a solution of $Ca(NO_3)_2 \cdot 4H_2O$ (4.246 g, 18.0 mmo1) in mixed solvent of ethanol (50 mL) and 2-ethoxyethanol (50 mL), P_2O_5 (0.906 g, 6.0 mmol) was added, and the solution was stirred at room temperature for 2h. $Ti(OiPr)_4$ (0.568 g, 2.0 mmo1) was gradually added to the solution, and the solution was stirred for 1 d. After removing small amount of precipitate by filtration, the clear filtrate (pH $\leqq$ 3) was used for coating. When phosphoric acid or its ammonium salt was used instead of P_2O_5, calcium ion was quickly precipitated and coating with its filtrate was failed. It is also noteworthy that phase separation was observed at higher concentration of $Ti(OiPr)_4$ (4 mmol against l6 mmol of $Ca(NO_3)_2 \cdot 4H_2O$) and transparent film was not obtained. The solution was coated on a glass substrate by dipping (withdrawing rate 24 cm/min), and it was quickly dried by a heat gun for approximately 10 s. The whole was calcined at 500 °C for 15 min. This process was repeated several times. Additionally, calcium hydroxyapatite (CaHAp) thin film without Ti was also prepared in the same way without $Ti(OiPr)_4$. Highly homogeneous, transparent, and colorless Ti-CaHAp and CaHAp films were obtained. TiO_2 film was prepared from NDH 510C coating solution (Nippon Soda Co., Ltd.).

It was revealed that the Ti-CaHAp film obtained by repeating 10 coating cycles was dense and that its thickness was approximately 700 nm by scanning electron

microscopy (SEM, 5-5200; Hitachi Co., Tokyo, Japan). Film thickness was also measured by ellipsometric method [7] against films coated on Si wafer in the same way (1 and 3 coating cycles), and it was confirmed that the film thickness per cycle was approximately 70 nm.

4.3 Results and discussion

Elemental analysis by X-ray photoelectron spectroscopy (XPS; Physical Electronics (PHI) Model 5600 spectrometer equipped with a hemispherical capacitor analyzer) was carried out. XPS spectrum of the obtained film was similar to that of Ti-CaHAp powder, [l] as shown in Figure 1. The ratio of Ti against Ca was estimated approximately 10 %. Si signals derived from substrate or any other signals from impurities except carbon from surface pollutants were not observed. XRD diffraction was also similar to that of the powder, although it was weak because of thin film. TiO_2 (anatase or rutile) was not detected. Therefore, the obtained films are chemically similar to Ti-CaHAp powder.

The obtained fllms were highly transparent and colorless (Figure 2), owing to low refractive index of hydroxy apatite (refractive index =1.5 at 590 nm, calculated from ellipsometric data). Interference color, which depends on refractive index and thickness, was slightly observed with increasing of film thickness; however, Ti-CaHAp thin film shows much weaker interference color than TiO_2 of higher refractive index. Absorption of HAp was mainly below ca. 240 nm, and that of Ti-CaHAp was below ca. 360 nm (absorption over 300 nm is very weak because of thin film and is partially hidden in light scattering). It is obvious that the absorption of Ti-CaHAp is changed from that of HAp by introducing Ti (IV) ion and is restricted to shorter wavelength region than TiO_2. Photocatalytic activity was evaluated by the decomposition of adsorbed Methylene Blue

(MB) decomposition under irradiation of UV light (Hg-Xe lamp, HOYA-SCHOTT UV light source EX250-W without any cut-off filter, 10 mW/cm^2) [8]. Ti-CaHAp coated glass (Ti-CaHAp thickness 2l0 nm) was immersed in MB aqueous solution (l mM) for 2 h and then dried. After UV irradiation, the film was kept under dark for 1 h and then the absorption spectrum was measured by UV-VIS spectrometer (Perkin-Elmer Lambda900). Figure 3a shows absorption spectra of MB adsorbed on Ti-CaHAp film under UV irradiation. MB was gradually decomposed, while MB adsorbed on a bare glass substrate was not decomposed under these conditions.

Photocatalytic activity was also evaluated by the decomposition of gaseous isopropyl alcohol (IPA) decomposition under irradiation of UV light (black fluorescent light bulb, l.7 mW/cm^2) [8]. The film on a glass substrate was set in a quartz made vessel, which had a volume of l000 ml, and then about 500 ppm of the reactant gas was injected. The sample was kept in the dark once the gas concentration remained constant, which implied that the IPA gas finished adsorbing onto the film surface. The component gas concentrations were measured by a gas chromatograph (Shimadzu GC-SA). Figure 3b clearly shows the decrease of IPA and increase of CO_2 by UV irradiation. IPA was decomposed under these conditions, although the observed efficiency was relatively low because of small coated surface area (5 × 5 cm^2) and small surface roughness. It is note worthy that acetone, an intermediate of decomposition of IPA, was clearly detected under UV irradiation. This fact is also an evidence of photooxidative ability of Ti-CaHAp.

Water contact angle (WCA) change under UV irradiation was also evaluated. WCA on a Ti-CaHAp film was =45° and not changed even after UV inadiation for 600 h.

In summary, transparent and colorless Ti-CaHAp film was prepared, and its

photocatalytic activity was evaluated. Both ofthe adsorbed MB and gaseous IPA decompositions were observed, although UV light absorption of Ti-CaHAp is very weak. These oxidative decompositions were not observed under dark; therefore, UV light inadiation was obviously required. This apparent effective photocatalytic decomposition may be derived from the chemical structure of Ti-CaHAp, which probably has an adsorptive site as a reaction site, and it was suggested that the reaction mechanism of Ti-CaHAp is different from that of TiO_2. Further investigation is now in progress.

References and Notes

(1) M. Wakamura, K. Hashimoto, and T. Watanabe, *langmuir*, **19**, 3428 (2003).

(2) N. Takeda, T. Torimoto, S. Sampath, S. Kuwabata, and H. Yoneyama, *J. Phys. Chem.*, **99**, 9986 (1995).

(3) T. Nonami, H. Taoda, N. T. Hue, E. Watanabe, K. Iseda, M. Tazawa, and M. Fukaya, *Mater. Res. Bull.*, **33**, 125 (1998).

(4) M. Cavalli, G. Gnappi, A. Montenero, D. Bersani, P. P. Lottici, S. Kaciulis, G. Mattogno, and M. Fini, *J. Mater. Sci.*, **36**, 3253 (200l).

(5) K. Cheng, G. Han, W. Weng, H. Qu, P. Du, G. Shen, J. Yang, and J. M. F. Ferreira, *Mater. Res. Bull.*, **38**, 89 (2003).

(6) W. Weng, S. Zhang, K. Cheng, H. Qu, P. Du, G. Shen, J. Yuan, and G. Han, *Surf. Coat. Technol.*,**167**,292 (2003).

(7) Thickness was evaluated by using variable-angle spectroscopic ellipsometry and WVASE32 software (VASE system, J. A. Woolam Co., Ltd.). The ellipsometric data were acquired at 70, 75 and 80° angle of incidence over the spectral range

250-1000 nm by l0 nm steps. A four-layer model (Si/ SiO_2/thin fllm/air) was used for determining the thickness. Native oxide thickness (2 nm) was separately determined for a cleaned substrate, and this value was used for evaluation of all samples. Surface roughness was modeled using an effective medium approximation layer consisting of 50 % of the material and 50 % void.

(8) UV light intensity was measured by UVR2 radiometer with UV detector unit UD-36 (TOPCON Corp., Japan). The measuring wavelength of this detector is 3l0-400 nm (mainly 365 nm).

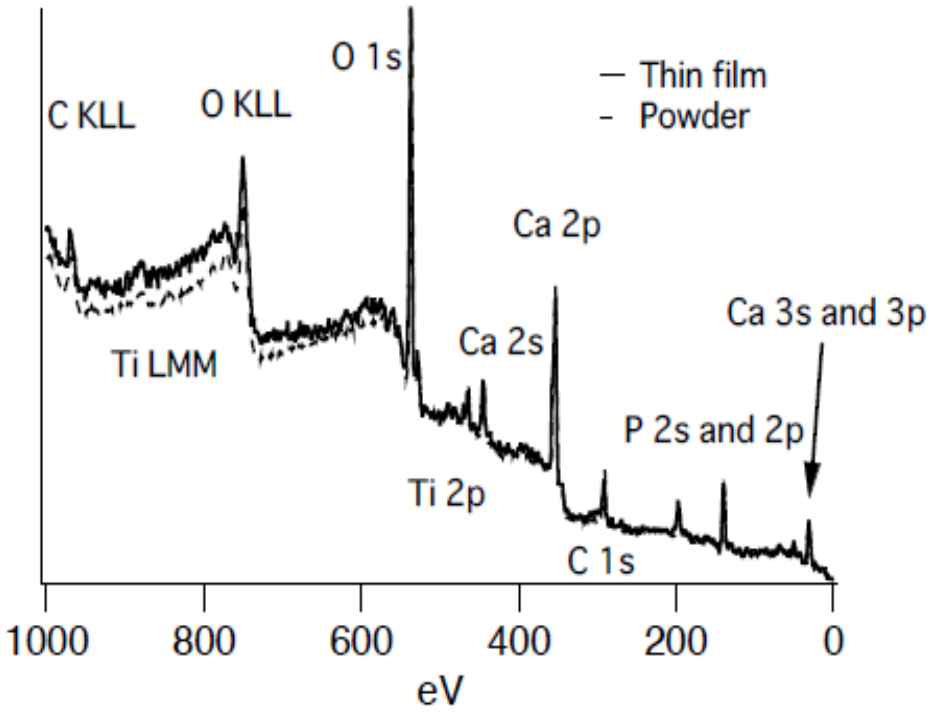

Figure 1 XPS spectra of Ti-CaHAp thin film (solid line) and powder (broken line).

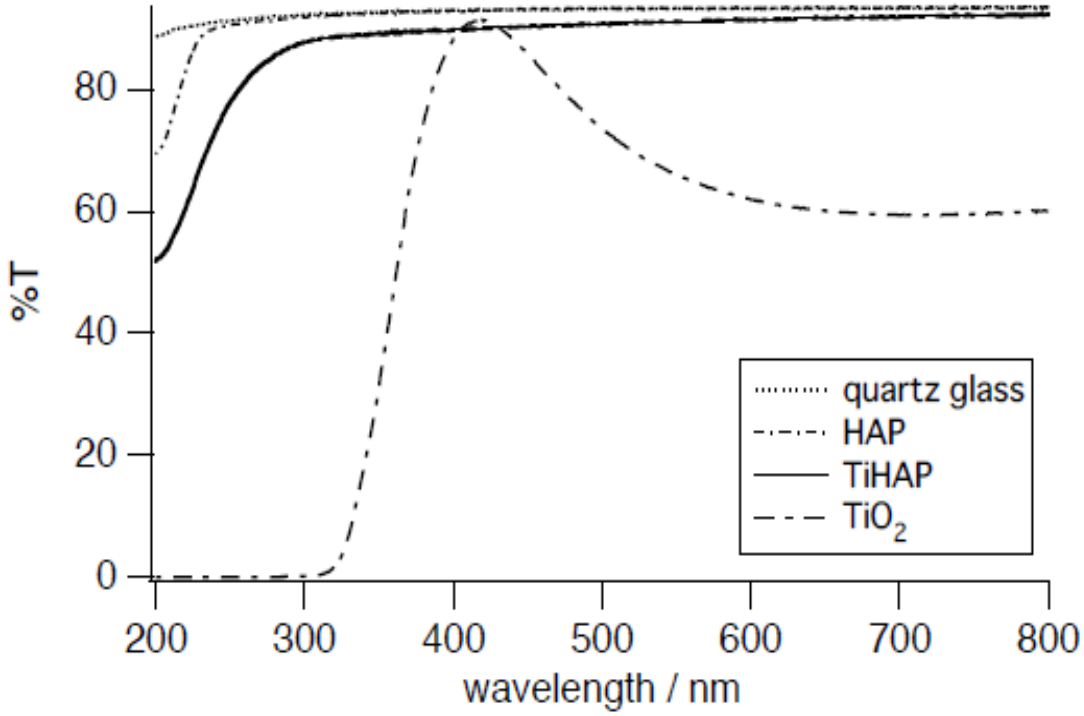

Figure 2 Transmission of quartz glass (substrate), CaHAp thin film (60 nm), Ti-CaHAp thin film (72 nm), and TiO_2 thin film (110 nm).

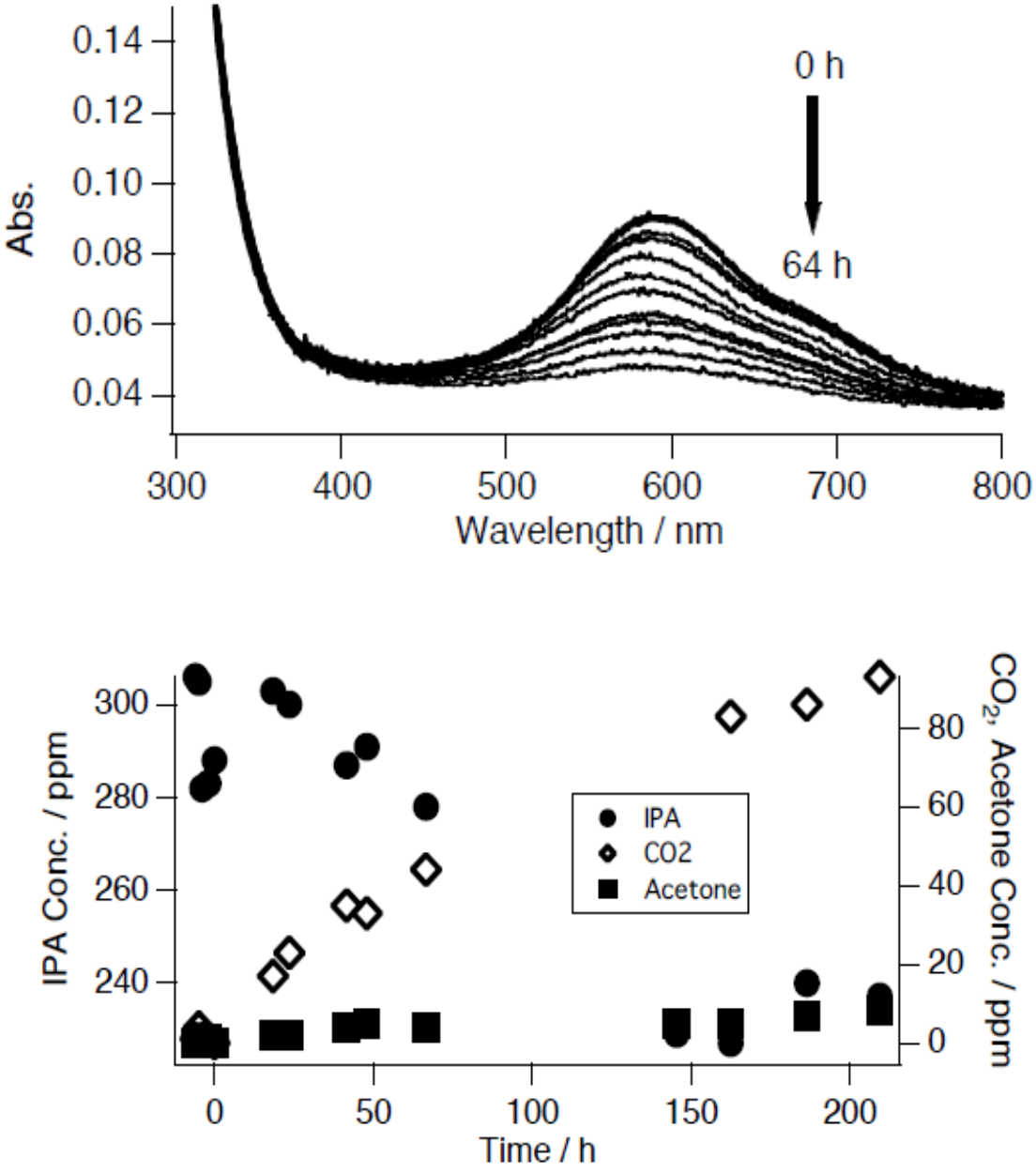

Figure 3 a) Adsorbed methylene blue decomposition and b) gaseous isopropyl alcohol alcohol decomposition under UV irradiation.

CHAPTER 5

Crystal structure and electron state of Ti-doped hydroxyapatite

5.1 Introduction

Calcium hydroxyapatite (CaHAp) is one of the primary constituents of the biological hard tissues, and has been of interest in the industrial, medical and dental fields. Synthetic CaHAp finds many applications as an adsorbent for chromatography to separate protein and enzymes, a catalyst for dehydration and dehydrogenetion of alcohols, methane oxidation, and artificial teeth and bones [(1)–(6)]. Perfect CaHAp crystal is a monoclinic type compound. However, typical CaHAp, which has a lattice deficiency, is a hexagonal type ionic compound that has the $P6_{3/m}$ space group, with 44 atoms per unit cell. The chemical formula of CaHAp is $Ca_{10}(PO_4)_6(OH)_2$. The Ca ions are separated into two inequivalent sites, one is a columnar site along the c axis [hereafter, "Ca-1"], and the other is located around OH [hereafter, "Ca-2"] [(1)]. Since CaHAp has a complicated structure, many kinds of cations can be induced into the apatite crystal structure. Therefore, substituting cations in CaHAp can be done easily. Up to now, numerous cations were examined to substitute Ca ions in CaHAp [(7)–(9)]. On the other hand, Wakamura et al. prepared Ti-substituted hydroxyapatite (Ti-CaHAp), in which the Ca ions had been substituted by 10 mol% of Ti ions, and reported that Ti-CaHAp showed photocatalytic activity for near ultraviolet (UV) light, similar to anatase-TiO_2 [(10)]. As for the photocatalytic properties of CaHAp, Nishikawa et al. have reported the generation of • OH and O_2 • − radicals on CaHAp after heat treatment at 200 ◦C and UV irradiation, and indicated the photocatalytic decomposition of methyl

mercaptane and dimethyl disulfide under UV irradiation [11]–[16]. However, they were using a deep UV (254 nm) light source for the irradiation. Such phenomena require higher photon energy than does Ti-CaHAp. Therefore, the photocatalytic activity of Ti-CaHAp seems to be a new phenomenon caused by Ti substitution of CaHAp.

After the paper by Wakamura et al., several papers were published concerning Ti substitution in CaHAp and the photocatalytic activity of Ti-CaHAp [17]–[20]. However, precise structural analysis has not been performed for Ti-CaHAp, so that the location of the Ti ion in the apatite structure is not yet clear. Moreover, band gap evaluation of Ti-CaHAp, which is very important for understanding its photocatalytic properties, has not been done yet either. Few studies have been conducted to evaluate the band gap of apatite materials including CaHAp. In one paper, the band gap of CaHAp was reported to be 3.95 eV by photoluminessence measurement [21]. Recently, the number of studies related to the electronic structures of CaHAp by first principles calculations using the density functional theory (DFT) has been gradually increasing [22]–[32]. In some of these papers, the band gap of CaHAp was calculated and reported to be around 4.51–5.4 eV [23]–[25]. However, these values are larger than the experimental value of the band gap which was reported in Ref. (21). In general, it is well known that a DFT calculation underestimates the value of the band gap compared with the true band gap. Therefore, it is impossible to interpret the band gap related electronic structure of CaHAp by depending on the experimental and theoretical results that have been obtained up to now. Moreover, there have been no studies conducted, either theoretically and experimentally on Ti-CaHAp, which is the target of this study. As a result, the photocatalytic mechanism of Ti-CaHAp remains unclear.

In this study, we evaluated the band gap of Ti-CaHAp both experimentally and

theoretically. At first, we confirmed the crystal structure of Ti-CaHAp to be a hexagonal structure, to determine the base model structure for the first-principles calculations. Next, we experimentally measured the band gap and calculated the electronic structure by using the first-principle density functional theory (DFT) method. Moreover, we proposed a photocatalytic model of Ti-CaHAp. Lastly, we experimentally evaluated the photocatalytic activity of Ti-CaHAp to confirm our photocatalytic model. In addition, we also evaluated CaHAp and anatase-TiO_2 in the same way to compare and understand the photocatalytic properties of Ti-CaHAp.

5.2 Experimental and computational procedure

5.2.1 Materials, crystal structure and band gap evaluation

We obtained the CaHAp and Ti-CaHAp powders from Taihei Chemical Industrial Co. Ti-CaHAp was prepared experimentally based on Ref. (10). The anatase-TiO_2 powder (ST-21) we used is a product of Ishihara Sangyo Kaisha Ltd. Ti-CaHAp powder, in which 10 mol% of Ca was substituted by Ti, was synthesized using the typical coprecipitation method in the similar way of CaHAp. Both CaHAp and Ti-CaHAp were calcined at 650 °C in 1 h by the authors. The details of the Ti-CaHAp preparation are described in Ref. (10). The particle size of all materials was less than 100 nm. The crystal structures of the prepared CaHAp and Ti-CaHAp powders were identified by the X-ray diffraction (XRD) method (RINT 1500, Rigaku) using Cu Kα radiation (60 kV, 200 mA). The band gap energy was evaluated with diffuse reflectance spectra using a UV–VIS spectrophotometer with an integrating sphere (UV-3101PC, Shimazu). The wavelength range was 200 – 2500 nm. The reflection spectra were measured and transformed into an absorption coefficient using the Kubelka–Munk function, and the

value of the band gap was determined by extrapolation.

5.2.2 Structure model and computational method

The electronic structure of Ti-CaHAp, CaHAp and anatase-TiO_2 was evaluated using a first principles pseudopotential calculation via the DFT method by using the Advance/PHASE code [33]. The generalized gradient approximation functional of Perdew, Burke, and Ernzerhof was used to calculate the exchange correlation energy [34]. The wave function was expanded in a plane wave basis set up to an energy cutoff of 500 eV. Integration over the Brillouin zone was performed using the Monkhorst Pack method with a 2 × 2 × 3 mesh. For geometrical optimization, all atoms were allowed to relax until their forces converged to less than 5×10^{-4} hartree / bohr (0.026 eV/Å). Furthermore, the total and projector density of states (DOS) was calculated using the tetrahedron method for integration over the Brillouin zone with a 4 × 4 × 6 mesh. The lattice parameter and bond angle of CaHAp and Ti-CaHAp were defined as a = b = 9.4172 Å, c = 6.8799 Å, $\alpha = \beta = 90°$, and $\gamma = 120°$, respectively. In the case of anatase TiO_2, the lattice parameter was defined as a = b = 3.7845 Å, c = 9.5413 Å, $\alpha = \beta = 90°$, and the k point mesh was set to 8 × 8 × 4. Other parameters for calculations were same as those of CaHAp and Ti-CaHAp.

5.2.3 Photocatalytic activity for acetaldehyde gas decomposition

The photocatalytic activity was estimated from the decomposition of acetaldehyde vapor under UV, VIS and UV + VIS irradiation. The light source was Xe lamps (LA-251Xe, Hayashi Watch Works Co., Ltd.). The UV light (1.25 mW/cm^2) was obtained by cutting VIS with a color filter (UV-D36A, Asahi-Glass Co., Ltd.). VIS light

(36200 lux) was also obtained by cutting UV with a color filter (Y-43, Asahi-Glass Co., Ltd.). Moreover, UV+VIS light was made by mixturing the above-mentioned UV and VIS light. The sample weight was decided on by adjusting the surface area of the sample powders to a constant value of 85.5 m^2 using the BET (Brunauer–Emmett–Teller) method. The samples were allowed to settle at the bottom of a 500 cm^3 cylindrical glass vessel sealed with a quartz top plate with 5 mm thick, using an O-ring. A mixed gas (N_2, 80%; O_2, 20%) was introduced into the vessel through the gas inlet to replace the air with the mixed gas, and then acetaldehyde vapor was injected into the vessel to obtain 1% acetaldehyde concentration of initial atmosphere in the vessel. The vessels were kept in a dark environment until an adsorption equilibrium was achieved. Then, the sample powders were irradiated for 3 h. The concentration of CO_2 in the vessel was measured every 1 h with a gas chromatograph equipped with a flame ionization detector (GC 390B, GL Sciences).

5.3 Results and discussions

5.3.1 XRD patterns and band gap of CaHAp and Ti-CaHAp

The XRD patterns of CaHAp and Ti-CaHAp powders are shown in Figure 1. The inset in Figure 1 shows enlarged diffraction patterns between 2θ of 35.0–39.5°. Both powders were revealed to be a single phase of an apatite structure. And in Ti-CaHAp, no TiO_2 phase was formed during synthesis. The arrows in the inset indicate the peak position of the monoclinic phase of CaHAp [22]. No monoclinic related peak appeared. Therefore, both CaHAp and Ti-CaHAp have a hexagonal structure.

Diffuse reflectance spectra of CaHAp, Ti-CaHAp and anatase TiO_2 powders are shown in Figure 2. The reflection edge wavelength of Ti-CaHAp was smaller than that of

anatase TiO_2. On the other hand, the reflection edge of CaHAp was out of our measurement range. In the case of anatase TiO_2, the reflection in the VIS range was imperfect and there seemed to be small absorption in the VIS range. The measured band gap energies, which were obtained from the diffuse reflection spectra, are listed in Table 1. Since the measured band gap energy of TiO_2, 3.27 eV, was similar to a generally known value of 3.2 eV [35], this measurement seems to be reliable. The measured band gap energy of CaHAp was greater than 6 eV. This means that the band gap of CaHAp exceeds the measuring limit of the equipment. Since the DFT-calculated band gaps of CaHAp reported in references were around 4.51–5.4 eV as mentioned above, our measured band gap is quite reasonable, considering the underestimation of the band gap energy produced with the DFT calculation. The measured band gap energy of Ti-CaHAp was 3.65 eV. This is larger than that of TiO_2; however, it appears that Ti-CaHAp exhibits photocatalytic activity in the near-ultraviolet region. It was reported in Ref. (10) that the photocatalytic activity of Ti-CaHAp was lower than TiO_2, and the results of this study seem to confirm the contents of Ref. (10).

5.3.2 Calculated band gap and density of states

At first, we started calculation of Ti-CaHAp depending on the chemical formula of $Ca_9Ti(PO_4)_6(OH)_2$ defined in Ref. (10). However, it may be impossible to maintain the charge neutrality by only substituting Ca^{2+} with Ti^{4+}. Accordingly, there was a possibility of a Ca deficiency existing at the nearest neighboring position of the Ti atom. We therefore defined the chemical formula of Ti-CaHAp as $Ca_8Ti(PO_4)_6(OH)_2$. Moreover, it was difficult to determine the Ti position simply, because the Ca ion can easily be exchanged with various cations [7]–[9]. Zhu et al. evaluated the occupation of

the metal ion in CaHAp and concluded that ions with a larger radius and larger electronegativity than the Ca ion seemed to occupy the Ca-2 site [36]. Ti has a larger electronegativity than Ca. However, its ionic radius is smaller. Therefore, it seems possible that Ti can occupy both the Ca-1 and Ca-2 site. Six Ti-CaHAp structure models were then premised as shown in Figure 3 visualized with VESTA software [37]. Figure 3(a) shows Ti-substituted Ca-1 site and three capable Ca deficient positions are indicated with the dashed circles from Model-1 to -3. In Figure 3(b), the Ti-substituted Ca-2 site and Ca deficient are indicated as Model-4 to -6 in the same manner in Figure 3(a).

The total energy and band gap energy in the six premised structures are listed with the Ti and Ca deficient position in Table 2. Among the structures in which Ti was substituted in the Ca-1 site, Model-3 shows the lowest total energy and seems to be the most stable. With the Ca-2 substituted structure, Model-6 seems to be the most stable. Therefore these two models seem to be possible Ti-CaHAp structures. The above mentioned two structures have band gap energies of 2.74 and 2.95 eV, respectively. The calculated band gap of anatase-TiO_2 was 2.23 eV, which was similar to the value shown in Refs. [38]–[40]. The band gap of Model-3 and Model- 6 is larger than that of the theoretically calculated anatase-TiO_2. This relative tendency of variation is similar with the experimental results shown in Table 1. The DOS of the Model-3 and Model-6 structures of Ti-CaHAp are shown in Figure 4(a) and (b) compared with CaHAp and anatase TiO_2 [Figure 4(c) and (d)]. Although the band gap energy of CaHAp was 4.95 eV in Figure 4(c), new states were formed in between the valence band and the conduction band when Ti were substituted into CaHAp as shown in Figure 4(a) and (b) of Ti-CaHAp. These states decreased the band gap energy and seemed to contribute to

the absorption edge increasing to near UV range.

The optimized unit cell structures of Ti-CaHAp, Model-3, and Model-6, are shown in Figure 5. In Model-6, two OH ions were dislocated and formed one H_2O molecule and one oxygen atom. It is possible for crystallohydrate to exist on the surface of Ti-CaHAp. However, when considering the heat treatment at 650 °C, it does not seem to be a real hydroxyapatite based structure, which has H_2O molecule in all unit cells after heat treatment. Therefore, Model-3 seems to be the most appropriate structure of photocatalytic Ti-CaHAp.

Figure 6 shows the total and projector DOS of O 2p and Ti 3d orbital of Model-3. The DOS of O 2p indicates the sum of DOS from the nine nearest neighboring O atoms around the Ti atom. Ti 3d and O 2p form a hybrid orbital. However, since these states were very narrow, the hybrid orbital was caused by weak covalent bonding of the Ti atom and O atoms. Such hybrid orbital seems to reduce the band gap energy and photo absorption edge of Ti-CaHAp compared with CaHAp. However, the hybrid orbital does not exist in the conduction band. Therefore, photocatalytic activity may not occur only with single photon absorption.

Following on from the above discussion, in Ti-CaHAp, a scenario of photo induced excitation is considered as follows: the electron in the valence band can be excited to hybridized states by absorption of the near UV photon and then subsequently excited to the conduction band by absorption of an additional photon. The schematic model of this scenario is shown in Figure 7 with the anatase TiO_2 model. In consideration of Figure 7(a), we anticipated that it would be possible for the second excitation to occur with the absorption of the VIS photon.

5.3.3 Photocatalytic activity for acetaldehyde gas decomposition by UV and VIS

To confirm the above discussed photocatalytic model and expectation of Ti-CaHAp, we evaluated acetaldehyde gas decomposition with UV and VIS light. The results are shown in Figure 8. CO_2 concentration resulting from acetaldehyde gas decomposition of Ti-HAp was smaller than that of anatase-TiO_2. This is because, as shown in Table 1, the band gap of Ti-CaHAp is larger than that of anatase-TiO_2. Moreover, the band gap of Ti-CaHAp exceeded the range of VIS. Therefore, almost no decomposition had occurred through irradiation of VIS in Figure 8(a). However, both UV and VIS were irradiated simultaneously on Ti-CaHAp, and the CO_2 concentration resulting from the gas decomposition increased and exceeded that when UV irradiation alone was applied. As Figure 8(b) indicates, anatase-TiO_2 also shows additional gas decomposition by UV + VIS irradiation compared with UV irradiation alone. The anatase TiO_2, evaluated in this study, showed an increase in the CO_2 concentration through irradiation of VIS. It seems that, as shown in Figure 2, reflection of anatase TiO_2 in the VIS area was smaller than that of Ti-CaHAp and CaHAp. Then, it may be possible for small acetaldehyde gas decomposition to occur through VIS irradiation to anatase TiO_2. Therefore, the photocatalytic phenomenon of Ti-CaHAp by UV + VIS irradiation seems to be different from that of anatase TiO_2.

Depending on the above results and discussion, our estimated atomic structure and photocatalytic model of Ti-CaHAp seems to be confirmed. However, in this study, the adapted atomic structure of Ti-CaHAp was premised only with DFT calculations, and so it is important to determine the Ti position in Ti-CaHAp experimentally. Experimental efforts to identify Ti positions are being conducted using the neutron

diffraction technique and X-ray absorption fine structure (XAFS) analysis.

5.4 Conclusions

In summary, we evaluated the band gap of Ti-CaHAp experimentally and theoretically in comparison with anatase TiO_2. The experimental band gaps of CaHAp, Ti-CaHAp, and anatase TiO_2 were greater than 6 eV, 3.65 eV, and 3.27 eV, respectively. The DFT calculated band gaps of CaHAp, Ti-CaHAp, and anatase TiO_2 were 4.95 eV, 2.74 eV, and 2.23 eV, respectively. By comparing optimized unit cell structures, in Ti-CaHAp, Ti seems to substitute the Ca-1 site with the Ca-1 site deficient. In Ti-CaHAp, Ti 3d orbital hybridized with the O 2p orbital and formed a lower state in the CaHAp band gap. It caused the absorption-edge lowering of Ti-CaHAp. The photocatalytic activity of Ti-CaHAp was enhanced with UV + VIS irradiation compared with only UV irradiation.

References

(1) J.C. Elliott, Structure and Chemistry of the Apatite and Other Calcium Orthophosphates, Elsevier, Amsterdam, 1994.

(2) R.Z. LeGeros, in: P.W. Brown, B. Constanz (Eds.), Hydroxyapatites and Related Materials, CRC Press, London, 1994.

(3) J.A.S. Bett, L.G. Christner, W.K. Hall, *J. Am. Chem. Soc.* **89** (1967) 5535–5540.

(4) S. Sugiyama, T. Minami, T. Moriga, H. Hayashi, K. Koto, M. Tanaka, J.B. Moffat, *J. Mater. Chem.* **6** (1996) 459.

(5) Y. Matsumura, H. Kanai, J.B. Moffat, *J. Chem. Soc. Faraday Trans.* **93** (1997) 4383–4389.

(6) F. Monroe, W. Votava, D.B. Bass, J. McMullen, *J. Dent. Res.* **50** (1971) 860–861.

(7) T. Suzuki, T. Hatsushika, Y. Hayakawa, *J. Chem. Soc., Faraday Trans.* **77** (1981) 1059–1062.

(8) T. Suzuki, T. Hatsushika, M. Miyake, *J. Chem. Soc., Faraday Trans.* **77** (1982) 3605–3611.

(9) H. Monma, *Shokubai* **27** (1985) 237–243 [in Japanese].

(10) M. Wakamura, K. Hashimoto, T. Watanabe, *Langmuir* **19** (2003) 3428–3431.

(11) H. Nisikawa, *Mater. Lett.* **58** (2003) 14–16.

(12) H. Nisikawa, K. Omamiuda, *J. Mol. Catal. A Chem.* **179** (2002) 193–200.

(13) H. Nisikawa, *J. Mol. Catal. A Chem.* **206** (2003) 331–338.

(14) H. Nisikawa, *J. Mol. Catal. A Chem.* **207** (2004) 149–153.

(15) H. Nishikawa, *Phos. Res. Bull.* **17** (2004) 101–104.

(16) H. Nishikawa, *Phos. Res. Bull.* **21** (2007) 97–102.

(17) C.C. Ribeiro, I. Gibson, M.A. Barbosa, *Biomaterials* **27** (2006) 1749–1761.

(18) H. Anmin, L. Ming, C. Chengkang, M. Dali, *J. Mol. Catal. A Chem.* **267** (2007) 79–85.

(19) C. Hu, J. Guo, J. Qu, X. Hu, *Appl. Catal. B Environ.* **73** (2007) 345–353.

(20) C. Ergum, *J. Eur. Ceram. Soc.* **28** (2008) 2137–2149.

(21) G. Rosenman, D. Aronov, L. Oster, J. Haddad, G. Mezinskis, I. Pavlovska, M. Chaikina, A. Karlov, *J. Lumin.* **122–123** (2007) 936–938.

(22) D. Haverty, S.A.M. Tofail, K.T. Stanton, J.B. McMonagle, *Phys. Rev. B* **71** (2005) 094103-1–094103-9.

(23) L. Calderin, M.J. Stott, A. Rubio, *Phys. Rev. B* **67** (2003) 134106-1–134106-7.

(24) P. Rulis, L. Ouyang, W.Y. Ching, *Phys. Rev. B* **70** (2004) 155104-1–155104-8.

(25) K. Matsunaga, A. Kuwabara, *Phys. Rev. B* **75** (2007) 014102-1–014102-9.

(26) D.U. Schramm, J. Terra, A.M. Rossi, D.E. Ellis, *Phys. Rev. B* **63** (2000) 024107-1–024107-14.

(27) M. Jiang, J. Terra, A.M. Rossi, M.A. Morales, E.M. Baggio Saitovitch, D.E. Ellis, *Phys. Rev. B* **66** (2002) 224107-1–224107-15.

(28) R. Astala, M.J. Stott, *Chem. Mater.* **17** (2005) 4125–4133.

(29) R. Astala, L. Calderín, X. Yin, M.J. Stott, *Chem. Mater.* **18** (2006) 413–422.

(30) X. Ma, D.E. Ellis, *Biomaterials* **29** (2008) 257–265.

(31) K. Matsunaga, *J. Chem. Phys.* **128** (2008) 245101-1–245101-10.

(32) K. Matsunaga, H. Inamori, H. Murata, *Phys. Rev. B* **78** (2007) 094101-1–094101-8.

(33) The original "PHASE" code is developed in the Frontier Simulation Software for Industrial Science project (FSIS) and commercialized as "Advance/PHASE" by AdvanceSoft Corporation. http://www.ciss.iis.u-tokyo.ac.jp/fsis/en/index. html, http://www.advancesoft.jp/product/advance phase.

(34) J.P. Perdew, K. Burke, M. Ernzerhof, *Phys. Rev. Lett.* **77** (1996) 3865–3868.

(35) L. Kavan, M. Grätzel, S.E. Gilbert, C. Klemenz, H.J. Scheel, *J. Am. Chem. Soc.* **118** (1996) 6716–6723.

(36) K. Zhu, K. Yanagisawa, R. Shimanouchi, A. Onda, K. Kajiyoshi, *J. Euro. Ceram. Soc.* **26** (2006) 509–513.

(37) K. Monma, F. Izumi, *J. Appl. Crystallogr.* **41** (2008) 653–658.

(38) W. Li, Y. Wang, H. Lin, S. Ismat Shah, C.P. Huang, D.J. Doren, S.A. Rykov, J.G. Chen, M.A. Barteau, *Appl. Phys. Lett.* **83** (2003) 4143–4145.

(39) H. Kamisaka, T. Adachi, K. Yamashita, *J. Chem. Phys.* **123** (2005) 084704-1–

084704-9.

(40) M. Long, W. Cai, Z. Wang, G. Liu, *Chem. Phys. Lett.* **420** (2006) 71.

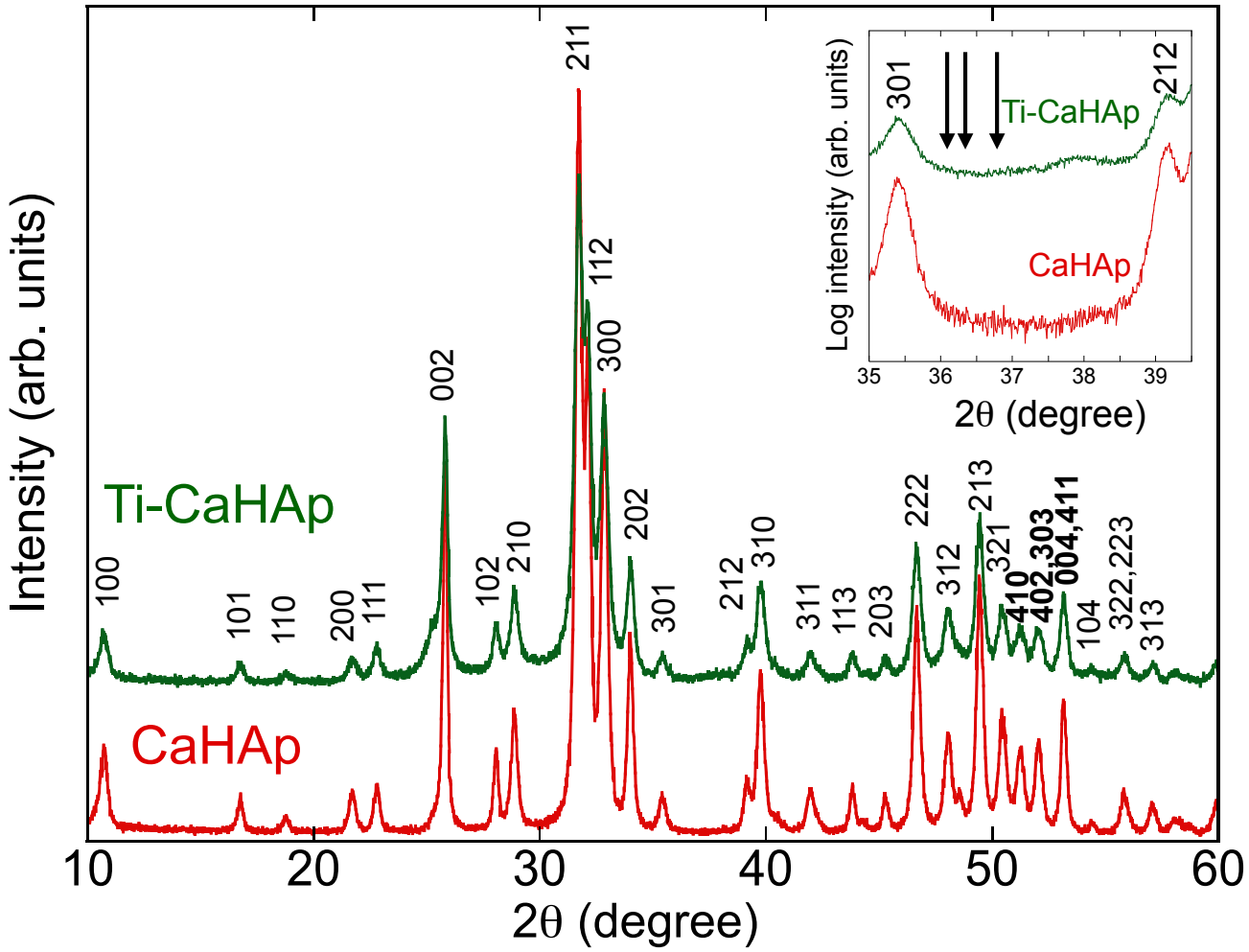

Figure 1 XRD patterns of CaHAp and Ti-CaHAp powders. Inset shows enlarged diffraction patterns between 2 θ of 35 – 39.5 °. The arrows in the inset indicate the peak position of the monoclinic phase.

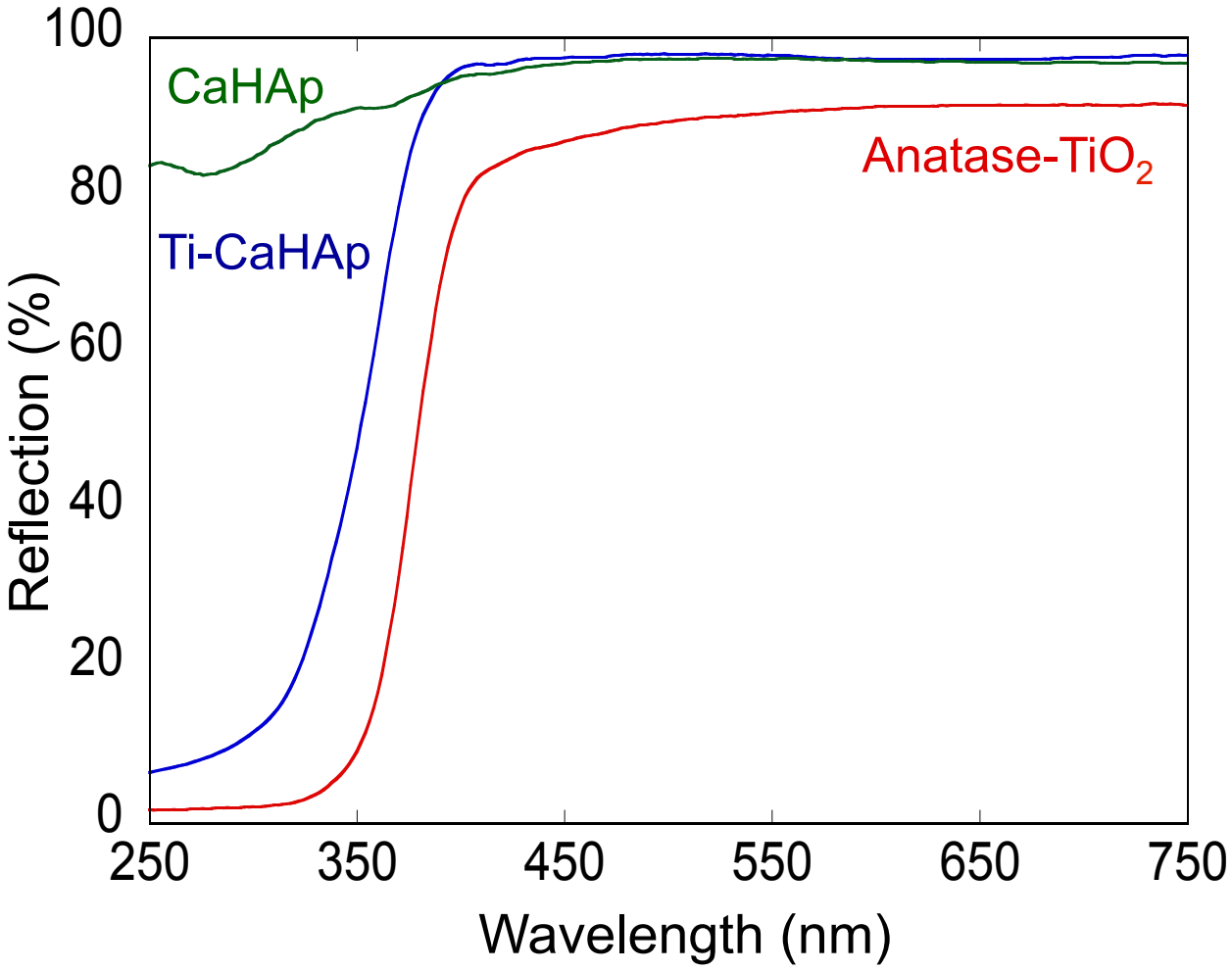

Figure 2 Diffuse reflectance spectra of CaHAp, Ti-CaHAp and anatase-TiO_2 powders.

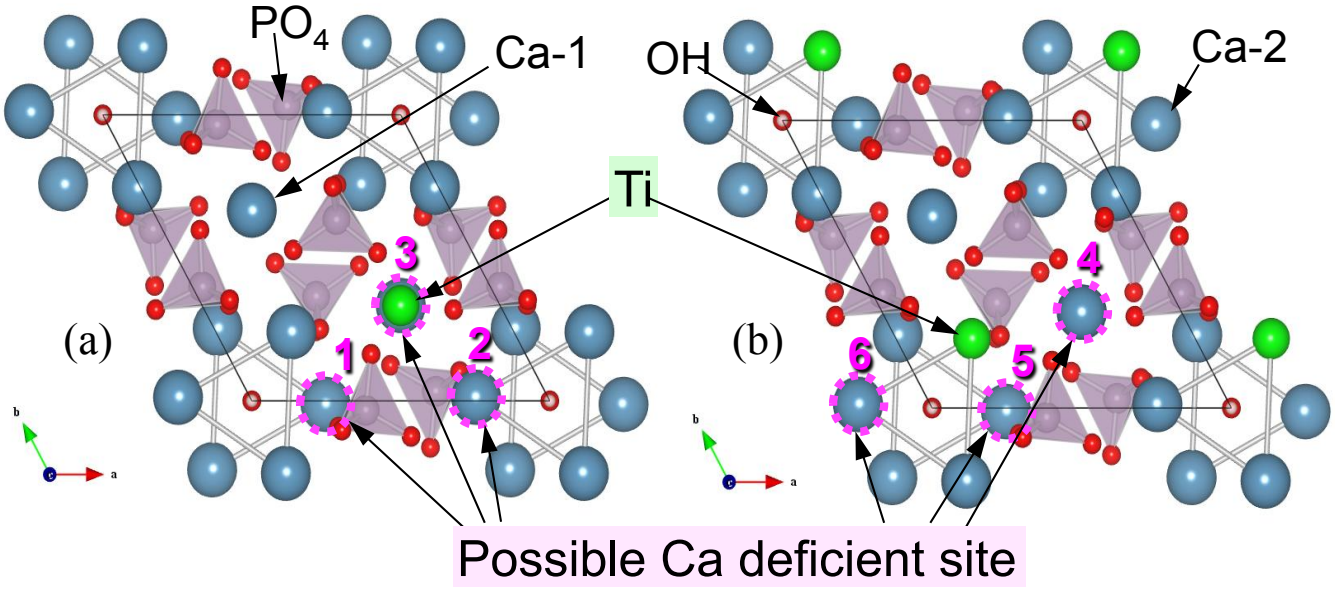

Figure 3 Estimated Ti-CaHAp unit cell structures: (a) Ti-substituted Ca-1, (b) Ti-substituted Ca-2 visualized by using VESTA[35]. The solid line indicates the solid line unit cell, and the dashed circles indicate the possible Ca-deficient positions.

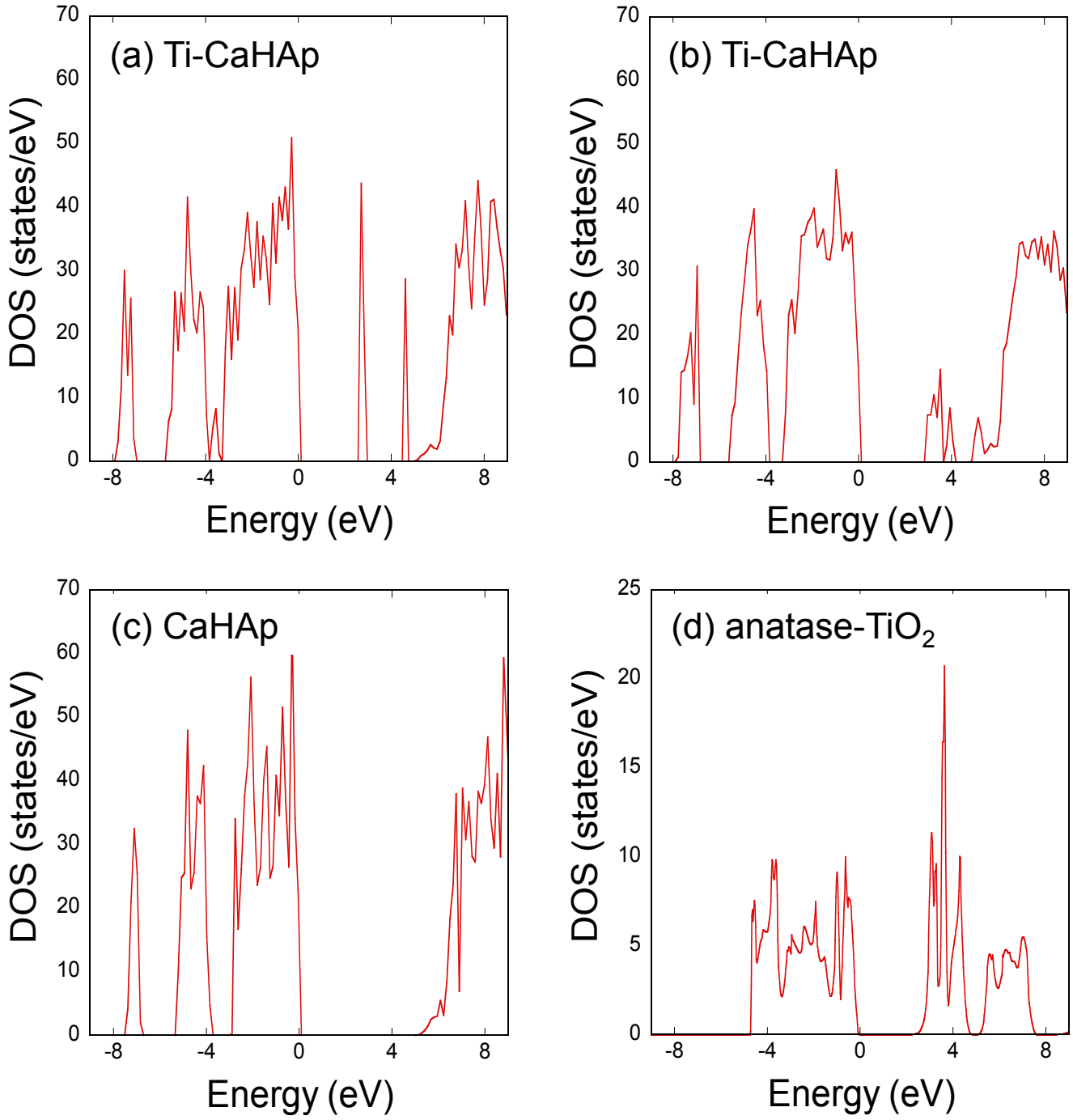

Figure 4 Density of states: (a) Ti-CaHAp [Model-3], (b) Ti-CaHAp [Model-6], (c) CaHAp, and (d) anatase-TiO_2, 0 eV indicate the Fermi level.

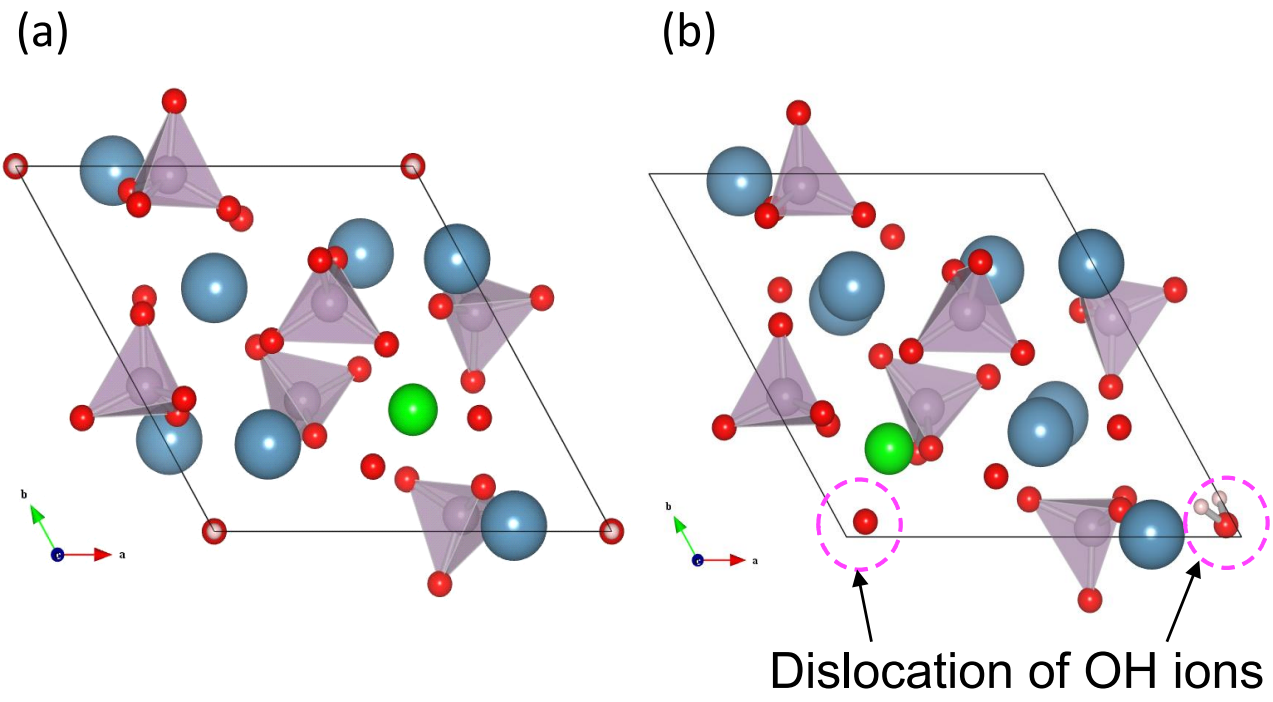

Figure 5 Optimized unit cell structure of Ti-CaHAp visualized by VESTA[35] : (a) Model-3, (b) Model-6.

Table 1 Band gap energy of CaHAp and Ti-CaHAp and Anatase-TiO_2 measured by diffuse reflectance spectroscopy.

Materials	Band gap energy (eV)
CaHAp	>6
Ti-CaHAp	3.65
Anatase-TiO_2	3.27

Table 2 Calculated today energy and band gap energy of estimeted Ti-CaHAp structures.

Structure	Ti position	Ca deficient	Total energy (Ry)	Band gap (eV)
Model-1	Ca-1	Ca-2	-697.3991	1.94
Model-2	Ca-1	Ca-2	-697.4000	1.82
Model-3	Ca-1	Ca-1	-697.4065	2.74
Model-4	Ca-2	Ca-1	-697.3809	1.94
Model-5	Ca-2	Ca-2	-697.3918	1.80
Model-6	Ca-2	Ca-2	-697.4252	2.95

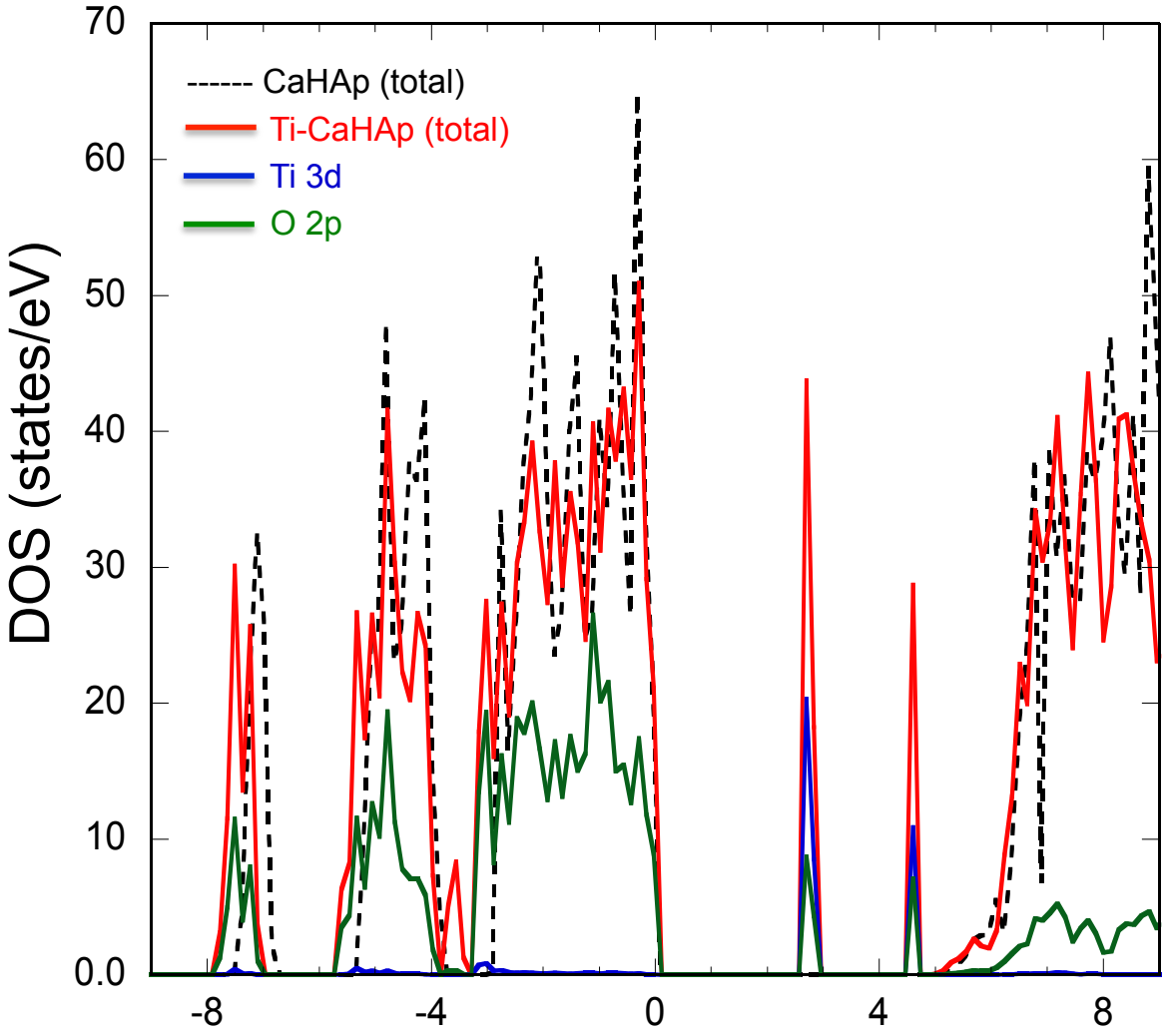

Figure 6 Total and projector DOS of Ti-CaHAp [Model-3]; 0 eV indicate the Fermi level.

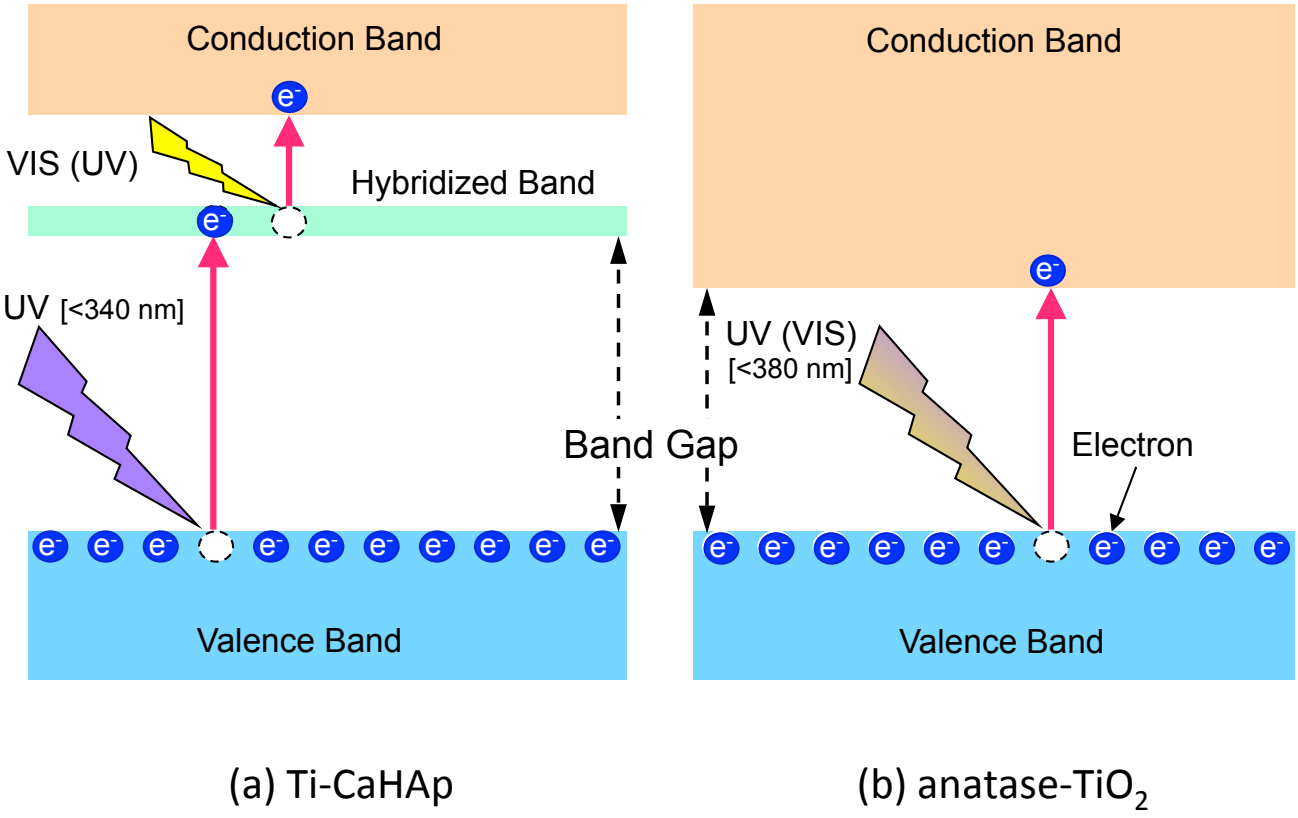

Figure 7 Schematic photocatalytic model of (a) Ti-CaHAp and (b) anatase-TiO_2.

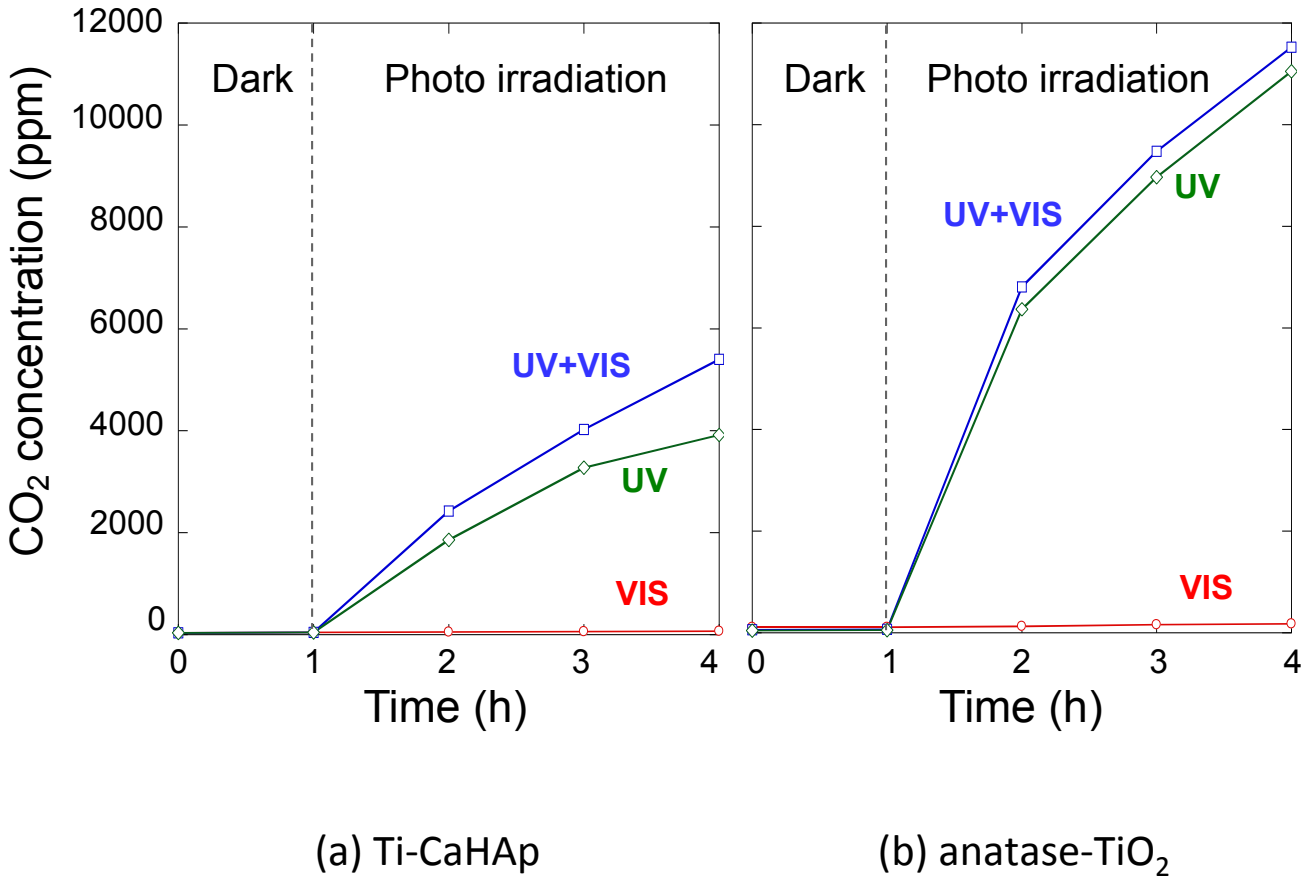

Figure 8 Photocatalytic activity of (a) Ti-CaHAp and (b) anatase-TiO_2 powder; decomposition of acetaldehyde to CO_2 by photo irradiation. Band pass filters: UV cut (≦ 420 nm), VIS cut (≧400 nm), Quantity of light: UV: 1.25 mW/cm^2, VIS: 36200 lux.

CHAPTER 6

Visible light photocatalytic activity of Ti-doped hydroxyapatite ion-exchanged with Cr(III)

6.1 Introduction

Calcium hydroxyapatite, $Ca_{10}(PO_4)_6(OH)_2$ designated as CaHAp, is a principal component of hard tissues and has been of interest in industry and medical and dental fields. Synthetic CaHAp finds many applications such as adsorbents for chromatography to separate protein and enzyme, catalysts for dehydration and dehydrogenation of alcohols, methane oxidation, and artificial teeth and bones [(1)-(6)]. Recently, CaHAp is received attentions in application for photocatalyst. Nishikawa has reported the generation of ·OH and $O^{\cdot}{}_2^-$ radicals on CaHAp by UV irradiation and indicated the photocatalytic decomposition of methyl mercaptane and dimethyl sulfide [(7)-(11)]. While, we indicated by decomposition of acetaldehyde and albumin under UV irradiation that the photocatalytic activity of CaHAp is enhanced by doping of Ti(IV) [(12)]. Further, the Ti(IV) doped CaHAp (Ti-CaHAp) possesses a high bactericidal effect owing to its higher affinity with proteins than titanium dioxide (TiO_2) [(12), (13)]. Since then, some researchers examine the structure, property and application of Ti-CaHAp [(14)-(17)]. Hu et al. have indicated that the CaHAp co-substituted with Ti(IV) and antibacterial ions (Ag(I), Cu(II) or Zn(II)) possesses the high efficiency for killing the Escherichi coli and Staphylococcus aureus [(14)]. Also, Anmin et al. reported that the photocatalytic activity of Ti-CaHAp is related to its particle size, crystalline quality, morphology,

specific surface area and surface state [15]. Most recently, Hung and co-workers suggested that the Ti-CaHAp has a great potential for use in biomedical applications such as bioactive scaffolds and coating on Ti implants [17]. However, UV light fractionally occupies the solar irradiation. For utilization of visible light (VIS), it is required the modification of Ti-CaHAp particles. Nonetheless, as far as we know, no study has been reported about such modification. In contrast, there are many studies about introduction of vis absorption property for TiO_2 photocatalyst by doping of transition metal ions such as Cr(III), Zr(IV), Al(III), Ni(II), Sn(IV), Zn(II), Cu(II), V(IV), Fe(III) and so forth [18]-[33], because the dopant transitional metal works by introducing a donor and/or acceptor level in the wide forbidden band of TiO_2 [31]. Among them, apparent band gap energy of anatase TiO_2 is effectively reduced by doping of Cr(III) [18], [27]-[33]. It seems, therefore, that the Cr(III)-doping into Ti-CaHAp particles is expected to give a photocatalytic ability under vis irradiation to this material.

The aim of this study was to introduce the photocatalytic ability under VIS irradiation to Ti-CaHAp. Therefore, synthetic Ti-CaHAp particles were treated with various Cr(III) concentrations in aqueous media and the surface structure and photocatalytic property of the materials were investigated by various means. Further, the relationship between photocatalytic activity and surface structure of Cr(III)-doped Ti-CaHAp was discussed based on the results obtained.

6.2 Experimental

6.2.1 Cr(III)-doping of Ti-CaHAp particles

Ti-CaHAp photocatalyst designed by the Fujitsu laboratories and the Tokyo University [12] was supplied from Taihei Chemical Industrial Co. Ltd. (catalog number: PCAP-100).

The Cr(III)-doping of Ti-CaHAp was carried out as follows. 1.5 grams of Ti-CaHAp particles were dispersed in 300 ml of 1.0×10^{-4} - 1.0×10^{-2} mol/dm^3 aqueous $Cr(NO_3)_3 \cdot 9H_2O$ solutions and they were stirred for 5 min at room temperature. After then, the samples were filtered off, thoroughly washed with distilled water and finally dried at 100 °C in an air oven for overnight.

6.2.2 Characterization

The samples thus obtained were characterized by a variety of conventional techniques. Powder X-ray diffraction (XRD) patterns were taken by a diffractometer (Rigaku RINT-2100) with a Ni-filtered CuKα radiation (30 kV and 20 mA). Particle morphology was observed by a transmission electron microscope (TEM, JEOL JEM-2100). Transmission IR spectra in vacuo at room temperature were recorded by a self-supporting disk method using a Fourier transform infrared (FTIR) spectrometer (JASCO FTIR-660plus) with a TGS sensor and vacuum cell. Prior to the measurement, the samples were evacuated at 300 °C for 2 h. Diffuse reflectance UV-VIS spectra were recorded with a UV-VIS spectrometer (JASCO V-560) with an integrating sphere (JASCO ISV-469). Cr, Ti, Ca and P contents were assayed by an inductively coupled plasma atomic emission spectrometer (ICP-AES, Seiko Vista-Pro) after leaching the samples in a concentrated HNO_3 solution and diluting the solution to a desired concentration with water. Specific surface area was obtained by fitting the BET equation to the N_2 adsorption isotherms measured at the boiling temperature of liquid nitrogen with an automatic volumetric apparatus constructed in our laboratory. X-ray photoelectron spectra (XPS) were recorded by a X-ray photoelectron spectroscopy (Seiko SSX-100) with a MgKα radiation (8 kV, 20 mA).

6.2.3 Photocatalytic activity under VIS irradiation

The photocatalytic activity of the samples was estimated from decomposition of acetaldehyde vapor under VIS irradiation. The light source used was a Xe Lamp with 42,000 lx (Hayashi Watch Works LA-251Xe). The UV light was cut using a UV cut color glass filter (Asahi Glass Y-43).

The sample weight was decided by adjusting the surface area of the samples as a constant value of 85.5 m^2 using the BET specific surface area. The samples were settled in the bottom of a 500 ml cylindrical glass vessel sealed with a quartz plate with 5 mm thickness using an O-ring. A mixed gas (N_2: 80%, O_2: 20%) was introduced into the vessel through the gas inlet to replace air by the mixed gas, and then acetaldehyde vapor was injected into the vessel, followed by keeping it in the dark to achieve adsorption equilibrium. Then, vis irradiation was taken place for 3 h. The concentrations of acetaldehyde and CO_2 in the vessel were hourly determined by a gas chromatograph with a FID sensor (GL-Sciences GC390B).

6.3 Results and discussion

6.3.1 Structure and chemical composition of Cr(III)-doped Ti-CaHAp

The XRD patterns of Ti-CaHAp treated with various Cr(III) concentrations showed only the peaks due to CaHAp (JCPDS card No. 9-432) and the crystallinity was essentially not altered with increasing the Cr(III) concentration. The color of the Cr(III)-treated Ti-CaHAp was light green and is different from white color of the original sample. From these results, Cr(III) is seemed to be doped into Ti-CaHAp particles. By the TEM observation, the original Ti-CaHAp particles were rod-shaped

with a size of ca. 60 nm in length and ca. 20 nm in width. No remarkable change of the particle morphology by treating with Cr(III) was recognized and no new particles were detected. Also, the adsorption isotherms of N_2 on all the particles belonged to Type II in the IUPAC classification and the specific surface area evaluating fitting the BET equation to the isotherms was almost constant of 46-50 m^2/g. Further, no micropores were detected by the t-plot analysis [34] of the N_2 adsorption isotherms. These results suggest that the Cr(III)-doping takes place on the particle surface of Ti-CaHAp.

To ascertain the chemical composition of Cr(III)-doped Ti-CaHAp, Ca, Ti, Cr and P contents in the particles were assayed by ICP-AES. Figure 1 plots the Ca, Ti, Cr and P contents in the material as a function of Cr(III) concentration. The Ca, Ti and P contents in the original Ti-CaHAp were 8.73, 0.794 and 5.17 mmol/g, respectively. On increasing the Cr(III) concentration, the amount of Cr increases and that of Ca decreases. While, the Ti and P contents are essentially not varied over the whole Cr(III) concentration range. These facts allow us to infer that the surface Ca(II) of Ti-CaHAp is exchanged with Cr(III). The Cr/Ca exchange ratios of Ti-CaHAp treated at 1.0×10^{-4}, 1.0×10^{-3} and 1.0×10^{-2} mol/dm^3 of Cr(III) were 0.68, 0.75 and 0.89, respectively. The exchange ratio at 1.0×10^{-4} mol/dm^3 is close to the theoretical ratio of 2/3 = 0.67. Nonetheless, the ratios at 1.0×10^{-3} and 1.0×10^{-2} mol/dm^3 are larger than theoretical ratio, inferring the existence of other uptake mechanism of Cr(III) in addition to the substitution of surface Ca(II) of Ti-CaHAp. This will be discussed later.

6.3.2 Surface structure of Cr(III)-doped Ti-CaHAp

Figure 2 shows the XPS spectra of Cr2p and Ca2p regions of Cr(III)-doped Ti-CaHAp. The binding energy of the spectra was calibrated using that of C1s. As is seen in

spectrum a of Figure 2(A), the peak due to Cr2p is not detected for the original sample. On the other hand, spectra b-d of the Cr(III)-doped Ti-CaHAp possess a peak at 577.5 eV and the peak is intensified on increasing the Cr(III) concentration without changing the peak position. The binding energy of these peaks almost corresponds to 577.7 eV for Cr_2O_3 but differs from 581.2 eV for CrO_3. Accordingly, the surface Cr atoms exist as a trivalent state. In Figure 2(B), XPS spectrum a of the original Ti-CaHAp possesses the peaks of $Ca2p_{3/2}$ and $Ca2p_{1/2}$ regions at 346.4 eV and 350.1 eV, respectively. As the Cr(III) peak develops, these peaks gradually weaken. This fact is again indicative that the substitution of surface Ca(II) of Ti-CaHAp particles with Cr(III). Besides, the Ca2p peaks shift to a higher binding energy on increasing the Cr(III) concentration. Since the ionic radius of Cr(III) (0.069 nm) is smaller than that of Ca(II) (0.099 nm), Cr(III)-doping seems to distort the crystal structure of surface phase of Ti-CaHAp, giving rise to the change in chemical environment of surface Ca(II).

Figure 3 plots the Cr/P atomic ratios of particle surface (X_s) and whole particle (X_w), respectively determined by XPS and ICP-AES against Cr(III) concentration. The results are shown in Figure 3. Clearly seen that the X_s is much larger than X_w over the whole Cr(III) concentration range. This proves that the Cr(III) is mainly concentrated at the particle surface of Ti-CaHap. While, the increment of X_w is larger than that of X_s at Cr(III) concentration from 1.0×10^{-3} to 1.0×10^{-2} mol/dm^3, inferring that a part of Cr(III) is doped not only on particle surface but also inside the particles by exchanged with Ca(II) of Ti-CaHAp. To get further insight into the surface structure of Cr(III)-doped Ti-CaHAp, in vacuo IR spectra were measured and were shown in Figure 4. Before the measurements, the samples were evacuated at 300 °C for 2 h. Spectrum a of the original Ti-CaHAp possesses a strong absorption band at 3570 cm^{-1} due to the

lattice OH^- ions in the Ti-CaHAp crystal [35]. Besides, two weak bands are detected at 3658 and 3735 cm^{-1}. The former band, which can be divided to three ones at 3658, 3668 and 3675 cm^{-1} in expanded region of Figure 4(B), is assignable to the O-H stretching vibration modes of surface P-OH groups [12] and the latter one is to the surface Ti-OH groups [35]. When the Ti-CaHAp is treated at 1.0×10^{-4} mol/dm^3 of Cr(III), the surface Ti-OH and P-OH bands almost vanish and new weak band develops at 3670 cm^{-1} (spectrum b). The 3670 cm^{-1} band is intensified with increasing the Cr(III) concentration (spectra c and d). In order to assign this band, isotope exchange of Cr(III)-doped Ti-CaHAp was done by D_2O adsorption after taking the spectrum d. The result is shown in Figure 4 of spectrum e. With the D_2O adsorption, the OH^- and 3670 cm^{-1} bands are weakened and OD^- band at 2633 cm^{-1} and a new band at 2706 cm^{-1} are developed. The wavenumber ratio of 3670 and 2706 cm^{-1} bands is 1.356, which is close to 1.356 of OH^-/OD^- and 1.374 of the theoretical ν_{OH}/ν_{OD} ratio. Thus, the 3670 cm^{-1} band is assignable to the surface OH groups. As has been already mentioned, the amount of surface Cr(III) increases with an increment of Cr(III) concentration. Therefore, the 3670 cm^{-1} band can be assigned to the O-H stretching vibration mode of surface Cr-OH groups, which are thought to be formed by following reactions:

surface M-OH $\rightarrow$ surface $M\text{-}O^- + H^+$ (M = P or Ti) (1)

The surface M-OH groups of Ti-CaHAp are dissociated in aqueous media to yield surface $M\text{-}O^-$ groups and protons via reaction (1).

surface $M\text{-}O^- + [Cr(OH)_2]^+ \rightarrow$ surface $M\text{-}O\text{-}Cr\text{-}(OH)_2$ (2)

The surface $M\text{-}O^-$ groups react with $[Cr(OH)_2]^+$ to yield $M\text{-}O\text{-}Cr(OH)_2$ via reaction (2), resulting the formation of surface Cr-OH groups.

From these results, it is likely that the increment of Cr(III) concentration forms the

$Cr(OH)_3$-like layer on the surface of Ti-CaHAp particles.

6.3.3 Photocatalytic activity of Cr(III) doped Ti-CaHAp under VIS irradiation

Figure 5 shows the diffuse reflectance UV-VIS spectra of Cr(III)-doped Ti-CaHAp. Spectrum of the Ti-CaHAp exhibits a strong UV absorption peak. This absorption has been ascribed to the charge transfer transition of $O^{2-} \rightarrow Ti^{4+}$ [12] and its band gap energy estimated from the absorption edge is 3.4 eV. When the sample is treated with 1.0×10^{-4} mol/dm^3 of Cr(III), new weak absorption peaks are found at 446 and 623 nm in VIS range in addition to the UV absorption peak, revealing that the VIS absorption property is able to be introduced to the Ti-CaHAp by doping of Cr(III). These peaks are respectively assignable to the $^4A_{2g} \rightarrow {}^4T_{2g}$ and $^2A_{2g} \rightarrow {}^2T_{1g}$, $^2E_{2g}$ transitions of Cr(III) in the Ti-CaHAp because similar peaks are seen in the spectrum of $Cr(OH)_3$ [36], [37]. Increasing the Cr(III) concentration enhances the VIS absorption property. The extended absorbance of Ti-CaHAp in the VIS region would provide a possibility for enhancing the photocatalytic behavior of Ti-CaHAp for solar energy application.

To confirm the photocatalytic activity of Cr(III)-doped Ti-CaHAp under VIS irradiation, acetaldehyde decomposition test was done. Figure 6 plots the acetaldehyde concentration against VIS irradiation period. For the original Ti-CaHAp, the acetaldehyde concentration slightly decreases on elapsing the VIS irradiation period, suggesting that the material possesses a weak photocatalytic activity. For the Cr(III)-doped Ti-CaHAp, the acetaldehyde concentration decreases on increasing the VIS irradiation period and reaches to zero at 3 h. It seems that the Cr(III)-doped Ti-CaHAp has a photocatalytic activity under VIS irradiation. To get further insight into

the ability of oxidative decomposition of acetaldehyde, Figure 7 plots the CO_2 concentration as a function of VIS irradiation period. For the Cr(III)-doped Ti-CaHAp, CO_2 concentration is almost linearly increased on elapsing the VIS irradiation period. On the other hand, the original sample shows less concentration change of CO_2 than Cr(III)-doped samples. This strongly reveals the enhancement of the ability of oxidative decomposition of acetaldehyde by doping of Cr(III). Note that the CO_2 concentration after VIS irradiation for 3 h is maximum at 1.0×10^{-4} mol/dm^3 of Cr(III). As indicated above, increasing the Cr(III) concentration leads not only substitution of surface Ca(II) to Ti-CaHAp with Cr(III) but formation of $Cr(OH)_3$-like layer on the particle surface. Hence, the formation of $Cr(OH)_3$-like layer would depress the ability of oxidative decomposition of acetaldehyde. To corroborate this, acetaldehyde decomposition test was taken place using the $Cr(OH)_3$. The results are represented by filled circles in Figure 6 and 7. Clearly seen that the acetaldehyde and CO_2 concentrations are essentially not altered by VIS irradiation as compared with Cr(III)-doped Ti-CaHAp meaning that the $Cr(OH)_3$ possesses no photocatalytic ability. These results imply that the photocatalytic ability of Ti-CaHAp under VIS irradiation can be introduced by doping of Cr(III), although the ability was depressed by surface $Cr(OH)_3$ like layer formed at higher Cr(III) concentration.

6.4 Conclusions

From the information presented in this publication, we can draw the following conclusions. The Cr(III) could be doped on particle surface of Ti-CaHAp without changing the crystal structure and particle morphology. Increasing the Cr(III) concentration increased the amount of Cr in the products while that of surface Ca(II) of

Ti-CaHAp decreased. This result indicated that the surface Ca(II) of Ti-CaHAp was substituted with Cr(III). At higher Cr(III) concentration a part of Cr(III) reacted with surface P-O^- and Ti-O^- groups to form surface P-O-$Cr(OH)_2$ and Ti-O-$Cr(OH)_2$ groups via reactions (1) and (2), resulting the formation of $Cr(OH)_3$-like layer on the particle surface. The Cr(III)-doped Ti-CaHAp possessed the VIS absorption property which was enhanced with increasing the Cr(III) concentration. The photocatalytic decomposition of acetaldehyde into CO_2 over Cr(III)-doped Ti-CaHAp particles was observed under VIS irradiation and the activity was depressed by the formation of $Cr(OH)_3$-like layer on the surface of Ti-CaHAp particles.

References

(1) J.C. Elliott, Structure and chemistry of the apatites and other calcium orthophosphates, Elsevier, Amsterdam, 1994.

(2) R.Z. LeGeros, in: P.W. Brown, B. Constanz (Eds.), Hydroxyapatites and Related Materials, CRC Press, London, 1994.

(3) J.A.S. Bett, L.G. Christner, W.K. Hall, Studies of the hydrogen held by solids. XII. Hydroxyapatite catalysts, *J. Am. Chem. Soc.* **89** (1967) 5535−5540.

(4) S. Sugiyama, T. Minami, T. Moriga, H. Hayashi, K. Koto, M. Tanaka, J.B. Moffat, Enhancement of the selectivity to carbon monoxide with feedstream doping by tetrachloromethane in the oxidation of methane on stoichiometric calcium hydroxyapatite, *J. Mater. Chem.* **6** (1996) 459.

(5) Y. Matsumura, H. Kanai, J.B. Moffat, Catalytic oxidation of carbon monoxide over stoichiometric and non-stoichiometric calcium hydroxyapatites, *J. Chem. Soc., Faraday Trans.* **93** (1997) 4383−4889.

(6) F. Monroe, W. Votava, D.B. Bass, J. McMullen, New calcium phosphate ceramic material for bone and tooth implants, *J. Dent. Res.* **50** (1971) 860−861.

(7) H. Nishikawa, Radical generation on hydroxyapatite by UV irradiation, *Mater. Lett.* **58** (2003) 14−16.

(8) H. Nishikawa, A high active type of hydroxyapatite for photocatalytic decomposition of dimethyl sulfide under UV irradiation, *J. Mol. Catal. A Chem.* **207** (2004) 149−153.

(9) H. Nishikawa, Photocatalytic activity of hydroxyapatite based on photoinduced excitation, *Phos. Res. Bull.* **21** (2004) 101−104.

(10) H. Nishikawa, Surface changes and radical formation on hydroxyapatite by UV irradiation for inducing photocatalytic activation, *J. Mol. Catal. A Chem.* **106** (2006) 331−338.

(11) H. Nishikawa, Photo-induced catalytic activity of hydroxyapatite based on photo-excitation, *Phos. Res. Bull.* **17** (2007) 97−102.

(12) M. Wakamura, K. Hashimoto, T. Watanabe, Photocatalysis by calcium hydroxyapatite modified with Ti(IV): albumin decomposition and bacterial effect, *Langmuir* **19** (2003) 3428−3431.

(13) N. Yoshida, M. Takeuchi, T. Okura, H. Monma, M. Wakamura, H. Ohsaki, T. Watanabe, Super-hydrophobic photocatalytic coatings utilizing apatite-based photocatalyst, *Thin Solid Films* **502** (2006) 108−111.

(14) C. Hu, J. Guo, J. Qu, X. Hu, Efficient destruction of bacteria with Ti(IV) and antibacterial ions in co-substituted hydroxyapatite films, *Appl. Catal. B Environ.* **73** (2007) 345−353.

(15) H. Anmin, L. Ming, C. Chengkang, M. Dali, Preparation and characterization of a

titanium-substituted hydroxyapatite photocatalyst, *J. Mol. Catal. A Chem.* **267** (2007) 79−85.

(16) C. Ergun, Effect of Ti ion substitution on the structure of hydroxyapatite, *J. Eur. Ceram. Soc.* **28** (2008) 2137−2149.

(17) J. Hung, S.M. Best, W. Bonfield, T. Buckland, Development and characterization of titanium-containing hydroxyapatite for medical applications, *Acta Biomater.* **6** (2010) 241−249.

(18) R.K. Sharma, M.C. Bhatnagar, G.L. Sharma, Mechanism of highly sensitive and fast response Cr doped TiO_2 oxygen gas sensor, *Sens. Actuators B* **45** (1997) 209−215.

(19) Y. Matsumoto, M. Murakami, T. Shono, T. Hasegawa, T. Furumura, M. Kawasaki, P. Ahmet, T. Chikyow, S.Y. Koshibara, H. Koinuma, Roomtemperature ferromagnetism in transparent transition metal-doped titanium dioxide, *Science* **291** (2001) 854−856.

(20) H. Kato, A. Kubo, Visible-light-response and photocatalytic activities of TiO_2 and $SrTiO_2$ photocatalysts codoped with antimony and chromium, *J. Phys. Chem. B* **106** (2002) 5029−5034.

(21) J.E. Lee, S. Oh, M. Dong, D.W. Park, Synthesis of nano-sized Al doped TiO_2 powders using thermal plasma, *Thin Solid Films* **457** (2004) 230−234.

(22) Y.H. Wang, S.W. Liu, M.K. Lu, S.F. Wang, F. Gu, X.Z. Gai, X.P. Cui, J. Pan, Preparation and photocatalytic properties of Zr^{4+} -doped TiO_2 nanocrystals, *J. Mol. Catal. A Chem.* **215** (2004) 137−142.

(23) D.Y. Wang, H.C. Lin, C.C. Yen, Influence of metal plasma ion implantation on photo-sensitivity of anatase TiO_2 thin films, *Thin Solid Films* **515** (2006)

1047−1052.

(24) Y.R. Uhm, S.H. Woo, W.W. Kim, S.J. Kim, C.K. Rhee, The characterization of magnetic and photo-catalytic properties of nanocrystalline Ni-doped TiO_2 powder synthesized by mechanical alloying, *J. Magn. Magn. Mater.* **304** (2006) e781−e783.

(25) X. Li, R. Xiong, G. Wei, Preparation and photocatalytic activity of nanoglued Sndoped TiO_2, *J. Hazard. Mater.* **164** (2009) 587−591.

(26) L.G. Devi, B.N. Murthy, S.G. Kumar, Photocatalytic activity of TiO_2 doped with Zn^{2+} and V^{5+} transition metal ions: influence of crystallite size and dopant electronic configuration on photocatalytic activity, *Mater. Sci. Eng. B* **166** (2010) 1−6.

(27) J.J. Criado, B. Macias, V. Rives, Physicochemical properties of Cr/TiO_2 solid solutions, *React. Kinet. Catal. Lett.* **27** (1985) 313−316.

(28) K. Shiba, H. Hinode, M. Wakihara, Catalytic oxidation of NO to NO_2 over Cr/TiO_2 and Cu/TiO_2 under oxidizing atmosphere, *React. Kinet. Catal. Lett.* **58** (1996) 133−137.

(29) A. Ruiz, A. Cornet, G. Sakai, K. Shimanoe, J.R. Morante, N. Yamazoe, Preparation of Cr-doped TiO_2 thin film of P-type conduction for gas sensor application, *Chem. Lett.* (2002) 892.

(30) T. Sumita, T. Yamaki, S. Yamamoto, A. Miyashita, Photo-induced surface charge separation in Cr-implanted TiO_2 thin film, *Thin Solid Films* **416** (2002) 80−84.

(31) J. Zhu, Z. Deng, F. Chen, J. Zhang, H. Chen, M. Anpo, J. Hung, L. Zhang, Hydrothermal doping method for preparation of Cr^{3+}-TiO_2 photocatalysts with concentration gradient distribution of Cr^{3+}, *Appl. Catal. B Environ.* **62** (2006)

329−335.

(32) M.H. Chan, W.Y. Ho, D.Y. Wang, F.H. Lu, Characterization of Cr-doped TiO_2 thin films prepared by cathodic arc plasma deposition, *Surf. Coat. Technol.* **202** (2007) 962−966.

(33) R. Dholam, N. Patel, M. Adami, A. Miotello, Hydrogen production by photocatalytic water-splitting using Cr- or Fe-doped TiO_2 composite thin film photocatalyst, *Int. J. Hydrogen Energy* **34** (2009) 5337−5346.

(34) B.C. Lippens, J.H. de Boer, Studies on pore systems in catalysts V. The t method, *J. Catal.* **4** (1965) 319−323.

(35) T. Ishikawa, M. Wakamura, S. Kondo, Surface characterization of calcium hydroxyapatite by Fourier transform infrared spectroscopy, *Langmuir* **5** (1989) 140−145.

(36) L. Vayssieres, A. Manthiram, 2-D Mesoparticulate arrays of a-Cr_2O_3, *J. Phys. Chem. B* **107** (2003) 2623−2625.

(37) H. Xu, T. Lou, Y. Li, Synthesis and characterize of trivalent chromium $Cr(OH)_3$ and Cr_2O_3 microspheres, *Inorg. Chem. Commun.* **7** (2004) 666−668.

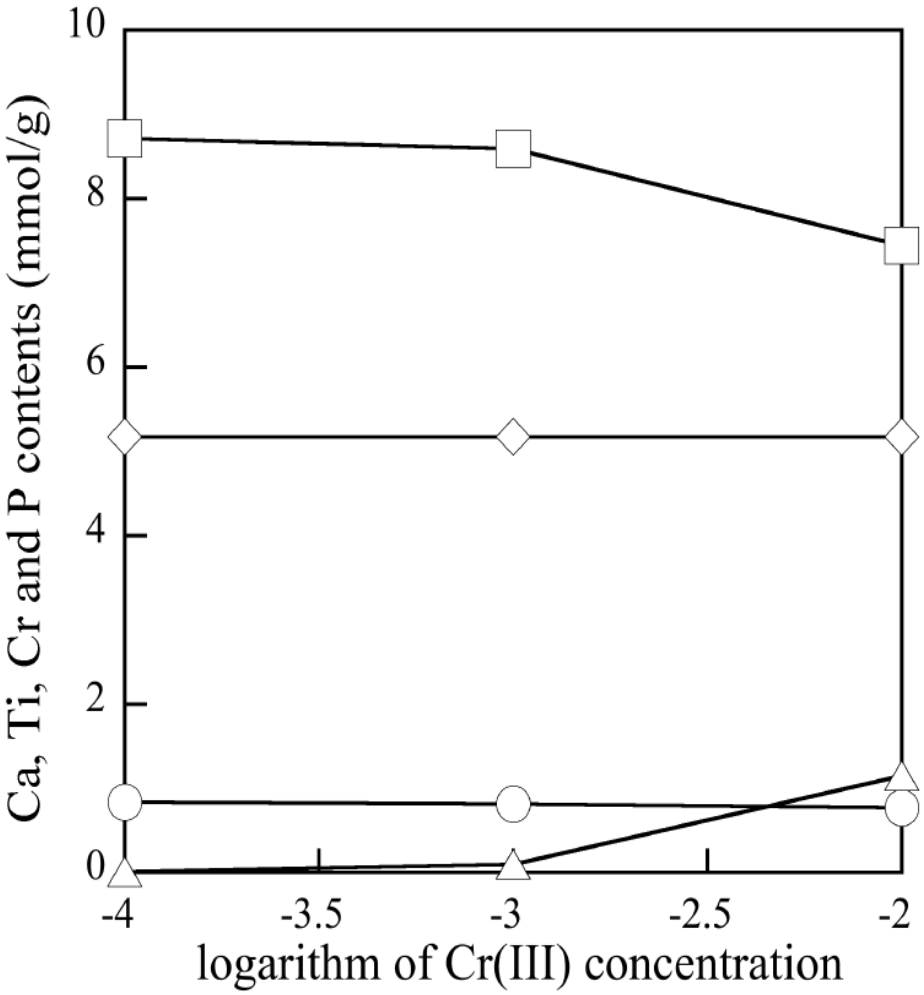

Figure 1 Plots of (□) Ca, (○) Ti, (△) Cr and (◇) P contents in the products as a function of Cr(III) concentration.

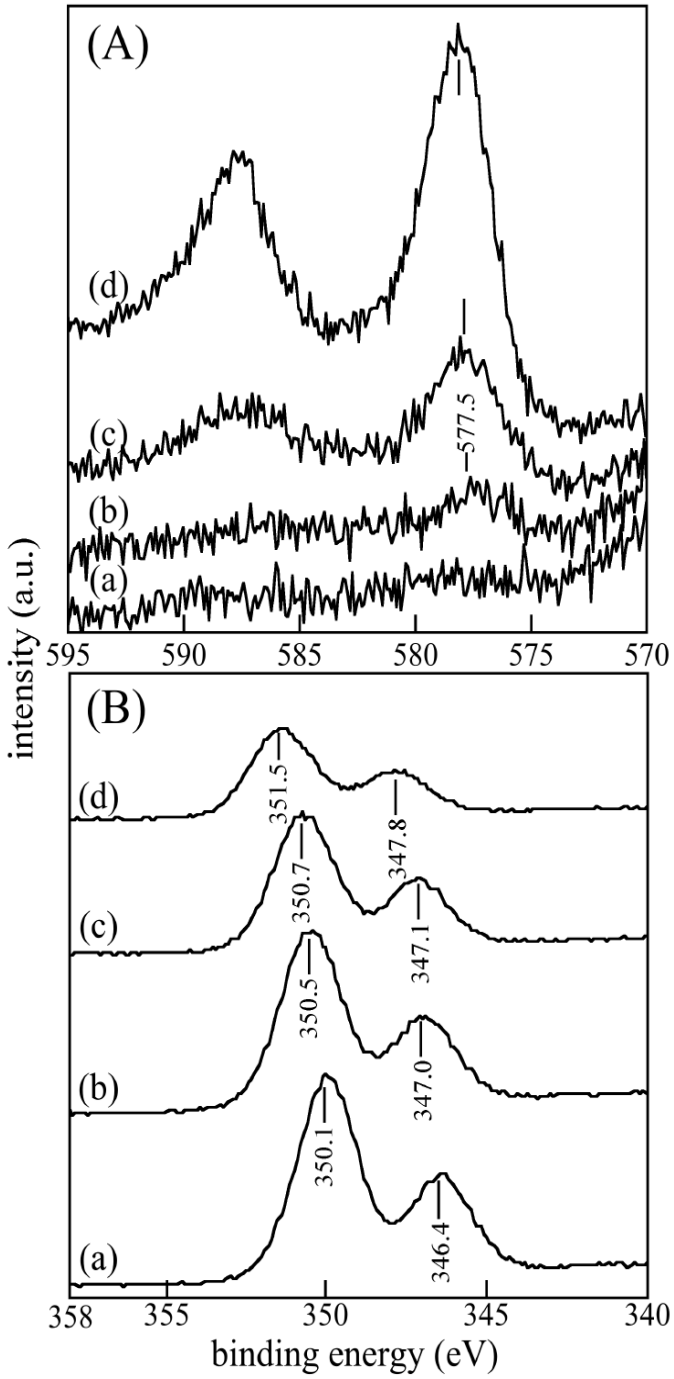

Figure 2 XPS spectra of (A) Cr2p and (B) Ca2P regions of Ti-CaHAp treated with various Cr(III) concentration (mol/dm^3): (a) 0, (b) 1.0 × 10^{-4}, (c) 1.0 × 10^{-3}, (d) 1.0 × 10^{-2}.

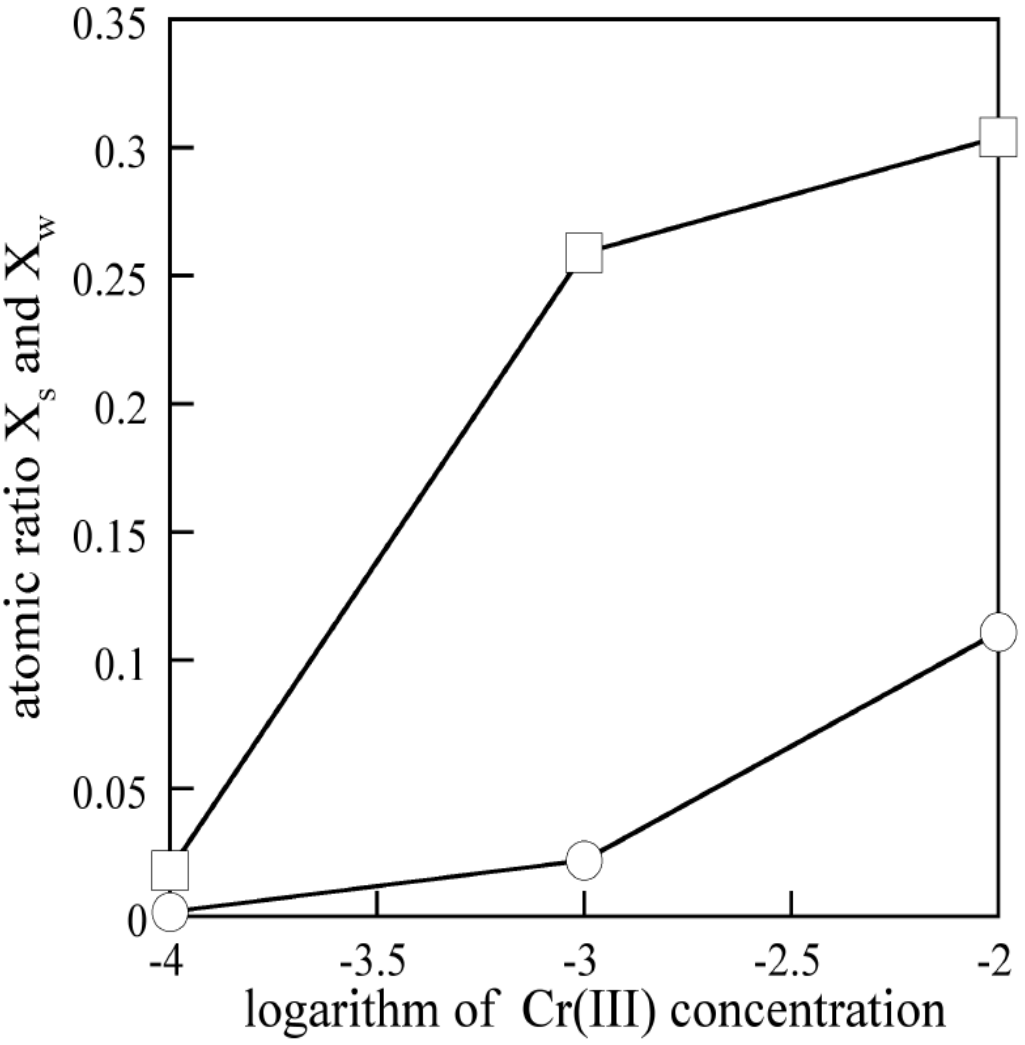

Figure 3 Plots of (□) Xs and (○) Xw against Cr(III) concentration.

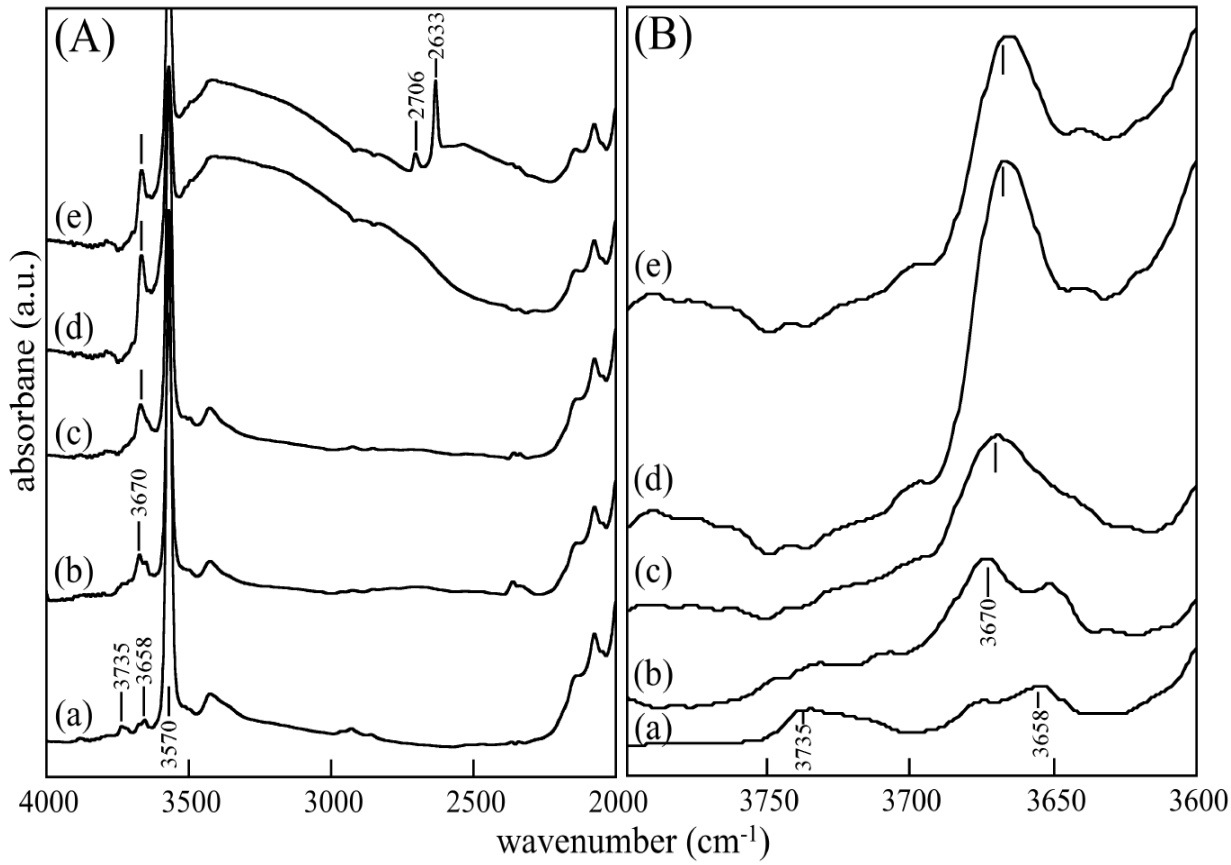

Figure 4 (A) IR spectra in vacuo of Ti-CaHAp modified with various Cr(III) concentration (mol/dm^3): (a) 0, (b) 1.0 × 10^{-4}, (c) 1.0 × 10^{-3}, (d) 1.0 × 10^{-2}. Spectrum (e) was taken after measuring the spectrum (d) and exposing the D_2O vapor for 1 h. (B) Expanded region of (A).

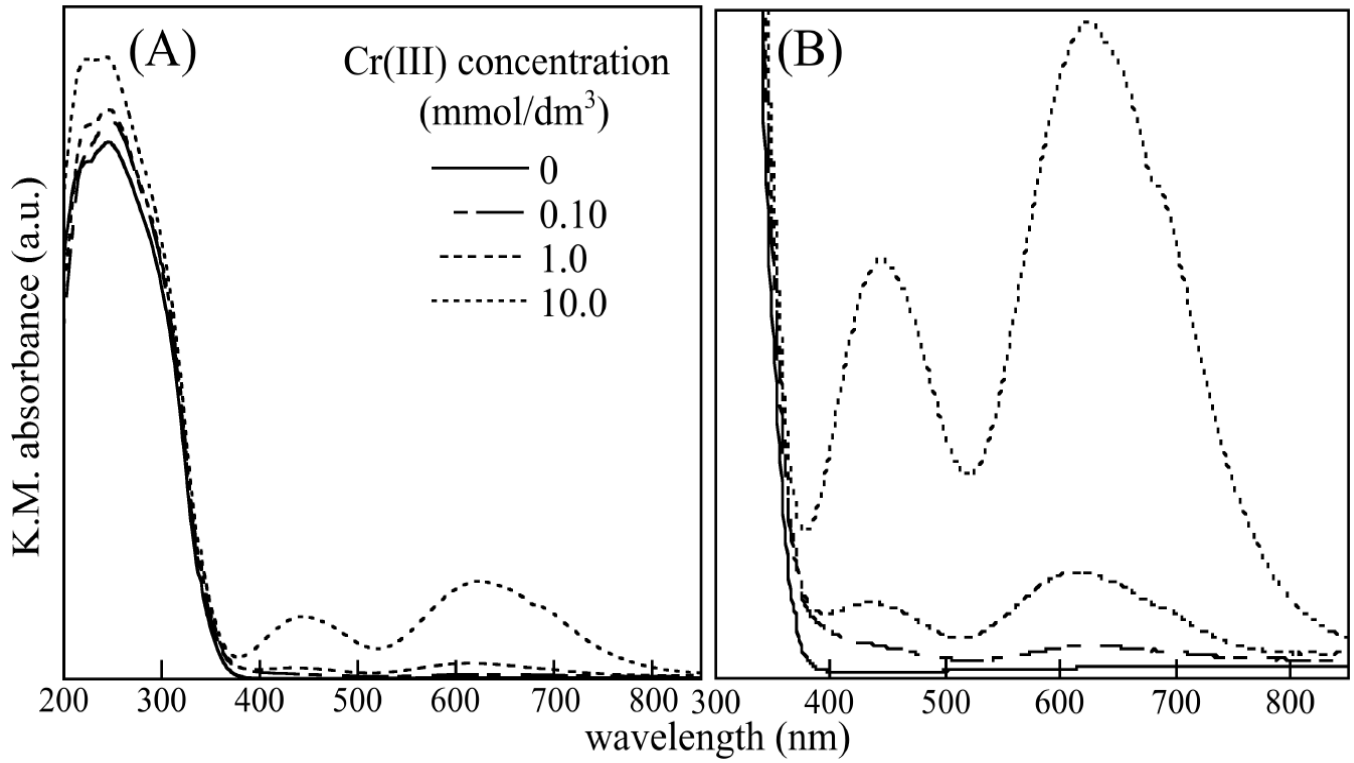

Figure 5 (A) Diffuse reflectance UV-VIS spectra of Ti-CaHAp treated with various Cr(III) concentrations . (B) Expanded region of (A).

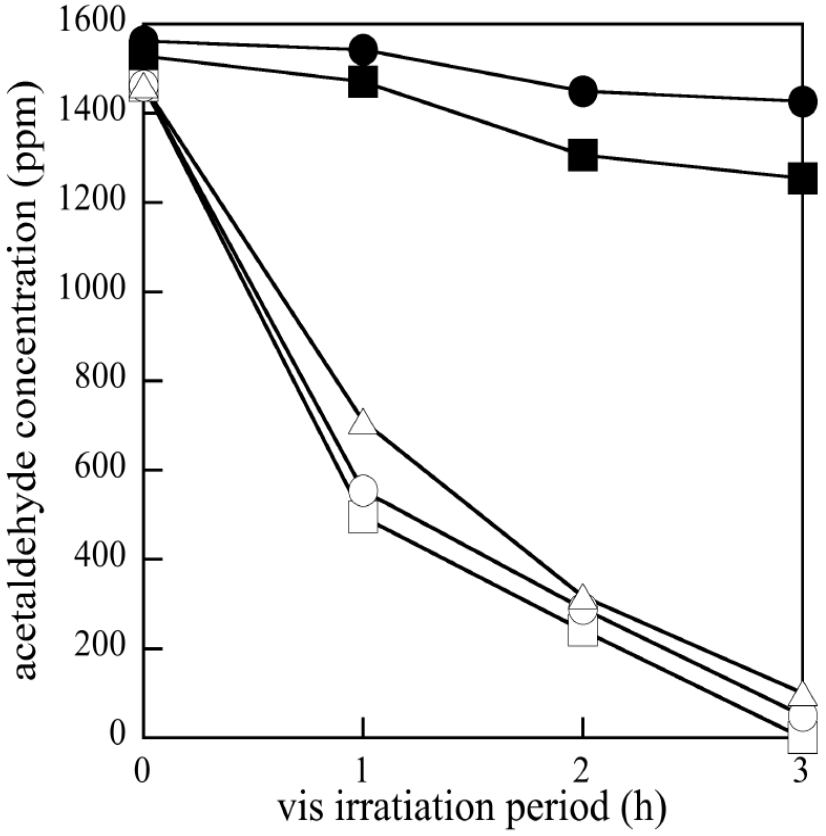

Figure 6 Plots of acetaldehyde concentration against VIS irradiation period. Cr(III) concentration (mol/dm^3): (■) 0, (□) 1.0×10^{-4}, (○) 1.0×10^{-3}, (△) 1.0×10^{-2} (●) $Cr(OH)_3$

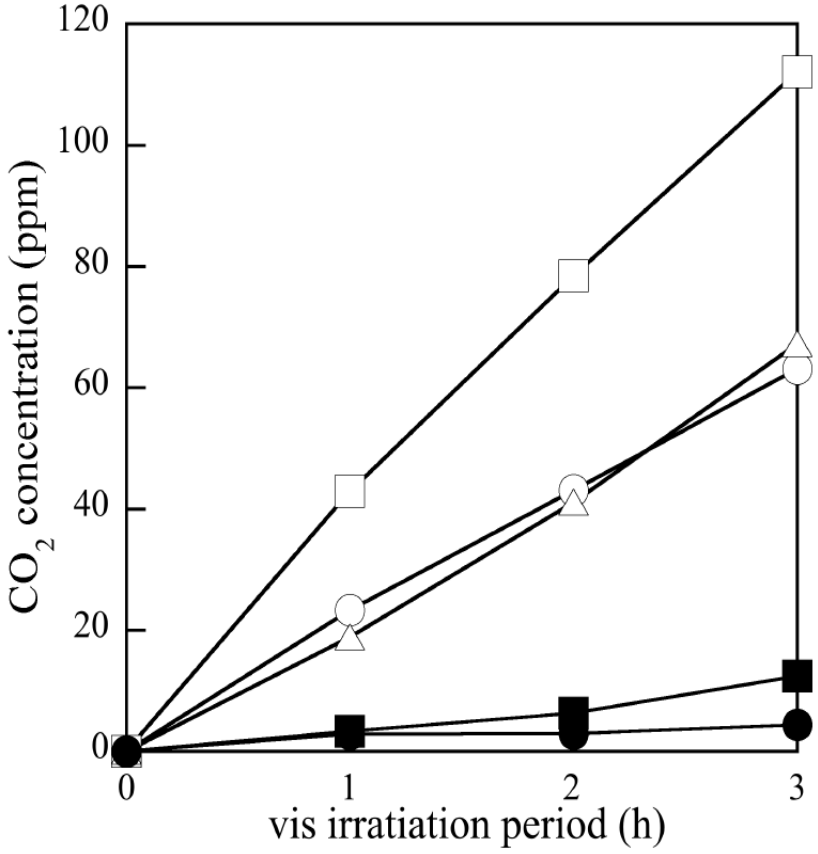

Figure 7 Plots of CO_2 concentration against VIS irradiation period. Cr(III) concentration (mol/dm^3): (■) 0, (□) 1.0×10^{-4}, (○) 1.0×10^{-3}, (△) 1.0×10^{-2} (●) $Cr(OH)_3$

CHAPTER 7

Antagonistic effect of Ti-doped hydroxyapatite for soft rot of moth orchid

7.1 Introduction

Soft rot disease is one of the main diseases of Phalenopsys. At the high temperature and humid environment, the soft rot bacterium (Pectobacterium carotovorum subsp. carotovorum) invades into the internal texture from the wound of leaf and root of Phalenopsys, and they infect and grow to attack the soft rot disease. The soft rot disease shows the symptom that the leaf rots to be water-soaked [(1)]. (Figure 1)

The disease control is difficult by spraying agents due to the fast infection so that the attack is enlarged over the field. A general preventing method is to remove and dispose the infected plants outside the field, but it is big problem for the cultivating famers. The method of spraying agent is insufficient, so it is required to establish new soft rot antagonistic technology.

The material that inactivates and decomposes the bacterium is adhered when pathogenic bacteria adsorb the surface of leaf and root and inhibits the invasion of bacillus is expected to show the soft rot antagonistic effect. The photocatalyst is well known as an inactivation technology of the phytopathogenic bacteria, and is thought to be used for controlling the plant disease. Titanium dioxide of the most universal photocatalyst material is investigated to use for waste disposal of water culture and decomposition of residual agricultural chemicals. However, there is no report on the

application of TiO_2 to the disease control because this material shows low adsorption ability to the microorganism and low disease control effect [2], [3]. On the other hand, calcium hydroxyapatite that is a kind of calcium phosphate is a mineral composition of human tooth and bone, and its property is easily modified by the ion-exchange with various transition metal ions [4] - [8].

The titanium apatite of a new photocatalyst material is synthesized by substituting a part of calcium ion with titanium ion. It shows the photocatalystic decomposition effect as same as TiO_2 to organisms of proteins, virus, bacillus, and allergen materials which are adsorbed more strongly than TiO_2 [9]. The air cleaning filter, the face mask inhibiting infection, and the antimicrobe cutting board, etc. have been sold as products using titanium apatite.

The present study is intended to apply titanium apatite, which shows high adsorption affinity and antibacterial effects, for the antagonistic technology of the Phalenopsys soft rot.

7.2 Experiment

7.2.1 Bacterium and plants

The soft rot bacterium (Erwinia carotovora PhT0510-4) was obtained by centrifugal separation from the contraction lobus collected in the cultivating field in Kochi Prefecture, Suzaki City in October, 2005. Phalenopsys (AMP17) uniformly grown was bought from cultivating farmers.

7.2.2 In vitro antimicrobial activity test to Phalenopsys soft rot bacterium

PhT0510 was cultured in the NA agar plate medium at 30 °C for 16-20 hours and the culture. The fungus liquid of 10^4 bacterium /ml was prepared by inoculating the bacterium into the 1/500 NA medium which was prepared by diluting nutrient broth with phosphate buffer solution by 500 times and adjusting to pH 7.0.

Titanium apatite (Taihei Chemical Industry, PHOTOHAP), hydroxyapatite (Taihei Chemical Industry, HAP100), TiO_2 (Ishihara Sangyo, ST21), and the copper ion antibiotic (Nihon Nohyaku, Z Bordeau copper solution) were respectively dispersed in 1/500 NA medium at 10 mg/ml to obtain 10 ml suspensions. The testing solution was made by inoculate 0.1 ml fungus liquid to 10 ml suspension. The testing solution was shaken at room temperature for 6 hours under shading and irradiating UV at 1 mW/cm^2. The plate count in the testing solution was measured by cultivating in the pour-plate cultivating method at 30 °C for 2 days using the SCDLPA ager medium (Japan Pharmaceutical). The initial plate count was measured as the reference by the similar test method using 1/500 NA medium.

7.2.3 Preventive effect test of Phalenopsys soft rot

The Phalenopsys cultivating section in the glass greenhouse made of aluminum (13.4 m^2 in area) was divided into different spraying processing of titanium apatite, hydroxyapatite, TiO_2, agricultural chemicals, and no processing, and Phalenopsys was grown by 30 stubs in each section. (Figure 2, 3) The aqueous dispersions of 10 mg/ml were prepared from each powder of titanium apatite, hydroxyapatite, and TiO_2. The copper ion system antibiotic solution was prepared by diluting by 500 times with water. Each aqueous dispersion was sprayed by a sprayer. The volume of spray was 100 ml/stub. The soft rot bacterium used was the same strain as an in vitro test. The soft rot

bacterium was cultivated for 6 days with the NA medium in dark place at 25 °C, and diluted to about 1×10^8 CFU with the sterilized water. After spraying 50 ml aqueous dispersion on the leaves of one stub, 10 places were damaged on the leaves by the sterilized needle. After 6 days at damage on the leaves, the number of attack parts to that of wound parts was counted and the disease percentage and preventive value were calculated from the following equation.

Disease percentage = (number of attack part ÷ number of damage parts) × 100

Preventive value = (1 - (process zone disease percentage ÷ no processing disease percentage)) × 100

This test was repeated 4 times and the cross table was made by the presence and absence of the chemical spray and those of the disease attack. (Table 2) The predominant property of the beneficial effect is verified according to the accurate probability assay of Fisher as is seen Table 3.

7.2.4 Curative effect test of Phalenopsys soft rot

Phalenopsys of 4 stubs were grown in the glass greenhouse made of aluminum (13.4 m^2 in area) without spraying process. The same strain as in vitro test was used. The soft rot bacterium was cultivated in the NA medium at the dark place at 25 °C for 5 days and diluted to about 1×10^8 CFU with sterilized water. After spraying 50 ml aqueous dispersion on the leaves of one stub, 10 places were damaged on the reaves by the sterilized needle. Three kinds of aqueous dispersions (3 %) prepared respectively from

titanium apatite, hydroxyapatite, and TiO_2 were sprayed to 3 stubs of the soft rot attack. A change with time of the diseased area after spraying the aqueous dispersion was observed for 2 days. The lesion area of attack part was calculated and compared in order to assess the curative effect quantitatively.

7.3 Results and discussion

7.3.1 In vitro antimicrobial activity against Phalenopsys soft rot bacterium

In case of titanium apatite, the plate count of soft rot bacterium at the start of light illumination (noted CSI bellow) was 7.9×10^5 pieces/ml and became below the detection limit after 6 hr. In the reference sample without titanium apatite, the plate count after 6 hr (noted C6 bellow) was 6.1×10^5 pieces/ml and did not almost change. Therefore, it is thought that the antibacterial effect of titanium apatite is caused by not ultraviolet but photocatalysis. On using hydroxyapatite, CSI shows that 8.1×10^5 pieces/ml and C6 is 5.5×10^5 pieces/ml that means no antibacterial effect. When TiO_2 was used, CSI was 8.1×10^5 pieces/ml and C6 is 1.1×10^3 pieces/ml, meaning that the decrease of plate count is due to the antibacterial effect by photocatalysis of TiO_2. In the system of copper ion antibacterial agent, CSI was 8.1×10^5 pieces/ml, and C6 became below the detection limit. Accordingly, titanium apatite shows the antimicrobial activity as well as the copper ion antibiotic agent, whereas no antimicrobial activity was detected in case of hydroxyapatite.

7.3.2 Preventive effect against Phalenopsys soft rot

Without spraying, the number of attack parts in all of the damaged parts (40 places)

(noted NAP hereafter) was 27 places, and the number of no attack place (noted NA hereafter) was 13 places. On spraying titanium apatite, NAP was 4 places, and NA was 36 places. The accurate precedence probability (noted APP hereafter) calculated from these data was 0.00 (both sides) and 0.00 (one side). Using hydroxyapatite gave NAP of 13 places, NA of 27 places, and APP of 0.030 (both sides) and 0.020 (one side). In case of TiO_2, NAP of 15 places, NA of 25 places, and APP of 0.013 (both sides) and 0.007 (one side) were obtained. On spraying the copper ion antibacterial agent, NAP and NA were 9 and 31 places, respectively and APP was 0.00 (both sides) and 0.00 (one side). The results mentioned above indicate that titanium apatite shows the same preventive effect as a copper ion antibiotic (pesticide) on Phalenopsys soft rot bacterium.

7.3.3 Phalenopsys soft rot curative effect test

The results are shown in Table 4. In case of hydroxyapatite, the lesion area was 52.00 cm^2 at first, 60.03 cm^2 after one day, and 82.20 cm^2 after 2 days. On spraying titanium dioxide the initial lesion area was 92.00 cm^2 at first, 114.40 cm^2 after one day, and 159.20 cm^2 after 2 days. These results indicate that all agents used in this study are not able to stop the increase of lesion area. Thus, it is important to prevent the invasion of bacterium from the wound of rots for the control of soft rot. After the bacterium invades, the disease progression is not inhibited by spraying agents. The sterilization and the suppression of bacterial growth by the photocatalyst prevent the invading of bacterium and control the accrual of soft rot. A high antagonistic effect can be expected by spraying titanium apatite as a precaution before attack.

7.4 Conclusion

It is important to inhibit the breeding of soft rot bacterium on the leaves and the invasion from the wound in order to prevent the soft rot. The antagonistic effect was observed by testing the prevention of breeding and extermination in the greenhouse though there was no photocatalystic antibacterial effect in hydroxyapatite in the in vitro test. The calcium phosphates such as apatites have high affinity for the protein and excellent adsorptivity. It was guessed that the invasion of the bacterium from the wound was effectively prevented according to an excellent adsorption affinity to the bacterium of hydroxyapatite and titanium apatite leading to controlling the attack of soft rot. Especially, a comparable antagonistic effect was exerted on the pesticide because the titanium apatite has the photocatalystic effect. In conclusion, titanium apatite with a strong sorption property and the antibacterial effect on protein shows remarkable antagonistic effect to Phalenopsys soft rot.

References

(1) Kishi, K., Phalenopsys soft rot, *Japanese plant disease cyclopedia* (1998) 722.

(2) Fujishima, A., Zhang, A., Tryk, D. A., TiO_2 Photocatalysis and Related Surface Phenomena, *Surface Science Reports,* **63** (2008) 515-582.

(3) Hashimoto, K., Otani, B., Kudoh, A., Photocayalysis, Basic, Material Development, application (2005) 987-1004.

(4) Ishikawa, T., Wakamura, M. and Kondo, S., Surface Characterization of Calcium Hydroxyapatite by Fourier Transform Infrared Spectroscopy, *Langmuir* **5** (1989) 140-144.

(5) Ishikawa, T., Wakamura, M., Kawase, T. and Kondo, S., Surface Characterization

by X-ray Photoelectron Spectroscopy and Fourier Transform Infrared Spectroscopy of Calcium Hydroxyapatite Coated with Silicate Ions, *Langmuir* **7** (1991) 596-599.

(6) Wakamura, M., Kandori, K. and Ishikawa, T., Influence of chromium(Ill) on the formation of calcium hydroxyapatite, *Polyhedron*, **16**, 12 (1997) 2047-2053.

(7) Wakamura, M., Kandori, K., Ishikawa, T., Surface composition of calcium hydroxyapatite modified with metal ions. *Colloids and Surfaces A: Physicochemical and Engineering Aspects,* **142** (1998) 107–116.

(8) Wakamura, M., Kandori, K., Ishikawa, T., Surface structure and composition of calcium hydroxyapatites substituted with Al(III), La(III) and Fe(III)ions. *Colloids and Surfaces A: Physicochemical and Engineering Aspects,* **164** (2000) 297–305.

(9) Wakamura, M., Hashimoto, K., Watanabe, T., Photocatalysis by Calcium Hydroxyapatite Modified with Ti(IV): Albumin Decomposition and Bactericidal Effect. *Langmuir*, **19** (2003) 3428-3431.

(10) Kandori, K., Protein adsorption to Calcium Hydroxyapatite: *PHOSPHORUS LETTER*, **27** (1996) 12-16.

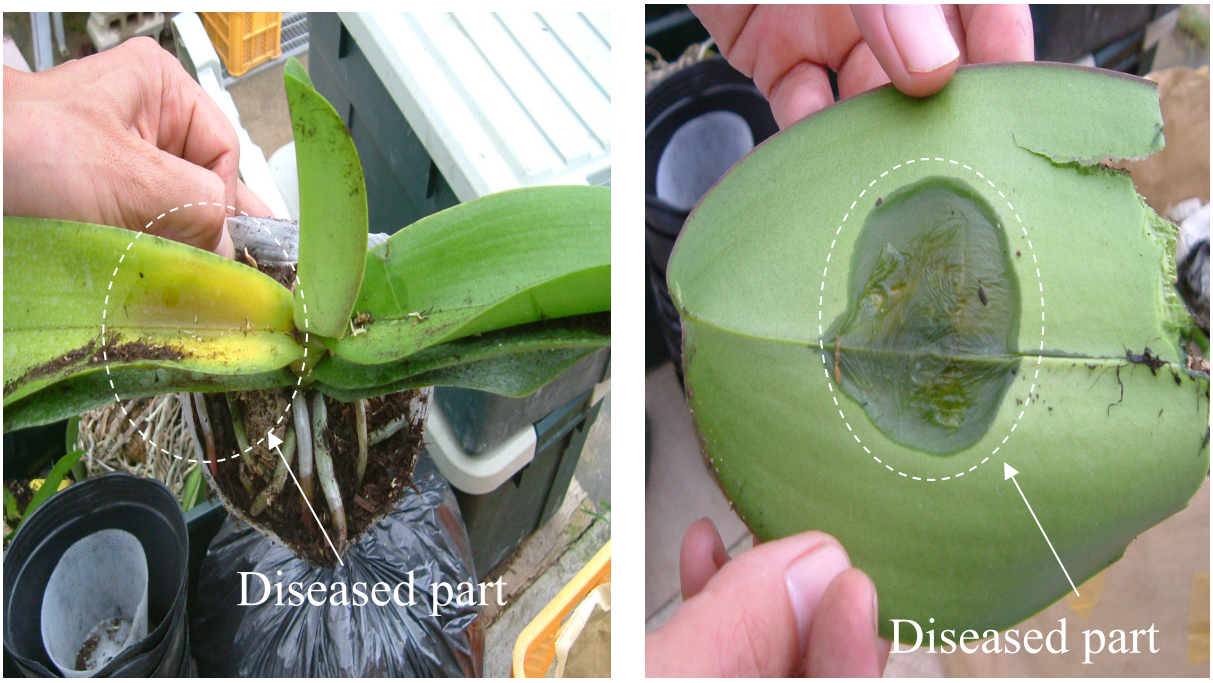

Figure 1 Soft rot disease of Phalenopsys

Tabele 1 In vitro antimicrobial activity test to Phalenopsys soft rot bacterium.

<10 : undetectability

agent		Plate count of start time	Plate count of 6h later
Agar media only irradiate	UV	8.1E+05	8.6E+05
	Keep in dark	5.4E+05	1.1E+06
Titanium apatite（10 mg/ml)	UV irradiate	7.9E+05	<10
	Keep in dark	2.6E+06	8.1E+05
Hydroxylapatite（10 mg/ml)	UV irradiate	8.1E+05	5.5E+05
	Keep in dark	5.4E+05	2.6E+06
Titanium dioxide（10 mg/ml)	UV irradiate	8.1E+05	1.1E+03
	Keep in dark	5.4E+05	1.4E+06
Copper ion system antibiotic (× 500)	UV irradiate	8.1E+05	<10
	Keep in dark	5.4E+05	<10

Japan Food Research Laboratories
Report No. 207060741-002 & 208111004-001

Glass greenhouse

Phalenopsys stub

Figure 2　Preventive effect test of Phalenopsys soft rot (1)

Titanium hydroxyapatite spraying zone

Sparger

Hydroxyapatite spraying zone

Copper ion system antibiotic

Titanium dioxide spraying zone

Copper ion system antibiotic spraying zone

No processing zone

Figure 3　Preventive effect test of Phalenopsys soft rot (2)

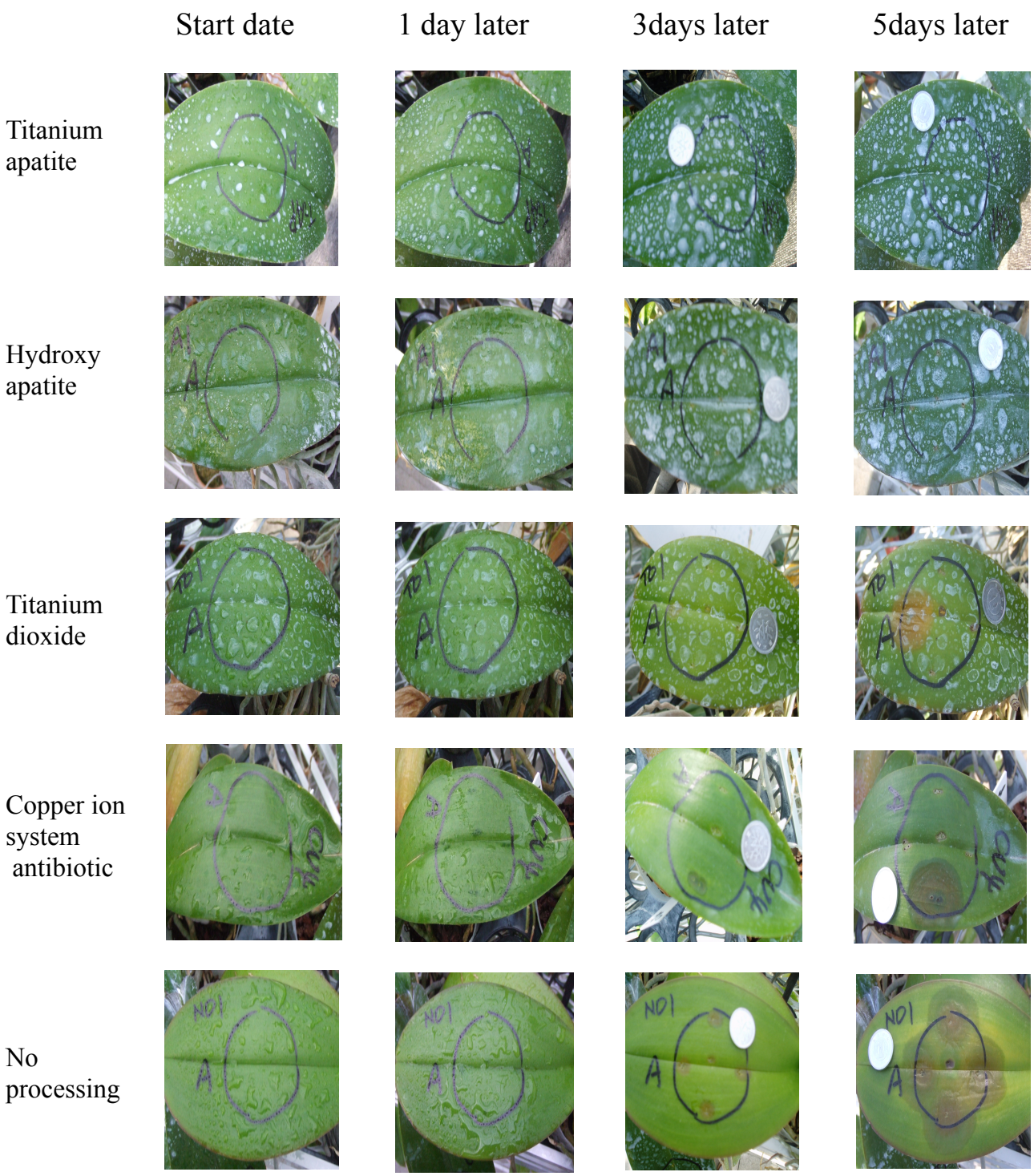

Figure 4 Results of preventive effect test of Phalenopsys soft rot

Table 2 Antagonistic effect test to Phalenopsys soft rot of various agents

Agent（concentration）		Number of attack parts of 6 days later to 10 damage parts			
		Repeat 1	Repeat 2	Repeat 3	Repeat 4
Titanium apatite (10 mg/ml)	Number of attack part	0	2	2	0
	Disease percentage (%)	0	20	20	0
	Preventive value	100	33	75	100
Hydroxyapatite (10 mg/ml)	Number of attack part	1	3	3	6
	Disease percentage (%)	10	30	30	60
	Preventive value	89	0	63	14
Titanium dioxide (10 mg/ml)	Number of attack part	3	3	3	6
	Disease percentage (%)	30	30	30	60
	Preventive value	67	0	63	14
Copper ion system antibiotic（×500）	Number of attack part	0	3	5	1
	Disease percentage (%)	0	30	50	10
	Preventive value	100	33	75	100
No processing	Number of attack part	9	3	8	7
	Disease percentage (%)	90	30	80	70

Test place：Fujitsu Akashi factory
Number of stub：4
Number of damage part：10/stub

Table 3 Statistical analysis on antagonistic effect test result

Agent (concentration)	Statistical analysis on number of attack parts of 40 damage parts by repeat at 4 times (Fisher straight line method)			
	No attack	attack	Accurate precedence probability(both side)	Accurate precedence probability(one side)
Titanium apatite (10 mg/ml)	36	4	0.000	0.000
Hydroxyapatite (10 mg/ml)	27	13	0.030	0.020
Titanium dioxide (10 mg/ml)	25	15	0.013	0.007
Copper ion system antibiotic (×500)	31	9	0.000	0.000
No processing	13	27	——	——

Table 4 Lesion progress suppression effect with chemical spray after attack

Agent (concentration)	Start date	1 day later	2 days later
	Lesion area（cm^2）	Lesion area（cm^2）	Lesion area（cm^2）
Titanium apatite (10 mg/ml)	53.23	88.30	166.00
Hydroxyapatite （10 mg/ml）	52.00	60.03	82.80
Titanium dioxide （10 mg/ml）	76.80	95.80	128.00
No processing	92.00	114.40	159.20

CHAPTER 8

Summary

8.1 Results and Conclusion

Synthetic calcium hydroxyapatite $Ca_{10}(PO_4)_6(OH)_2$, referred to as hydroxyapatite (CaHAp), would easily undergo Ca^{2+} ion exchange with various transition metal ions giving various materials with different properties. CaHAp shows excellent affinity to bio-organic materials such as proteins, viruses and bacteria. In this study, we focused to a develop novel photocatalyst with high affinity to biomaterials by atomic level composition modification of photocatalytic CaHAp particles with Ti(IV) ions. This modification of CaHAp particles was performed by co-precipitation methods.

A general overview of the chemistry of CaHAp, colloid and surface chemistry in particular, is given in this chapter. In the beginning, an account on the previous work of widely studied photocatalyst titanium dioxide, especially on fundamental studies, property enhancements and approaches for application in environmental purification is presented. Further, present technology issues of titanium dioxide and the importance of development of alternative materials are also discussed. Finally, the objectives of this study and our research strategy on photocatalst development are explained.

CaHAp particles were modified with Ni^{2+}, Cu^{2+}, Co^{2+} and Cr^{3+} ions by ion exchange and co-precipitation methods. The CaHAps doped with these ions were characterized by various analytical methods including FTIR, XPS, TEM and ICP. The atomic ratio of the exchanged metal ions, metal/(Ca+metal), of the surface phase (X_s) of the particles modified with Ni^{2+} and Cu^{2+} by co-precipitation were much less than that of the whole

particle (X_w), while the X_s of the particles modified with Cr^{3+} was roughly equal to their X_w. In the case of ion exchange modification, X_s was larger than X_w, except for the Ni^{2+} substituted samples, where X_s was identical to X_w. The population of the surface P–OH group has decreased due to cation exchange of the protons of the P–OH groups with Ni^{2+}, Cu^{2+} and Co^{2+} in both modification methods. On the other hand, Cr^{3+} ions selectively exchanged with Ca^{2+} ions in the surface phase by anion exchange of the surface phosphate ions with hydrated chromium hydroxide anions. CaHAp particles were also modified by ion-exchange with Al^{3+}, La^{3+} and Fe^{3+} by co-precipitation and immersion methods. The growth of CaHAp particles was observed on substituting with these metal ions by co-precipitation. The exchange ratios of Ca^{2+} with the metal ions revealed that Fe^{3+} replaces Ca^{2+} as hydroxo ions, and the substitution with La^{3+} accompanies OH^- deficiency. In the case of immersion substitution, the exchange ratios for all the metal ions were less than the theoretical ratio of 1.5, verifying the exchange with metal hydroxo ions. IR spectra of the CaHAp particles substituted by Al^{3+} in both methods exhibited several peaks due to surface Al-OH, besides the surface P-OH peaks, whereas the CaHAp substituted with La^{3+} showed no surface La-OH bands. The surface Fe-OH was found on the CaHAps substituted by the co-precipitation, but not on those substituted by the immersion.

CaHAp samples doped with Ti(IV) ions in different atomic ratios (X_{Ti}) by co-precipitation method were characterized by TEM, UV, FTIR, XPS, and ICP-AES. The photocatalytic activity of the modified CaHAp samples was examined by decomposition of acetaldehyde and albumin, and colon bacillus antibacterial test. The Ca(II) of CaHAp was one-to-one substituted by Ti(IV) at $X_{Ti} = 0.1$. In these samples, when X_{Ti} is greater than 0.1, irregular particles of amorphous titanium phosphate have

formed, besides long rectangular particles of CaHAp. The X_{Ti} of the surface phase of the particles was much lower than that of the whole particles. The Ti(IV) content in the surface phase was found to be smaller than that of the bulk material. From UV-VIS measurements on undoped and Ti-doped samples, it was found that only the Ti(IV) modified CaHAp samples exhibited UV absorption. Also, photo-catalytic studies revealed that Ti-doped samples can readily decompose acetaldehyde and albumin upon irradiation. Furthermore, theses samples showed antibacterial activity even in the dark, unlike TiO_2 that does not exhibit antibacterial activity under this condition.

Highly transparent films with a very little color interference were prepared form the novel apatite-based photocatalyst of Ti(iV) doped CaHAp (Ti-CaHAp) by wet process. SEM, XPS, and UV-VIS investigations revealed that the obtained films have properties similar to that of the Ti-CaHAp power. The films showed photocatalytic activity against adsorbed Methylene Blue and vaporized isopropyl alcohol, but did not exhibit photo-induced hydrophilicity.

The effect of Ti-substitution in CaHAp on the band gap of CaHAp was evaluated experimentally and theoretically using three samples, namely CaHAp, 10 mol% Ti substituted CaHAp prepared by co-precipitation and commercially available anatase TiO_2 photocatalytic powder. X-ray diffraction patterns showed that both CaHAp and Ti-CaHAp have a hexagonal apatite structure. The experimentally obtained optical band gap energies of Ti-CaHAp, CaHAp and TiO_2 powder measured by diffuse reflectance spectroscopy were 3.65 eV, 6 eV and 3.27 eV, respectively. Depending on the total energy evaluation and structure optimization by the first principle density functional calculation, the Ti position in the apatite structure was predicted to be at columnar Ca(I) sites, the sites with Ca(I) site deficiency. In Ti-CaHAp, Ti-3d orbitals hybridized with

O-2p orbitals to form an internal state in the CaHAp band gap, causing absorption edge lowering of Ti-CaHAp. Based on the band structure, we proposed a photocatalytic model of Ti-CaHAp as a two-step excitation model. Moreover, acetaldehyde gas decomposition efficiency of Ti-CaHAp upon UV-VIS irradiation appeared to enhance compared with UV irradiation alone. From this observation, we confirmed the validity of the proposed band gap model.

Ti-CaHAp particles were treated with different concentrations of aqueous $Cr(NO_3)_3 \bullet 9H_2O$ solutions and the obtained materials were characterized by a variety of conventional methods. The crystal structure and particle morphology of the Ti-CaHAp were not necessarily altered by treating with Cr(III) solutions. Here, with increasing the Cr(III) concentration, the amount of Cr(III) in the products increased and that of the Ca(II) decreased. XPS results revealed that the valency of the Cr ions in surface layer of Ti-CaHAp was trivalent. These facts allow us to postulate that Cr(III) substitution occurred at the Ca(II) sites of the Ti-CaHAp surface. Besides, IR results proved that increasing the Cr(III) concentration enhanced the surface Cr-OH band while the surface Ti-OH and P-OH bands of Ti-CaHAp disappeared. This suggests that the formation of surface P-O-$Cr(OH)_2$ and Ti-O-$Cr(OH)_2$ groups, resulting a $Cr(OH)_3$-like layer on the surface of the Ti-CaHAp particles. The Cr(III)-doped Ti-CaHAp showed absorption peaks at 446 and 623 nm in the VIS range in addition to the UV absorption of charge transfer transition of $O^{2-} \rightarrow Ti^{4+}$. The VIS absorption peaks enhanced on raising the Cr(III) concentration. The photocatalytic decomposition of acetaldehyde into CO_2 over Cr(III)-doped Ti-CaHAp was detected under VIS irradiation, and the activity weakened due to the formation of $Cr(OH)_3$-like layer on the particle surface.

In order to develop a control system for soft rot disease of Moth orchid caused by

Pectbacterium Carotovorum subsp. Carotovorum, the effectness of Ti-CaHAp was evaluated by in vitro test and field test in a glass greenhouse. This study revealed that Ti-CaHAp has an antagonistic effect similar to pesticides due to photocatlytic activity of the material. Therefore, this material is expected to be useful as a new bio-control agent.

From computer simulation studies it can be verified that the appearance of photocatalytic activity in Ti-CaHAp is due to the formation of hybrid orbitals between the titanium atoms and oxygen atoms of the phosphate ion. However, the photocatalytic efficiency of hydrothermally synthesized Ti-CaHAp was found to lower than that of titanium dioxide. Thermal analysis results indicated that a large amount of crystallization water remained in the crystals, and thermal treatment above 650 °C is necessary to evaporate this water. By thermal treatment above 650 °C, the photocatalytic activity of Ti-CaHAp can be improved to the same level of titanium. This result suggests that the crystallization water of Ti-CaHAp would inhibit the formation of hybrid orbitals between the titanium ion and the oxygen atom of the phosphate ions. In order to achieve a high photocatalytic activity in Ti-CaHAps, it is necessary to promote the formation of hybrid orbitals between the titanium ions and the oxygen atoms of phosphate ions.

8.2 Future works

In this study, physical property improvement of CaHAp was conducted by using the cation exchange property of CaHAp. As a result, it was found that when the CaHAp crystals were doped with titanium ions, the new material exhibited photocatalyst activity. Moreover, it was understood that physical properties of the material can be

predicted and controlled through computer simulations. The development of highly reliable synthesis technologies for the designed materials remains the future task of this study. If we see a success in this task, it will pave the way to develop new materials with new and advanced functionalities within a short period of time.

List of Publication

Published papers

1) K. Kandori, M. Oketani, **M. Wakamura**; "Effects of Ti(IV) Substitution on Protein Adsorption Behaviors of Calcium Hydroxyapatite Particles", *Colloids and Surfaces B: Biointerfaces*, **101**, 68-73 (2013).
2) K. Kandori, M. Oketani, Y. Sakita, **M. Wakamura**; "FTIR Studies on Photocatalytic Activity of Ti(IV)-doped Calcium Hydroxyapatite Particles", *Journal of Molecular Catalysis A: Chemical*, **360**, 54-60 (2012).
3) K. Kandori, T. Kuroda, **M. Wakamura**; "Protein Adsorption Behaviors onto Photocatalytic Ti(IV)-doped Calcium Hydroxyapatite Particles", *Colloids and Surfaces B: Biointerface*, **87**, 472-479 (2011).
4) M. Tsukada, **M. Wakamura**, N. Yoshida, T. Watanabe; "Band Gap and Photocatalytic Properties of Ti-Substituted Hydroxyapatite: Comparison with Anatase-TiO_2", *Journal of Molecular Catalysis A: Chemical*, **338**, 18-23 (2011).
5) **M. Wakamura**, H. Tanaka, Y. Naganuma, N. Yoshida, T. Watanabe; "Surface Structure and Visible Light Photocatalytic Activity of Titanium–Calcium Hydroxyapatite Modified with Cr(III)", *Advanced Powder Technology*, **22**, 498-503 (2011).
6) K. Kandori, S. Toshima, **M. Wakamura**, M. Fukusumi and Y. Morisada; "Effects of Modification of Calcium Hydroxyapatites by Trivalent Metal Ions on the Protein Adsorption Behavior", *Journal of Physical Chemistry B*, **114**, 2399-2404 (2010).
7) N. Yoshida, M. Takeuchi, T. Okura, H. Monma, **M. Wakamura**, H. Ohsaki, T. Watanabe; "Super-Hydrophobic Photocatalytic Coatings utilizing Apatite-based Photocatalyst", *Thin Solid Films*, **502**, 108-111 (2006).
8) N. Yoshida, T. Ishida, C. Saiki, **M. Wakamura**, H. Osaki, K. Hashimoto, T. Watanabe; "Preparation of Transparent Thin Film of Novel Apatite-based Photocatalyst", *Chemistry Letters*, **34**, 1666-1667 (2005).
9) **M. Wakamura**, K. Hashimoto, T. Watanabe; "Photocatalysis by Calcium Hydroxyapatite Modified with Ti(IV): Albumin Decomposition and Bactericidal Effect", *Langmuir*, **19**, 3428-3431 (2003).

10) **M. Wakamura**, K. Kandori, T. Ishikawa; ”Surface Structure and Composition of Calcium Hydroxyapatites Substituted with Al(III), La(III) and Fe(III) ions”, *Colloids and Surfaces A: Physicochemical and Engineering Aspects*, **164**, 297-305 (2000).

11) **M. Wakamura**, K. Hashimoto, T. Watanabe; “Surface Structure and Photocatalysis of Calcium Hydroxyapatite Modified with Titanium ions”, *Phosphorus Research Bulletin*, **10**, 323-328 (1999).

12) **M. Wakamura**, K. Kandori, T. Ishikawa; “Surface composition of Calcium Hydroxyapatites Modified with Metal ions”, *Colloids and Surfaces A: Physicochemical and Engineering Aspects*, **142**, 107-116 (1998).

13) **M. Wakamura**, K. Kandori, T. Ishikawa; “Influence of Chromium(III) on The Formation of Calcium Hydroxyapatite”, *Polyhedron*, **16**, 2047-2053 (1997).

14) T. Ishikawa, **M. Wakamura**, T. Kawase, S. Kondo; “Surface Characterization by X-ray Photoelectron Spectroscopy and Fourier Transform Infrared Spectroscopy of Calcium Hydroxylapatite Coated with Silicate Ions”, *Langmuir*, **7**, 596-599 (1991).

15) T. Ishikawa, **M. Wakamura**, S. Kondo: “Surface Characterization of Calcium Hydroxylapatite by Fourier Transform Infrared Spectroscopy”, *Langmuir*, **5**, 140-144 (1989).

Acknowledgement

I would like to express my gratitude to a number of people who have assisted me and contributed to this thesis. This research was carried out at Fujitsu Laboratories Ltd., and Research Center of Advanced Science and Technology, The University of Tokyo for 15 years.

I am very grateful to Professor Akira Nakajima, Professor Takaaki Tsurumi, Professor Junzo Tanaka, Professor Etsuro Sakai, Associate professor Sachiko Matsushita, Department of Inorganic Materials, Graduate School of Science, Tokyo Institute of Technology and Professor Toshiya Watanabe and Kazuhito Hashimoto of Tokyo University, Associate professor Naoya Yoshida of Kogakuin University for their useful advice and valuable suggestions.

Special thanks are due to Dr. Seiichi Kondo, Dr. Tatsuo Ishikawa and Professor Kazuhiko Kandori, Osaka University of Education, Associate professor Hidekazu Tanaka of Shimane University, for their valuable suggestion and experimental support.

I would like to express my sincere gratitude to Dr. Mineharu Tsukada and Dr. N. F. Cooray, Fujitsu Labratories Ltd., for their helpful discussion and suggestions.

Finally, I would like to thank my father, mother and members of my relative for their unending encouragement and gratis support over the years.

June 2014

Masato Wakamura